

THE UNIVERSITY OF HULL

Quantitative Non-destructive Evaluation Using  
Laser Generated Ultrasonic Pulses

being a Thesis Submitted for the Degree of

Doctor of Philosophy

in the University of Hull

by

Ross Andrew Crosbie, BSc. (Strathclyde)

November 1987

### Acknowledgements.

I would like to thank my supervisors, Prof. Stuart Palmer and Dr. Richard Dewhurst, for advice and guidance throughout the project. I am also grateful to Alan Aindow, Chris Edwards, Jerry Cooper and Andy McKie for many useful discussions and to the latter for the use of his interferometer. I would also like to thank the staff of the mechanical workshop and John Lawrence for technical assistance and Alan Boyer for drawing many of the diagrams used in this thesis.

I am indebted to the SERC for providing a research grant for three years and to the CEGB for providing a CASE award. Thanks also go to Dr. Phil Richards of the CEGB for discussions and arranging for sample manufacturing facilities to be made available.

Summary of Thesis submitted for Ph.D. degree  
by Ross Andrew Crosbie  
on  
Quantitative Non-destructive Evaluation Using  
Laser Generated Ultrasonic Pulses

The work presented here utilises features of laser generated ultrasound for the detection of defects in solids. Ultrasound is generated non-contactively by this method and likewise many of the detection devices used do not require direct coupling to the test pieces, thus acoustic pulses with high frequency components are able to be produced and monitored on a range of samples.

Steel samples coated with between 3 and 7mm of plasma-transferred arc depositions are examined for bond quality via measurements of attenuation caused by porosity in the coatings, found to be related to weld current. Surface breaking cracks, (of depth  $< 3\text{mm}$ ), in such claddings are quantitatively detected by a method which utilises Rayleigh pulses. A two sided automated scanning system is described which examines samples for subsurface defects. Results from the examinations of a dural test piece, plasma sprayed steel bars and carbon fibre composite samples are presented. Resolution of defects is shown to be within 0.5mm for a 1mm thick section of the composite material. A second scanning technique, requiring access to only one sample face, is presented which employs an interferometer for detection and is thus a truly remote system.

Laminar flaws are modelled using flat-bottomed holes, the dimensions of which are measured using the resonance of the bodies. A theoretical investigation using various boundary conditions suggests possible applications for quantitative NDE of structures with well defined natural vibration frequencies. The propagation of acoustic transients in plates is also examined. Possible future work concerning laser/ultrasonic NDE is discussed.

## CONTENTS.

### CHAPTER 1

INTRODUCTION	1
--------------	---

### CHAPTER 2

#### LASER GENERATED ULTRASONIC PULSES IN METALS

2.1/ Introduction	5
2.2/ Thermoelastic Source	7
2.3/ Plasma Source	10
2.4/ Modified Surface	13
2.5/ Laser generated Surface Acoustic Transients	15
2.6/ Some Applications of Laser Generated Ultrasound	18
2.7/ Laser Generated Ultrasound for Flaw Detection	
2.7a/ Advantages of a Non-contacting System	23
2.7b/ Reported Uses for Flaw Detection	25

### CHAPTER 3

#### PROPAGATION OF TRANSIENT ULTRASONIC PULSES IN ELASTIC PLATES

3.1/ Introduction	30
3.2/ Off Epicentral Motion due to a Surface Vertical Force	31
3.3/ Experimental Details	37
3.4/ Results and Discussion	38

### CHAPTER 4

#### ULTRASONIC TRANSDUCERS AND METHODS FOR NON-DESTRUCTIVE EVALUATION

4.1/ Piezoelectric Devices	41
4.2/ EMATs	46

4.3/ Capacitance or Electrostatic Methods	50
4.4/ Optical Detection Techniques	
4.4a/ Knife Edge Technique	53
4.4b/ Interferometers	53
4.5/ Methods of Ultrasonic NDE	
4.5a/ History	58
4.5b/ Methods of Display	60
4.6/ Comments	60

## CHAPTER 5

### APPLICATIONS OF LASER GENERATED ULTRASOUND TO NON-DESTRUCTIVE EVALUATION OF PLASMA TRANSFERRED ARC CLAD SAMPLES

5.1/ Rayleigh Pulse Interactions with Defects	62
5.2/ Interaction of Laser Generated Rayleigh Pulses with Surface Breaking Slots	65
5.3/ Plasma Transferred Arc Clad Samples	68
5.4/ Detection and Sizing of Real Cracks on a Weld Bead	71
5.5/ Variation of Acoustic Scatter with Weld Integrity	
5.5a/ Sample Manufacture	75
5.5b/ Experimental Technique	77
5.5c/ Discussion	83

## CHAPTER 6

### TWO-DIMENSIONAL SUB-SURFACE FLAW VISUALISATION

6.1/ Introduction	86
6.2/ Samples	88

6.3/ Through Transmission Experiments	
6.3a/ Experimental Technique	89
6.3b/ Results	
(i) Dural Test Sample	92
(ii) Plasma Sprayed Steel Samples	93
(iii) Carbon-fibre Composite Samples	95
6.4/ Single Sided Non-contact Inspection	99
6.5/ Discussion	102
CHAPTER 7	
FLEXURAL RESONANCE MEASUREMENTS OF DISKS	
7.1/ Introduction	104
7.2/ Classical Two-dimensional Theory of Flexural Motions of Elastic Plates, (Thin Plate Theory)	107
7.3/ Effects of Shear Deformation and Rotatory Inertia, (Thick Plate Theory)	109
7.4/ Boundary Conditions	113
7.5/ Experimental Procedure	117
7.6/ Results and Discussion	
7.6a/ Fully Clamped Disks	118
7.6b/ Flat-bottomed Holes	119
7.6c/ Resonance Build up	122
7.6d/ Bonded Samples	124
7.7/ Conclusions	125
CHAPTER 8	
DISCUSSION	127
REFERENCES	134

CHAPTER 1.

INTRODUCTION

This thesis develops some applications of laser generated ultrasound for the non-destructive evaluation, (NDE), of solids. Fundamental principles involved in producing acoustic pulses in metals due to interaction with pulsed laser energy are already understood. Models have been developed describing the various generation mechanisms which fall into three regimes. These are thermoelastic, (heating the surface), plasma, (ablating a small amount of material), and modified surface. The models predict bulk directivity patterns, epicentral and surface displacements which exhibit good agreement with experimentally produced waveforms.

The work presented here utilises features of laser generated ultrasonic pulses for the detection of defects in solids. Laser generated ultrasound is at present a laboratory tool lacking practical application in industry. This work contributes to the development of practical NDE using a laser-acoustic source on a range of samples containing artificial and real defects. Samples are examined for both surface breaking defects and for buried flaws, quantitative measurements being made in most cases.

The following chapter reviews firstly the models developed for the laser-acoustic source and secondly the applications of the technique. Particular emphasis is placed on reported methods for flaw detection.

Off-epicentral waveforms in plates are considered in Chapter 3. A model based on work by Pilant, (1979), is presented which shows good agreement with experimental waveforms produced by an ablation source. Multiple arrivals due to reflections are neglected in this treatment but were included in the work of Pao et al, (1979), which is also considered.

Traditional methods and a brief history of ultrasonic NDE are discussed in Chapter 4. Probe design and scanning systems are considered as well as giving an outline of some techniques currently in practice. Transducers used for detection of ultrasound in this thesis are described with particular attention being given to electromagnetic acoustic transducers, (EMATS).

Chapters 5 to 7 describe applications of laser generated ultrasonic pulses to non-destructive evaluation of solids. In the first of these chapters steel samples coated with plasma-transferred arc depositions are examined for both bond quality and surface breaking defects. The model presented by Cooper et al, (1986), utilising Rayleigh pulse interaction to characterise surface breaking slots is used. Results are presented here for sizing of real cracks using information from such interactions in the time domain. Experimental enhancement of the signal reflected from the

defect is necessary due to both the relatively poor quality of the sample surface and the irregular shape of the crack tip. Rayleigh pulses are also used to investigate bond quality via attenuation measurements due to scatter. A similar experiment for the estimation of bond quality is performed using bulk laser generated ultrasonic pulses.

Sub-surface defects were also examined and sized. The bulk of Chapter 6 is devoted to describing two sided automated scanning of flat samples containing sub-surface delaminations. Variations between ultrasonic pulses which propagated through a 3mm duraluminium plate and through regions of the plate which contained a saw cut at half thickness are initially examined. The observations from this study are then used to set two criteria for flaw detection. The first of these criteria relies on the time of flight of the ultrasonic pulse whereas the second depends on the amplitude of ultrasonic signal detected after a set time. These methods are then used for the detection of artificial defects in carbon-fibre composite samples and for the investigation of bond quality in plasma sprayed steel bars. A second scanning system is presented which employs an interferometer for ultrasonic detection and is thus a totally non-contact method. The duraluminium sample containing saw cuts was used here.

In Chapter 7 laminar flaws are modelled as flat-bottomed holes. The resonant frequencies of fully-clamped, simply-supported and free edge disks are calculated for both acoustically thick and thin plates. Resonant

frequency values of fully-clamped aluminium plates and flat-bottomed holes milled into duraluminium excited by laser pulses are presented. The correlation between experimental and theoretical data suggests a possible application for quantitative NDE of delaminations. It is demonstrated that the calculated frequency values for thick plates having fully-clamped edges give good agreement with both sets of experimental data.

The results from each section are brought together in the concluding chapter where possible future work concerning laser based NDE is also discussed.

CHAPTER 2.

LASER-GENERATED ULTRASONIC PULSES IN METALS.

2.1/ Introduction.

In the following chapters experiments using ultrasonic pulses produced by laser irradiation of solids are described. Laser-generated ultrasound dates back to 1963 when White irradiated metals with a variety of sources of electromagnetic radiation to produce transient stress pulses. Ledbetter and Moulder, (1979), were the first to demonstrate that a laser acoustic source produces longitudinal, shear and surface, (Rayleigh), ultrasonic pulses in solids, although little detail was given of the relationship between acoustic amplitude and laser energy. The generation mechanisms of these pulses are now well understood and several reviews on the subject exist, (Scruby et al; 1982, Hutchins; 1986, Hutchins and Tam; 1986). A brief description of the mechanisms of generation with the resulting epicentral and surface displacement waveforms and associated directivity patterns are given here together with a comparison with experimental waveforms. There then follows a review of the applications of the laser-acoustic source with particular emphasis being placed

on its uses for NDE.

The field of photoacoustics also encompasses acoustic generation by electromagnetic radiation in fluids, first noted by Bell in 1880. Interest in this effect has recently increased due to the invention of the laser and the improvement of detection systems. Details of the physics and applications of this effect can be found in many reviews on the subject, (Pao; 1977, Rosencwaig; 1980, Tam; 1983, Hutchins and Tam; 1986, Tam; 1986), and shall not be discussed here.

The mechanisms of ultrasonic generation by lasers in solids are dependent on the incident optical power density used. Two regimes have been identified. At low power densities the absorbed energy causes thermal expansion at the metal surface, this is known as the thermoelastic source. At very high power densities a plasma is formed causing ablation of material from the surface, this being the plasma or ablation source. In the latter case the ablation of material following melting leads to a momentum transfer to the surface and the subsequent creation of normal forces. A similar momentum transfer may be achieved by evaporating a thin coating, such as an oil layer, from the surface and has the advantage of not marking the material.

Research in the subject has mainly used irradiation from commercially available Nd:YAG lasers, ( $\lambda=1.06\mu\text{m}$ ), with pulses of full-width half maximum, (FWHM), between 20 and 40ns incident on metal, (typically aluminium), surfaces.

## 2.2/ Thermoelastic Source.

Optical power densities of less than  $10^6 \text{Wcm}^{-2}$  incident on a metal surface are insufficient to change its state. A small part of the incident energy, (about 7% for polished aluminium), is absorbed and converted into heat while the rest is reflected. The absorption takes place within the electromagnetic skin depth of the metal which, for  $1.06\mu\text{m}$  radiation incident on aluminium, is about 5nm. The temporal and spatial profiles of the resultant temperature rise within the solid may be estimated, (Aindow; 1986), using theories such as those presented by Ready, (1971). Thermal conductivity over the duration of the laser pulse causes an increase in the thermal source thickness. An incident pulse of 30ns duration will increase the effective source thickness in aluminium by  $10^3$  with respect to the skin depth. This dimension will normally be far smaller than the diameter of the laser beam, (typically 3mm), and hence the source can be approximated as a thin expanding disk, fig 2.1. The heating of the surface occurs rapidly over the duration of the laser pulse, but the cooling time is dependent on the thermal diffusion properties of the sample and will be far longer. The forces caused by this source can therefore be approximated as acting with a step function dependence in time. The principal stresses set up by the thermoelastic source are radial, acting parallel to the surface. The boundary conditions state that the surface should be stress free,

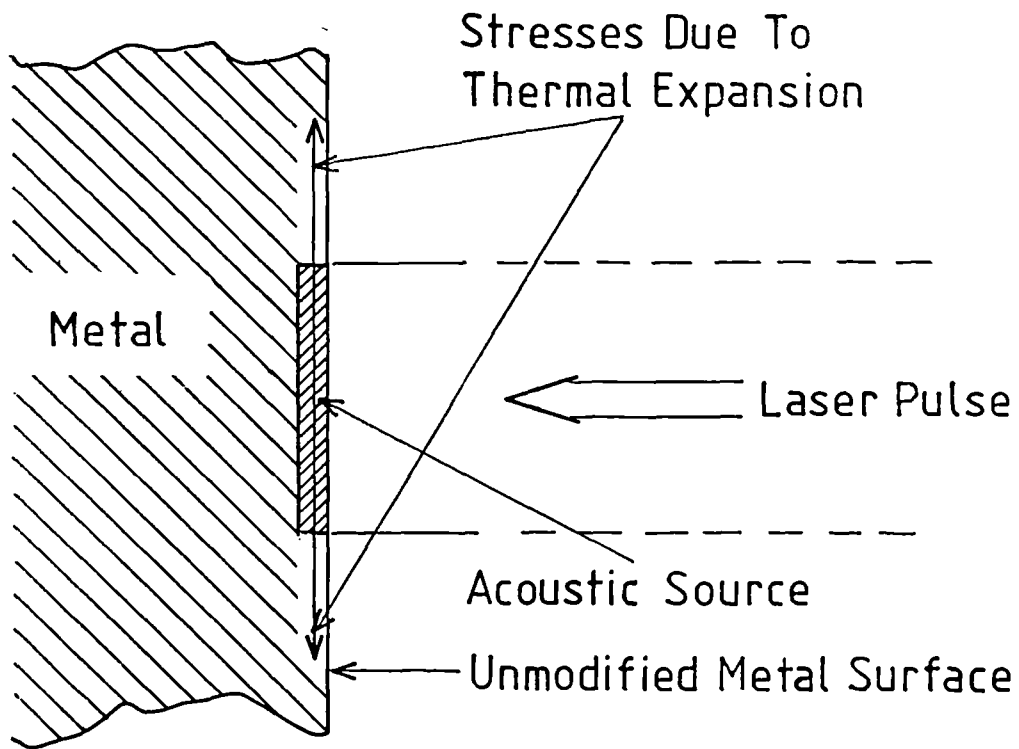
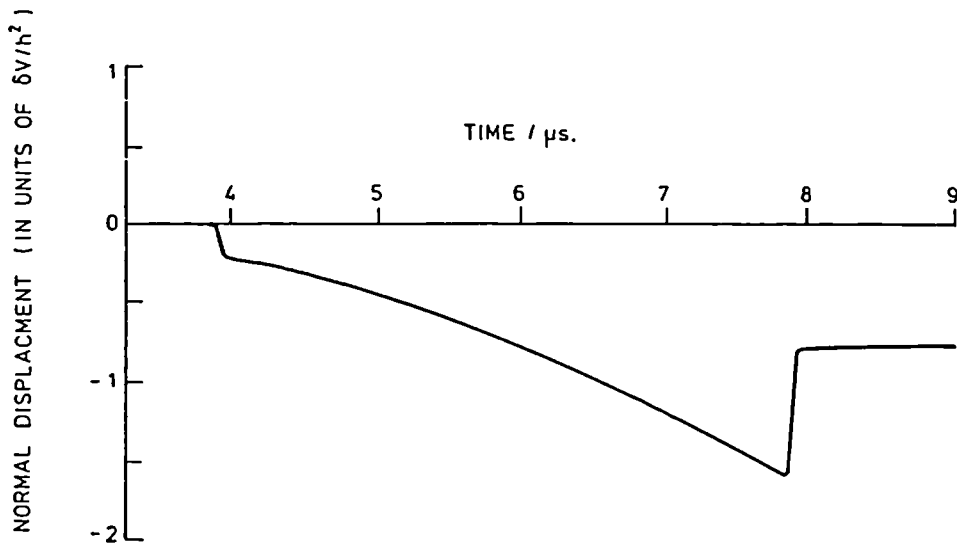


Fig 2.1 Schematic diagram of thermoelastic source. Incident laser power density  $< 10^6 \text{Wcm}^{-2}$ .

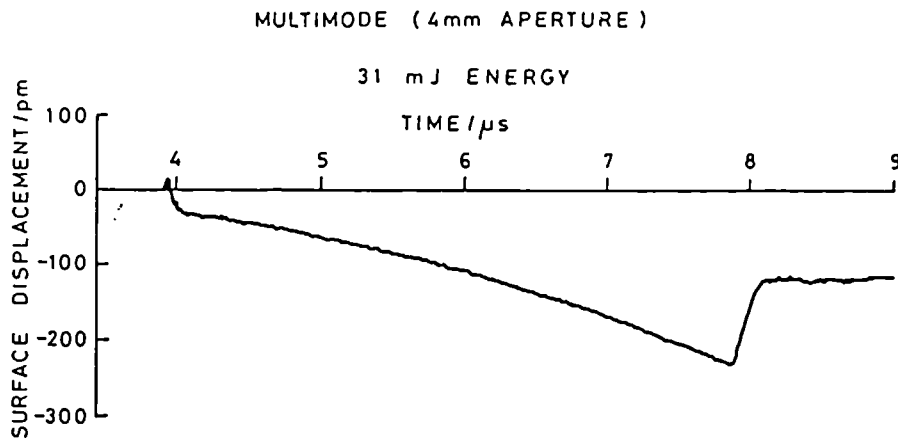
however small force dipole components normal to the surface are created probably due to the normal stresses set up in the finite depth of the source, (Doyle; 1986).

Scruby et al, (1980), modelled the thermoelastic source as an instantaneous expansion of a point volume of metal at the surface. Thermal diffusion was neglected and the model relied on unpublished work by Sinclair. The theoretical normal surface displacement generated at the epicentre of a plate using this model, fig 2.2a, does however agree well with an experimental waveform captured at the epicentre of a 1" aluminium plate, fig 2.2b. The neglected thermal diffusion may account for the positive going spike of the longitudinal arrival not being predicted by the theory. In a later publication, (Dewhurst et al; 1982), thermal diffusion was taken into account by including a small normal force dipole due to heat propagating from the source into the metal. This led to the waveform shown in fig 2.2c which has improved correlation with experiment. The method used by Achenbach, (1973), to derive the surface displacements of a half space due to a normal point load was expanded by Cooper, (1985), who presented an alternative model for the point thermoelastic source. In this treatment a point, radial, in plane force of arbitrary magnitude and Heaviside time dependence was used as a representation of the source. The waveform derived using the above method was qualitatively consistent with that obtained by Rose, (1984), and with experiment.

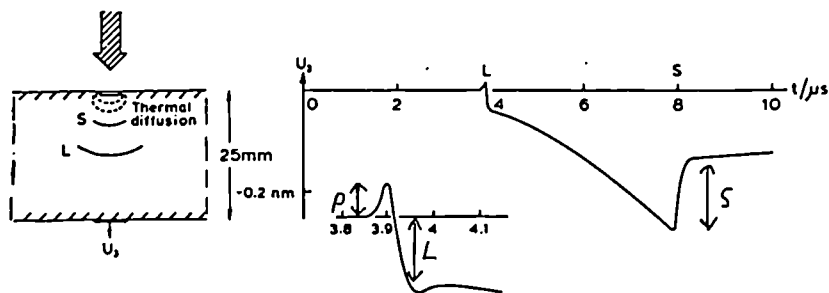
The initial acoustic event from the thermoelastic



(a)



(b)



(c)

Fig 2.2 Epicentral displacements from a thermoelastic source.  
 (a) Theory after Scruby et al, (1980).  
 (b) Experiment after Scruby et al, (1980).  
 (c) Theory assuming the source to be an expansion over a diameter 4mm diffusing into plate with diffusivity  $8.6 \times 10^{-5} \text{ m}^2 \text{ s}^{-1}$ , detector diameter 6mm. After Dewhurst et al, (1982).

source is seen from fig 2.2 to be a small positive pulse, (p-pulse), and negative step, (l-step), which is the arrival of the longitudinal pulse, followed at approximately twice this time by a shear step. It has been found, (Scruby et al 1980), that on epicentre the shear step has about four times the normal displacement amplitude of the longitudinal. Scruby et al, (1981), suggested that the amplitudes of acoustic displacements produced by a thermoelastic source in a given material were directly proportional to the incident laser energy and independent of both the beam area and source thickness. Aindow et al, (1981), demonstrated the linear relationship between incident laser energy and acoustic amplitude, fig 2.3a. Ultrasonic signals were generated on a 25mm thick aluminium sample with the resultant ultrasonic disturbances monitored non-contactingly on epicentre. A similar experimental arrangement was used by Dewhurst et al, (1982), who showed that the changes in power density at the surface did not have an appreciable effect on the acoustic amplitudes provided that plasma breakdown didn't occur, fig 2:3b. A nominally fixed laser energy was used with converging and diverging lenses inserted to vary the incident power density.

The directivity of the thermoelastic source was determined experimentally for an acoustic line source by Hutchins et al, (1981). Pulses of power density  $(13 \pm 2) \text{ MWcm}^{-2}$  were incident at the centre of the flat surface of an aluminium hemisphere with a resonant PZT

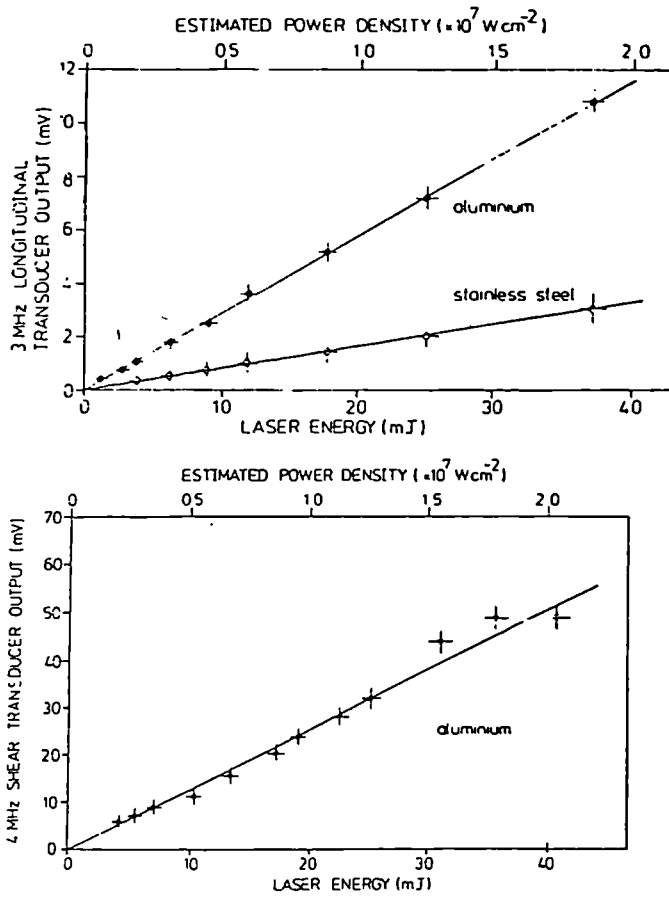


Fig 2.3(a) Variation of acoustic pulse amplitude, (peak to peak voltage from the transducer), in non plasma regime. After Aindow et al, (1981).

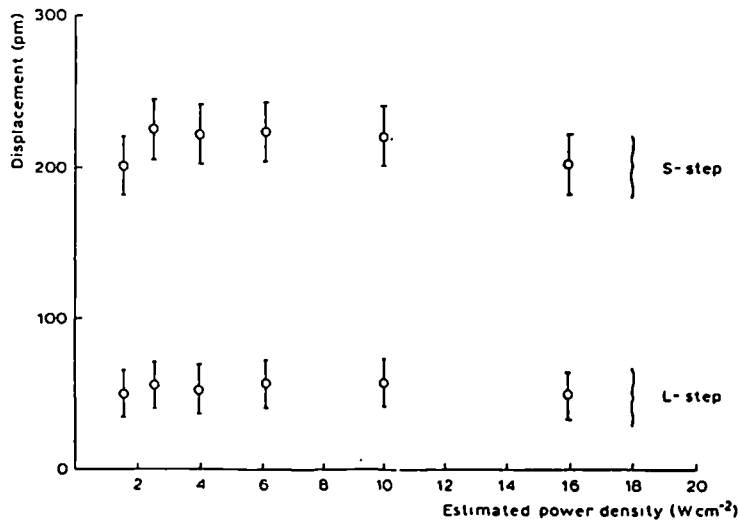


Fig 2.3(b) Amplitude of L and S steps as a function of incident laser power density after propagating through a 25mm aluminium sample. Incident laser energy = 33mJ. After Dewhurst et al, (1982).

transducer moved around the curved face, fig 2.4. The magnitude of the acoustic signal at any angle was measured in terms of the initial peak to peak voltage across the longitudinally sensitive PZT. The radius of the hemisphere, 5cm, was sufficiently large that measurements were made in the farfield. Both 1 and 5MHz transducers were used. The directivity for longitudinal and shear pulses are shown in fig 2.5a and b, respectively. A quasi-cw theory was used to model this source. The angular dependence of the resultant radial displacements caused by longitudinal waves and the tangential displacements from shear waves in the farfield were calculated. Although in reality the acoustic source is pulsed, surprisingly good agreement with experiment was obtained, fig 2.6. More surprising perhaps is the degree of correlation between the experimentally measured radial component of the shear pulse, fig 2.5b, and the calculated tangential component of the shear wave, fig 2.6b.

The directivity patterns show that most of the longitudinal energy is radiated at an angle of  $\sim 50^\circ$  from the normal with the signals detected perpendicular and parallel to the surface being far smaller. In contrast, a significant amount of shear wave energy is radiated normal to the source with maximum energy propagation at  $\sim 30^\circ$  from the normal.

### 2.3/ Plasma Source.

If the incident power density is increased, either by increasing the energy in the laser pulse or by focusing the spot, then the surface temperature will rise until the

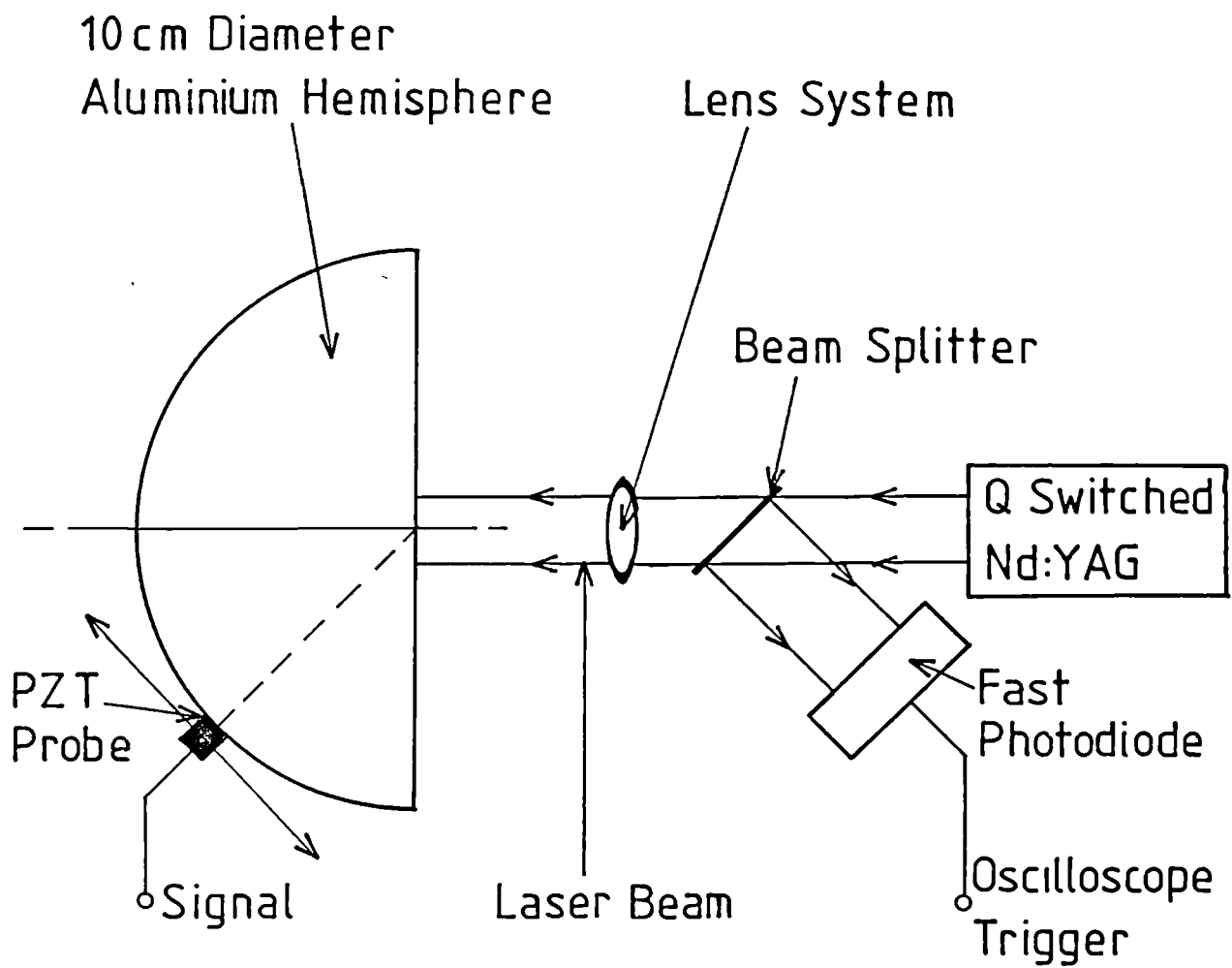


Fig 2.4 Experimental arrangement used by Hutchins et al, (1981), to measure the directivity of the laser-ultrasonic source. A focusing lens was used to produce a plasma source, whereas defocusing and cylindrical lenses were used for the thermoelastic line source.

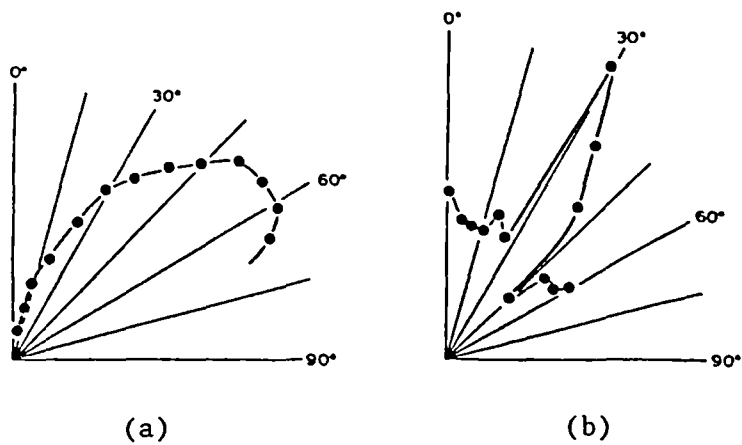


Fig 2.5 Experimental ultrasonic directivity patterns at 1MHz generated by a thermoelastic laser line source. (a) longitudinal.  
 (b) shear.  
 After Hutchins et al, (1981).

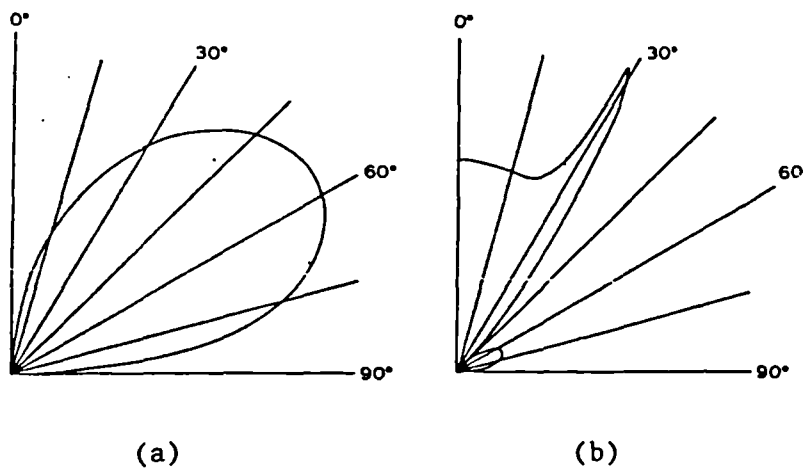


Fig 2.6 Theoretical ultrasonic directivity patterns for an infinitely long line source with shear drive. (a) longitudinal.  
 (b) shear.  
 After Hutchins et al, (1981).

melting point is reached. On further increasing the power density, to above  $\sim 10^7 \text{Wcm}^{-2}$ , ablation of the metal occurs creating normal forces in the sample due to momentum transfer from the plasma, fig 2.7. The rate of evaporation and hence the recoil force follows the form of the laser pulse. Cooper, (1985), estimated the amount of material ejected from an aluminium sample on irradiation with a focused 30mJ pulse to be  $2.7 \times 10^{-8} \text{g}$ , with the average velocity of the expanding vapour plume as  $1.6 \times 10^4 \text{ms}^{-1}$ . From this he estimated the peak force on the surface to be about 20N. The plasma continues to expand and thus exert a pressure on the surface after the duration of the laser pulse, falling off approximately as the inverse of time. The normal force from the ablation is an order of magnitude larger than that developed by the thermoelastic interaction and so dominates the latter.

Dewhurst et al, (1982), calculated the normal displacements produced by the plasma source on epicentre. In this treatment the force exerted on the surface was initially assumed to have Heaviside dependence in time, the resultant displacement is shown in fig 2.8a. The comparable experimental waveform, fig 2.8b, (power density  $\sim 4.5 \times 10^8 \text{Wcm}^{-2}$ ), shows the same general features. The longitudinal arrival is seen as a step, in the opposite sense to that caused by the thermoelastic source, followed by a gradual rise of the surface before the arrival of the shear pulse. The plasma source, as already discussed, does not have the Heaviside time dependence assumed. The dip in

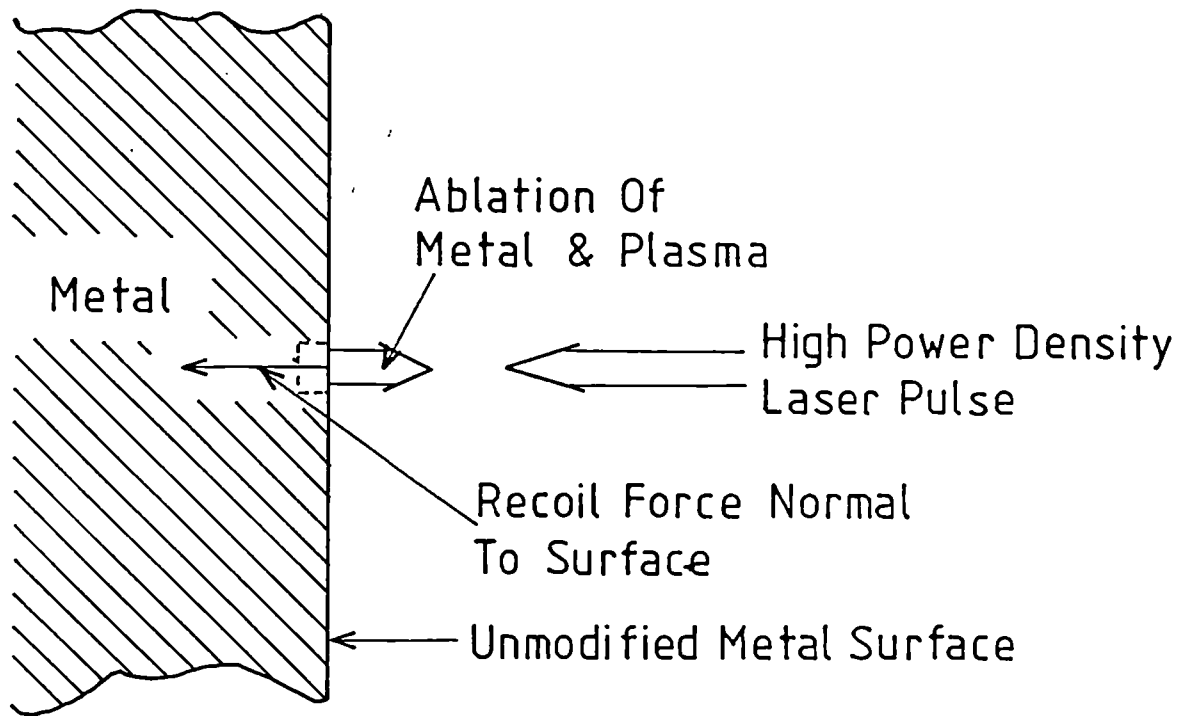


Fig 2.7 Schematic diagram of plasma or ablation source. Incident laser power density  $> 10^7 \text{ Wcm}^{-2}$ .

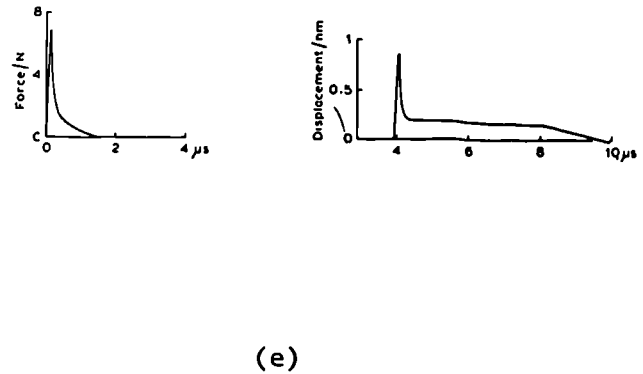
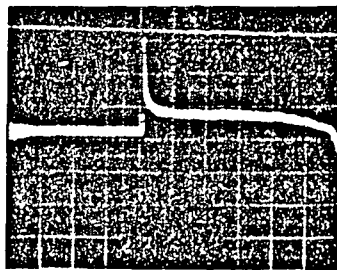
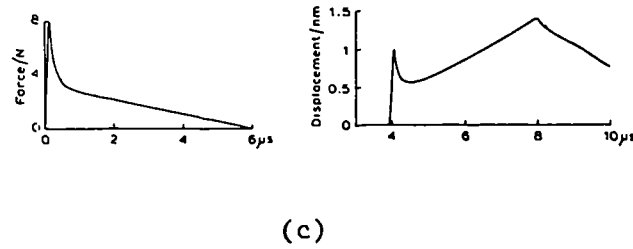
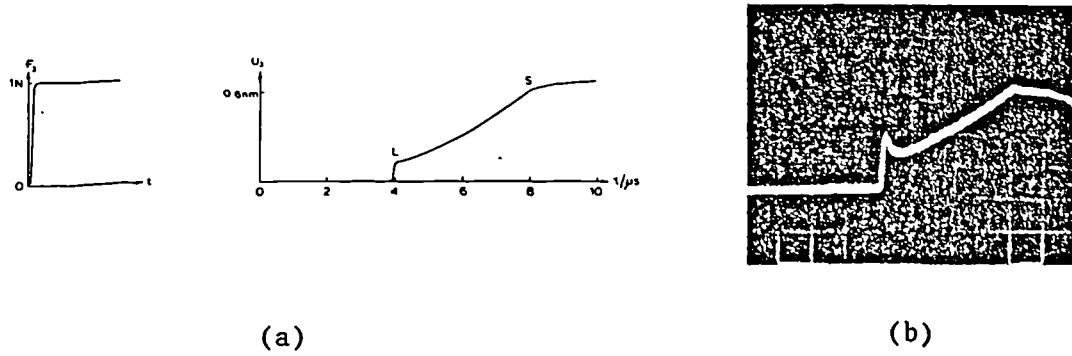


Fig 2.8 Plasma source epicentral waveforms after Dewhurst et al, (1982).  
 (a) Theoretical displacement waveform assuming the source to be a point force normal to the surface with step-function time dependence.  
 (b) Experimental waveform from a 50mm diam x 25mm thick aluminium sample. Laser power density =  $4.5 \times 10^8 \text{ Wcm}^{-2}$ .  
 (c) Calculated ultrasonic waveform, assuming the source to be a normal force. The corresponding time dependence of the force is also shown.  
 (d) Experimental waveform as (b) for laser power density =  $1.8 \times 10^8 \text{ Wcm}^{-2}$ .  
 (e) Calculated waveform assuming the source to be a combination of normal force and thermoelastic expansion with asymmetric time dependence on normal force.

the experimental waveform after the longitudinal arrival and the difference in gradients after the shear arrival are evidence of this. The normal source force function was modified so that it became asymmetric with a fast rise and slow fall. The resultant calculated epicentral displacement waveform, fig 2.8c, shows improved agreement with experiment. When the power density is lower, (approximately  $10^8 \text{ Wcm}^{-2}$ ), then the normal force on the surface has an approximate Gaussian time dependence approximately following that of the optical pulse. Such an impulse produces an epicentre displacement as shown in fig 2.8d. In this regime the normal force from the recoil is not strong enough to totally dominate thermoelastic expansion terms. Both mechanisms were included in the model which produced fig 2.8e.

The same authors, (Dewhurst et al), experimentally measured the variation of epicentre displacement amplitude with incident power density, fig 2.9. The p-step at the beginning of the longitudinal arrival initially increased with power density, reaching a maximum as the plasma spark was clearly visible, and subsequently decreased due to the masking effect of the plasma. The shear step however decreased to a point where it became a change in gradient. It was also shown that the shape of the experimental waveform remained constant for constant power density when the incident laser energy was varied. The amplitude of the features did however increase linearly with increasing incident energy, fig 2.10.

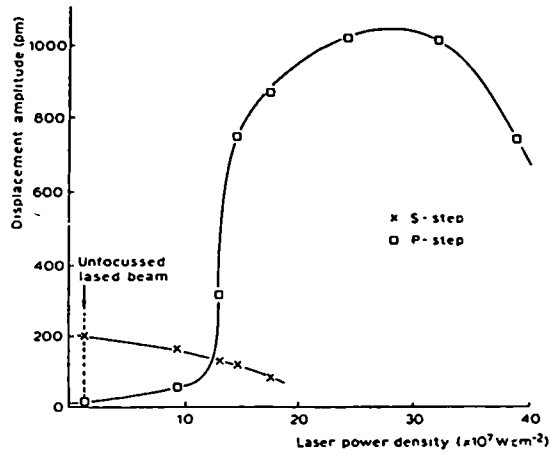


Fig 2.9 Variation in acoustic amplitude as a function of laser power density at a constant energy of 33mJ. After Dewhurst et al, (1982).

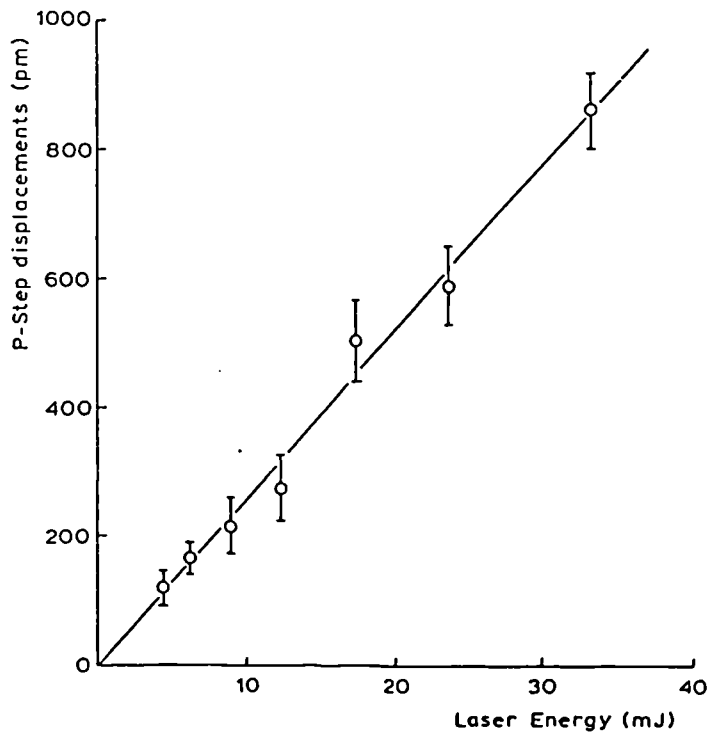


Fig 2.10 Amplitude of P-step against incident laser energy at a constant power density of  $180 \text{ MW cm}^{-2}$ . After Dewhurst et al, (1982).

The experimental apparatus described by Hutchins et al, (1981), for measuring the variation of amplitude with angle for a thermoelastic source, fig 2.4, was used in the corresponding experiment for a plasma source. A power density greater than  $10^8 \text{Wcm}^{-2}$  was found to produce the directivity pattern for longitudinal pulses shown in fig 2.11. A harmonic model was again used. Here a disk source with normal drive predicted the longitudinal and shear displacements shown in fig 2.12. Again good agreement between theoretical and experimental measurement of the longitudinal energy was observed.

Thus it is noted that increasing the laser power density to above the plasma formation threshold has significantly altered the directivity of the source. Most of the longitudinal energy is now radiated in a broad lobe normal to the surface whilst there is little radiation of shear energy in this direction.

#### 2.4/ Modified Surface.

In 1963 White suggested that the efficiency of conversion from optical energy to ultrasonic energy might be improved by using a layer to constrain the generation surface. This has since been demonstrated by several authors, (e.g. Fairand et al; 1974, von Gutfeld and Melcher; 1977, Anderholm; 1970). A solid layer, transparent at the laser wavelength, is cemented rigidly to the sample. The surface is no longer free so at low power densities a stronger normal force is created.

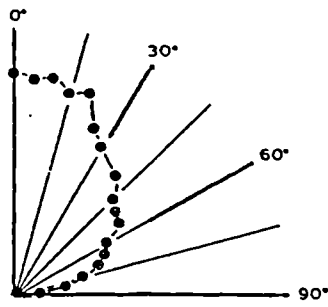


Fig 2.11 Experimental ultrasonic longitudinal directivity pattern in the presence of plasma formation. 1mm diameter source area of irradiation, 1MHz transducer for detection.  
After Hutchins et al, (1981).

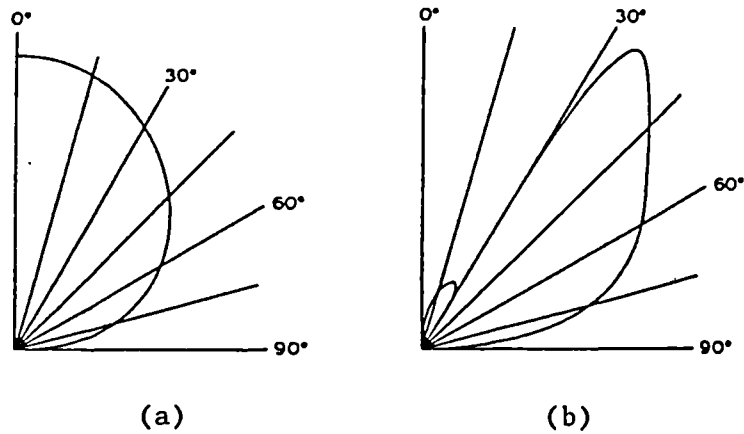


Fig 2.12 Theoretical ultrasonic directivity patterns for a disk source with normal drive, (a) longitudinal  
(b) shear.  
After Hutchins et al, (1981).

A separate technique demonstrated by Fox, (1974), and O'Keefe and Skeen, (1972), enhances generation by evaporating coatings, usually of higher absorption than the metal, from the sample surface at higher power densities. The acoustic generation mechanism here being based on momentum transfer from the recoil of the evaporated film. A normal force is produced as in the case of the plasma source usually with a temporal profile approximately following that of the laser pulse, i.e. it is a transient event.

Surface modifications were more rigorously investigated by Hutchins et al, (1981b). Power densities were varied from thermoelastic to plasma regimes and the effect of both types of surface modification to metals were examined using longitudinal and shear transducers to detect epicentral displacements. It was reported that both types of surface modification significantly increased the generation of longitudinal pulses, (typically by >25dB), at low optical power densities, ( $<10^7 \text{Wcm}^{-2}$ ). The constraining layer produced significantly greater enhancement of the shear pulse, (about 10dB), than an evaporated coating for the same power density. As the power density was increased to above  $5 \times 10^7 \text{Wcm}^{-2}$ , coatings of both thin oil and grease were found to enhance the generation of both shear and longitudinal pulses as was the glass constraining layer. Again the latter method gave greater enhancement to the shear pulse, an increase of ~50dB compared to ~25dB, the longitudinal enhancements being approximately 30dB in both

cases.

Hutchins et al also obtained experimental directivity patterns for longitudinal pulse energy using the apparatus shown in fig 2.4 with a 5MHz longitudinally sensitive PZT detector. A power density of  $<10^7 \text{Wcm}^{-2}$  was used and no ablation of metal occurred. The directivity pattern for a constraining layer is shown in fig 2.13a, for light oil in fig 2.13b and for silicon resin in fig 2.13c. It is seen that surface modification dramatically changes the directivity pattern when contrasted with that for the longitudinal pulse from the thermoelastic source, fig 2.5a. The modified surface source was compared to that of a vibrating piston whose normal driving force led to the directivity pattern shown in fig 2.14. Silicon resin was thus not as effective in inducing normal stresses as the other modifications examined.

Because these last directivity patterns were produced at low optical power densities it is thought that this source may be important to NDE methods which rely on a strong normal longitudinal signal.

## 2.5/ Laser Generated Surface Acoustic Transients.

In 1968 Lee and White used a Q-switched ruby laser to generate surface pulses which were detected by a resonant piezoelectric device. There has been broadband detection and qualitative modeling of these pulses. A point normal force having a step time dependence was applied to a surface in the theory of Pekeris, (1955). From this, expressions for

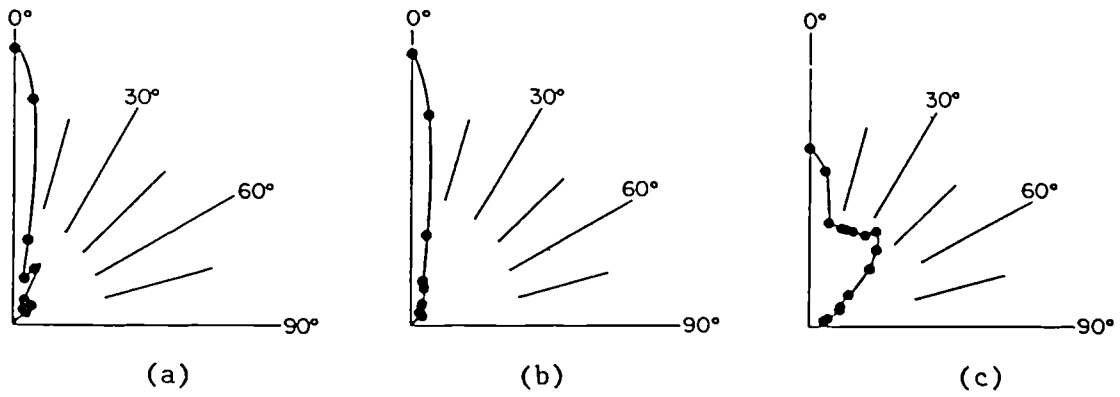


Fig 2.13 Experimentally determined longitudinal directivity patterns at 5MHz for various states of an aluminium alloy surface. An unfocused, multimode laser pulse of 30mJ energy was used.  
 (a) constraining layer  
 (b) light oil  
 (c) silicon resin.  
 After Hutchins et al, (1981b).

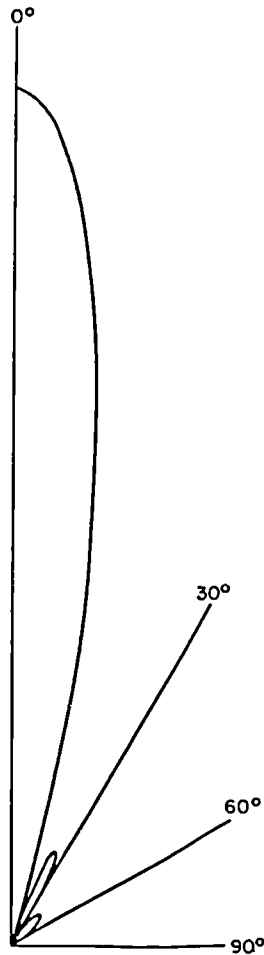


Fig 2.14 The classical longitudinal directivity of 5MHz longitudinal waves from a vibrating piston of width 5mm, assuming radiation into a medium of bulk modulus similar to that of aluminium.  
 After Hutchins et al, (1981b).

the vertical and horizontal components of the surface displacement, at a distance,  $R$ , produced on a semi-infinite body were derived. Aindow et al, (1983), used these expressions to model the surface pulses produced by both thermoelastic and ablation sources. A normal force with delta function time dependence gives a displacement equivalent to the differential of that produced by a normal Heaviside force. The latter function was calculated and convolved with the time dependence of the ablation process and plasma lifetime. The surface displacements given by this model for the ablation source are shown in fig 2.15a. These compare well with experimental surface waveforms detected by a wide band capacitance probe, fig 2.15b. The reciprocity principle was used to relate a horizontal force with step time dependence to the vertical displacements produced by the thermoelastic source, fig 2.16a. Good agreement was shown with the corresponding experimental waveforms, fig 2.16b.

It is seen from figures 2.15 and 2.16 that a fast surface wave,  $(L)$ , is generated as well as the larger Rayleigh disturbance and that the polarity of the bipolar Rayleigh pulse is reversed at low power densities. Shear energy also travels along the surface, with a velocity slightly higher than that of the Rayleigh pulse and accounts for the change in gradient before the arrival of the bipolar pulse shown in figures 2.15 and 2.16.

Aindow, (1986), studied experimentally the relationship of surface pulse height with incident energy in

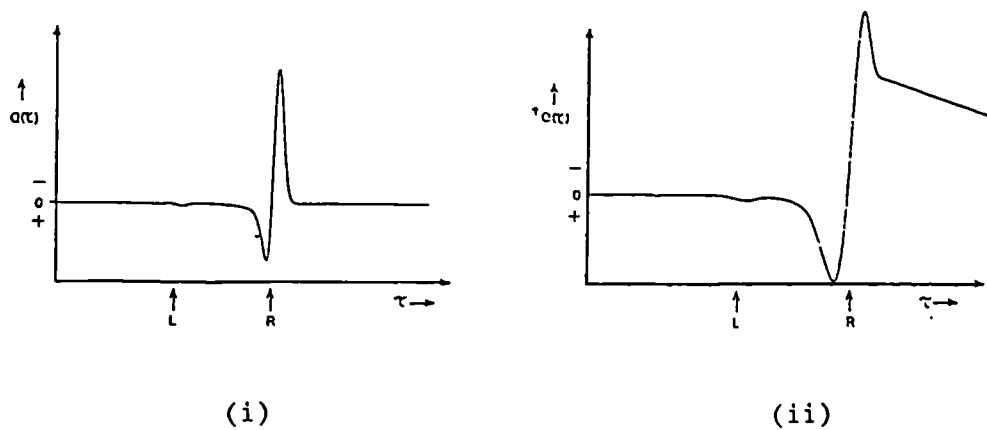


Fig 2.15 (a) Theoretical surface waveforms at high laser intensities. (i) weak plasma (ii) strong plasma. Arbitrary vertical scale. L and R denote the surface longitudinal and Rayleigh wave arrivals respectively. After Aindow et al, (1983).

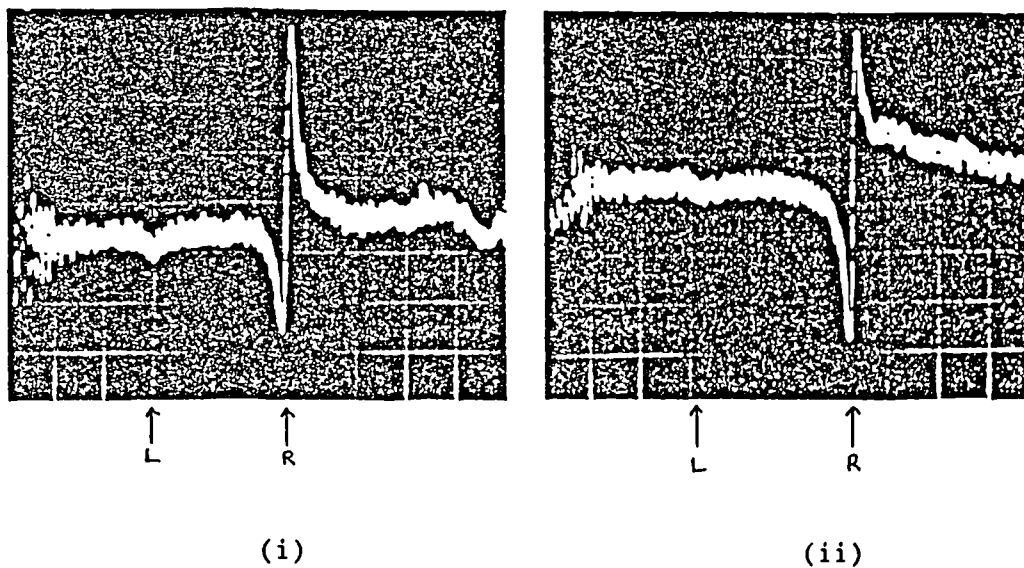


Fig 2.15(b) Capacitance probe traces corresponding to the theoretical traces 2.15(a). 30mJ incident laser pulse focused with focal length lens (i) 250mm (ii) 25mm. ~20mm between source and detector. Arbitrary vertical scale. After Aindow et al, (1983).

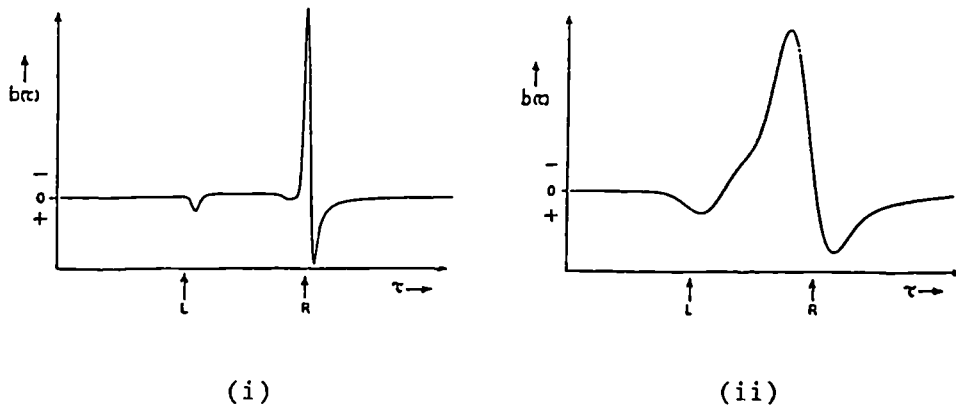


Fig 2.16(a) Theoretical surface waveforms at low laser intensities. (i) for a point source where a 10MHz bandwidth limit has been assumed (ii) 3mm diameter source. Arbitrary vertical scale. After Aindow et al, (1983).

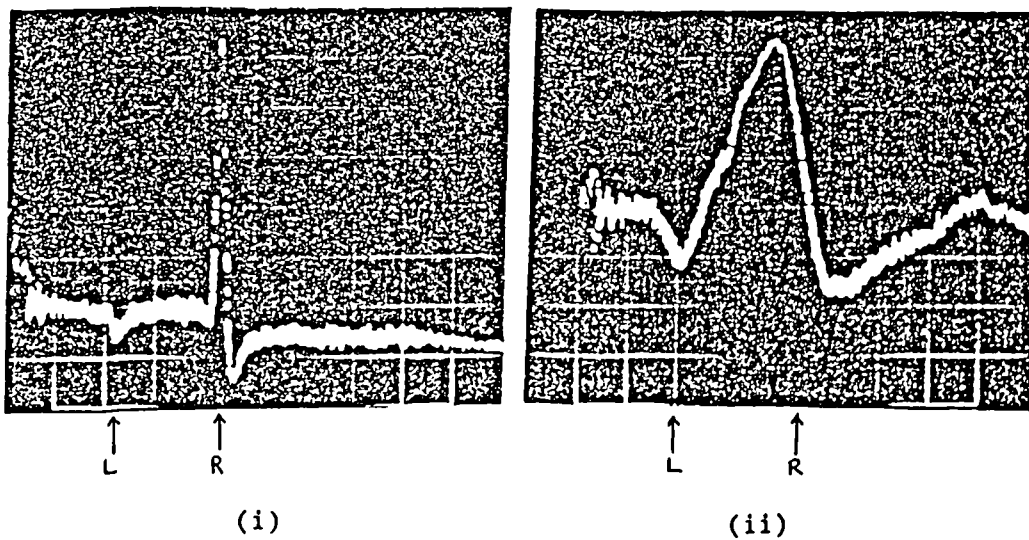
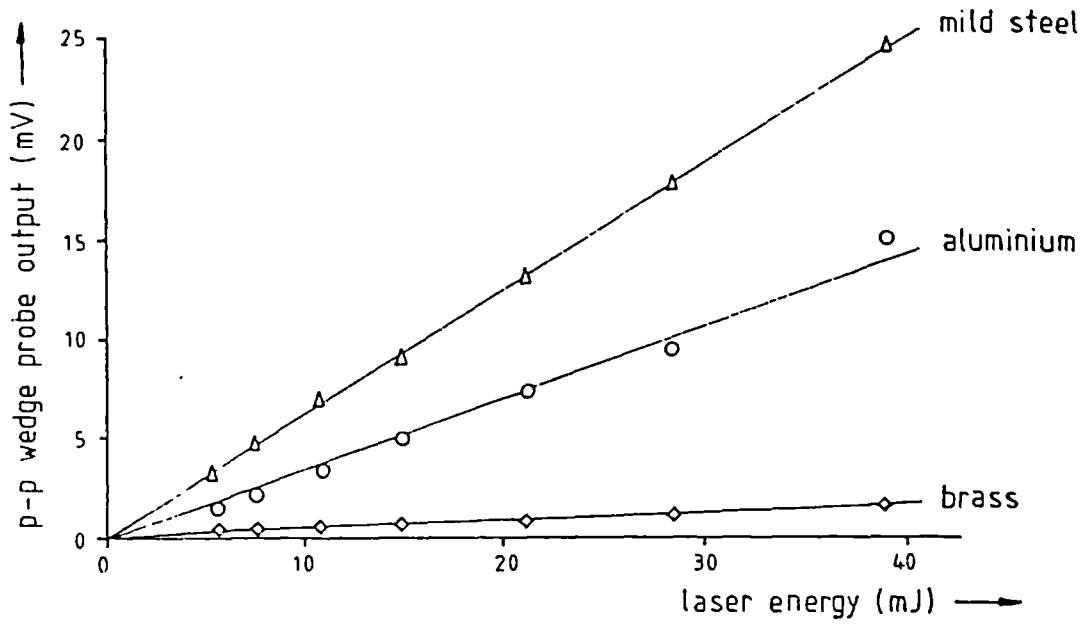


Fig 2.16(b) Capacitance probe traces corresponding to theoretical waveforms 2.16(a). Produced by (i) a 9mJ focused laser pulse (ii) unfocused 30mJ pulse with an estimated diameter of 3mm. Arbitrary vertical scale; 12mm between source and detector. After Aindow et al, (1983).

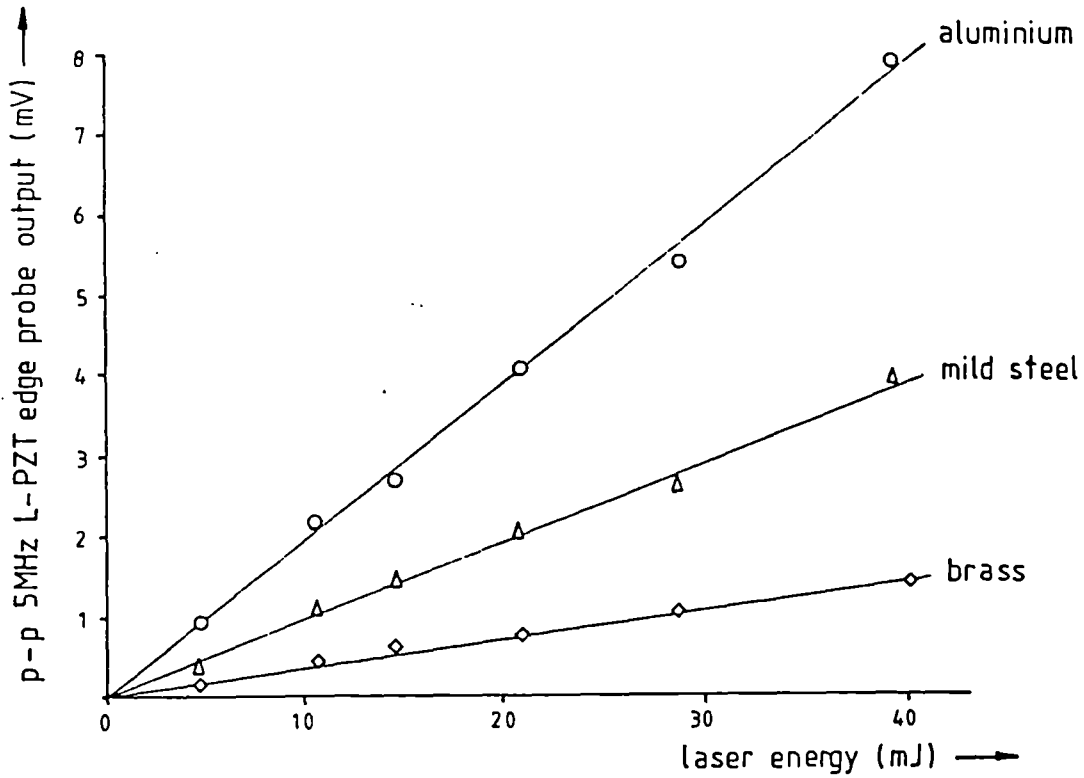
the thermoelastic regime. A linear relationship was found for both the surface longitudinal, (L), and Rayleigh pulses, fig 2.17, as is the case for bulk waveforms. He also demonstrated that the width of the Rayleigh pulse in this regime, measured as the time between the maximum and minimum points, does not vary with source\detector distance. For a given source however the width did vary between metals. Altering the laser beam diameter also affected the width and it was shown that the duration of the Rayleigh pulse is determined by the acoustic transit time across the source diameter.

Scruby and Moss, (1985), showed that the compressional surface pulse amplitude is proportional to  $R^{-1}$ , fig 2.18, and the Rayleigh to  $R^{-1/2}$ , fig 2.19, for both thermoelastic and ablation sources. The maximum value of R examined was <15cm and it was suggested from calculations that the compressional pulse should attenuate as  $R^{-2}$  for large distances.

Directional surface pulses have been produced. Aindow et al, (1982), focused energy from a Nd:YAG laser to a line on an aluminium surface to produce highly directional Rayleigh pulses, fig 2.20. Jen et al, (1985), produced annular surface acoustic waves using an axicon lens to focus the beam, (see fig 2.23). Both of these systems allow large amplitude ultrasonic disturbances to be generated without damaging the sample surface.



(a) Rayleigh pulse



(b) Longitudinal pulse

Fig 2.17 Variation of surface pulse amplitudes with laser energy, (a) Rayleigh (b) longitudinal. Unfocused multimode pulses at a source/detector distance of ~10mm. After Aindow, (1986).

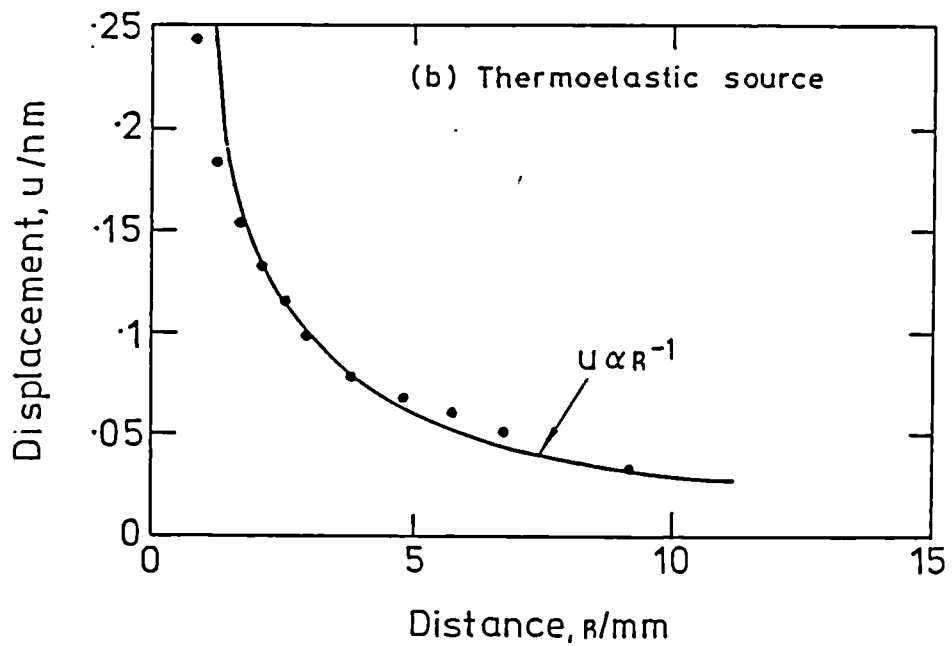
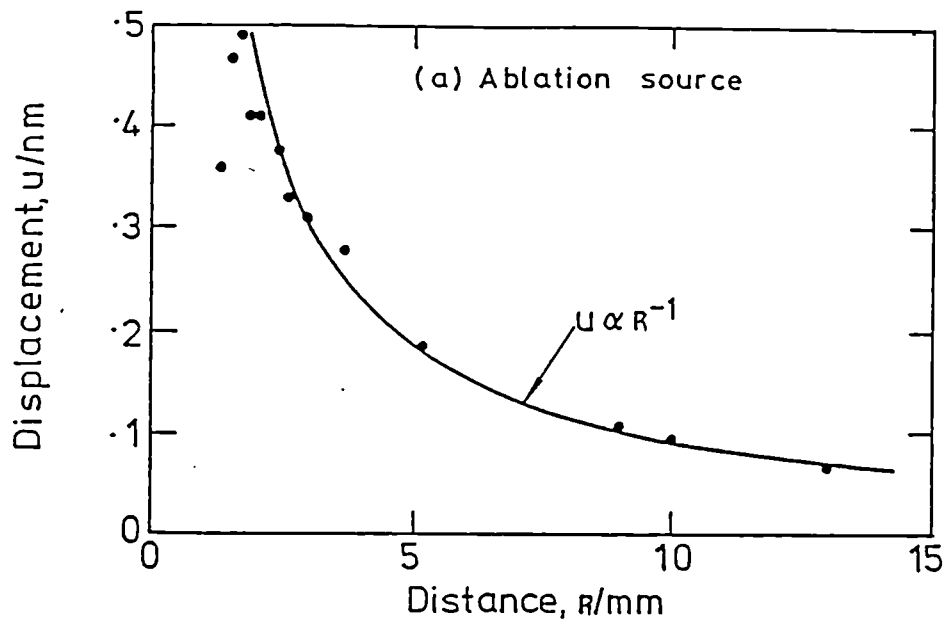


Fig 2.18 Amplitude of direct surface longitudinal pulse as a function of distance. Experimental points fit  $u \propto R^{-1}$  except for small  $R$ . (a) Ablation source, (b) Thermoelastic source. After Scruby and Moss, (1985).

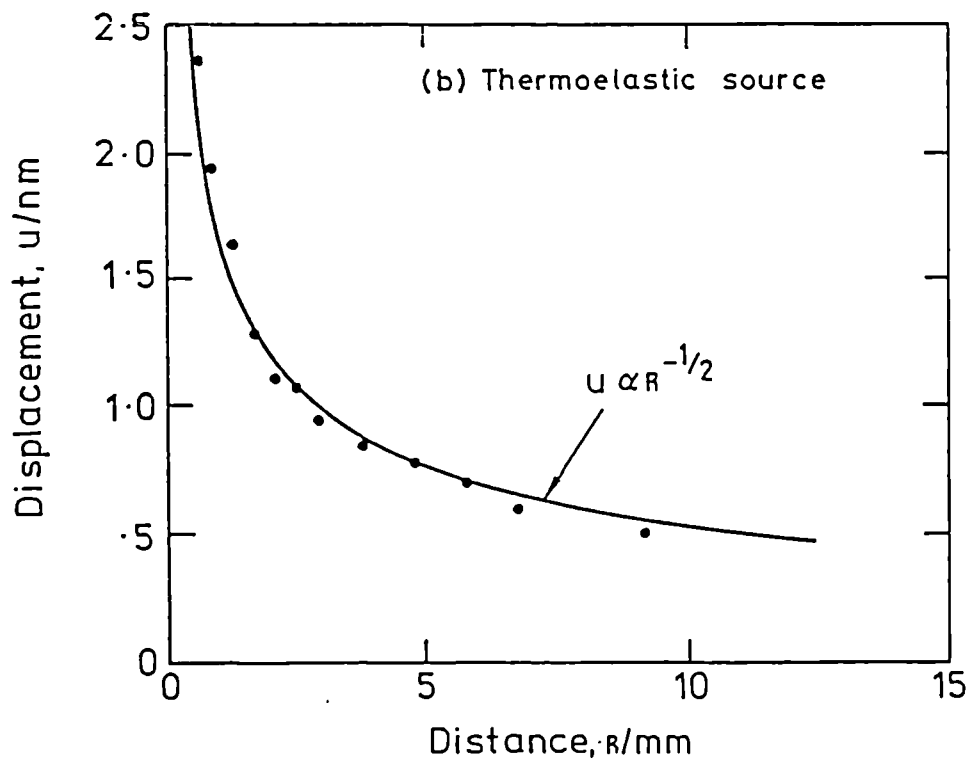
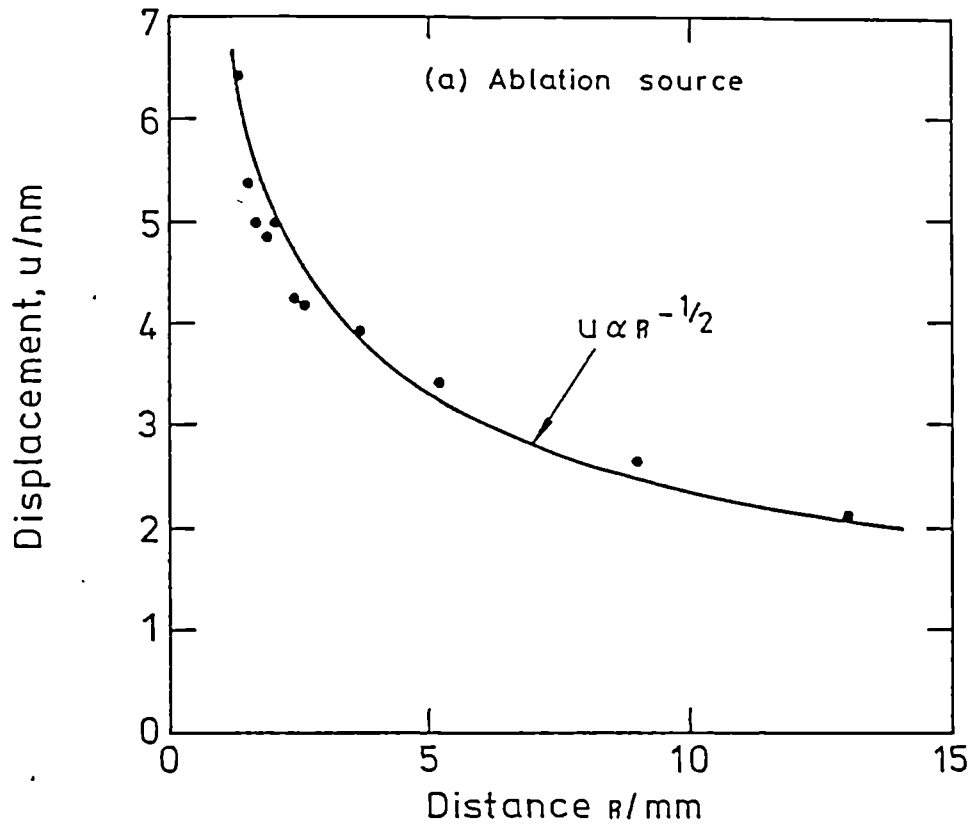


Fig 2.19 Amplitude of Rayleigh pulse as a function of distance, shown to fit  $u \propto R^{-1/2}$ .  
 (a) Ablation source, (b) Thermoelastic source.  
 After Scruby and Moss, (1985).

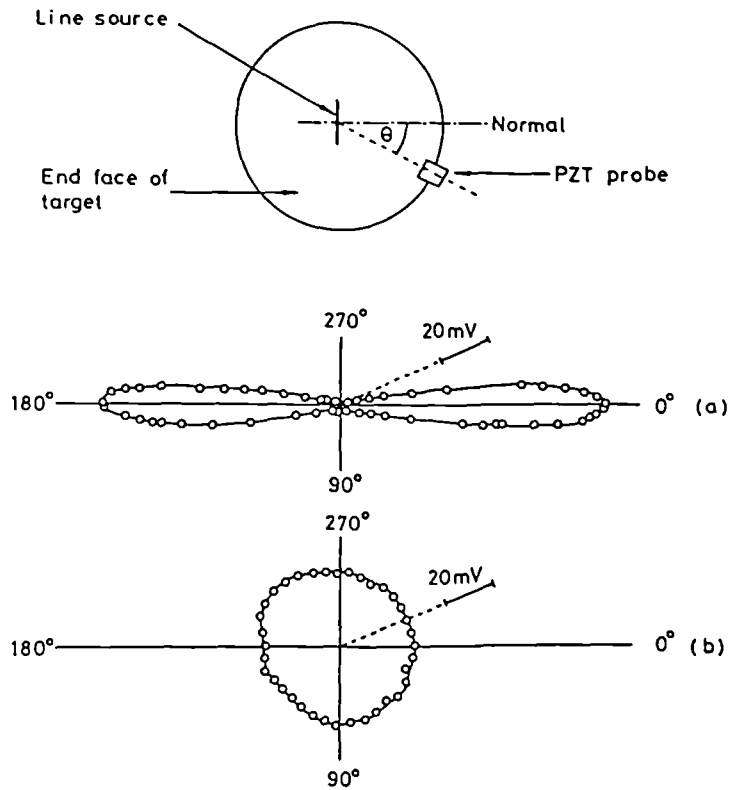


Fig 2.20 Schematic diagram defining  $\theta$ , followed by surface directivity patterns on aluminium for (a) 4mm x 0.1mm line source and (b) 1mm diameter circular source. The Nd:YAG laser pulse contained 5mJ of energy in both cases. After Aindow et al, (1982).

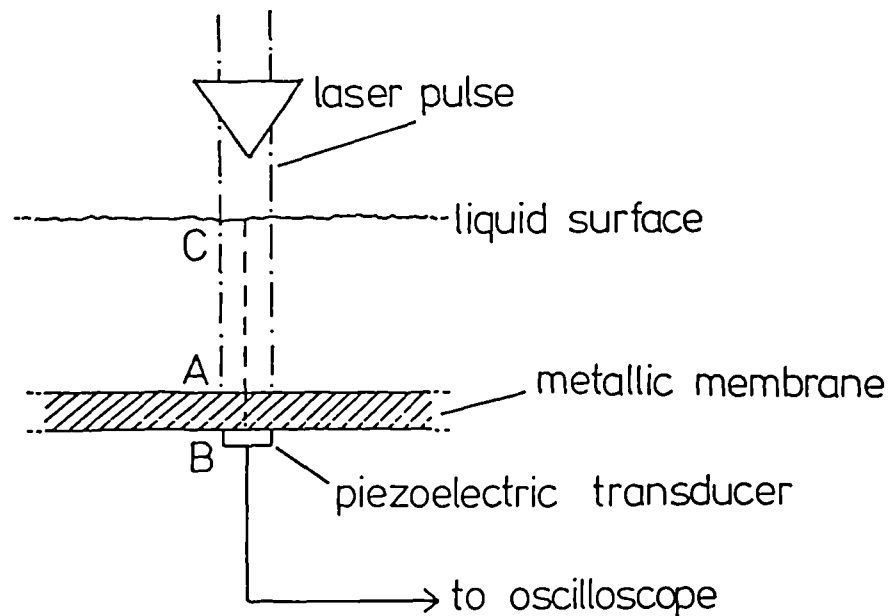


Fig 2.21 Scheme for liquid depth measurement. After Hutchins et al, (1980).

## 2.6/ Some Applications of Laser Generated Ultrasound.

Many applications have been suggested for the laser acoustic source since the first reported generation of ultrasound in solids by laser in 1963. The major techniques are outlined below with the following section devoted to reported flaw detection experiments.

The measurement of ultrasonic velocity and hence the calculation of elastic constants has been demonstrated by several authors. Bondarenko et al, (1976), calculated the elastic modulus of a steel rod from a remote measurement of the longitudinal velocity of sound in the sample. The acoustic pulses were generated by a Q-switched ruby laser, and detected by a stabilised Michelson interferometer. Unfortunately no values of elastic moduli were presented in the paper. A Nd-glass laser and 10MHz ultrasonic transducer were used by Wilcox and Calder, (1980), to determine elastic constants of 11 materials. Here the velocities of both longitudinal pulses, generated by the laser, and shear pulses caused by mode conversions, were measured. Agreement with values obtained using the conventional contacting ultrasonic pulse method was generally within 1 to 2 percent. The compressional wave velocities in both solid and liquid lead were also measured using this non-contacting technique, (Calder and Wilcox; 1980). There was a considerable drop in velocity for the liquid sample as expected, both values agreeing well with published results. Tam and Leung, (1984), used 10ns ultrasonic pulses generated by a nitrogen laser to measure

the elastic anisotropy in a sample of extruded aluminium alloy, type 6061-T6. The sample was disk shaped and the propagation time for an acoustic pulse to traverse the diameter was measured for varying directions by rotating the sample. The precision of the ultrasonic velocity measurement was approximately 0.02%. The longitudinal velocities at  $\pm 45^\circ$  from the extruding direction, Z, were found to be 2% larger than the velocity along Z, indicating that most of the aluminium crystals are oriented with a principal axis parallel to Z. The observed acoustic anisotropy remained essentially unchanged after thermal annealing, with the ultrasonic velocity increasing by about 0.5% in all directions.

Broadband acoustic pulses are generated by the pulsed laser source and this led Scruby et al, (1982), to suggest a totally non-contacting system for ultrasonic attenuation measurement. Since frequencies of up to  $\sim 100$ MHz may be generated by the laser source, frequency analysis of wave arrivals after propagation through a known thickness of material should enable the ultrasonic attenuation to be measured. Burov et al, (1985), made an attenuation measurement using modulation of the generating laser beam to generate different frequencies on a YX-cut quartz plate. The modulated output from an Ar laser incident on two sections of the plate generated surface acoustic waves from two line sources. The modulation caused alternating maxima and minima in the acoustic field intensity due to surface acoustic wave interference which were monitored using a

He-Ne laser beam probe. Using this technique accuracies of the order of  $10^{-3}\%$  can be obtained for SAW velocities. A velocity of  $3160\text{ms}^{-1}$  and an attenuation coefficient of  $0.025\text{cm}^{-1}$  were obtained from experimentally measured values where the frequency used was from 5.489MHz to 6.016MHz. This would appear to be the first reported quantitative measurement of attenuation using the laser ultrasonic source. Bondarenko et al, (1976), deduced a value of  $0.143\text{Npcm}^{-1}$  for the attenuation of bulk acoustic pulses in stainless steel using a laser-generated ultrasonic pulse. Unfortunately this value was not referred to any particular frequency. Scruby et al, (1986), measured the rise-time of an epicentral longitudinal pulse and those of its reflections. Comparative attenuation measurements were made on two pure steel samples from the pulse broadening with increased number of transits across the samples. The larger grained sample was found to attenuate more strongly. Slight surface damage was caused by the oil\ablation source used. The 'noise' detected between the longitudinal and shear pulses was shown to be repeatable for each sample and its frequency content was found to be related to grain size. It was suggested that these signals were due to forward scattering of the ultrasonic pulses by the materials internal structure. After frequency analysis of these signals it was found that the smaller grained sample caused less scatter, in agreement with the attenuation measurements.

The generation of ultrasound by pulsed laser has

also been suggested as a standard acoustic source in metals, (Hutchins et al; 1981c). Three distinct sources may be generated dependent upon the surface conditions of the sample and the incident power density. This is of particular interest to workers in seismology and acoustic emission where a flexible standard acoustic source has been previously lacking. A number of methods exist for calibrating acoustic emission systems, (Sachse and Hsu; 1980), however all differ in some aspect from a true source which is typically a short duration transient event. It has been shown, (Scruby et al; 1981), that the dipolar stress field, the time duration and the amplitude of a typical acoustic emission event from a microcrack can be reproduced using a thermoelastic source generated by a pulsed laser.

Transducers may also be calibrated using a pulsed laser. Since the acoustic signals produced by the laser are highly reproducible from shot to shot, quantitative comparisons can readily be made between the outputs from two separate transducers, (Scruby et al; 1982).

In another context, scanning acoustic microscopes may use ultrasonic waves having frequencies greater than 2GHz, and hence, wavelengths of the order of  $1\mu\text{m}$  dependent upon the propagation medium. Generally the generation and detection of the ultrasonic signal is by sputtered ZnO transducers, (Atalar et al; 1979), which has low efficiency at high frequencies. The ultrasound undergoes attenuation through a sapphire lens, used to obtain a spot size of the order of  $1\mu\text{m}$ , and through the water coupling medium between

the sample and transducer. As an alternative acoustic source, Wickramasinghe et al, (1978), used mode-locked pulse trains from a Nd:YAG laser to generate ultrasound at 210MHz and higher harmonics directly on the sample. The receiver was made of sputtered ZnO with a response centered near 800MHz, hence detecting the fourth harmonic at 840MHz. This system eliminated the problem of coupling acoustic energy to the sample.

Hutchins et al, (1980), proposed a scheme for liquid depth measurement using laser generated ultrasound where characteristics of the metallic membrane and any transducer bond need not be considered. Here a pulse from a Nd:YAG laser was incident at the liquid/metal interface where the acoustic signal is produced, fig 2.21, radiating into both media simultaneously. A longitudinally polarized 5MHz piezoelectric plate was bonded to the far side of the metal, (25mm thick, 60mm diameter aluminium or steel disk), to detect the acoustic signals. The acoustic pulse in the solid propagated through the metal and bond to the transducer. A pulse was also radiated to the surface of the liquid and reflected, returning to the liquid-metal interface. Assuming there is no gross acoustic impedance mismatch there, a secondary longitudinal pulse may be detected by the transducer after transmission through the metal. The separation in time of these two longitudinal arrivals, and subsequent arrivals due to multiple reflections in the liquid, is directly proportional to the liquid depth. Liquid depths of 4mm were measured to an

accuracy of 1% using this technique on both oil and water samples.

Most of the suggested applications of the laser acoustic source however concern its use in non-destructive testing. A review is presented below.

## 2.7/ Laser Generated Ultrasound for Flaw Detection.

### 2.7a/ Advantages of a Non-contacting System.

Piezoelectric materials, as discussed in Chapter 4, are widely used as generators and detectors of ultrasound for the testing of metals. Systems built around such materials are small, portable and relatively inexpensive when compared to laser based systems which also require the adherence to laser safety regulations. However advantages of a non-contacting system are that hot samples may be tested, such as steel on a rolling mill or welds immediately after deposition. Also, samples become accessible even when they are situated in an environment contaminated by ionising radiation, where operators of conventional ultrasonic probes cannot work. It is mainly for applications such as these that the laser generated ultrasonic source is being investigated as a possible technique in NDE since existing techniques have proven satisfactory for a wide range of applications.

The laser source has several other attractive features which may be exploited. Acoustic pulses so generated are of wide bandwidth. For example a laser pulse with a 30ns rise time will generate an ultrasonic

disturbance in aluminium which has frequency components of up to 10MHz and hence is capable of interacting with defects with dimensions of less than 1mm. Deadtime problems are sometimes encountered in NDE when examining defects lying close to a samples surface. An acoustic pulse emitted from a transducer bonded directly to a metal plate, will propagate a distance  $c \Delta t$  during the time,  $\Delta t$ , the transducer is activated, where  $c$  is the velocity of sound in the metal. Hence in a system where a single transducer is used in pulse echo configuration, reflections from any defects which lie at a depth of less than  $c \Delta t/2$  cannot be detected. In conventional testing this problem may be overcome by using a delay medium between the transducer and the sample. This may be done either by bonding a delay rod to the front face of the piezoelectric element or by carrying out the experiment underwater in an immersion tank. This latter technique is also used to achieve reasonable acoustic coupling to samples with irregular surfaces or complex geometries and also to introduce beams at various angles into the test specimen. However for many applications this may be inconvenient, making a laser based system attractive. Since generation is at the surface of the material to be inspected there are no couplant problems regardless of surface irregularities, although the amplitude of the acoustic signal may vary as the optical absorption coefficient of the surface changes. The laser beam can easily be steered optically and hence can work on awkwardly shaped test-pieces. It may also be rapidly moved so as to scan large areas faster than can be done with

conventional systems.

Another advantage of the laser generated ultrasonic system over piezoelectric devices is that longitudinal, shear and Rayleigh pulses are produced on each shot. These various modes have a known directivity, (Hutchins et al; 1981), for a given incident power density. This directivity may be varied by changing the focusing of the beam. Hence a degree of beam steering is possible. However, the longitudinal pulse has a large amplitude at normal incidence for an ablation source which causes slight surface damage and a very small amplitude in the low incident power density regime.

A comprehensive review of the uses of lasers in non-destructive evaluation has been presented by Birnbaum and White, (1984). Laser-generated ultrasound is discussed in that review along with other uses of lasers. For example to produce thermal waves, for carrier injection in semiconductors and in various optical detection techniques.

For maximum advantage to be taken from a laser-acoustic source, a non-contacting broadband device must be used for detection. Various optical, electromagnetic and capacitance techniques which are suitable are discussed in Chapter 4.

#### 2.7b/ Reported Uses for Flaw Detection.

Bondarenko et al, (1976), detected an artificial macrocrack using ultrasonic pulses generated by a Q-spoiled ruby laser and detected using a Michelson type stabilised



interferometer. Two polished steel plates were clamped together with a thin oil film deposited at the interface lubricating a small part of them. This experiment was carried out in transmission, an acoustic signal being detected only when the excitation zone passed over a lubricated area of the interface. The unlubricated zone of the surfaces, simulating the macrocrack, was precisely determined from the disappearance of acoustic signal. Power densities of the order of  $50\text{MWcm}^{-2}$  were used here so a plasma may have formed at the point of generation. Von Gutfeld and Melcher, (1977), reported the detection of 0.04cm deep, 0.04cm diameter drill holes on the surface of an aluminium cylinder having a 4mil microscope cover slide acoustically bonded to it. A pulsed rhodamine dye laser was used to generate elastic pulses at the interface, with a piezoelectric transducer bonded to the opposite face of the cylinder detecting the acoustic signals. The difference in the detected waveforms were therefore due to the changing boundary conditions where the ultrasonic pulses were produced. A subsequent experiment by von Gutfeld, (1980), used elastic pulses produced by laser irradiation on a constraining layer to interact with a drill hole extending halfway through an aluminium sample. Scattered waves were observed from this defect using a 20MHz transducer bonded to the side of the specimen. A system for the detection of holes in a thin aluminium sample was also presented. The experiment was carried out in a water tank, fig 2.22, with the acoustic pulses being generated at the liquid\metal

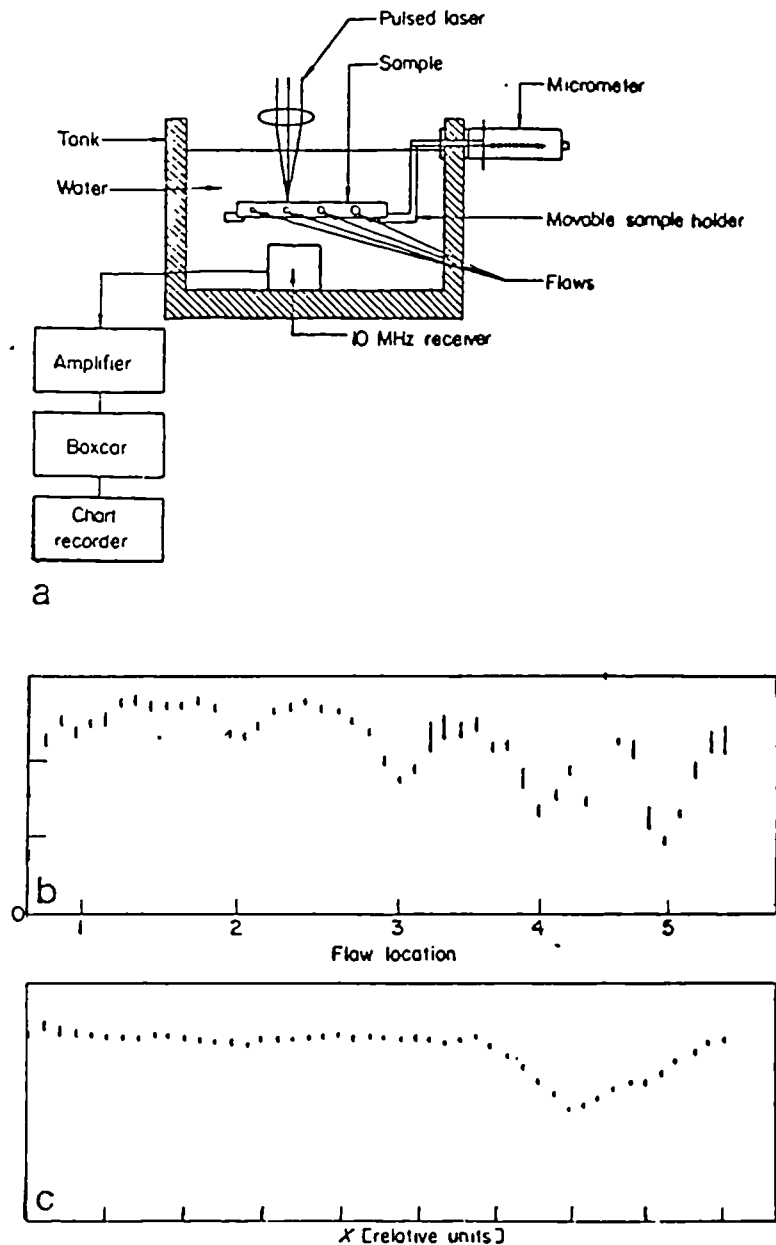


Fig 2.22 (a) Laser absorption by a sample immersed in water with thermoelastic generation at the sample-water interface. Scanning is achieved by movement of the sample relative to the fixed laser beam and receiver. (b) Data using 5ns laser pulses to interrogate an aluminium sample 0.32cm thick. Edge holes, 2mm deep, serve as flaws of diameter 1) 0.036cm, 2) 0.055cm, 3) 0.092cm and 4) 0.1cm. The flaw at 5) is a crack caused by the joint between the sample and its support. (c) Transmission data taken with two piezoelectric transducers replacing the laser. Poor resolution compared to (b). After von Gutfeld, (1980).

interface. Detection was done by a 10MHz piezoelectric transducer at the bottom of the tank. The results compared favourably to an experiment using piezoelectric transducers for both generation and detection. These latter three experiments take advantage of the increased signal obtained using a constraining layer which enabled very low incident laser energies to be used.

A 1.5mm diameter hole drilled at the mid-thickness of a 25mm thick aluminium plate was detected non-contactively by Calder and Wilcox, (1980). A 12J pulse from a Q-switched Nd-glass laser was incident on one face of the sample, detection being done on epicentre interferometrically. If the longitudinal wave velocity is assumed for all arrivals, then the direct signal and one round-trip echo from the main pulse are detected along with an arrival due to a reflection from the drill hole. Since the elastic pulses are generated in the plasma regime this assumption may be valid. However the choice of geometry is unfortunate since the arrival attributed to a reflection from the drill hole is at a time comparable to that of the arrival of a direct shear pulse. The authors show that a 12J laser pulse causes appreciable local surface damage.

The testing of the minute welds used for the joining of thin sheet materials is not practical using conventional ultrasonic techniques. Bar-Cohen, (1979), makes use of the very short duration pulses, (10-40ns), of narrow beam cross-section, (0.5-1.0mm), that can be generated from the output of a Nd:YAG laser to examine such microwelds. Again

the experiment was carried out in transmission, detection being done by a wideband transducer coupled to the sample by a thin water layer. At any point where there is separation of the sheets, no pulse was received by the transducer. Power densities of greater than  $10^8 \text{Wcm}^{-2}$  were used which must have resulted in ablation at the sample surface.

Two separate flaw detection experiments requiring access to one sample face only are described by Wellman, (1980). Pulses from a Ruby laser producing power densities in excess of  $500 \text{MWcm}^{-2}$  were incident on the same side of the sample as the readout spot from a Michelson interferometer. Again ablation at this power density must have caused pitting of the surface. In the first experiment described, two parallel drill holes in the bulk of a 25mm thick, 50mm diameter polished steel sample were detected using longitudinal bulk waves. The drill holes were 2mm in diameter, separated by 1mm at a depth of 16.5mm. From the signals obtained by this system, echoes from the separate holes could be resolved. A similar experimental system was also described for the detection of longitudinal surface breaking flaws in a 105mm shell casing. The detection system had to be modified due to the diffuse nature of the curved, unpolished shell casing. A simulated flaw, 2mm deep by 10mm long was detected using this technique, where the generation and detection points straddled the defect.

Cielo et al, (1985), heated a circular region on an aluminium surface to produce converging surface pulses. A 1mm deep, 0.1mm wide machined slot across the surface of the

sample affected the form of the waveforms being detected off the centre of convergence by an interferometer, fig 2.23. Detailed interpretation of the waveforms are difficult however due to the complex geometry of the experiment.

This thesis presents a contribution to the development of remote techniques for NDE. In particular it addresses itself to the problems of quantifying both surface breaking defects in weld materials and subsurface flaws in laminates. A technique for the sizing of artificial surface breaking cracks has been described by Aindow et al, (1983b). This method is explained in Chapter 5 and extended to interactions with real surface breaking cracks. In Chapters 6 and 7 two distinct techniques for the detection and sizing of sub-surface laminar flaws are presented.

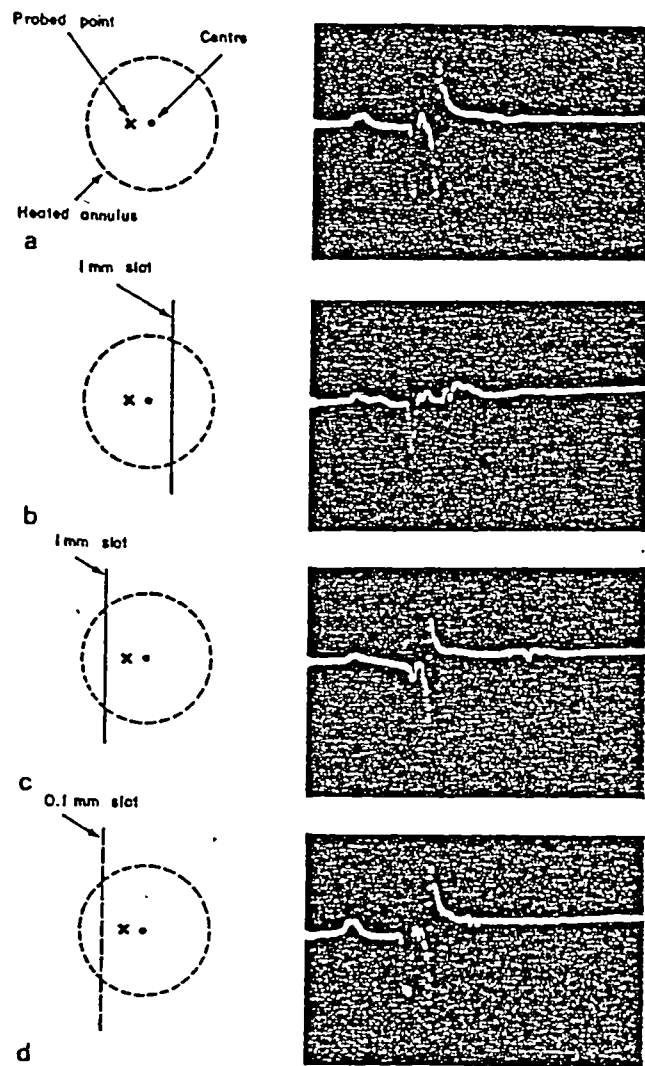


Fig 2.23 Defect detection using directional surface pulses. Waveforms obtained on an aluminium sample in the presence of a slot, with an out of centre probe. Annulus heated by 0.1J, 15ns Nd:YAG pulses. (a) No slot, (b) 1mm deep slot on the opposite side of the probe, (c) 1mm deep slot on the same side as the probe, (d) 0.1mm deep slot on the same side as the probe. After Cielo et al, (1985).

CHAPTER 3.

PROPAGATION OF TRANSIENT ULTRASONIC PULSES  
IN ELASTIC PLATES.

3.1/ Introduction.

Previous work presented on laser generated ultrasound concentrates on the study of surface and bulk epicentral responses of acoustically thick plates. For such an approach to be useful in the NDE of thin plates or for cases where access to points on directly opposite faces is not possible, then standard off-epicentral waveforms must firstly be understood. Variation of pulse shape with plate thickness as the plate becomes acoustically thin also requires investigation.

Scruby, (1985), compared ultrasonic waveforms detected on epicentre with those at  $45^{\circ}$  on a steel plate. The laser acoustic source was varied from thermoelastic, ablation to an oil constrained surface. A strong longitudinal pulse was detected at  $45^{\circ}$  irrespective of source type, contrasting with the large change in compressional pulse shape and amplitude at epicentre discussed in the previous chapter. Longer timescale events were not examined and head waves were not considered.

In their analysis of the mechanisms of the source of acoustic emission Pao et al, (1979), studied the response of elastic plates, having a Poisson's ratio of 1/4, using a variety of source functions. The model presented was based on the generalized ray theory, fig 3.1, and Cagniard's method. Transient solutions were obtained by evaluating the ray integrals with a complex algorithm. Motions on both faces of the plate were calculated and compared with experimentally obtained waveforms for a glass plate. In this chapter experimental waveforms from dural plates are compared to the above and with a simpler theory which yields only the initial acoustic arrivals at any point in the bulk of a solid. This latter theory is give by Pilant, (1979), in his treatment of Lambs problem, and is considered below.

### 3.2/ Off Epicentral Motion due to a Surface Vertical Force.

The elastic wave equation for isotropic homogeneous media is

$$\underline{f} + (\lambda+2\mu)\nabla(\nabla\cdot\underline{u}) - \mu\nabla \times (\nabla\times\underline{u}) - \rho\dot{\underline{u}} = 0 \quad (3.1)$$

where  $\underline{f}$  are the body forces acting such as gravity,  $\rho$  is density and  $\underline{u}$  the displacement vector.  $\lambda$  and  $\mu$  are Lamé elastic constants, (e.g. Achenbach; 1980).

Taking the Laplace transform with respect to time of (3.1) yields,

$$v_p^2 \nabla \nabla \underline{U} - v_s^2 \nabla \times \nabla \times \underline{U} = s^2 \underline{U} \quad (3.2)$$

where

$$\underline{U}(x,y,s) = \int_0^{\infty} e^{-st} \underline{u}(x,y,t) dt \quad (3.3)$$

$v_p$  and  $v_s$  are the velocities of compressional and shear wave

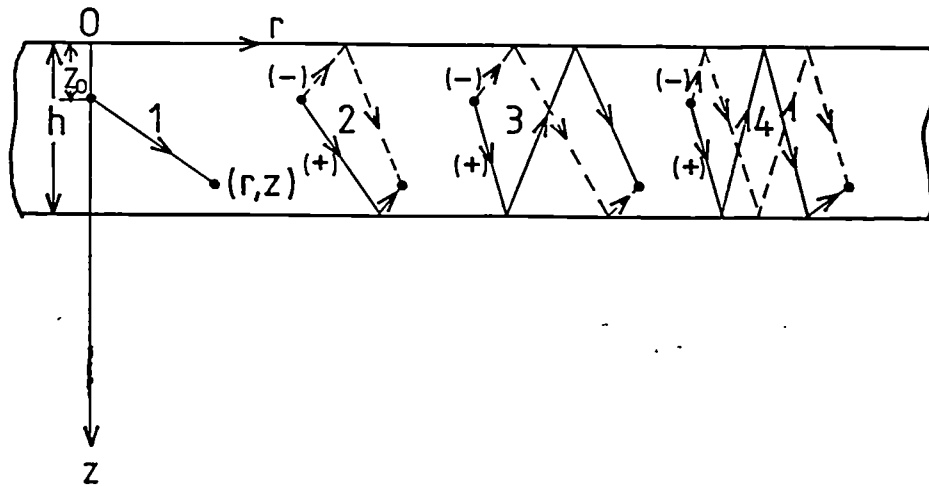


Fig 3.1 Illustration of the generalised ray theory showing four ray groups from a buried source in an infinite plate. After Pao et al, (1979).

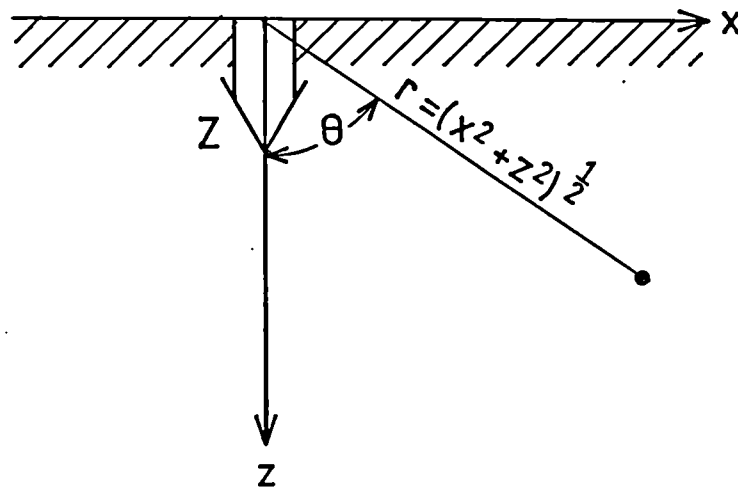


Fig 3.2 Geometrical relationship for a vertical force of magnitude  $Z$  on the surface of a half-space. After Pilant, (1979).

motion respectively.

The transformed displacement vector  $\underline{U}$  can be related to the Lamé potentials  $\Phi$  and  $\Psi$ , (Pilant; 1979),

$$U_x = \frac{\delta\Phi}{\delta x} - \frac{\delta\Psi^+}{\delta z} \quad (3.4)$$

and

$$U_z = \frac{\delta\Phi}{\delta z} + \frac{\delta\Psi^+}{\delta x} \quad (3.5)$$

where

$$\Psi^+ = l \frac{\delta\Psi}{\delta x} \quad (3.6)$$

We need only consider the out of plane motion, (to which our transducer is sensitive),  $U_z$ .

The potentials satisfy the transformed wave equations

$$\nabla^2 \Phi - \frac{s^2}{v_p^2} \Phi = 0 \quad (3.7)$$

and

$$\nabla^2 \Psi - \frac{s^2}{v_s^2} \Psi = 0 \quad (3.8)$$

which yield general solutions in the positive  $z$ , positive  $x$  quarter space,

$$\Phi(x,y,s) = \int_{-\infty}^{\infty} A(q) e^{\frac{s}{v_p} \{iqx - (q^2 + a^2)^{1/2} z\}} dq \quad (3.9)$$

and on setting  $l = \frac{v_s}{s}$

$$\Psi^+(x,y,s) = \int_{-\infty}^{\infty} B(q) e^{\frac{s}{v_s} \{iqx - (q^2 + 1)^{1/2} z\}} dq \quad (3.10)$$

where  $q$  is a dimensionless separation parameter introduced for later convenience and  $a = \frac{v_s}{v_p}$ .

The source acts on the surface and so can be input to the model through the boundary conditions. A line source of magnitude  $Z$  acting downwards on the surface, fig 3.2, with

delta function time dependence yields, (Pilant; 1979).

$$A(q) = -\frac{Z}{2\pi\mu} \frac{v_s}{s} \frac{(2q^2+1)}{R(q)} \quad (3.11)$$

$$B(q) = \frac{Z}{2\pi\mu} \frac{v_s}{s} 2iq \frac{(q^2+a^2)^{1/2}}{R(q)} \quad (3.12)$$

where

$$R(q) = (2q^2+1)^2 - 4q^2(q^2+a^2)^{1/2}(q^2+1)^{1/2} \quad (3.13)$$

Inputing (3.11) and (3.12) into (3.9) and (3.10)

respectively and from (3.5) we obtain

$$U_z(x,y,s) = \frac{Z}{2\pi\mu} \int_{-\infty}^{\infty} \left[ \begin{array}{l} (2q^2+1)e^{-s/v_s}(q^2+a^2)^{1/2}z \\ -2q^2e^{-s/v_s}(q^2+1)^{1/2}z \end{array} \right] \frac{e^{s/v_s}iqx}{R(q)} (q^2+a^2)^{1/2}dq \quad (3.14)$$

Rewriting the above in terms of  $r$  and  $\theta$ , where  $x = r\sin\theta$ ,  $z = r\cos\theta$  and using the evenness and oddness of the integrands, we obtain

$$U_z^p(r,\theta,s) = \frac{Z}{\pi\mu} \operatorname{Re} \int_0^{\infty} \frac{(2q^2+1)e^{sr/v_s} \{iq\sin\theta - (q^2+a^2)^{1/2}\cos\theta\}}{R(q)} (q^2+a^2)^{1/2}dq \quad (3.15)$$

$$U_z^s(r,\theta,s) = -\frac{Z}{\pi\mu} \operatorname{Re} \int_0^{\infty} \frac{2q^2e^{sr/v_s} \{iq\sin\theta - (q^2+1)^{1/2}\cos\theta\}}{R(q)} (q^2+a^2)^{1/2}dq \quad (3.16)$$

Assuming  $\theta > 0$  then for convergence we must have  $\operatorname{Im}\{q\} \geq 0$ ,  $\operatorname{Re}\{(q^2+a^2)^{1/2}\} \geq 0$  and  $\operatorname{Re}\{(q^2+1)^{1/2}\} \geq 0$

Making use of the Cagniard - de Hoop technique, (Pilant; 1979), we make the following change of variable.

$$\cos\theta(q^2+a^2)^{1/2} - iq\sin\theta = \tau = v_s t/r \quad (3.17)$$

The inverse of this transform is

$$q(\tau) = i\tau\sin\theta + \cos\theta(\tau^2-a^2)^{1/2} \quad (3.18)$$

and we also note that

$$\frac{dq}{d\tau} = i\sin\theta + \tau\cos\theta(\tau^2-a^2)^{-1/2} \quad (3.19)$$

We now examine the path taken by  $q$  as the

transformed integration limits run from 0 to  $\infty$ . At  $\tau = 0$ ,  $q = i a \cos \theta$ . The derivative changes at  $\tau = a$ , i.e. the variable  $q$  runs up the imaginary axis to  $q = i a \sin \theta$  and then branches out into the first quadrant. The original integration path can be deformed with no real part of (3.15) from 0 to  $ia$ . Hence the lower limit will be  $r/v_p$  and the upper limit  $\infty$ . Equation (3.15) on insertion of  $t$  from (3.17) can now be recognized as the Laplace transform of the factor,

$$U_z^p(r, \theta, t) = \frac{Zv_s}{\pi \mu r} \operatorname{Re} \left\{ \frac{(q^2 + a^2)^{1/2} (2q^2 + 1)}{R(q)} \frac{dq(\tau)}{d\tau} \right\} H(\tau - a) \quad (3.20)$$

The above is an exact expression for the compressional motion in the  $z$ -direction anywhere on the interior of the half-space. A useful approximation can be made by considering only those motions caused by singularities and neglecting the slowly varying portions. This is the First Motion Approximation developed by Knopoff, (1958). Investigation of (3.20) by Pilant showed that the function varies quite smoothly except for the factor  $\frac{dq}{d\tau}$  near the scaled time  $\tau = a$ , and the factor  $R(q)$  near  $q = ib$ , ( $b = \frac{v_s}{v_R}$ ,  $v_R =$  the Rayleigh wave velocity), when  $\theta$  is near  $90^\circ$ . Looking at the former singularity, the value of  $q$  corresponding to  $\tau = a$  from (3.18) is

$$q_0 = i a \sin \theta \quad (3.21)$$

Expanding about this singular point we find that

$$\frac{dq}{d\tau} \approx \frac{\tau \cos \theta}{(\tau^2 - a^2)^{1/2}} \approx \frac{a^{1/2}}{2^{1/2}} \frac{\cos \theta}{(\tau - a)^{1/2}} \quad (3.22)$$

We can now write

$$U_z^p \approx \frac{Zv_s^{1/2}}{\pi \mu r^{1/2}} \frac{a^{3/2}}{2^{1/2}} \left[ \frac{\cos^2 \theta (1 - 2a^2 \sin^2 \theta)}{(1 - 2a^2 \sin^2 \theta)^2 + 4a^3 \sin^2 \theta \cos \theta (1 - a^2 \sin^2 \theta)^{1/2}} \right] \frac{H\left(t - \frac{r}{v_p}\right)}{\left(t - \frac{r}{v_p}\right)^{1/2}} \quad (3.23)$$

For the shear motion a different change of variable is required. Here we have

$$\cos\theta(q^2+1)^{1/2} - iq\sin\theta = \tau = v_s t/r \quad (3.24)$$

Inversely

$$q(\tau) = i\tau\sin\theta + \cos\theta(\tau^2-1)^{1/2} \quad (3.25)$$

and

$$\frac{dq}{d\tau} = i\sin\theta + \tau\cos\theta(\tau^2-1)^{-1/2} \quad (3.26)$$

Applying the same reasoning that led to (3.20) we obtain

$$U_z^s = -\frac{Zv_s}{\pi\mu r} \operatorname{Re} \left[ \frac{2q^2(q^2+a^2)^{1/2}}{R(q)} \frac{dq}{d\tau} \right] H(\tau-1) ; (\theta < \theta_c) \quad (3.27)$$

$$= -\frac{Zv_s}{\pi\mu r} \operatorname{Re} \left[ \frac{2q^2(q^2+a^2)^{1/2}}{R(q)} \frac{dq}{d\tau} \right] H(\tau-\tau_c) ; (\theta > \theta_c) \quad (3.28)$$

where

$$\tau_c = \frac{t_c v_s}{r} \equiv \tau(i a \sin\theta) = (1-a^2)^{1/2} \cos\theta + a \sin\theta = \cos(\theta - \theta_c) \quad (3.29)$$

The form (3.28) occurs because there is a contribution along the vertical segment from  $q=ia$  to  $q = i\sin\theta$  as in fig 3.3.

The function (3.27) is smoothly varying except for the factor  $\frac{dq}{d\tau}$  at  $\tau = 1$ . However (3.28) has a discontinuity at  $\tau=1$ , a change in slope at  $\tau = \tau_c$  and a large bump due to the smallness of  $R(q)$  near  $q=ib$  when  $\theta$  is close to  $90^\circ$ . As the S-motion due to the singularity  $\tau=1$  occurs whether or not  $\theta < \theta_c$  we can analyse for it and take account of the value of  $\theta$  in the formulation. At this singular point we must evaluate the product

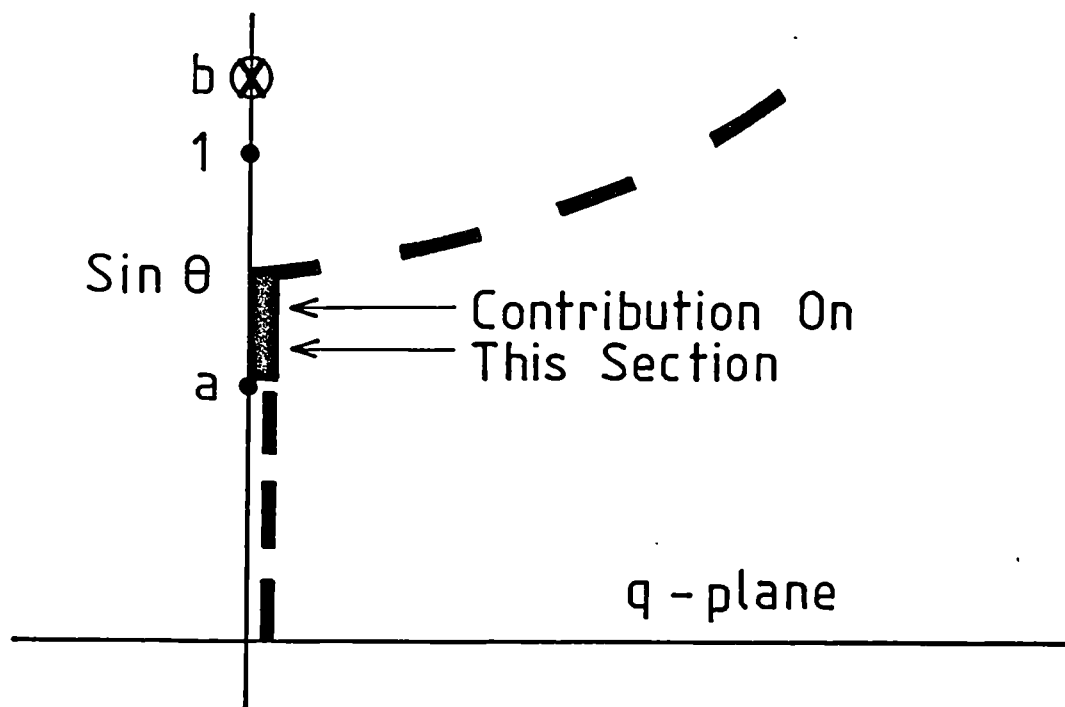


Fig 3.3 The deformed path of integration for S-motion. The contribution from the imaginary axis between  $q=ia$  and  $q=iasin\theta$  produces the head-wave motion. After Pilant, (1979).

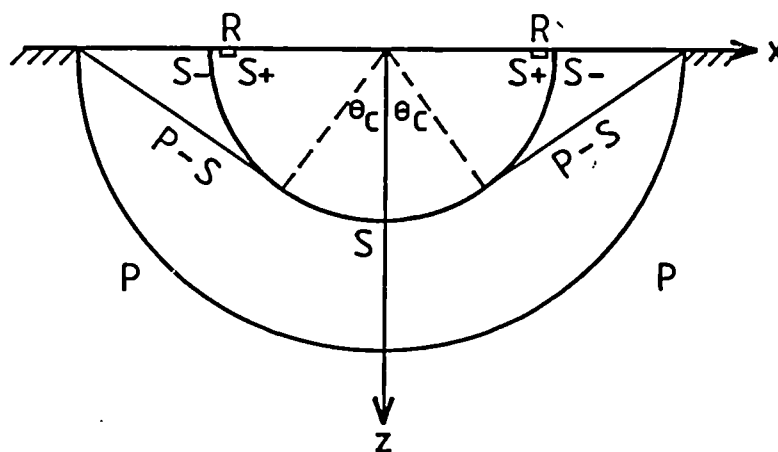


Fig 3.4 Wavefronts for Lamb's problem. R,S and P correspond to Rayleigh, shear and longitudinal wave motion respectively. Head waves arising from the surface longitudinal pulse are radiated into the bulk and travel at the shear wave velocity and are denoted by P-S.

$$\begin{aligned} q \frac{dq}{d\tau} &= \tau(\cos^2\theta - \sin^2\theta) + i \left[ (\tau^2-1)^{1/2} + \frac{\tau^2}{(\tau^2-1)^{1/2}} \right] \sin\theta \cos\theta \\ &\approx \frac{i \sin\theta \cos\theta}{2^{1/2}(\tau-1)^{1/2}} = - \frac{\sin\theta \cos\theta}{2^{1/2}(1-\tau)^{1/2}} \end{aligned} \quad (3.30)$$

For our case we are investigating for  $\theta > \theta_c$  hence the square root factor in  $R(q)$  takes the form

$$(a^2 - \sin^2\theta)^{1/2} = i(\sin^2\theta - a^2)^{1/2} \quad (3.31)$$

Then for  $\tau > 1$ ,  $\theta_c < \theta < \pi/2$  we have

$$U_z^{s+} \approx \frac{Zv_s^{1/2}}{\pi\mu r^{1/2}} \frac{1}{2^{1/2}} \operatorname{Re} \left[ \frac{8\sin^4\theta \cos^2\theta (\sin^2\theta - a^2)}{(1-2\sin^2\theta)^4 + 16\sin^4\theta \cos^2\theta (\sin^2\theta - a^2)} \right] \frac{H\left(t - \frac{r}{v_s}\right)}{\left(t - \frac{r}{v_s}\right)^{1/2}} \quad (3.32)$$

where the  $s+$  superscript stands for the approximate motion after the shear arrival.

For  $\tau < 1$ ,  $\theta_c < \theta < \pi/2$  we have

$$J_z^{s-} \approx - \frac{Zv_s^{1/2}}{\pi\mu r^{1/2}} \frac{1}{2^{1/2}} \operatorname{Re} \left[ \frac{2\sin^2\theta \cos\theta (\sin^2\theta - a^2) (1-2\sin^2\theta)^2}{(1-2\sin^2\theta)^4 + 16\sin^4\theta \cos^2\theta (\sin^2\theta - a^2)} \right] \frac{H\left(\frac{r}{v_s} - t\right)}{\left(\frac{r}{v_s} - t\right)^{1/2}} \quad (3.33)$$

The normal arrival due to head waves, fig 3.4, is also computed by Pilant, (1979). The arrival at  $\tau = \tau_c$  corresponding to  $q=ia$  is analyzed by examining the components of  $U_z^s$  in the vicinity of  $q=ia$ . This yields

$$U_z^{p-s} \approx - \frac{Zv_s^{3/2} (2a)^{3/2}}{\pi\mu r^{3/2}} \left[ \frac{(1-a^2)^{3/4} \sin\theta_c}{(1-2a^2)^2 \sin^{3/2}(\theta - \theta_c)} \right] (t-t_c)^{1/2} H(t-t_c) \quad (3.34)$$

A plasma source was used in the experiments reported later in this chapter which can be approximated as producing a point vertical force with Heaviside time dependence. Evaluating equations (3.23), (3.32), (3.33) and (3.34) at the appropriate times gives the response of a solid, at any given  $\theta$  between  $\theta_c$  and  $\pi/2$ , to a vertical line force with delta function time dependence. Numerically integrating the resultant displacement waveform with respect to time will

yield the appropriate first motion approximation.

The above theory allows the appropriate elastic moduli to be input to the problem through the wave velocities. The method used by Pao et al, (1979), was restricted to a Poisson's ratio of 1/4. However this latter, more complex, theory had the advantage that it introduced a second boundary and accounted for multiple reflections. These authors calculated plate responses based on the generalized ray integrals for transient waves in layered solids, given by Pao and Gajewski, (1977). A generalized ray is specified by the path along which the wave propagates and by the modes of the wave motion, fig 3.1. Integral representations of the Laplace-transformed wave motion along the ray path, known as ray integrals, are constructed by assembling the source function, reflection and refraction coefficients and the receiver and phase functions. For the case considered here both surfaces of the plate were stress free except for a point normal force with Heaviside time dependence. A complex algorithm which employed Cagniards method was used by Pao et al to evaluate the generalized ray integrals.

### 3.3/ Experimental Details.

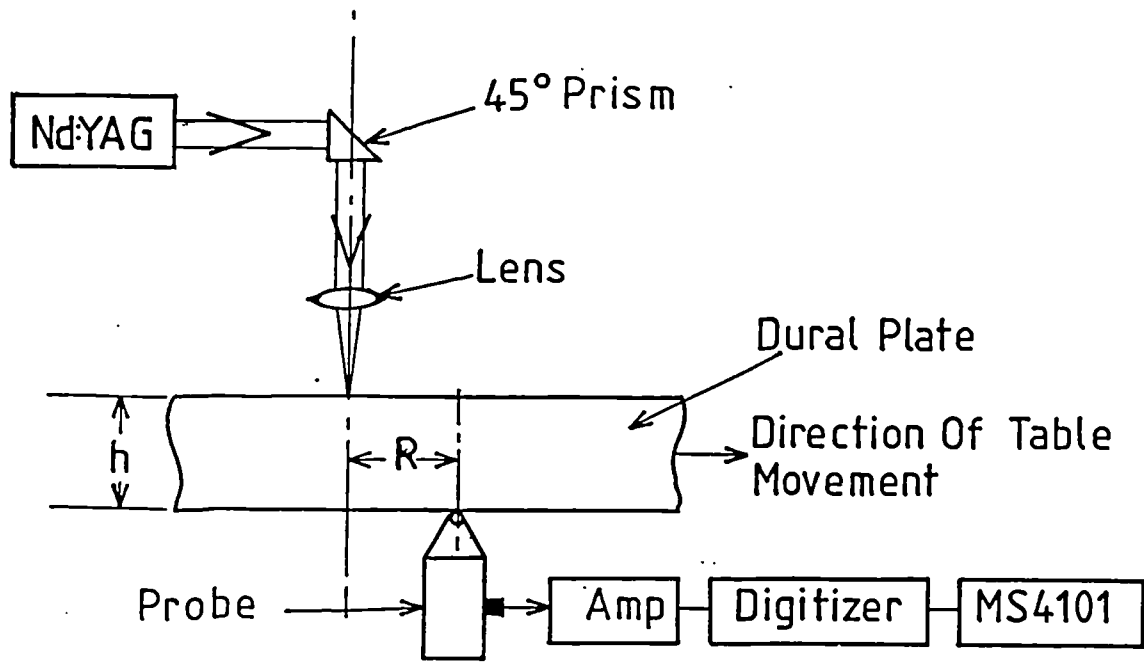
The experiments reported in this and subsequent chapters used a J.K. Lasers, System 2000 Nd:YAG laser which produced multimode pulses at  $1.06\mu\text{m}$  with  $\sim 35\text{ns}$  rise time,  $\sim 40\text{ns}$  full-width at half maximum of up to 50mJ of energy. A portion of the laser output was diverted to a fast

photo-diode, the output from which was used for triggering purposes. Ultrasonic waveforms detected by devices described in the next chapter were either monitored on a Tektronix 464 storage oscilloscope or captured on a Tektronix 7912AD 9-bit digitizer. The digitizer was integrated in a Tektronix MS4101 mini-computer system, based on a PDP-11/34 on which signal processing was done. In some cases the samples were positioned by an x-y table which was also controlled through the MS4101.

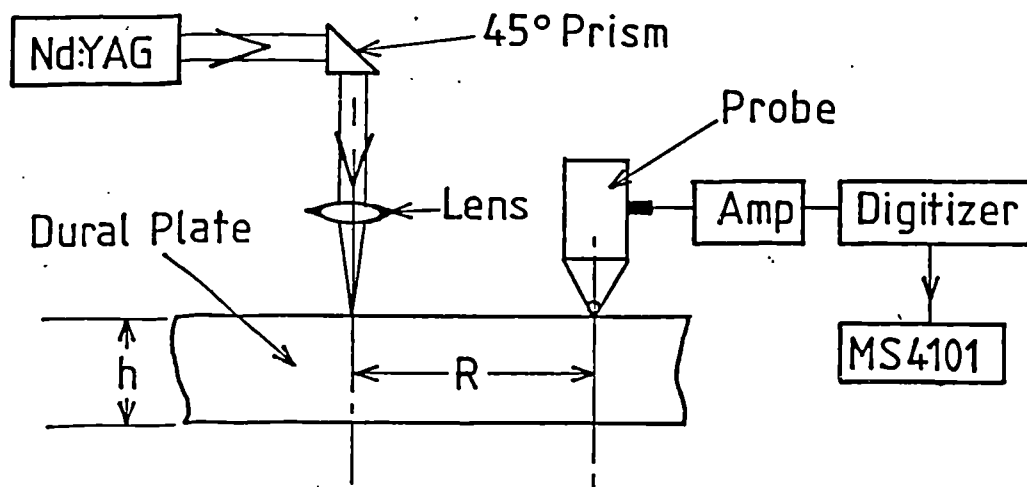
The experimental arrangements used to investigate ultrasonic waveforms in plates are shown in fig 3.5. Several flat duraluminium plates, type NP8M, of thickness between 2 and 25mm were examined. A circular lens was used to focus the laser pulse to produce a power density of  $\sim 10^9 \text{Wcm}^{-2}$  hence forming a plasma on the top surface of the sample. The ball capacitance probe described in Chapter 4 was used to monitor the surface displacements on either face of the sample, its output being amplified by a Harwell charge amplifier. The samples and detector were mounted on the x-y table and so could be moved to vary the acoustic propagation distance.

### 3.4/ Results and Discussion.

The arrangement shown in fig 3.5a was used for the off-epicentral experiments. Results were obtained for detector displacements from epicentre, R, from 0 to 4h, where h is plate thickness. These results were compared with the first motion approximation outlined in section 3.2.



(a)



(b)

Fig 3.5 Schematic diagrams of experimental arrangements. The plate and capacitance probe were both mounted on an x-y table and were moved relative to the laser spot.  
 (a) Off-epicentre set-up.  
 (b) Surface pulse set-up.

Experimentally determined values of 6400 and  $3300\text{ms}^{-1}$  were used for the longitudinal and shear velocities respectively. The waveforms were normalized to the time taken for a longitudinal pulse to travel  $h$ . i.e.

$$T = \tau_p / v_s = v_p t / h \quad (3.35)$$

so that direct comparison could also be made with the waveforms presented by Pao et al, (1979).

Fig 3.6 shows the displacements detected at  $1h$  from epicentre for plates between 2 and 25mm thick. Good agreement is evident between experiment and theory despite the assumptions made in the first motion approximation. The correlation is poor after the shear arrival due to multiple arrivals. Temporal normalization causes the features to sharpen as the laser rise-time becomes more transient-like with increasing plate thickness. The misalignment of the experimental waveforms was due to error in measuring the detector distance from epicentre.

There is still good agreement with Pilant's treatment when the detector was moved to  $2h$ , fig 3.7. Also included in fig 3.7 are results obtained by Pao et al, (1979), for a similar detector position. At  $R=3h$  multiply reflected waves reached the detector before the shear pulse and so agreement decreased, fig 3.8. In this case better agreement was obtained with the generalized ray theory of Pao et al, (1979). The differences in elastic moduli however caused divergence with experiment at larger  $R$ , fig 3.9. For example at  $R=4h$  the ray groups reached the detector at different times and with different amplitudes than those

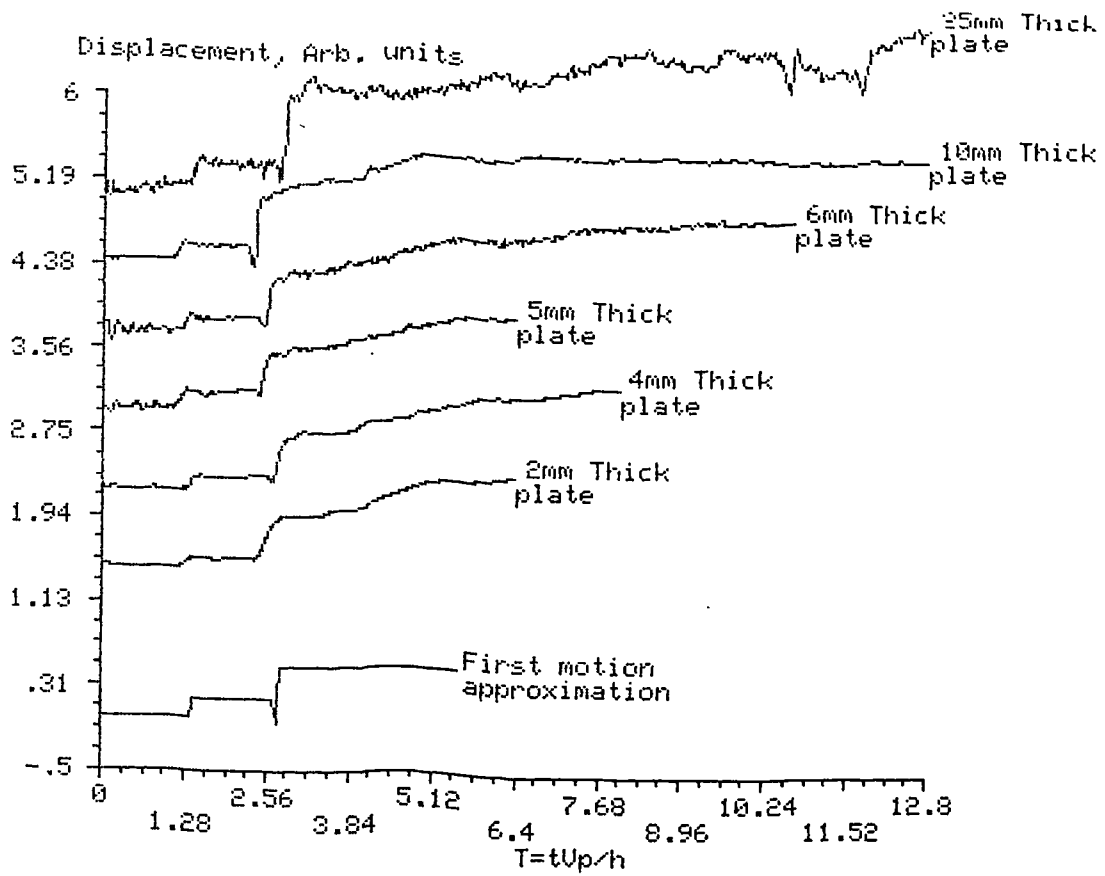


Fig 3.6 Comparison of first motion approximation with experimentally produced off-epicentral waveforms. Set-up as in fig 3.5(a) with the detector displaced from epicentre by a distance equal to the plate thickness, (i.e.  $R=h$ ).

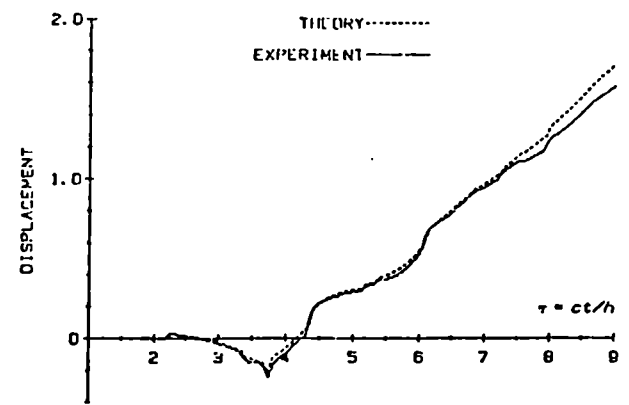
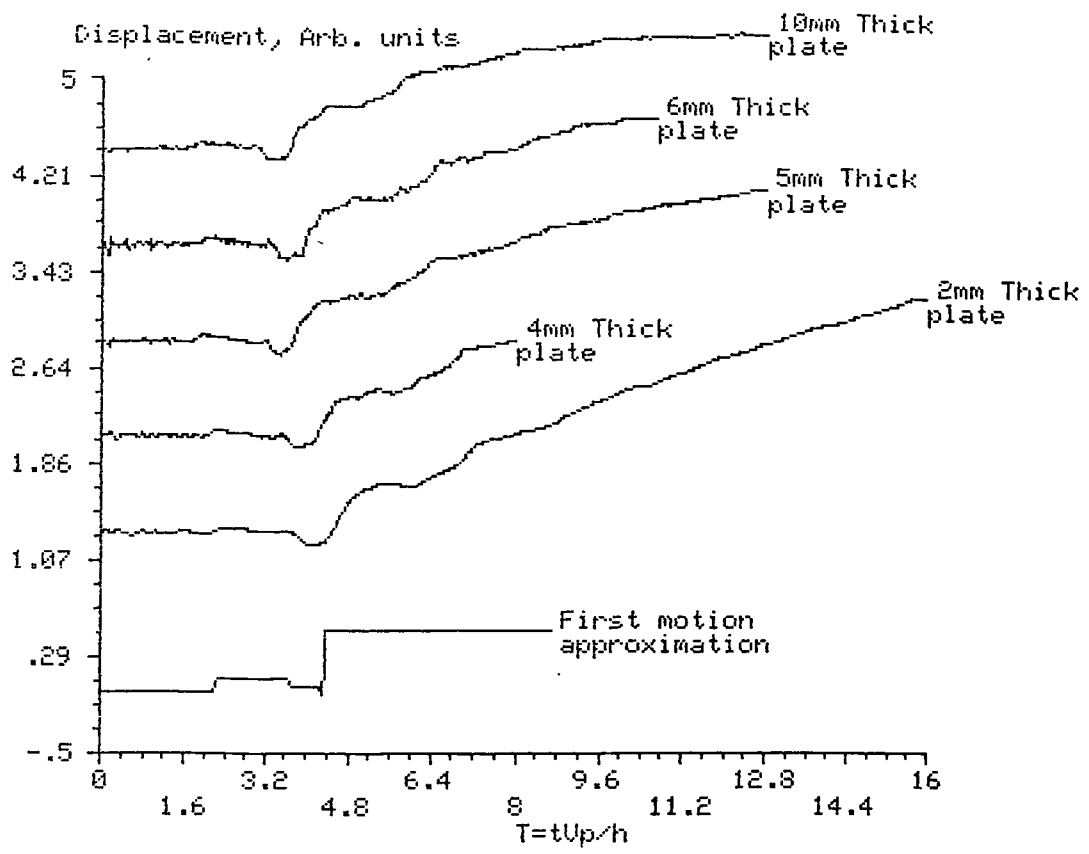


Fig 3.7 Experimental off-epicentral waveforms at  $R=2h$  compared with first motion approximation and generalised ray theories.

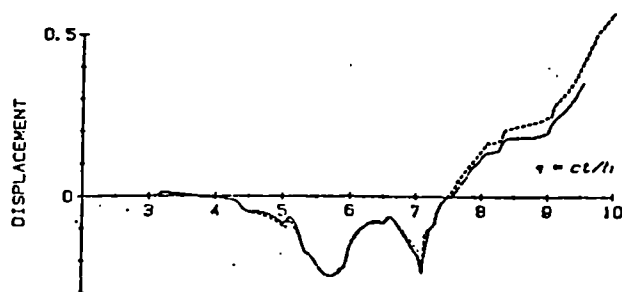
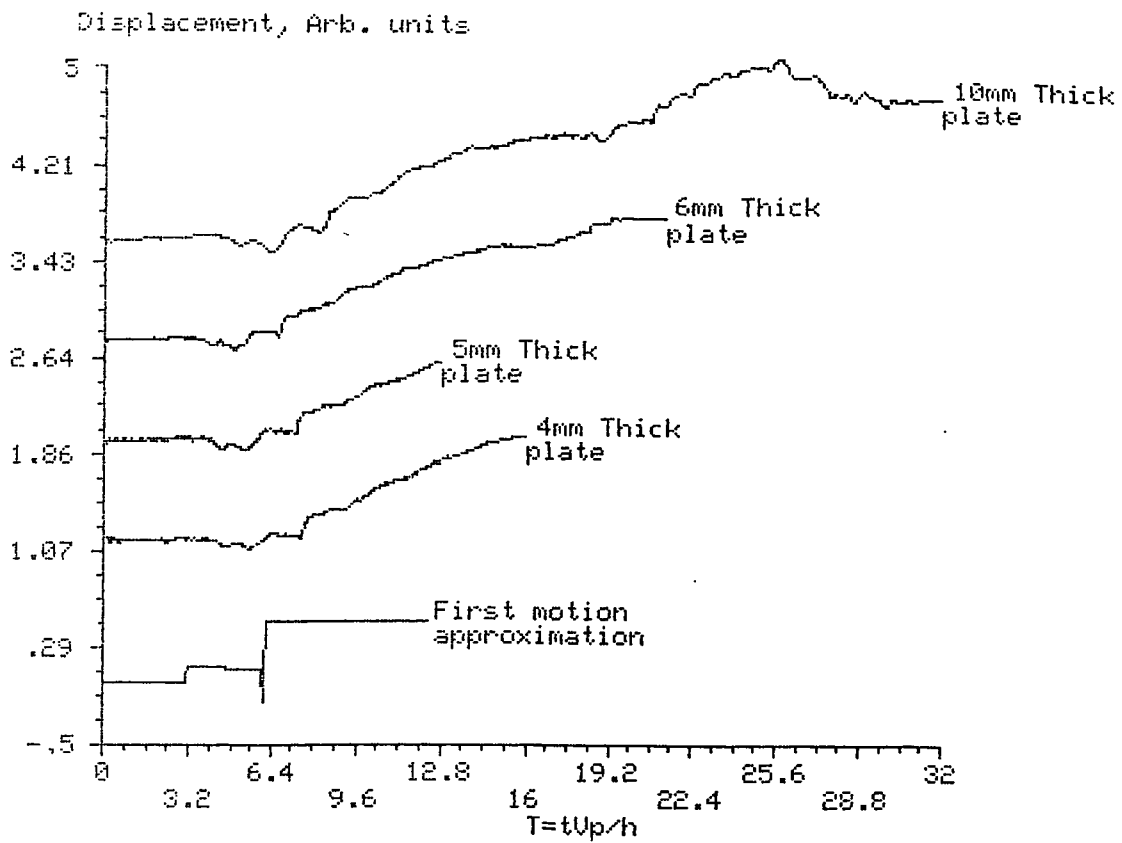


Fig 3.8 Experimental off-epicentral waveforms at  $R=3h$  compared with first motion approximation and generalised ray theories.

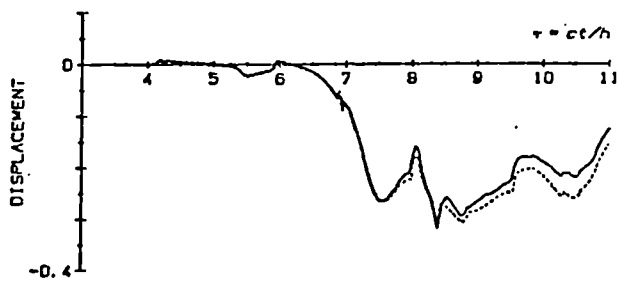
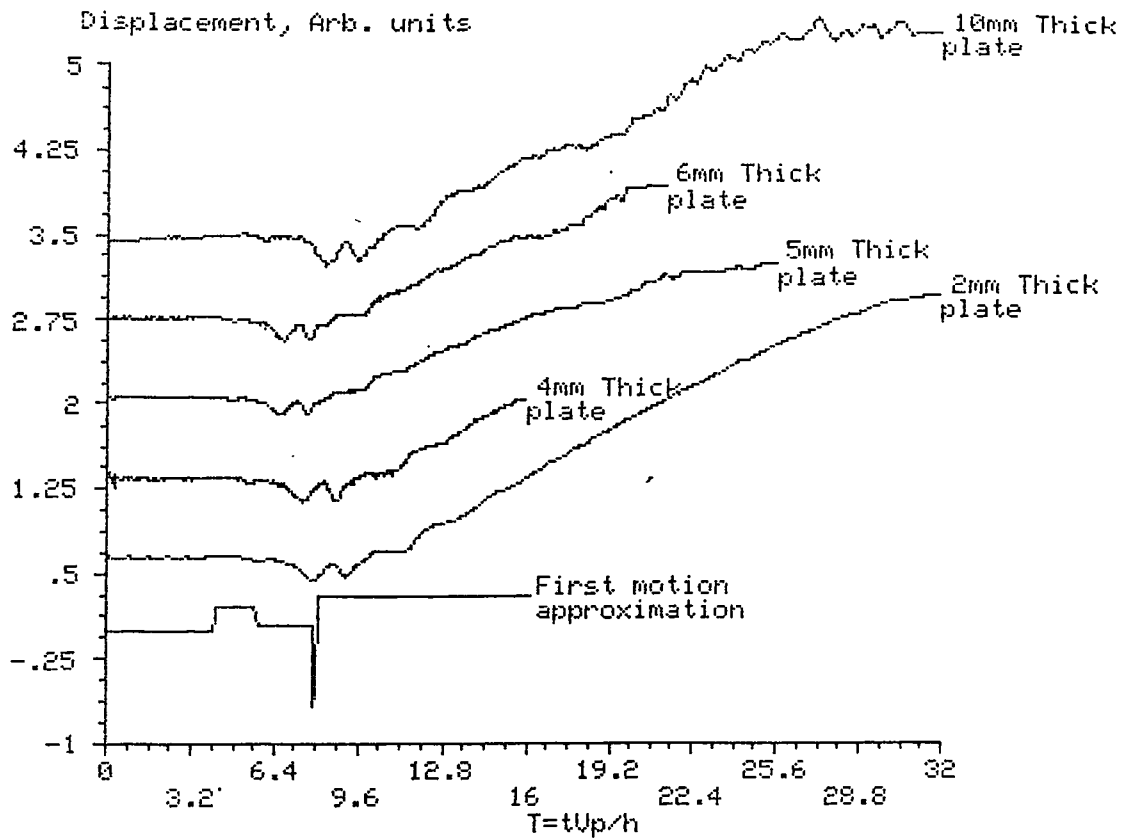


Fig 3.9 Experimental off-epicentral waveforms at  $R=4h$  compared with first motion approximation and generalised ray theories.

calculated.

The detector was then moved to the top face of the sample, fig 3.5b. Waveforms were collected for source-detector displacements,  $R$ , from  $2h$  to  $6h$ . Figures 3.10 to 3.12 show the waveforms detected at  $2h$ ,  $4h$ , and  $6h$  respectively and compare them with the generalized ray theory. Again agreement is good for small  $R$  and  $h$ . As  $R$  increased then the difference between theoretical and experimental elastic constants affected the shape of the waveforms. At larger  $R$  and  $h$  it is thought that the effect of the laser source not having true Heaviside time dependence also led to divergence between experiment and theory. The poor low frequency response of the amplifier also contributed to the latter effect.

In conclusion, it has been shown that a simple treatment of Lamb's problem can be used to understand off-epicentral motion in dural plates at detector displacements of up to  $2h$ . At larger detector distances from epicentre multiple arrivals have to be accounted for. This has previously been done by Pao et al, (1979), for a material having a Poisson's ratio of  $1/4$ . This is at variance with that in dural, ( $\sigma = 0.34$ ), which leads to discrepancies most evident at large  $R$ . Discrepancies were also caused by assuming that the plasma source used had Heaviside time dependence. This latter theory was also used for a comparison with waveforms detected on the same surface of plates as the laser-acoustic source.

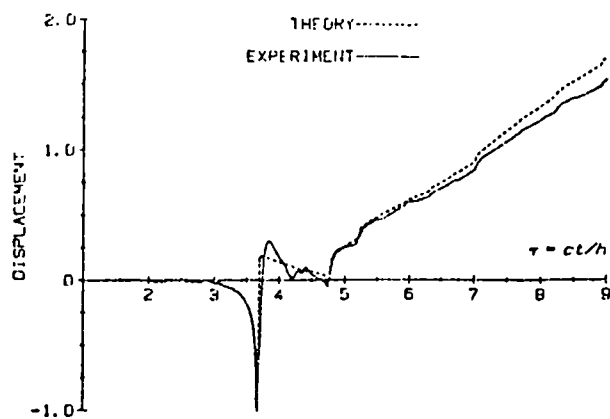
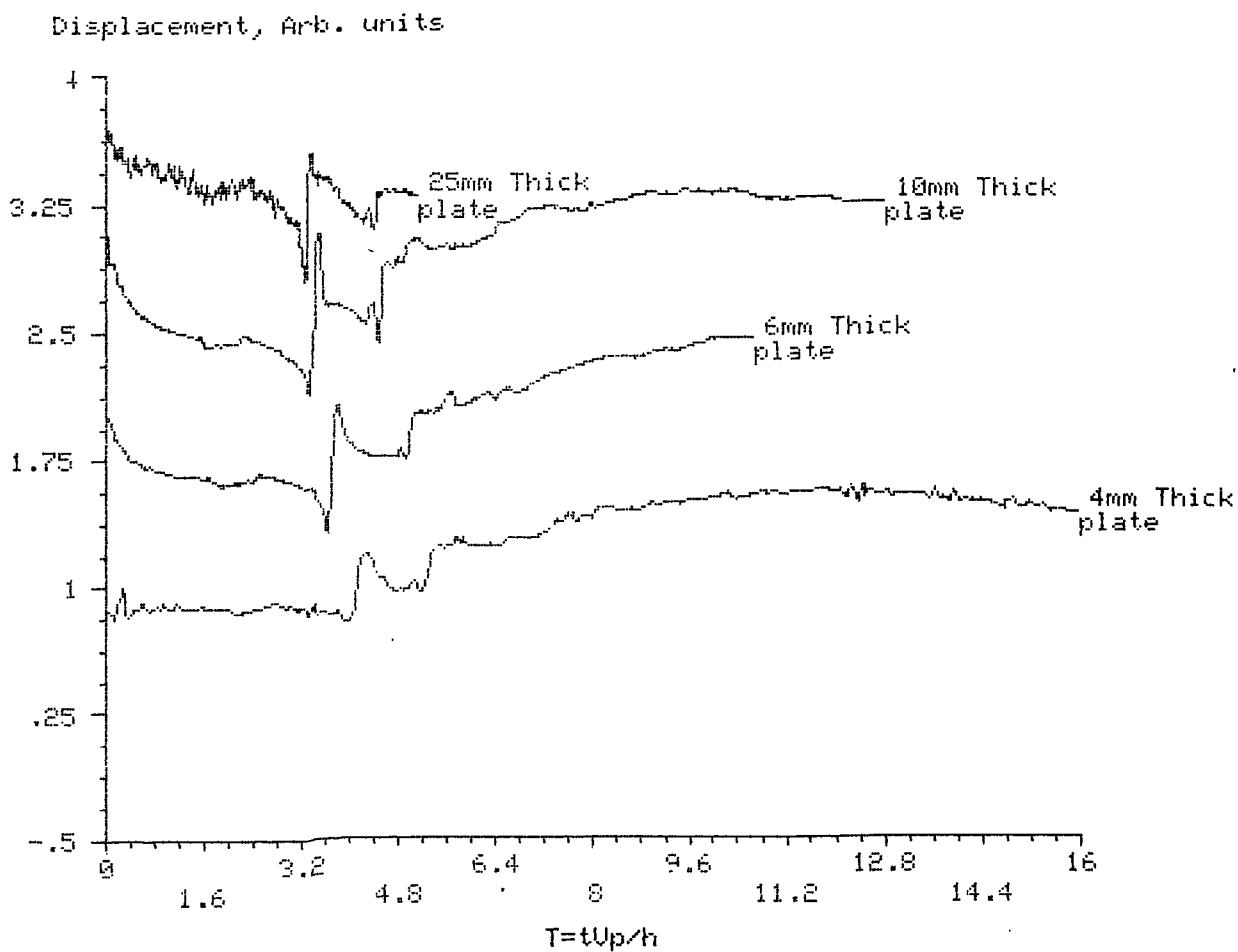


Fig 3.10 Experimental surface waveforms with the detector displaced from the source by a distance equal to twice the plate thickness, (i.e.  $R=2h$ ). Set up as shown in fig 3.5b. Waveforms compared to the generalised ray theory.

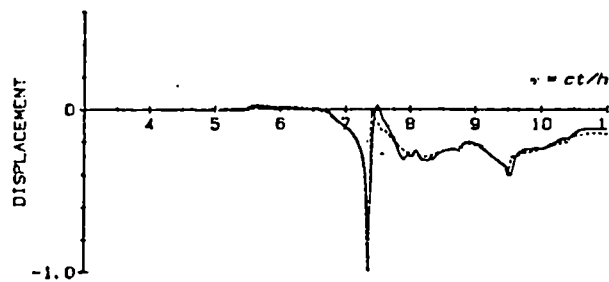
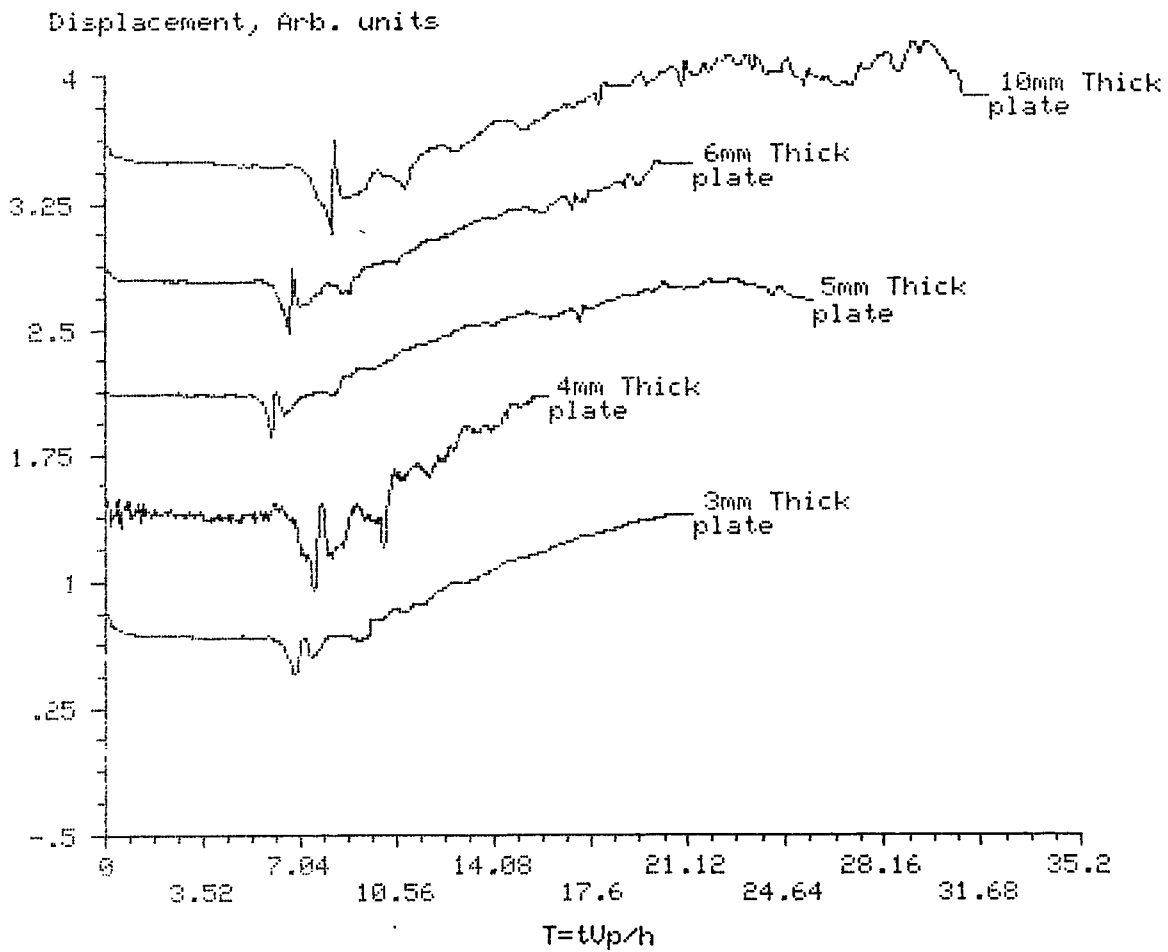


Fig 3.11 Experimental surface waveforms at  $R=4h$  compared with the generalised ray theory.

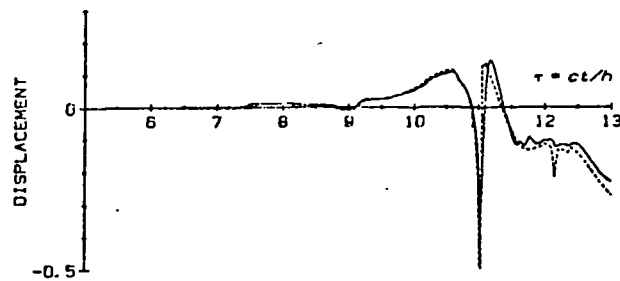
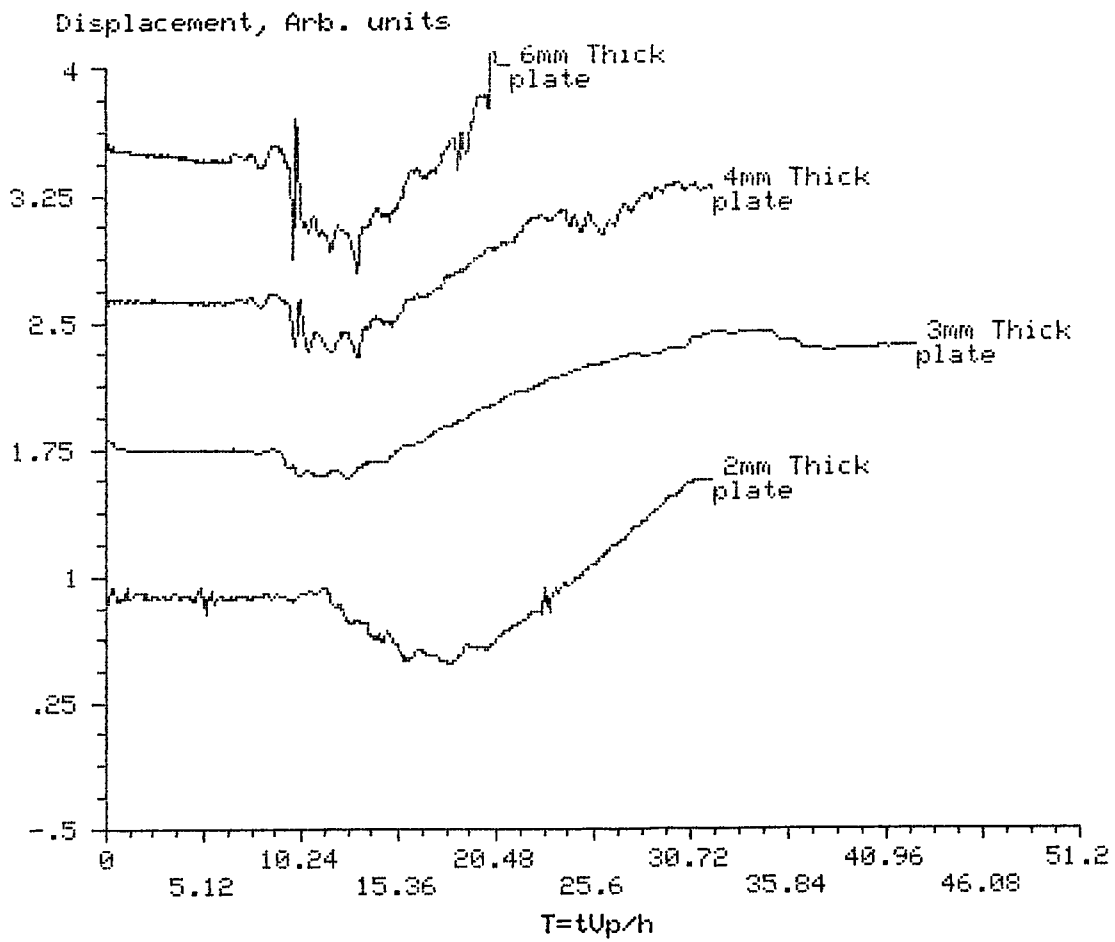


Fig 3.12 Experimental surface waveforms at  $R=6h$  compared with the generalised ray theory.

CHAPTER 4.

ULTRASONIC TRANSDUCERS AND METHODS FOR  
NON-DESTRUCTIVE EVALUATION.

4.1/ Piezoelectric Devices.

The most common type of ultrasonic probe presently used is the piezoelectric device. Certain crystals have lattice structures such that plates cut out of them at a given orientation with respect to the crystallographic axes will change dimensions when subjected to an electric field in a particular direction. This change may be a contraction or expansion dependent on the polarity of the field. Conversely, when an external mechanical force deforms the crystal plate, electric charges appear on its opposite surfaces, (the piezoelectric effect).

When a dielectric material is placed in an electric field the elementary dipoles become polarized and then stretched by the electrostatic forces. This is the electrostrictive effect. Polarization disappears in most dielectrics when the electric field is removed, however there are some which can be permanently polarized in a strong field. This process enhances the electrostrictive effect in these materials, (ferroelectrics), and makes them

exhibit piezoelectric properties. They are ceramic materials of polycrystalline structure, such as the lead-zirconate titanate group commonly called PZT, by far the most popular transducer material in use today.

Piezoelectric elements typically need a 1kV potential to expand or contract by 1 micron. The transducer elements are therefore encased in probes to minimise the risk of electric shock, as well as preventing mechanical damage. The probe housing normally contains a sound-absorbent backing cemented to the transducer to broaden the frequency response of the device although this decreases its sensitivity. Damped probes are required to produce and receive short pulses, (i.e. wide bandwidth, 1MHz say), or for use in resonance techniques where the resonance of the transducer itself must be suppressed. Epoxy resin loaded with tungsten powder is usually used as the damping slug since it strongly attenuates and its impedance can easily be matched to that of the piezoelectric element. A thin steel shim or a layer of aluminium oxide is cemented onto the bottom of the probe to protect against wear. Such a probe, as shown in fig 4.1a would launch\detect longitudinal pulses into\from a sample at normal incidence. Details of these probes have been reviewed by Blitz, (1963), Szillard, (1982), and Silk, (1984).

It is frequently necessary to examine samples using ultrasonic beams from a number of different angles. This increases the probability of detection of planar

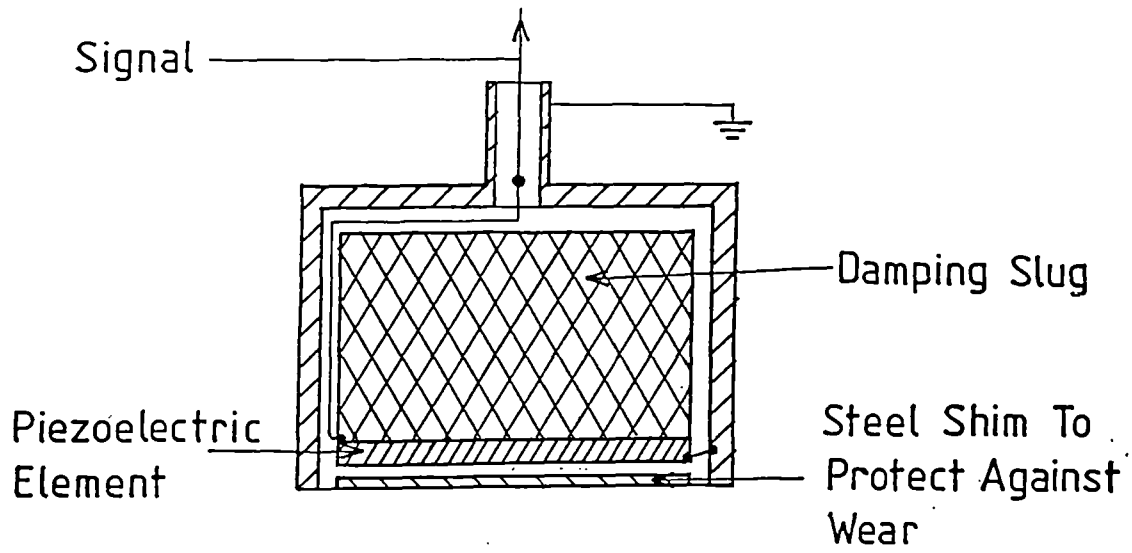


Fig 4.1(a) Normal incidence piezoelectric probe.

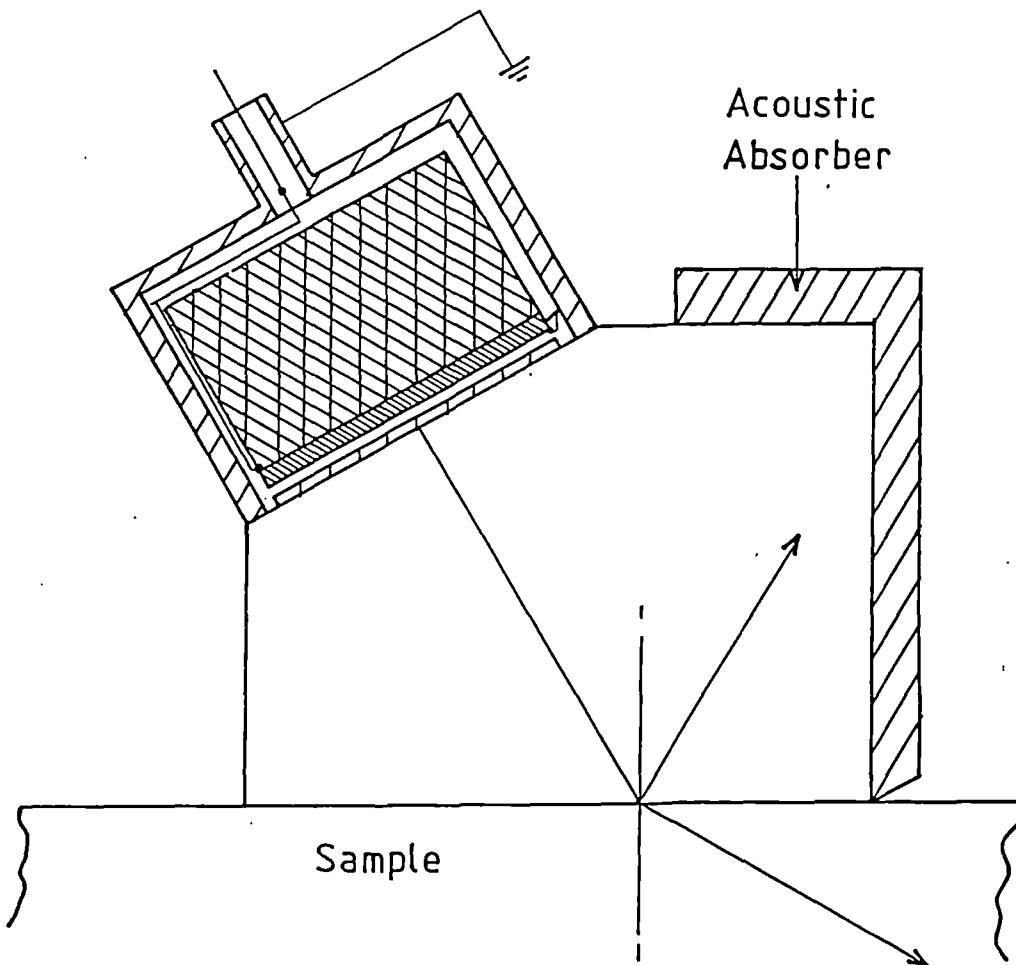


Fig 4.1(b) Typical angled piezoelectric probe.

defects which may not be favourably oriented, (Wustenberg et al 1976). Angled beams can be achieved by bonding the transducer to a wedge of appropriate geometry and acoustic properties, fig 4.1b. The acoustic pressure for the incident wave is directed obliquely to the boundary and can be resolved into two components, one acting along the boundary and the other perpendicular to it. This gives rise to shear waves as well as transmitted and reflected compressional waves. For plane waves Snell's law governs the direction of the various modes dependent on their velocities, fig 4.2.

$$\frac{C_1}{\sin\theta_1} = \frac{C_1'}{\sin\theta_1'} = \frac{C_2}{\sin\theta_2} = \frac{C_2'}{\sin\theta_2'} \quad (4.1)$$

where  $C_1$  and  $C_2$  are the compressional wave velocities in the first and second media, respectively, and  $C_1'$  and  $C_2'$  are the corresponding shear wave velocities.  $\theta_1$  is the angle of incidence and reflection and  $\theta_2$  the angle of refraction of the longitudinal waves.  $\theta_1'$  and  $\theta_2'$  are respectively the angles of reflection and refraction for the shear waves. As the angle of refraction increases, an increasing proportion of the incident longitudinal wave will be converted at the boundary into shear. Under such conditions testing is ambiguous. However once the critical angle for total internal reflection is reached for longitudinal pulses in the wedge then only transverse waves will be present in the sample and these may be used for NDE. Rayleigh waves may be propagated along the sample

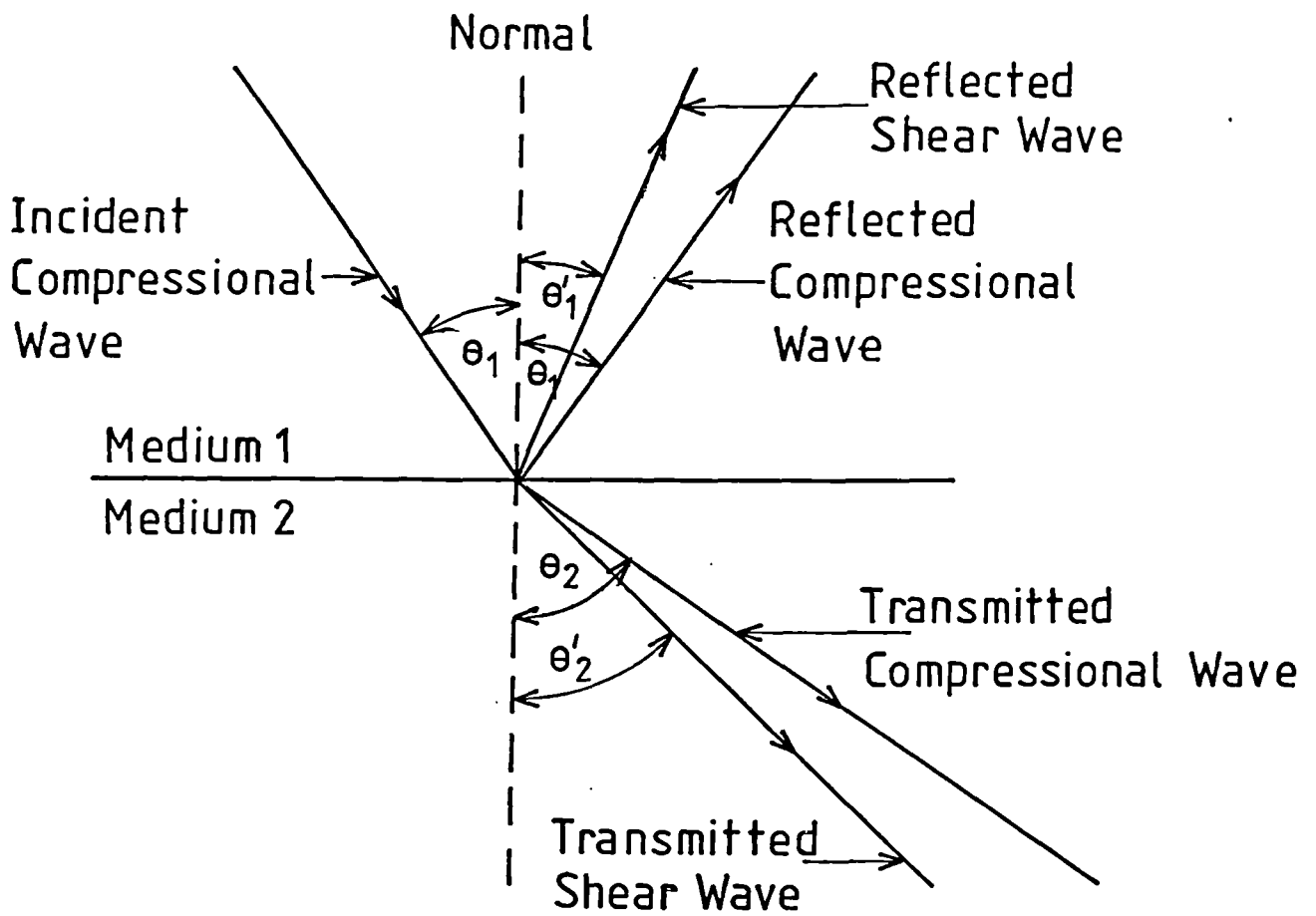


Fig 4.2 Illustration of Snell's law.

surface by inclining the probe to a further critical angle given by

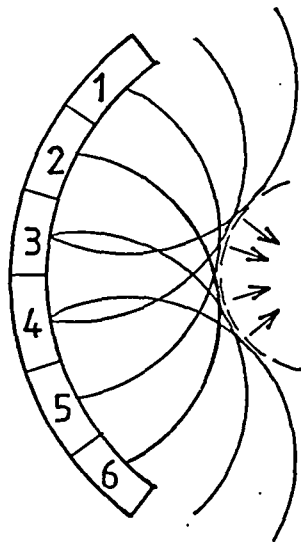
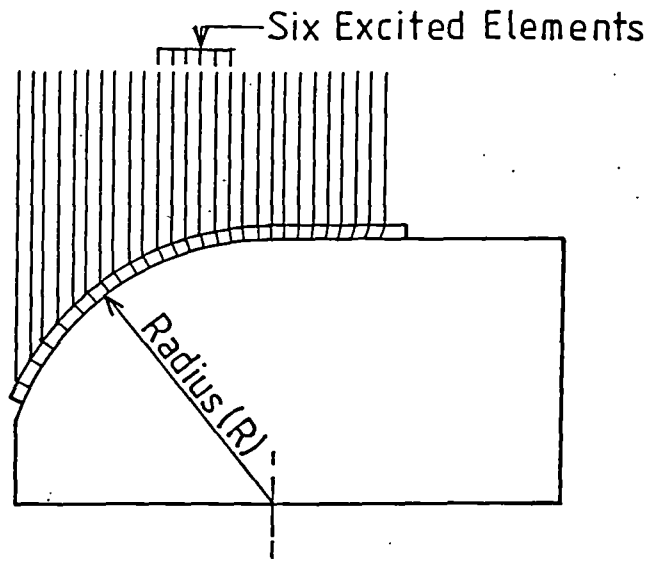
$$\sin\theta_R = \frac{C_1}{C_R} \quad (4.2)$$

where  $C_R$  is the Rayleigh wave velocity in the sample, (Victorov; 1967).

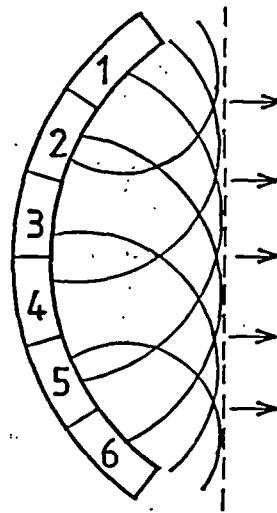
Using a perspex wedge on a steel sample, an angle of approximately  $30^\circ$  is required for total internal reflection of longitudinal waves although an angle of at least  $40^\circ$  is normally set for unambiguous testing, (Szilard; 1982). For the generation of Rayleigh waves this angle is between  $60^\circ$  and  $70^\circ$ . The wedge blocks are usually partly surrounded by sound absorbing material to suppress spurious echoes.

A variable angle probe was suggested by Piggins and Farley, (1979). The probe, fig 4.3, consists of an array of narrow piezoelectric elements on the curved surface of a hemi-cylindrical perspex shoe. Groups of six elements are selected to generate the required beam angle. To compensate for the curvature of the shoe, inter-element delays are necessary.

Transducers based on thick piezoelectric ceramic blocks have been used for wideband detection of ultrasound at normal incidence. Dewhurst et al, (1983), described two such devices for the detection of acoustic transients generated by a laser source. One of these is a 12mm thick, 15mm diameter cylinder of PZT5A ceramic, polarized along its axis in the direction perpendicular to the parallel end faces. The basic principle is that the block should be



Effect Of Curvature



Electronic Defocusing

Fig 4.3 Variable angle piezoelectric probe.  
After Piggins and Farley, (1979).

sufficiently thick for resonances to be absent over the acoustic time-scales of interest. Movement of the face adjacent to the metal surface gave a voltage output across the device which represented closely the acoustic pulse displacement. Only when the opposite face of the ceramic had been perturbed by the acoustic pulse was the output distorted by the finite thickness of the probe. Another non resonant piezoelectric transducer was described by Cooper, (1985). Here a disk of PZT was cemented onto an exponential brass horn. The impedances of the two substances matched well so that most of the acoustic energy entered the brass but, because of its shape and high attenuation, little of it returned to affect the PZT for a second time. Both of the latter two devices were spring loaded to ensure good mechanical contact with the test sample. A major disadvantage with piezoelectric devices is that they require good acoustic bonding via mechanical coupling and/or through some medium such as oil, grease or water. The sample surface is therefore loaded instead of being stress free. This coupling can lead to variations in amplitude from shot to shot for a given transducer since it is sensitive to the amount of loading applied. The Curie temperature of the piezoelectric prohibits the use of such devices for testing in hostile environments as does the manual nature of current NDE techniques.

The plastic PVDF is currently being developed as a broadband transducer, (>10MHz), with specific application to under-water devices, (e.g. Milenin et al; 1969, Murayama

et al; 1976, Bui et al; 1976).

All types of device mentioned so far require either direct bonding to the sample or coupling through some liquid medium. Three different non-contact devices for generation and/or detection of ultrasound in metals are now discussed.

#### 4.2/ EMATs.

Acoustic waves were first generated in a metallic sample using electromagnetic radiation incident on the sample in the presence of a static magnetic field in 1967 by Gantmaker and Dolgoplov. Most of the work done on these devices concern their use as generators of ultrasound, however these electromagnetic acoustic transducers, (EMATs), may also be used for detection.

A coil carrying high frequency current in the vicinity of a metal object will induce eddy currents in it. The eddy current produces a dynamic magnetic field,  $\underline{H}$ , which is approximately related to the local eddy current density by  $\underline{J} = \underline{\nabla} \times \underline{H}$ . An acoustic disturbance can be produced in the metal if a static magnetic induction,  $\underline{B}_0$ , is applied at the same time. This interaction between the eddy current and the magnetic field is due to Lorentz forces.

It has been shown, (Dobbs; 1973), that for the case where the electromagnetic skin depth,  $\delta$ , is much less than the acoustic wavelength,  $\lambda$ , the amplitude of elastic vibration,  $\xi$ , is given by

$$|\xi| = \frac{|E|B_0}{\rho C \omega (1 + \beta^2)^{1/2}} \quad (4.3)$$

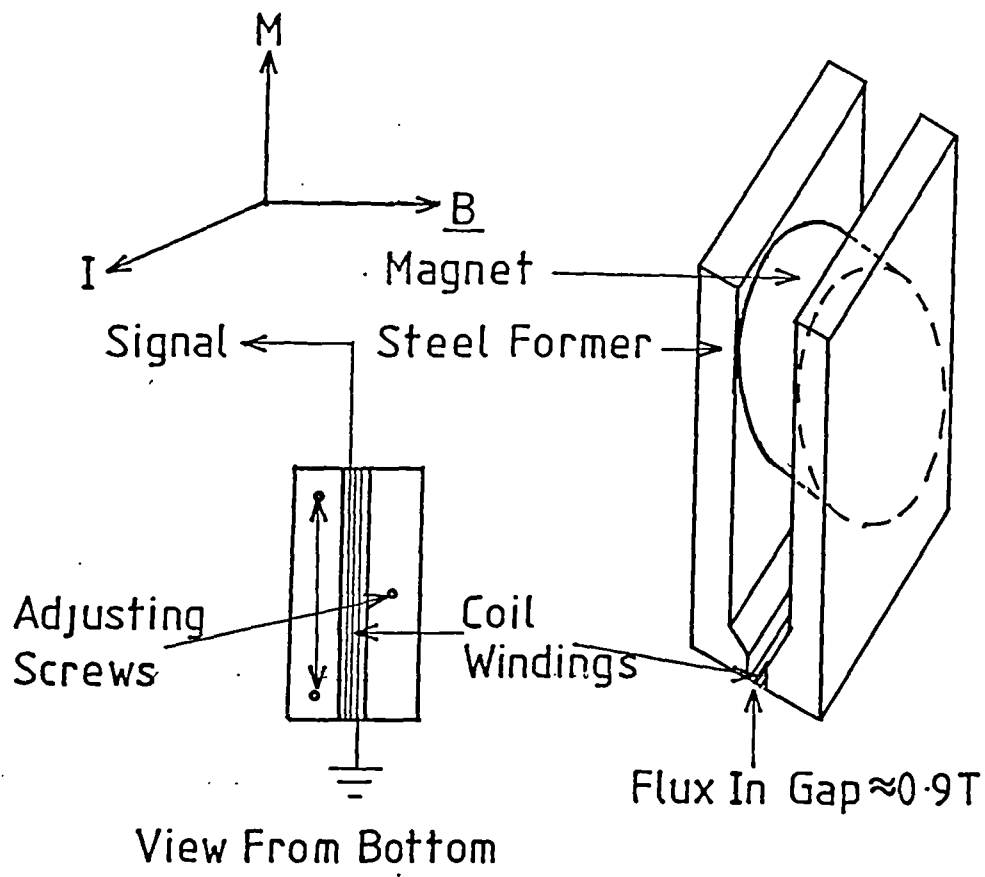
where  $\rho$  is the density of the metal and  $\beta = \left(\frac{\omega \delta}{C}\right)^2$  is the skin depth parameter. Hence the amplitude of an ultrasonic wave is directly proportional to the amplitudes of both the static and dynamic magnetic fields and inversely proportional to the frequency,  $\omega$ , and speed of sound,  $C$ .  $\beta \ll 1$  for longitudinal and shear waves of a few MHz in aluminium and steel and thus has a very small effect.

Most of the energy incident upon the surface as electromagnetic radiation is lost as joule heating. The ultrasonic conversion efficiency,  $\eta$ , is given by, (Frost; 1979),

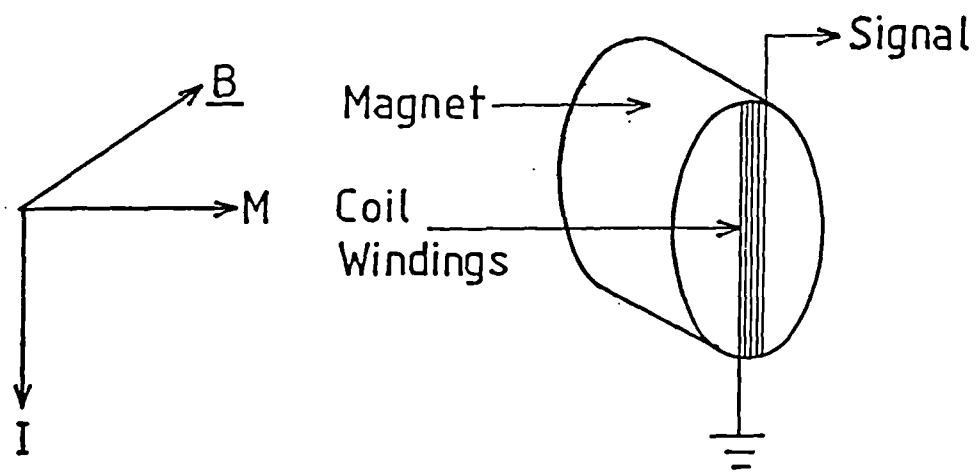
$$\eta = \frac{2B_0^2}{\mu_0 C \omega \delta (1 + \beta^2)} \quad (4.4)$$

The conversion process is reversible so that for generation and detection of ultrasonic signals with a single coil in the pulse-echo mode, the overall efficiency is  $\eta^2$ .

In this thesis, two types of EMATs were developed for use as detectors. The first was sensitive to out of plane motion and had  $B_0$  parallel to the sample surface, fig 4.4a. The static magnetic field was supplied by a  $SmCo_5$  magnet with the detection coil being made out of 60 turns of 54 gauge copper wire. A steel former guided the lines of flux producing a field of the order of 0.9T in the gap which housed the detection coil. Three grub screws on the face of the former allowed the transducer to be



(a)



(b)

Fig 4.4 Schematic diagrams of EMATS.  
 (a) EMAT sensitive to out of plane motion.  
 (b) EMAT sensitive to motion in the plane of the surface. Guard ring not shown.

accurately positioned above the surface, typical separation being  $\sim 0.1\text{mm}$ . Signals obtained on epicentre of a 25mm thick duraluminium sample when using this detector with the laser source are shown in fig 4.5. The signals were fed through a high input impedance Harwell charge amplifier before capture. Fig 4.5a shows the signal detected from a thermoelastic source. Numerical integration of this waveform yields the trace shown in fig 4.5b, which exhibits the main features of a thermoelastic displacement waveform, (c.f. fig 2.2b). Minor differences between the traces, for example the lack of detection of the p-step in the integration are symptoms of the lower bandwidth of the EMAT. The signal from the plasma source, fig 4.5c, can be directly compared with the displacement waveform obtained from a weak ablation of the surface, (normal force with approximate Gaussian time dependence), fig 2.8d. Fig 4.5c is essentially the differentiation of the waveform produced for a Heaviside normal force fig 2.8b. It is deduced therefore that this system is sensitive to out of plane velocity of the surface, consistent with similar conclusions by Hutchins et al, (1985).

The second type of EMAT employed was intended for polarized horizontal shear wave detection. An  $\text{Nd}_{15}\text{Fe}_{77}\text{B}_8$  magnet provided a field of  $\sim 0.4\text{T}$  normal to the sample surface. The detection coil consisted of approximately 50 turns of 48 gauge copper wire which was wound around a circular former then flattened and positioned on the face of the magnet, fig 4.4b. This device was therefore

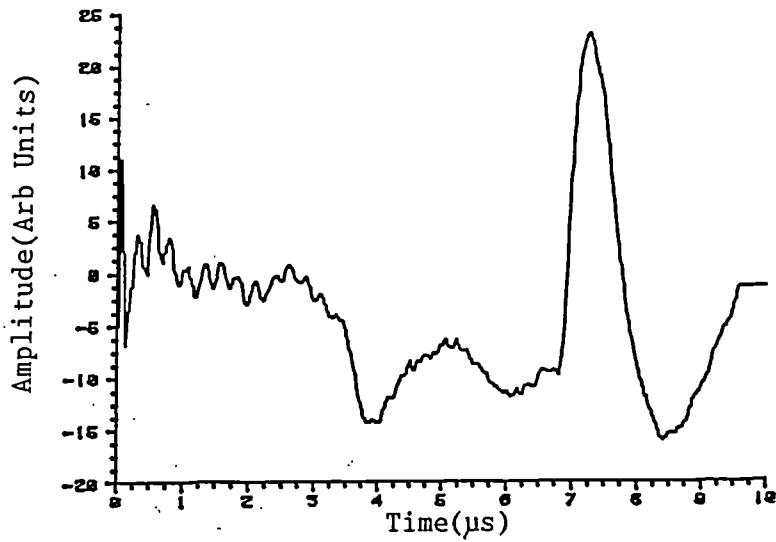


Fig 4.5(a) Signal detected by the EMAT of fig 4.4(a) at epicentre of a thermoelastic source after propagation through a 25mm thick dural sample.

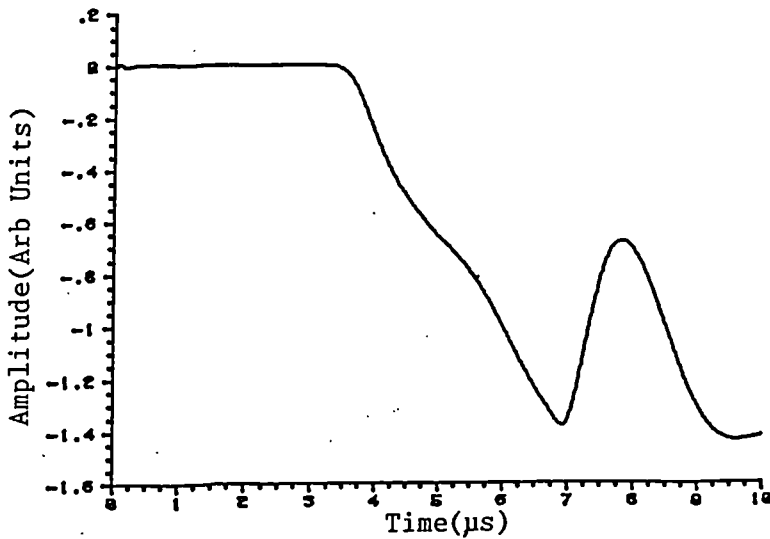


Fig 4.5(b) Numerical integration of fig 4.5(a).

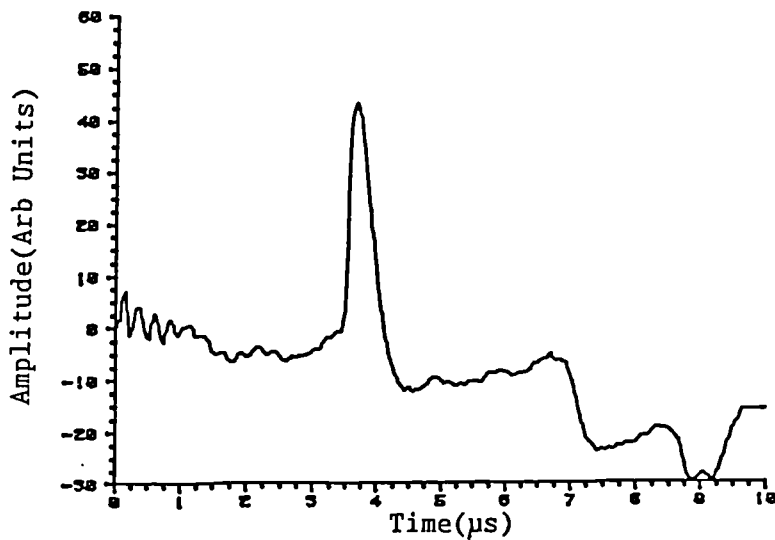


Fig 4.5(c) Signal detected by EMAT of fig 4.4(a) at epicentre of a plasma source after transmission through a 25mm thick dural sample.

sensitive to in-plane motion of the surface normal to the line of the detection coil. A guard ring shielded the coil and was adjustable so that the lift off from the surface could be varied. Hutchins and Wilkins, (1985), used an EMAT, sensitive in the same plane, to measure the directivity of a thermoelastic laser line source. These authors placed the detector at the epicentre of an aluminium test piece and rotated it with respect to the laser line.

As has previously been discussed, (section 2.2), a thermoelastic laser line source produces maximum tangential displacements in the bulk of aluminium at an angle of approximately  $30^\circ$  from the normal. The signal at this angle from such a source has been detected and is shown in fig 4.6a. Here a cylindrical lens was used to focus the incident laser beam to a line 11mm long by 0.5mm wide on the surface of a 4.5mm thick dural sample. The EMAT was positioned on the opposite face and displaced from epicentre by  $(2.6 \pm 0.4)$ mm. The coil windings were parallel to the laser line, and approximately 0.1mm from the metal surface, fig 4.7. The detector was then rotated, in the plane of the sample, around a point at the middle of the epicentre of the line source. Taking the peak to peak amplitudes of the signals at  $15^\circ$  intervals a directivity pattern was obtained, fig 4.6b, which demonstrates that polarized shear pulses are produced from a line source. This is consistent with the work of Hutchins and Wilkins, however, the directivity was not as marked for their case

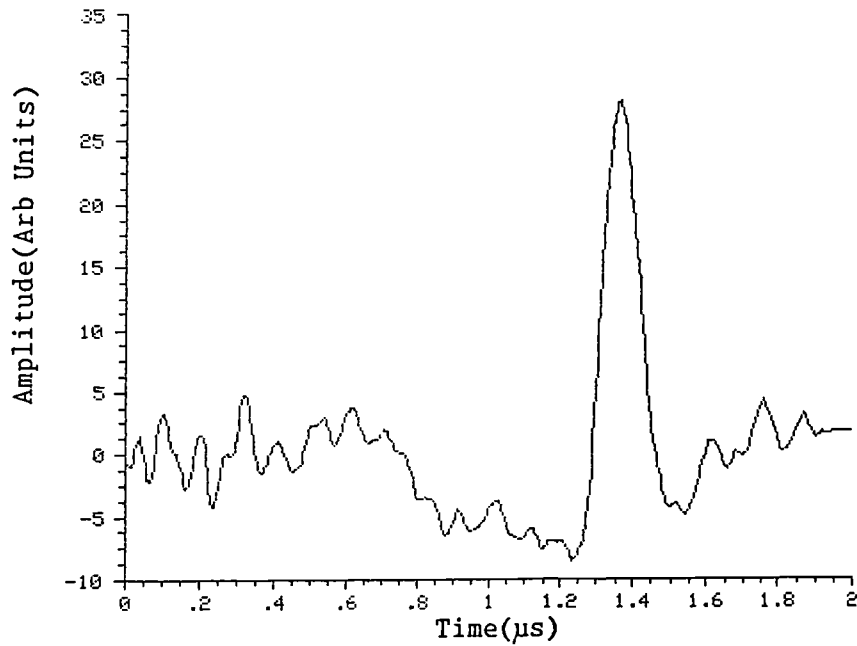


Fig 4.6(a) Signal detected at  $30^\circ$  from epicentre of a 4.5mm thick dural plate. EMAT of fig 4.4(b) used with its coil aligned parallel to thermoelastic laser line source.

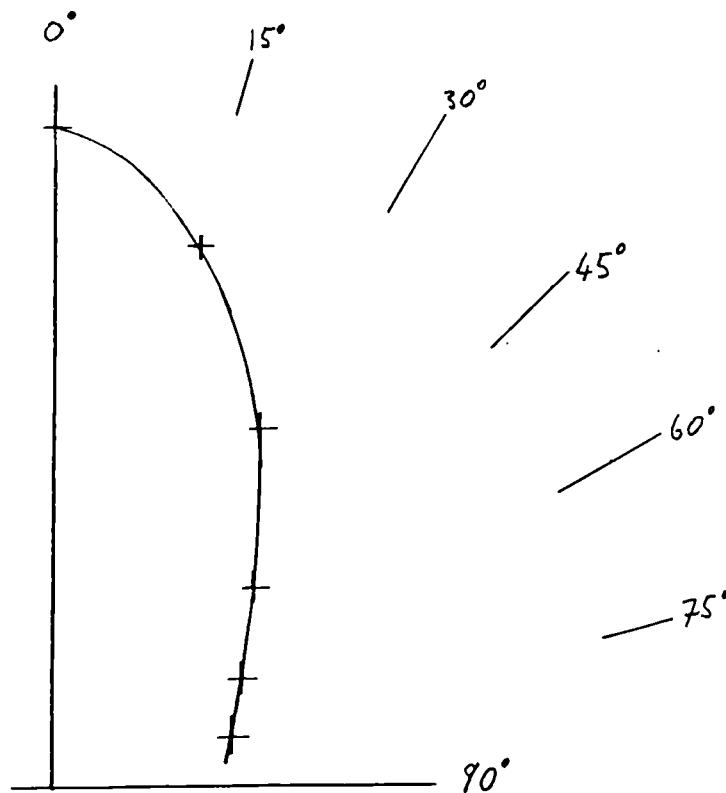


Fig 4.6(b) Variation of in plane component of shear pulse with angle. Set up as in fig 4.7.

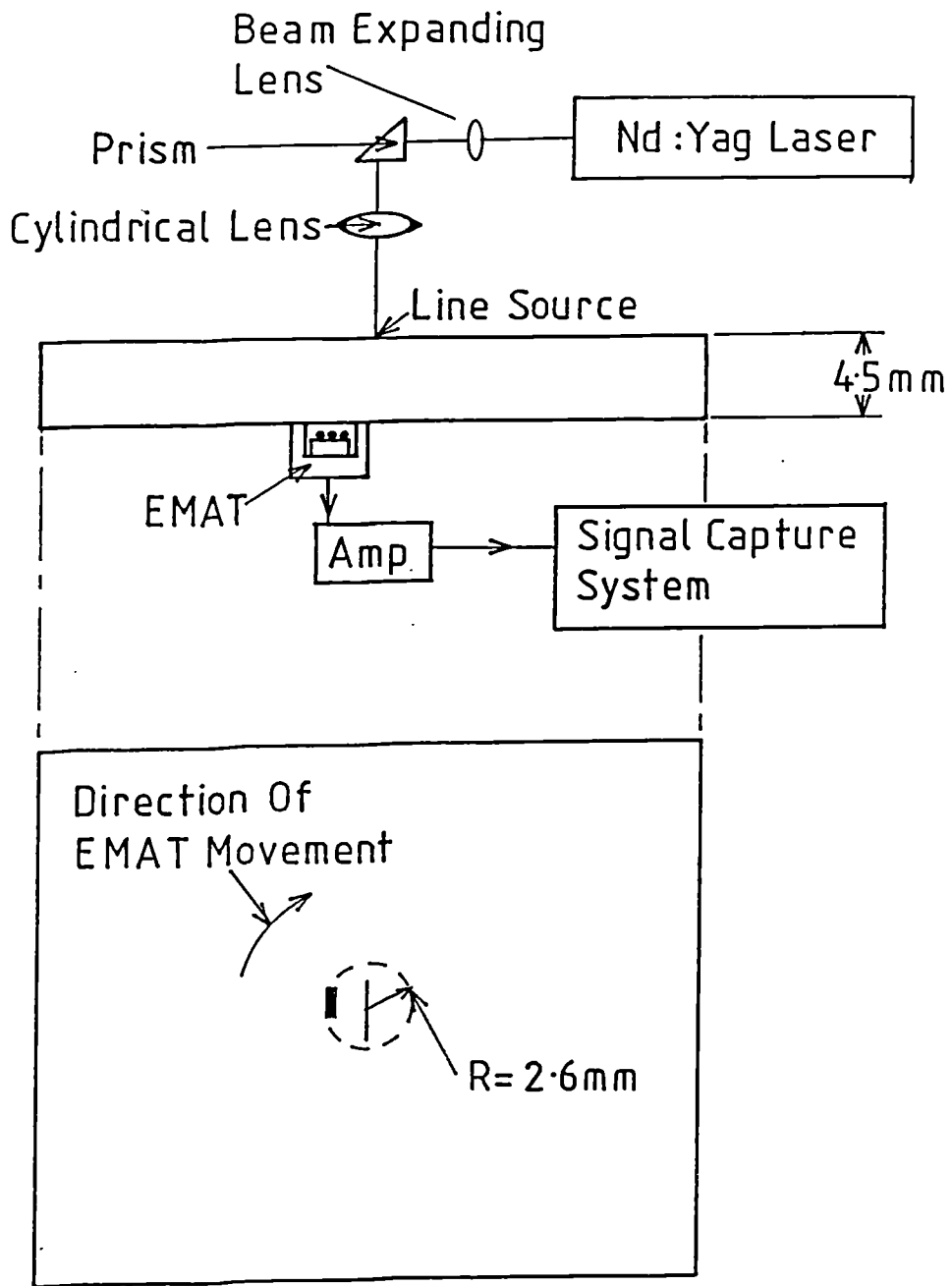


Fig 4.7 Schematic diagram of apparatus used for the directivity of polarised shear pulses from a thermoelastic line source.

possibly due to their experimental geometry.

#### 4.3/ Capacitance Or Electrostatic Methods.

The electrodes in a capacitor have a force,  $F$ , attracting them

$$F = -V^2 \frac{\epsilon \epsilon_0 s}{d^2} \quad (4.5)$$

where  $V$  is the voltage,  $\epsilon$  the dielectric constant,  $\epsilon_0$  the permittivity of free space,  $s$  the surface area and  $d$  the separation between the electrodes. Therefore, using a metal sample as one of the electrodes and applying a sinusoidal voltage across the plates an acoustic signal will be generated, at twice the driving frequency, in the sample. This doubling of frequency is due to the force between the electrodes always being attractive regardless of the polarity of the voltage. By applying a bias voltage,  $V_0$ , such that  $V_0$  is greater than the maximum a.c. voltage the acoustic frequency is made equal to the frequency of oscillation of  $V$ . The electrostatic forces in the case of metals act at right angles to the surface resulting in the preferential generation of longitudinal bulk waves. This system has a very high bandwidth, (up to 200MHz; Legros et al 1972), but the acoustic power generated is low. The force increases with the square of the voltage which may only be so high as not to cause electrical breakdown across the plates.

In a reciprocal manner flat plate capacitance transducers for ultrasonic displacement detection have been

described by Scruby and Wadley, (1978), and by Hutchins and MacPhail, (1985). Here the parallel plates of the capacitor are the polished surface of the test piece which is earthed, and the transducer plate held at a potential  $V$  at a distance  $\xi$  above the sample. The capacitance,  $C$ , of the transducer will change due to the oscillation of the sample surface on the arrival of an acoustic signal. This movement of the surface by an amount  $\delta\xi$  causes the capacitance to change by  $\delta C$ , which leads to a charge,  $\delta q$  being induced on the electrode,

$$\delta q = V\delta C$$

since

$$C = \frac{\epsilon S}{\xi}$$

where  $\epsilon$  is the permittivity of the gap. The sensitivity of the transducer is therefore

$$\frac{dq}{d\xi} = - \frac{\epsilon V S}{\xi^2} \quad (4.6)$$

Hence by increasing the voltage across the plates and decreasing the air gap, the sensitivity can be increased, however electrical breakdown is again a limiting factor here. Sensitivity is also improved by increasing the surface area of the transducer but this introduces further constraints on sample flatness and alignment as well as decreasing the frequency bandwidth for non plane wavefronts from the bulk or for surface acoustic waves. Such acoustic disturbances can be generated by a pulsed laser source. For wider frequency response, Aindow et al, (1987), developed a

capacitance transducer capable of resolving surface acoustic transients. In this system a 4mm diameter ball electrode is held typically  $4\mu\text{m}$  from the surface of the earthed sample, fig 4.8. For a +200V d.c. bias voltage across the transducer, a sensitivity of  $1.5\text{mV/nm}$  was reported, using a charge amplifier which produced  $250\text{mV/pC}$ . A bandwidth for Rayleigh wave detection in excess of 5MHz was obtained. It was demonstrated that this system had a higher frequency bandwidth than the flat plate device described by Scruby and Wadley. Since the transducer has a relatively small active area, the sample does not have to meet the stringent requirements of being polished optically flat and positioning of the device is also easier. Sensitivity is reduced when compared with a plane parallel capacitance probe although surface displacements are measured with a nanometer resolution.

In other work Boler et al, (1984), used a capacitance transducer having a point-like probe which had a flat frequency response from 100kHz to 6MHz. Aindow, (1986), developed a capacitance arc probe sensitive to the normal component of surface pulse motion. The system described had a wide bandwidth, ( $>3\text{MHz}$ ), and high sensitivity, ( $10\text{mV/nm}$ ).

The major advantages of capacitance transducers are that they are wide bandwidth, non-resonant devices which may be absolutely calibrated. However they require good charge amplifiers, polished surfaces, are insensitive compared to piezoelectric devices and need fine adjustment

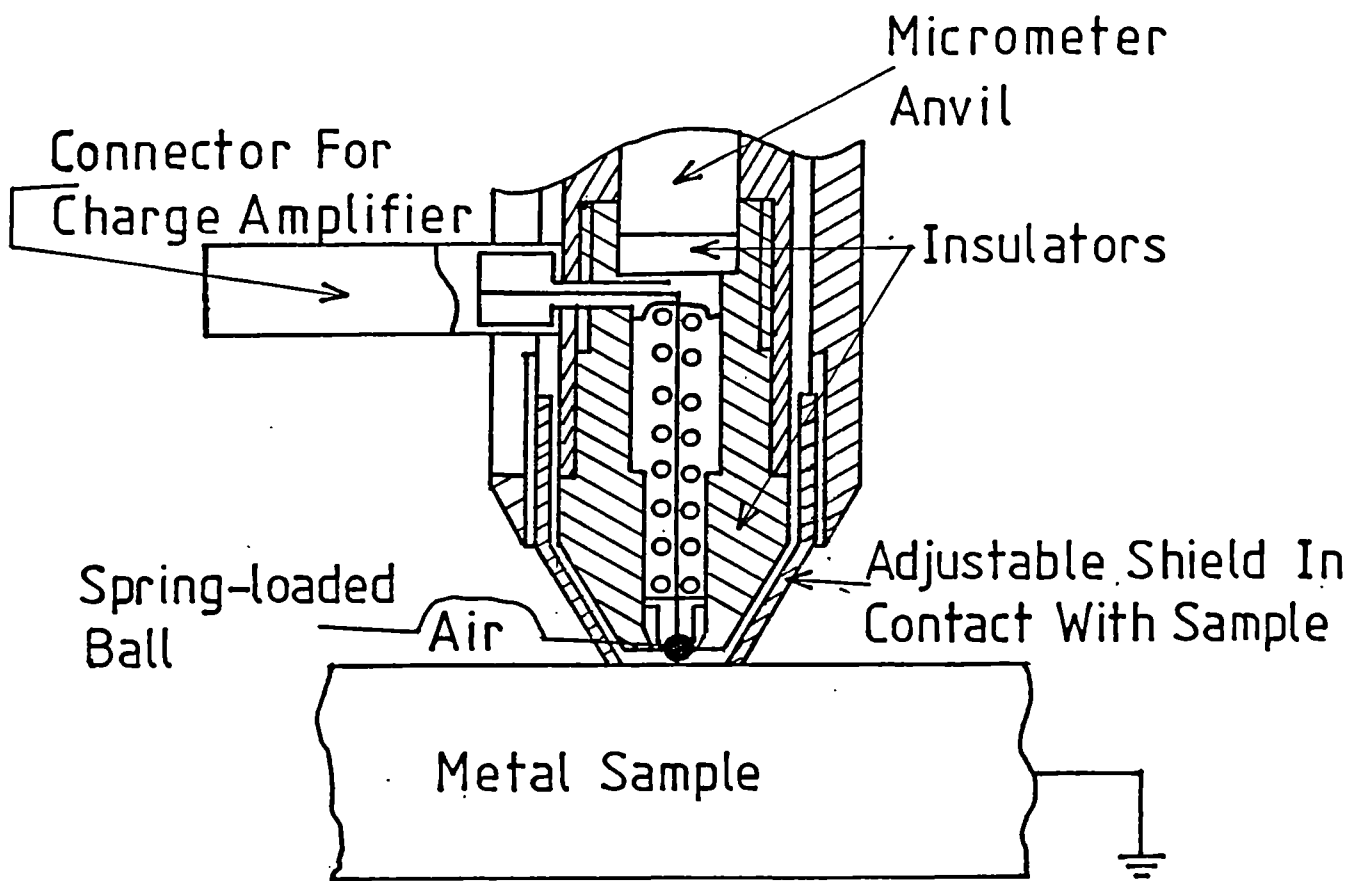


Fig 4.8 Schematic of ball capacitance probe. The ball is typically held a few microns above the surface at a potential of +200V.

by micrometer since the plate separation is typically a few microns.

#### 4.4/ Optical Detection Techniques.

##### 4.4a/ Knife Edge Technique.

If the reflection of light from a highly coherent reproducible source, such as a laser, incident at an angle on a polished surface is partially blocked, then a surface wave propagating on the sample will cause a variation in the light intensity incident on a detector placed behind the partial aperture. This technique, fig 4.9, was first described by Adler et al, (1968), who reported a minimum detectable displacement of  $10^{-11}$  m using 8MHz c.w. waves on steel and ceramic samples.

##### 4.4b/ Interferometers.

In 1881 Michelson and Morley carried out a famous experiment to investigate the possible existence of ether drift. The optical interference technique described by them has since been used for the measurement of the standard metre, measurements of refractive indices and spectroscopy as well as monitoring small displacements. In a Michelson interferometer, fig 4.10a, light of wavelength  $\lambda$  from a coherent monochromatic source, (such as a He-Ne laser), is divided in amplitude by a plate beamsplitter. The two beams obtained are sent in different directions against plane mirrors before being recombined to form interference fringes. A compensating plate in the signal arm ensures

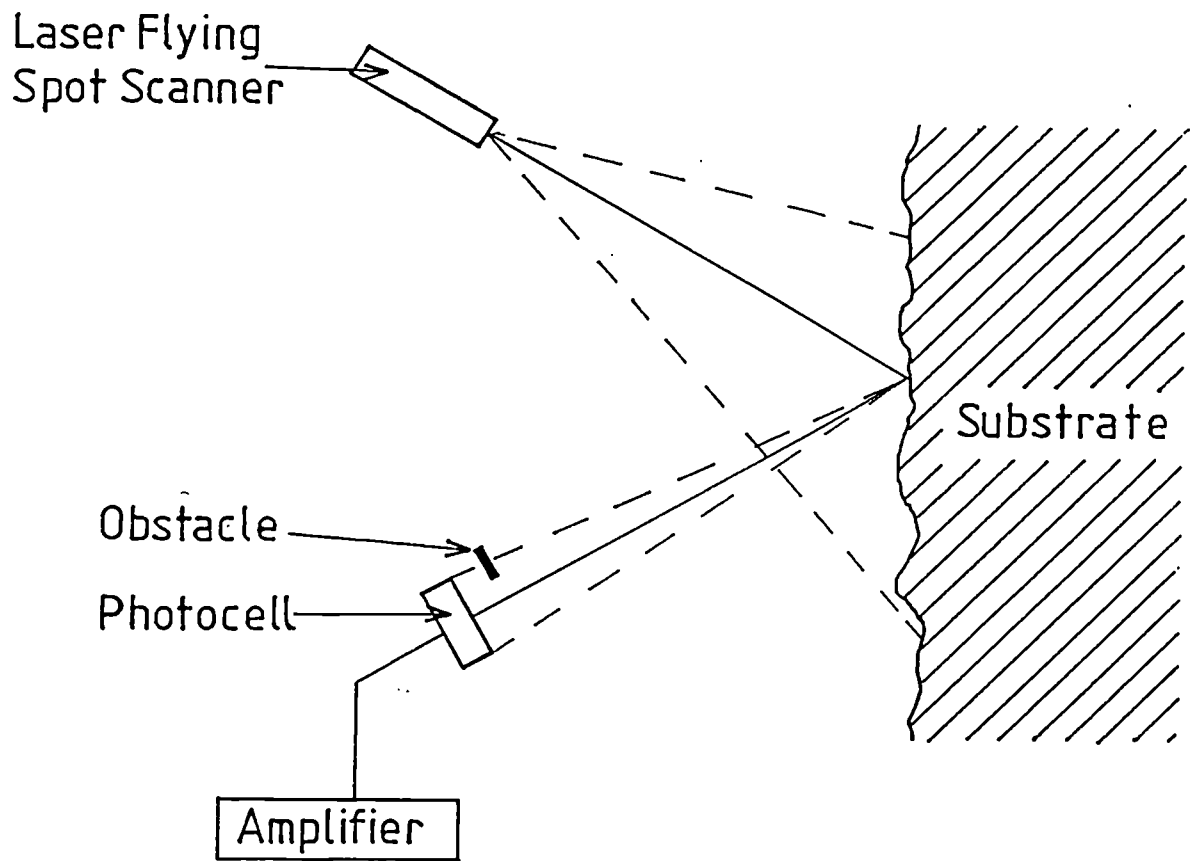


Fig 4.9 Knife edge technique for the detection of surface acoustic waves.  
After Adler et al, (1968).

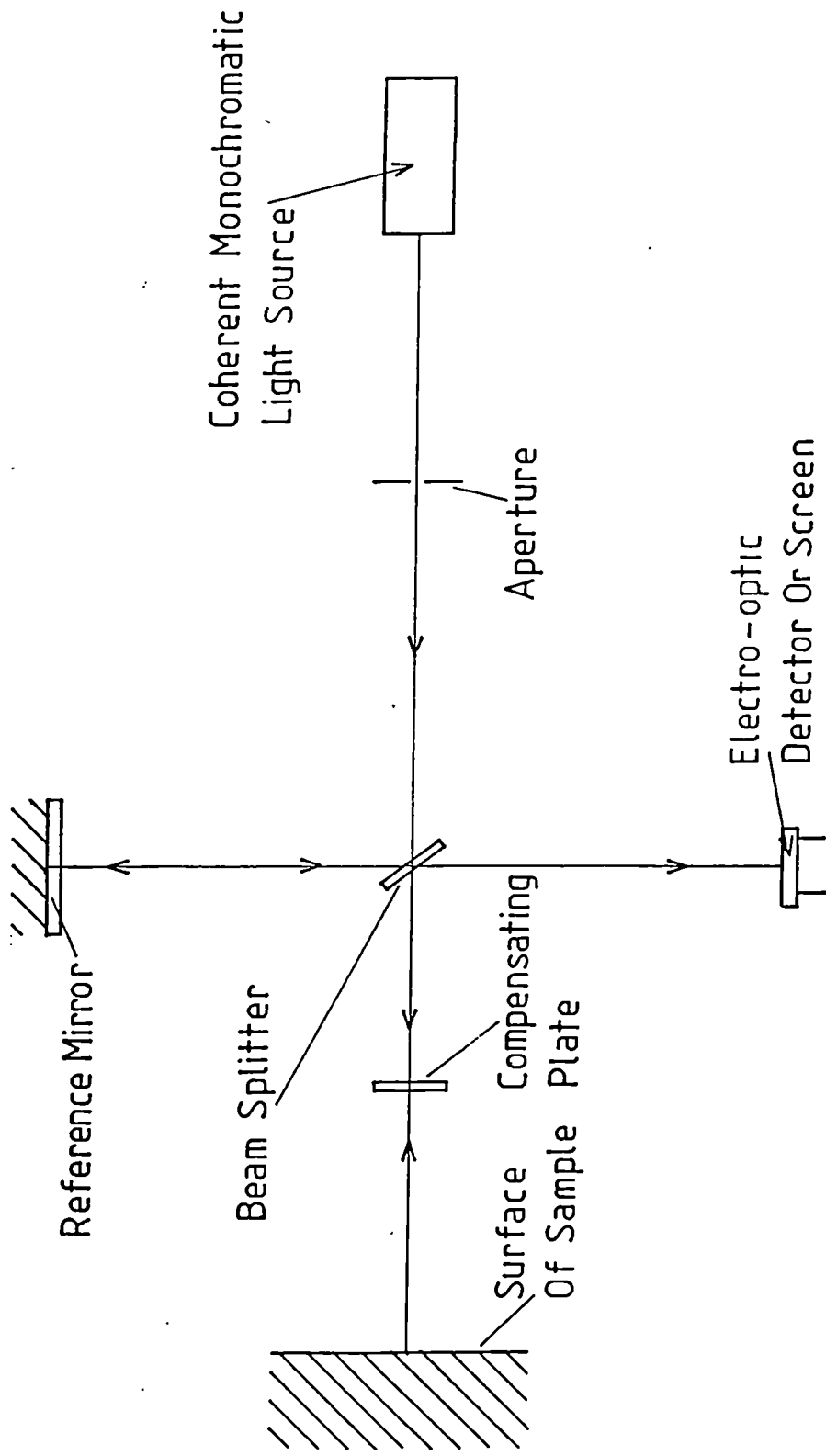


Fig 4.10(a) Schematic diagram of a Michelson interferometer.

that the path length through glass is the same for both beams. Motion of one of the mirrors causes the interference pattern to move. For large displacements it is possible to count whole numbers of fringes, each representing a motion of  $\frac{\lambda}{4}$ . For displacements smaller than  $\frac{\lambda}{4}$  the change in position may be calculated from the variation in fringe intensity. Ultrasonic displacements produced by the laser source are typically only a thousandth of a fringe, or less, (tenths of nm), when using this device with a He-Ne laser source. Thus it has been necessary to use phase information to resolve these small displacements. Due to noise effects there are displacements of typically 1 $\mu$ m to 50 $\mu$ m present at low frequencies, (less than 5kHz). Several types of interferometer have been developed to measure small, high frequency displacements using various techniques for low frequency compensation. Calder and Wilcox, (1978), overcame the difficulty of background vibrations using a modified Michelson interferometer. The detector, a photomultiplier tube, was pulsed on just prior to the arrival of the acoustic pulse. This also permitted operation at a higher ambient light level and provided high sensitivities. In a differential interferometer, (Palmer et al 1977), low frequency vibrations are compensated for by having both the signal and the reference beams incident on the sample. This system however required complicated receiving electronics and a sinusoidal acoustic displacement was assumed in the theory. Vilkomerson, (1976), used a variant of the Michelson interferometer

where there are two output signals that vary with optical path difference,  $x$ , but are in phase quadrature such that one output signal is proportional to  $\sin(4\pi x/\lambda)$  and the other to  $\cos(4\pi x/\lambda)$ . This is known as a quadrature dual interferometer which never has a zero in sensitivity. Squaring and summing the signals effectively stabilises the operating point of the device at the high sensitivity point, and eliminates the effect of environmental vibrations. Vibratory displacements down to 1pm have been reported using this apparatus.

In a heterodyne interferometer, (Rudd 1983), the interference is between two optical fields of differing frequency, the superposition of which yields a time dependent intensity. The beat frequency is chosen to be high enough so that low frequency signals due to background noise are insignificant, but it must be low enough, (<100MHz), to be resolved by opto-electronic detectors. The acoustic signals are superimposed on the carrier frequency and are extracted by subsequent electronic signal processing. Krautkramer, (1979), describes an optical technique based on the Mach-Zehnder interferometer. Light from a high power Nd:YAG laser is pulsed onto the sample surface, part of the reflected light being fed directly to a photo-detector. The remaining light is delayed by 25ns before being recombined with the first beam. The delay path is such that the direct and delayed beams have a phase difference of  $90^\circ$  when the sample is at rest. High frequency motion of the surface causes a change of phase relation

between both beams. There is no change in phase relation at low frequencies and hence the interferometer is insensitive in this region, (below 100kHz). Due to the high energies used this interferometer is sensitive on non polished metals.

Another system to make use of a delay in one arm is the fibre optic interferometer described by Bowers, (1982), which detects surface waves propagating at a predetermined frequency. In this device half of the incident light travels around an optical fibre loop clockwise, whereas the rest goes around the same loop anti-clockwise. Hence there is zero path difference between the two signals and any phase difference between the two components is due to motion of the surface. Variations in phase difference due to environmental effects will occur over longer time scales and will not be detected. A piezoelectric phase modulator is used in one of the arms so that the device is not working around a zero static phase difference. Garg and Claus, (1983), also made use of optical fibres in their differential interferometer. Optical components were placed in a vibration isolated chamber, remote from the sample. The placing of optical fibres containing the reference and signal arms inside the cable minimised the chance of thermal or mechanical vibration affecting one arm without affecting the other.

Most optical detectors of ultrasound, like capacitance transducers, require polished surfaces to obtain sufficient sensitivity. Monchalin, (1985), however

described a system based on a confocal Fabry-Perot interferometer which had a high enough etendu or light gathering efficiency to work on a machined, not polished, steel surface. A direct ultrasonic pulse and at least three echoes were detected after propagation through a 1/2" steel plate, the ultrasound being generated by a Nd:YAG laser pulse focused on a water film. This interferometer detects optical frequency change and so the device is sensitive to the surface velocity of the sample. A small part of the laser output was sent through the Fabry-Perot along the same path as the light received from the target, this was used to stabilise the device for maximum sensitivity by controlling a PZT element on one of the interferometer mirrors.

Many Michelson type interferometers have been stabilised by separating out the low frequency components of the photocurrent, (0 to 5kHz), amplifying this signal and using it to displace the reference mirror, again via a piezoelectric element, to maintain the correct phase difference in the two arms, fig 4.10b, (Bondarenko et al; 1976, Hutchins and Nadeau; 1983). This type of system can however jump out of stabilisation in the presence of sufficiently large background vibrations. Piezoelectric elements have typical sensitivities of 1000 volts per micron displacement. To overcome this jumping Emmony et al, (1983), used a 3mm long piezoelectric bimorph element with an aluminised mirror at the free end which displaced  $1\mu\text{m}$  for an applied p.d. of 150V. McKie, (1985), described

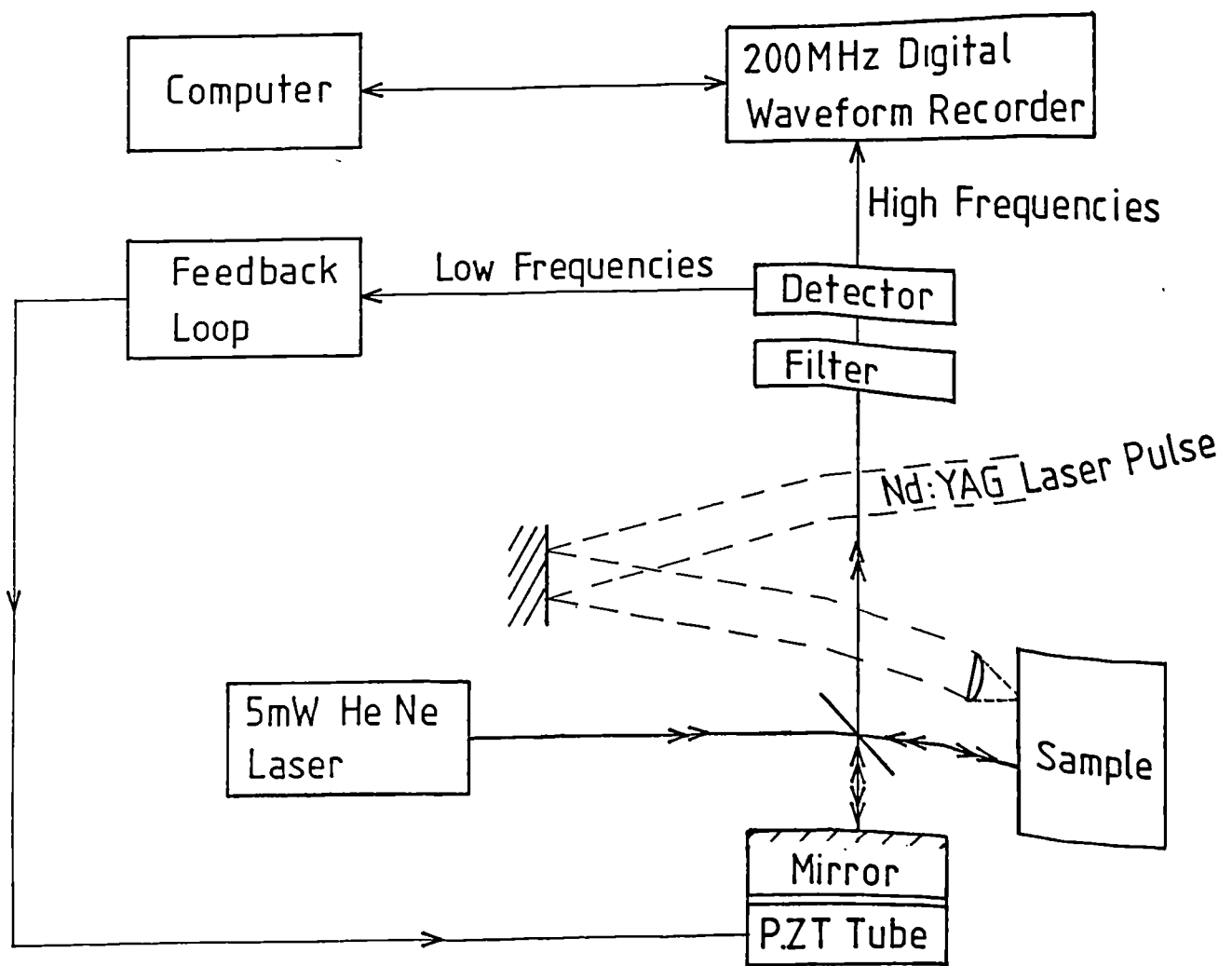


Fig 4.10(b) System for the remote detection of ultrasound as used by Hutchins and Nadeau, (1983). The low frequency components of the photocurrent is amplified and used to displace the reference mirror via the PZT tube. This maintains the current phase difference in the two arms of the interferometer in the presence of low frequency noise.

a stabilisation system based on an electro-mechanical vibrator which requires only ~4.5 volts to achieve stabilisation. This interferometer has a minimum displacement detection limit of ~47pm with a bandwidth of 130MHz.

#### 4.5/ Methods of Ultrasonic NDE.

##### 4.5a/ History.

Sokolov, (1929), first suggested the use of ultrasound to locate defects in metal objects. The acoustic pulses from a quartz plate were coupled to the test piece via a bath of mercury. Interestingly, one of the detection methods suggested was observing how the transmitted pulse deflected a light beam shone on to a screen coupled to the mercury, fig 4.11. This is an example of through transmission, a technique which is not widely used now because of difficulties with alignment of the probes, variable acoustic coupling and effects due to diffraction at the edges of any defect present. Very thin cracks constitute an impenetrable barrier to ultrasonic waves in metals hence any defect in the path of an ultrasound beam will cast an acoustic shadow on the receiver, fig 4.12a. However, because of diffraction this technique is sensitive to transducer area, the depth of the flaw relative to the overall sample thickness, the flaw size and the frequency used. Through transmission testing may also be carried out with access to one face only, fig 4.12b.

In the 1940s a major innovation occurred with the

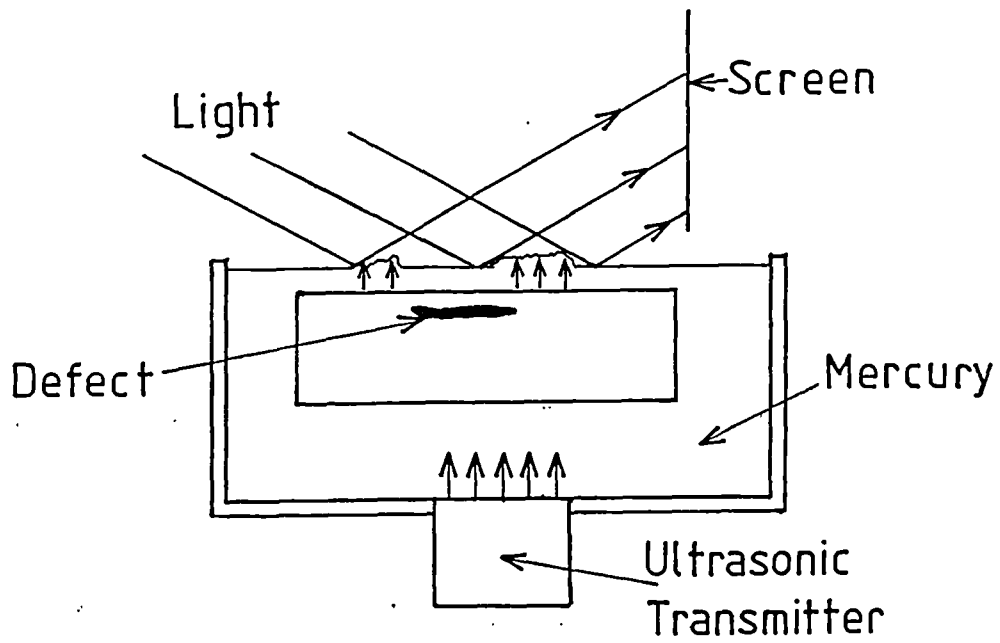


Fig 4.11 An early ultrasonic non-destructive testing method.  
After Sokolov, (1936).

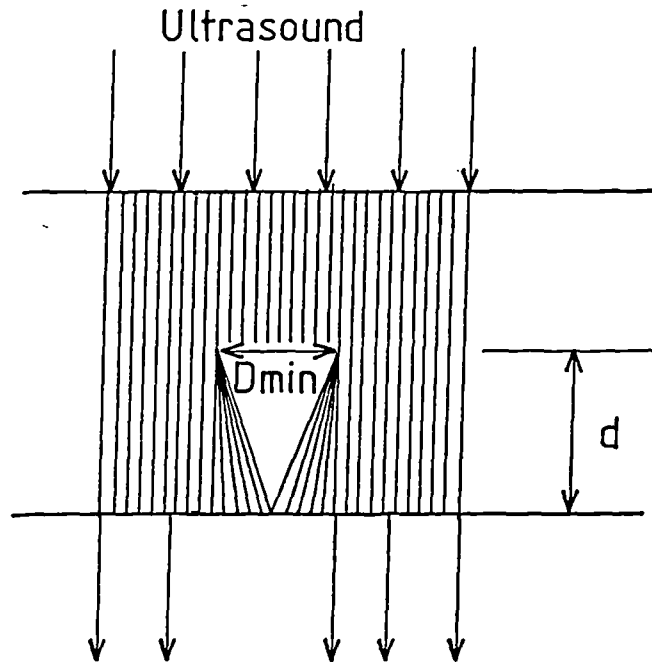


Fig 4.12(a) The detectability of a defect is dependent on its position in the bulk of the sample because of diffraction effects. This is wavelength dependent, the wavelength should always be smaller than the defect diameter. An absence of signal on epicentre will occur if the defect size is greater than  $2d \tan \theta$ , however there will still be a reduction in signal in this region for smaller flaws.

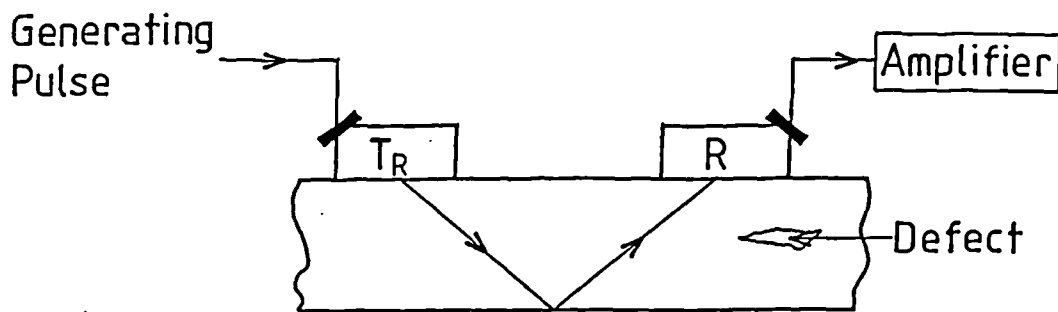


Fig 4.12(b) An example of through transmission with access to only one face. A drop in signal reaching the receiver, R, Indicates the presence of defects in the sample.

introduction of the pulse-echo flaw-detector, (Firestone; 1940, Desch et al; 1946). Signals from such a system are easier to interpret leading to its incorporation in sophisticated automated scanning systems. It is by far the most popular ultrasonic technique used for non-destructive evaluation. A single transducer may be used, fig 4.13a, or a pair of angled probes, fig 4.13b. An ultrasonic pulse is sent into the test piece and echoes will return from defects or boundaries of the object. The depths of these features can be calculated from the time of flight of the pulse, knowing the velocity of sound in the medium. The amplitude of the signal however will depend on the orientation of any defect, the reflectivity of the interface, attenuation along the path of the beam, coupling between the probe and sample as well as the characteristics of the transducer. Much of the information obtained is dependent upon the skill and experience of the operator.

There is currently a trend towards automated scanning in an attempt to remove the human factor from testing. When using piezoelectric probes, water jets are required to obtain reliable and uniform acoustic coupling. Systems currently under development can run at high speeds, although there are still problems using the pulse-echo technique on thin samples.

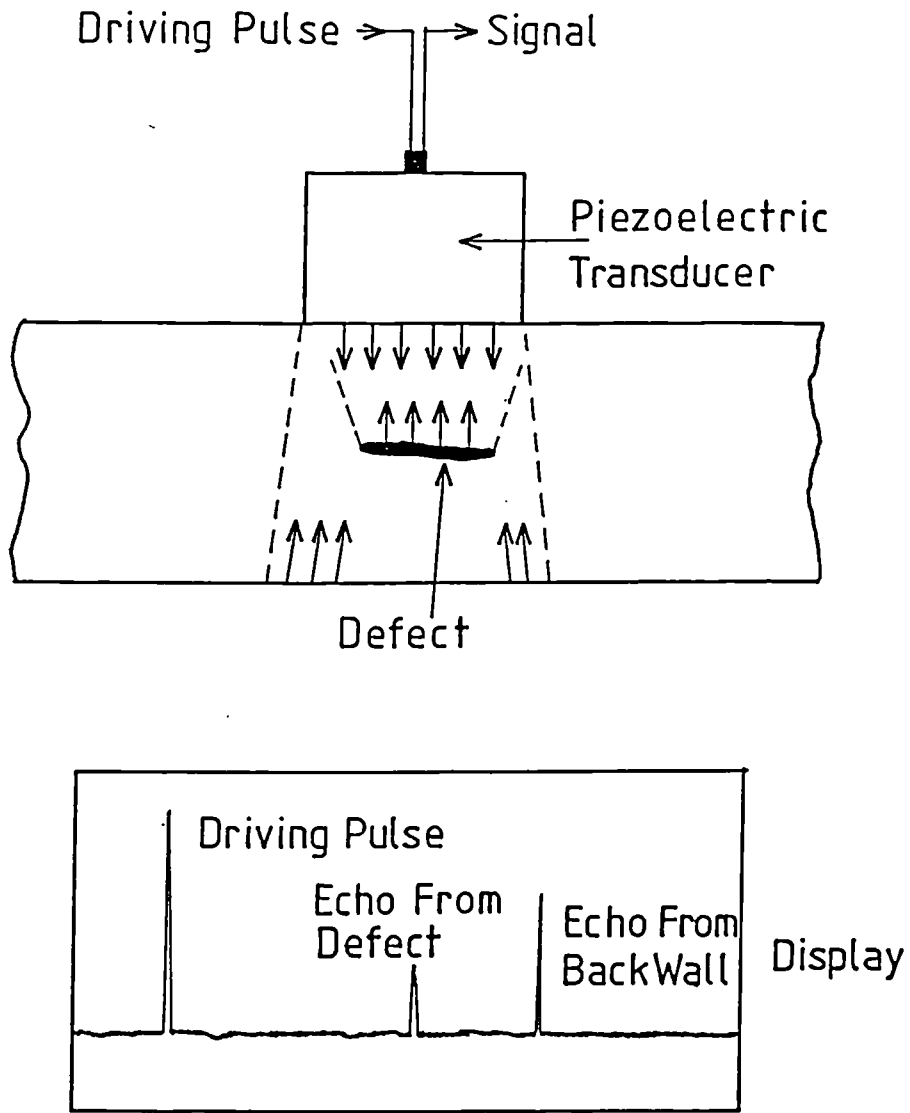


Fig 4.13(a) Simple pulse-echo apparatus using a single probe to both generate and detect.

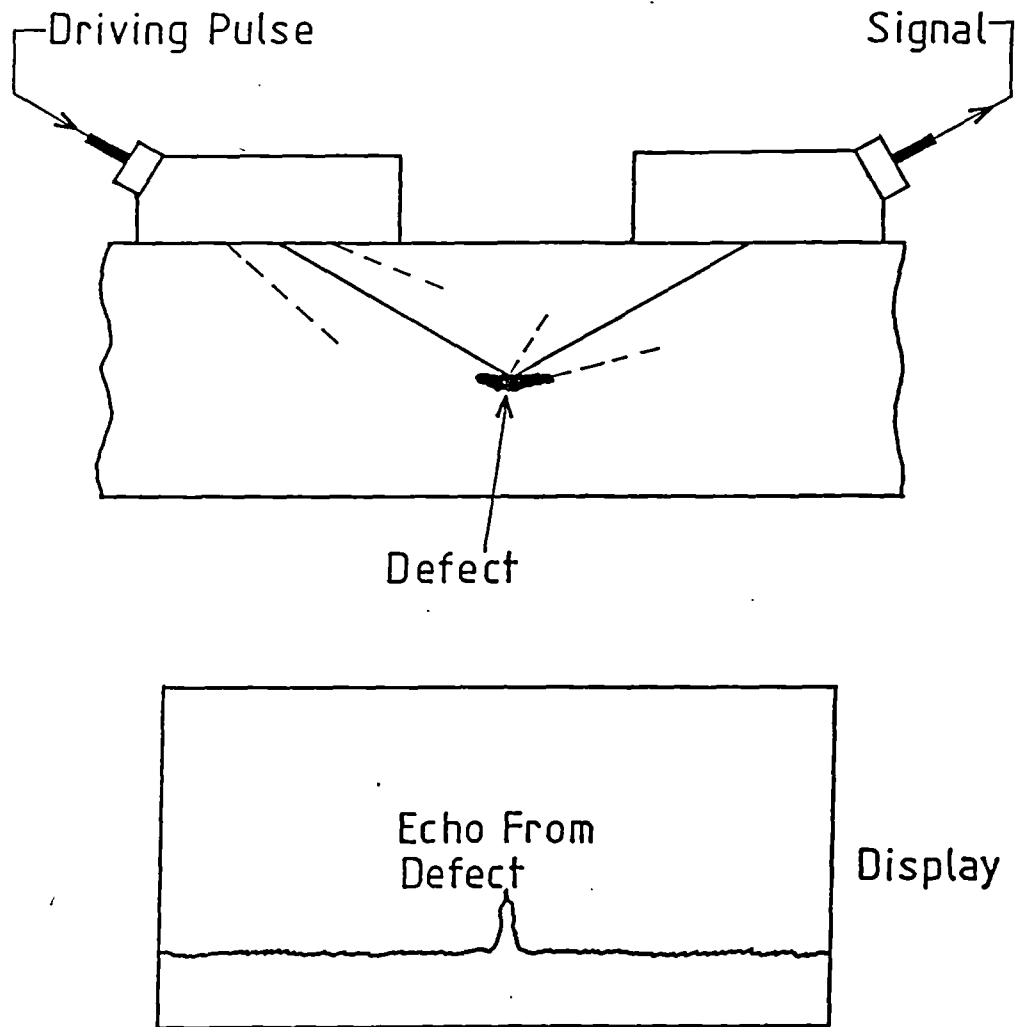


Fig 4.13(b) Pulse-echo flaw detection with a pair of angled probes. In the absence of defects no signal will reach the detector.

#### 4.5b/ Methods of Display.

The simplest mode of display is given by the one-dimensional A-scan presentation, fig 4.14. This may be displayed on an oscilloscope where the x-axis represents time of flight of the pulse, (related to distance via acoustic velocity), and the y-axis representing the amplitude of the echoes, for the probe in one stationary position. The probe may be shifted along a test line in a given direction to obtain a B-scan presentation. Fig 4.15 shows such a system where the x-axis represents the position of the flaw in one direction and the y-axis is related to the depth of the flaw or the transit time to and from a reflector. This requires a threshold level to determine when a signal is a significant echo. Plates may be tested over their area to produce C-scans, fig 4.16, again a threshold level is required. This results in a plan view of the test piece from which may be estimated the size and location of defects but not their depth. Techniques used to build up these displays given by the scans are reviewed by Krautkramer and Krautkramer, (1983).

#### 4.6/ Comments.

The types of transducers used for detection of ultrasonic pulses in this thesis have been detailed in this chapter along with a short review concerning transducer design. The history and current procedures used in ultrasonic NDE have also been briefly discussed. This forms a useful comparison to work detailed in subsequent chapters

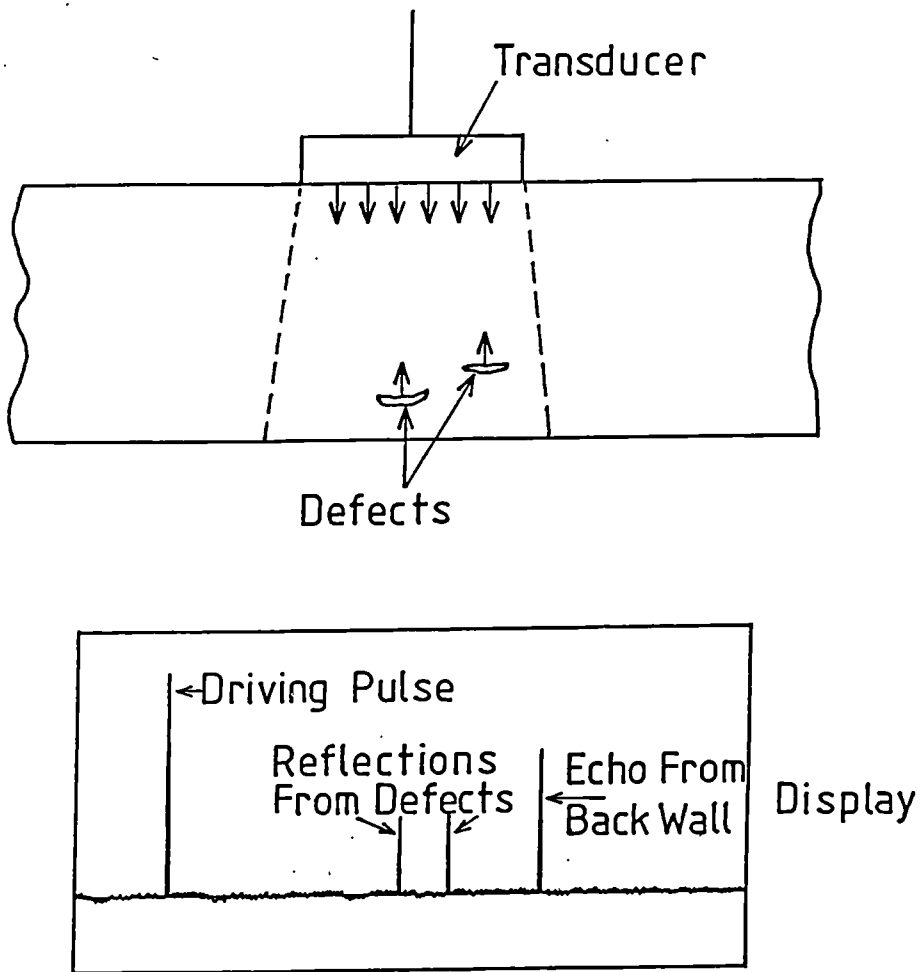


Fig 4.14 A one dimensional description is given for a particular test point in an A-scan arrangement. The depth of any defect is proportional to the arrival time of its echo.

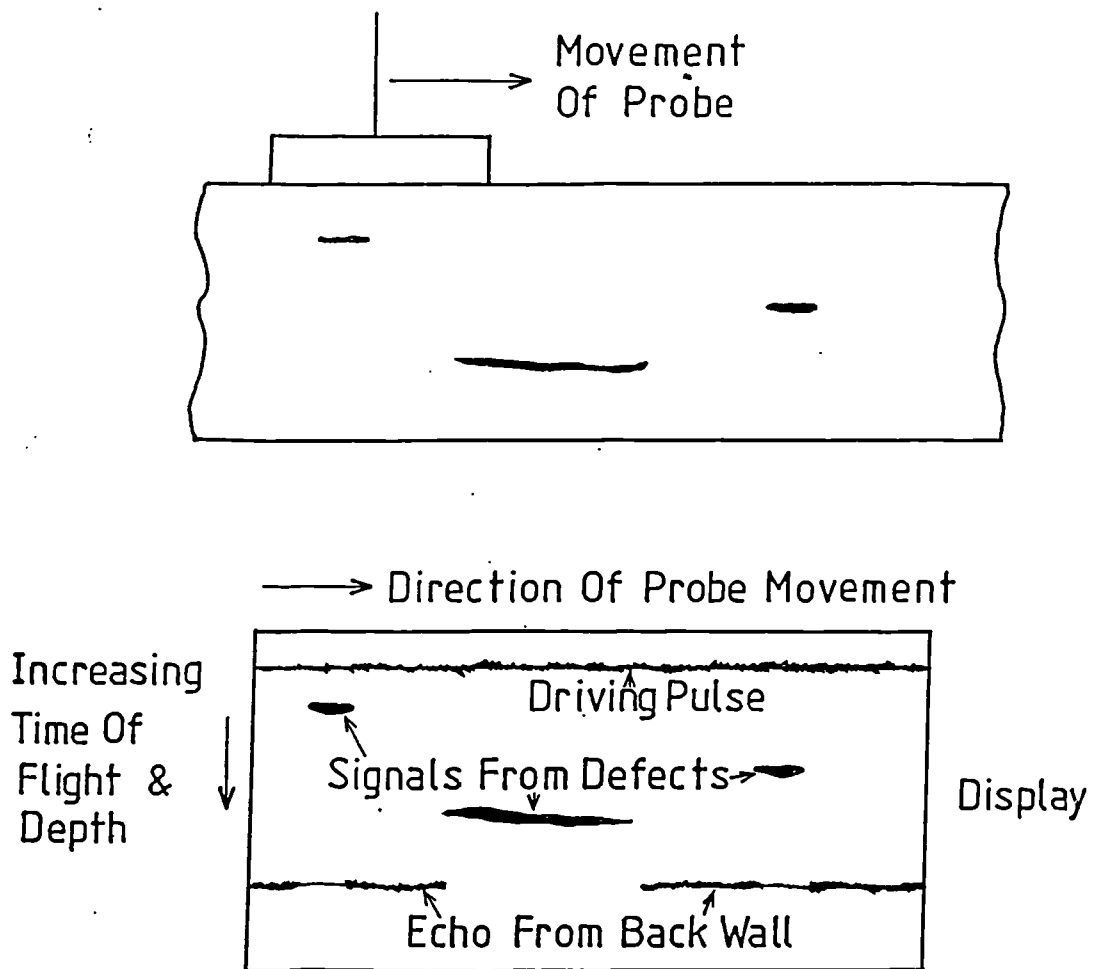


Fig 4.15 Schematic diagram of the B-scan technique. A threshold level is set, above which a signal is shown on the display with depth representing time of flight. The probe is moved linearly along the sample surface and a representation of a cross sectional area of the test piece is built up.

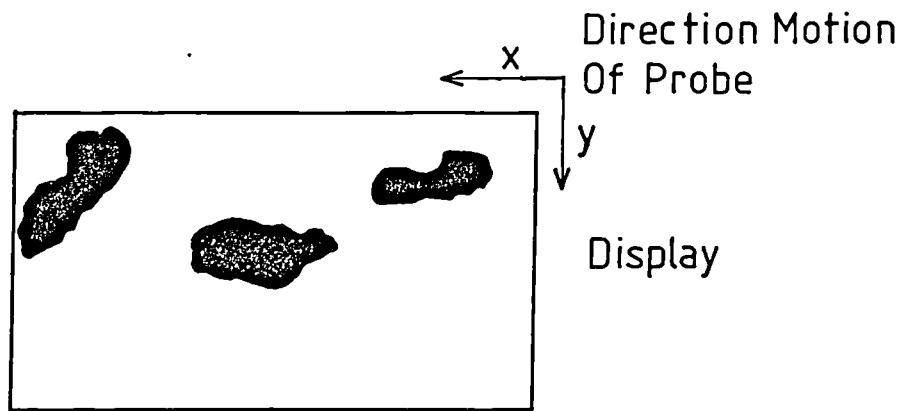
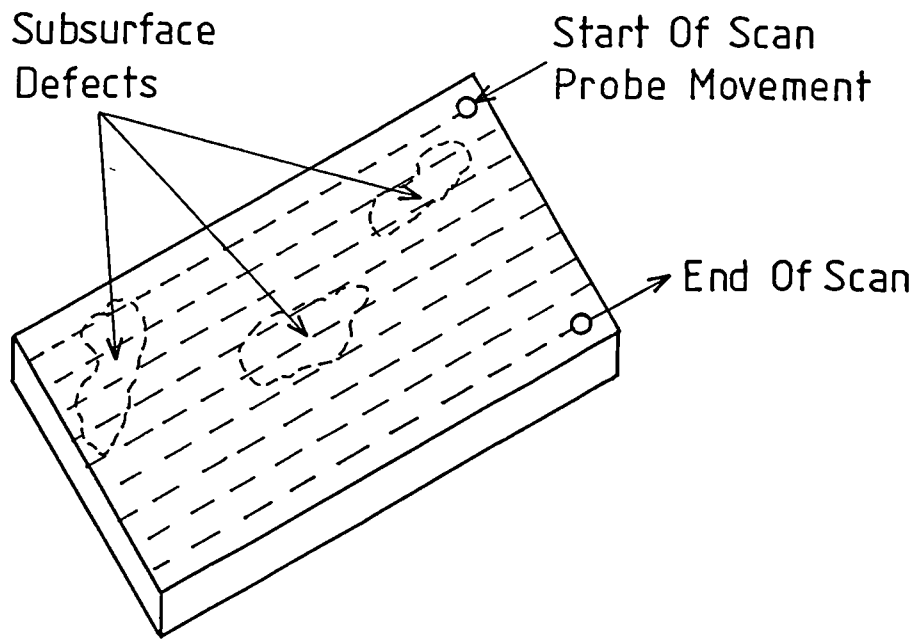


Fig 4.16 Schematic diagram of a single probe, pulse-echo, C-scan system. If a pulse is detected of amplitude greater than a set threshold level and at a time before a back wall echo is expected, then a signal is shown on the display. A two dimensional indication of flaws is built up but with no indication of their depth. For transmission C-scan testing a reduction of signal indicates the presence of flaws.

concerning quantitative NDE using laser produced ultrasonic pulses. In these later chapters the relevant features of laser generated ultrasound are outlined and scanning systems are developed using features of those described above.

CHAPTER 5.

APPLICATIONS OF LASER GENERATED ULTRASOUND TO  
NON-DESTRUCTIVE EVALUATION OF PLASMA TRANSFERRED  
ARC CLAD SAMPLES.

5.1/ Rayleigh Pulse Interactions with Defects.

A substantial amount of the total acoustic energy generated by the laser is contained in surface acoustic pulses, mainly in the Rayleigh pulse. Rose, (1984), suggested that on a material with a Poisson's ratio of 1/3 a harmonic surface centre of expansion, (used to model the thermoelastic source), produces acoustic disturbances with the partition of energies of shear motion,  $P_T$ , longitudinal motion,  $P_L$ , and Rayleigh motion,  $P_R$ , given by

$$\frac{P_L}{P_T} \approx 0.093; \quad \frac{P_R}{P_T} \approx 3.58$$

$$\Rightarrow \frac{P_R}{P_L + P_T} \approx 3.28$$

i.e. the Rayleigh pulse contains over three times the energy of the other two modes combined. It is therefore expected that laser based non-destructive testing systems will make particular use of surface acoustic disturbances.

Some applications to NDE have already been demonstrated. An NDE technique with analogies in sonar and radar has been described using directional laser generated surface acoustic pulses, (Aindow et al; 1983). A cylindrical lens was used to focus a pulsed laser beam into a line on the surface, producing an acoustic source propagating away from and normal to the line. The laser line was incident on the centre of the top face of an aluminium cylinder, almost coincident with a PZT detector. Displacements were detected from echo returns of surface waves from the circumference of the cylinder, and from an artificial surface defect cut into the sample. The cylindrical lens was rotated through small angles between successive laser shots to vary the direction of the acoustic propagation. A two-dimensional echo-scan was gradually built up from these signals which showed the position and extent of the surface breaking crack.

It has recently been shown that some elastic mode conversion of Rayleigh pulse energy takes place in the region of surface breaking slots in metal, (Cooper; 1985, Hutchins et al; 1986). The interaction is complex, producing surface waveforms which not only show the presence of the slot but also contain information of its depth. At the slot, fractions of the Rayleigh pulse are converted into shear and longitudinal modes which may be either reflected back along the surface, scattered into the bulk, or transmitted beyond the slot. In contrast to those of frequency analysis techniques used in acoustic

spectroscopy, (Burger and Testa; 1981), the collected waveforms may be conveniently analysed in the time domain to reveal information on the slot location and depth.

Several techniques have been reported which determine the depth of surface breaking cracks using conventional transducers. Fatigue crack depths down to 2mm were measured by monitoring the time taken for a surface wave to propagate around the crack, (Cook; 1972). This method is only valid in the region where the acoustic wavelength is smaller than the crack depth so that the Rayleigh wave may travel down the face of the defect and up the other side. Morgan, (1974), attempted to relate time dependent features occurring in the reflected pulse to the corner discontinuities at the top and the bottom of a slot. However this system, using interdigital transducers, (with stated bandwidths in excess of 1 to 10MHz), for generation and detection, could only resolve the reflection from the top of a 1.4mm deep slot in aluminium. A spectroscopic method was necessary to obtain depth information. Lidington et al, (1975), measured slot depths in the range 2mm to 30mm using the time delay between Rayleigh surface wave reflections from the opening and the base of the slot. Time of flight techniques based on the combination of incident Rayleigh wave and crack generated bulk waves have also been used to examine crack depth, (e.g. Hudgell; 1974, Lloyd; 1975).

5.2/ Interaction of Laser Generated Rayleigh Pulses  
with Surface Breaking Slots.

It has been shown, (Cooper; 1985, Cooper et al; 1986), that information on the dimensions of a surface breaking slot may be obtained from its interaction with a laser generated Rayleigh pulse. The experimental arrangement used is shown in fig 5.1. Results were obtained for both transmission and reflection of a Rayleigh pulse from the milled slot. It was evident from these experiments that on transmission through a slot, high frequency components were lost causing the pulse to broaden. Fig 5.2a shows the waveform after transmission across a 0.75mm deep slot in aluminium, whereas fig 5.2b shows the incident and reflected pulses from the same slot. The frequency components of the various pulses may be compared by performing numerical Fast Fourier Transforms, (FFTs). The spectra of the incident and transmitted Rayleigh pulses are shown in fig 5.3a. It is seen that for the transmitted spectrum high frequency components are attenuated with the drop off becoming strong at about 1MHz, corresponding to a Rayleigh wavelength of 3mm. This supports the view that long wavelength components with a penetration significantly greater than the slot depth do not strongly interact with the slot. It is seen that frequency components of the reflected signal below 2MHz are significantly attenuated when compared with those of the incident Rayleigh pulse, fig 5.3b. This frequency corresponds to a Rayleigh wavelength of 1.5mm, (about twice the depth of the slot).

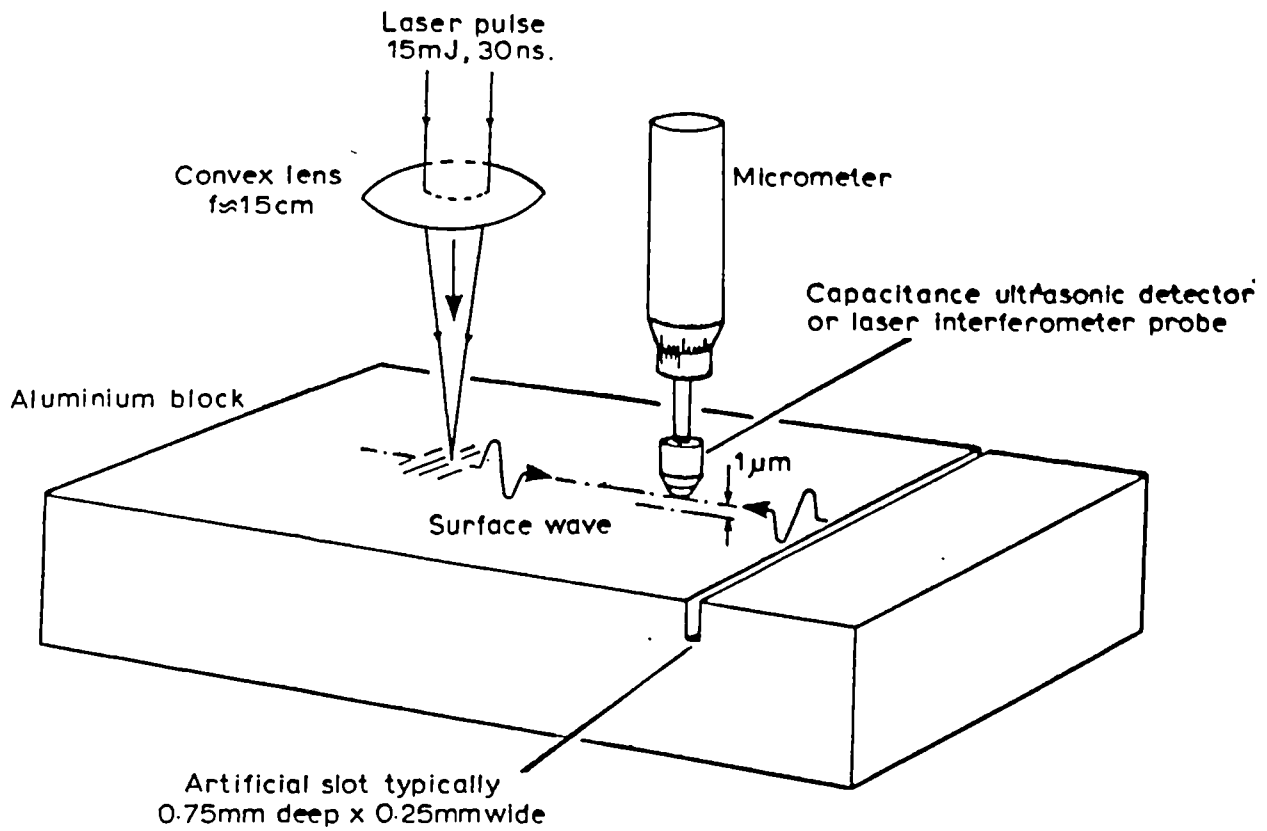
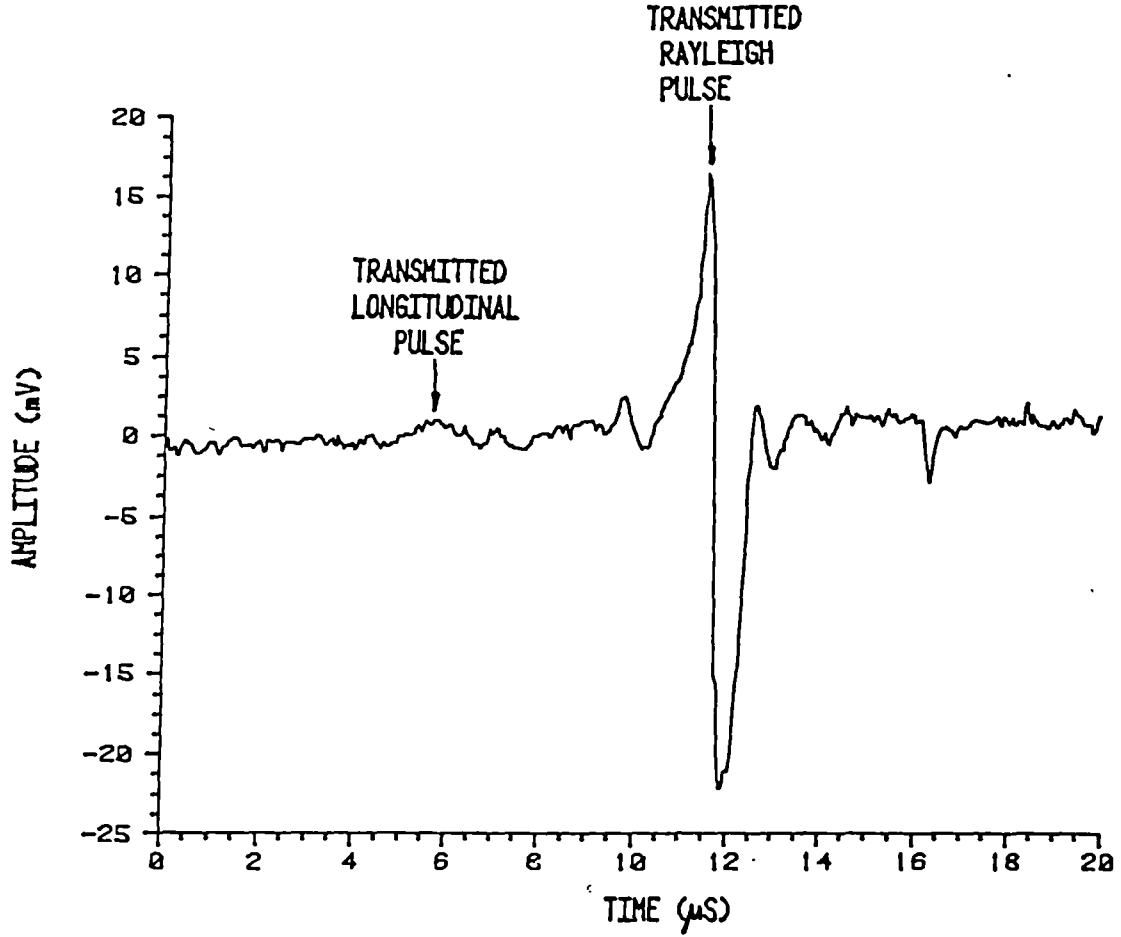
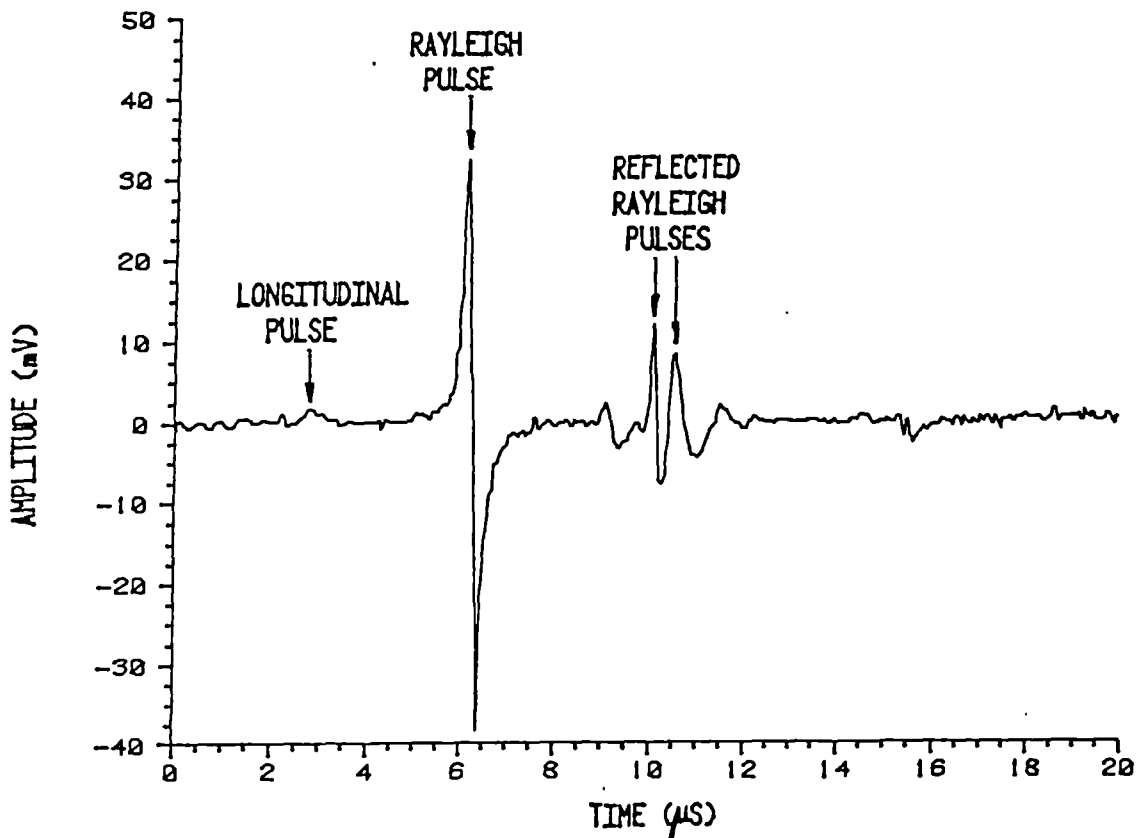


Fig 5.1 schematic diagram of the apparatus used by Cooper et al, (1986), for the detection and sizing of surface breaking milled slots in dural.



(a)

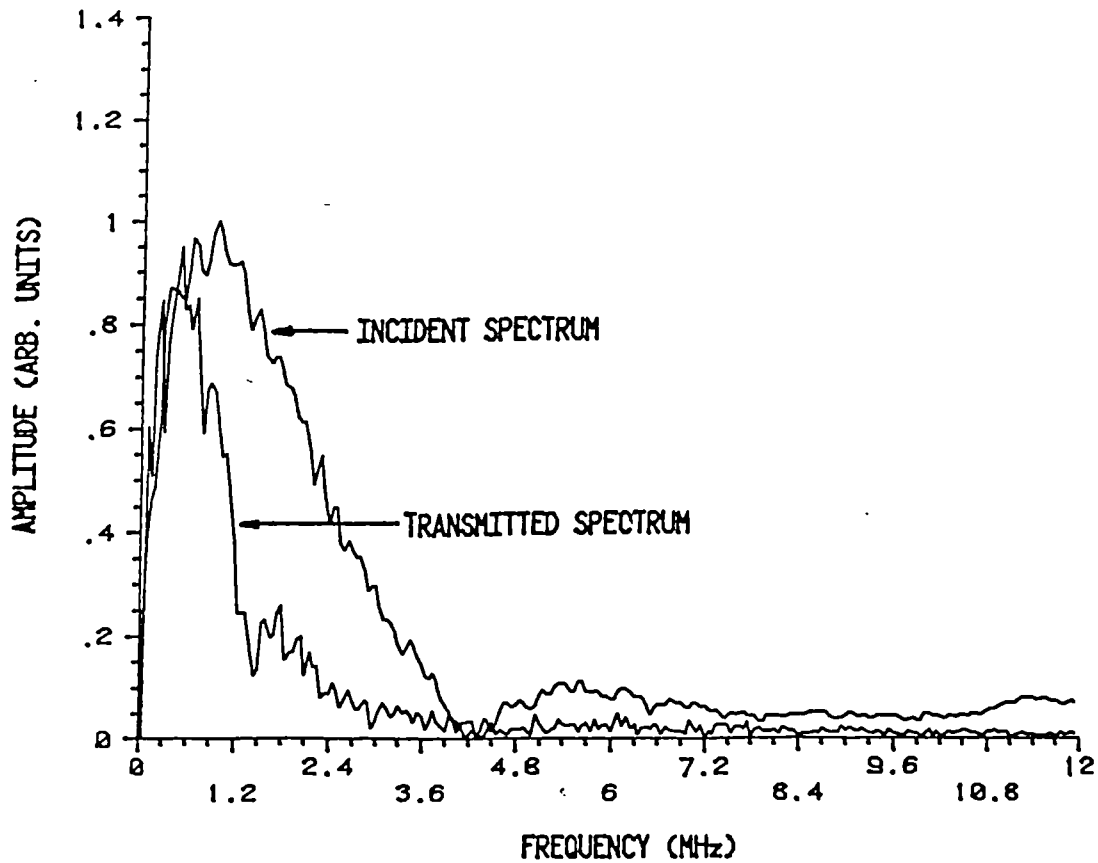


(b)

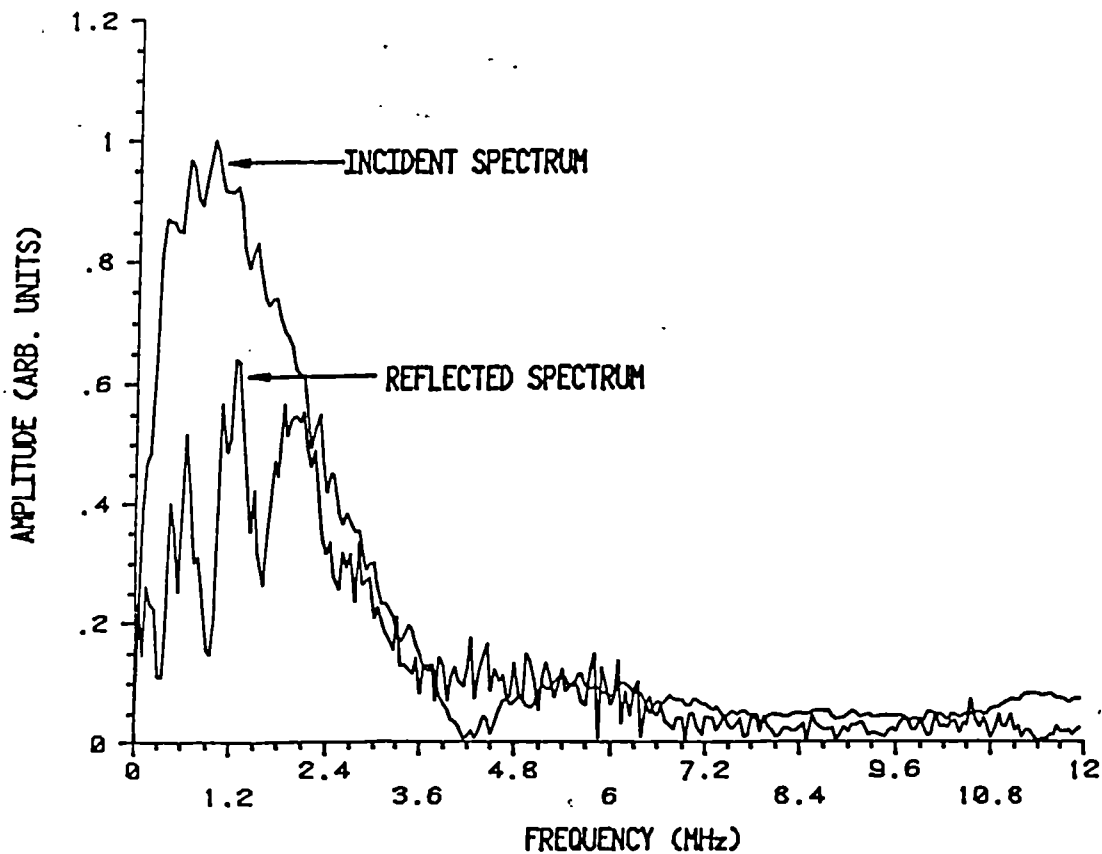
Fig 5.2 Surface waveforms detected by Cooper et al, (1986), from a dural sample containing a 0.75mm deep surface breaking slot.

(a) after transmission across slot.

(b) Incident and reflected pulses from slot.



(a)



(b)

Fig 5.3 Numerical Fast Fourier Transforms of the data of fig 5.2.  
 (a) High frequency components of the transmitted Rayleigh pulse are attenuated with respect to the incident signal.  
 (b) A corresponding loss in low frequency components is evident in the transform of the reflected spectrum.  
 After Cooper et al, (1986).

It would be expected that Rayleigh waves of this wavelength and less would be substantially reflected by the side-wall of the slot. Rayleigh wave or Rayleigh pulse interactions with slots have been analysed previously, (e.g. Viktorov; 1967, Achenbach et al; 1980, Hirao et al; 1982, Yew et al, 1984).

Information on the slot depth can however be obtained in the time domain from fig 5.2b, without recourse to frequency analysis. This information is contained in the reflected signal which consists of a double peak travelling at the Rayleigh velocity. A model has been presented, (Cooper et al; 1986), to describe the interactions leading to the formation of this detected signal. The first peak arises from partial reflection of the incident Rayleigh pulse by the  $90^\circ$  corner. A strong Rayleigh pulse is also transmitted around the corner to interact with the bottom of the slot, which may be thought of as two  $270^\circ$  corners. Computer simulations of acoustic surface waves, (Bond; 1979), suggest that strong mode conversion to bulk shear wave energy occurs at a  $270^\circ$  corner. It was suggested that a back-scattered component of this shear wave lobe arrives at the metal surface and is mode-converted back to a surface wave. This surface wave produces the second peak observed in the reflected signal of fig 5.2b. It is already known that a Rayleigh pulse can appear at the surface from a buried source, (Pekeris et al ; 1957).

A geometric model has been proposed, (Cooper et al; 1986), for what is really a complex interaction. For

aluminium it has been demonstrated that the time delay,  $\Delta t$ , between the two peaks of the reflected Rayleigh pulse, for a given slot depth  $d$ , may be described by

$$\Delta t = \frac{d}{C_R} + \frac{d}{C_s \cos \theta_c} - \frac{d \tan \theta_c}{C_R} \quad (5.1)$$

where  $\theta_c$  is some onset angle for the conversion of shear to Rayleigh pulse energy at a surface and  $C_R$  and  $C_s$  are the Rayleigh and shear wave velocities respectively. Cooper suggested that for aluminium,  $\theta_c = 30^\circ$  and so equation (5.1) may be rewritten as,

$$d \approx \frac{\sqrt{3} \Delta t C_R C_s}{(\sqrt{3}-1)C_s + 2C_R} \quad (5.2)$$

Artificial cracks with depths in the range 0.3 to 5mm were examined and there was overall agreement with this model for slot depths greater than 2mm, fig 5.4. The discrepancy for shallow slots was thought to be associated with the round-trip transit time of a Rayleigh pulse travelling along the bottom of the slot. A modification to equation (5.2) adequately describes the experimental data.

$$d \approx \frac{\sqrt{3} \Delta t C_R C_s}{(\sqrt{3}-1)C_s + 2C_R} - 2w \quad (5.3)$$

where  $w$  is the width of the slot, fig 5.4. A well defined second peak is dependent on the slot width at the tip being small, i.e.  $w \rightarrow 0$ . That is, the discontinuity should be close to  $360^\circ$  which is the situation in the case of real

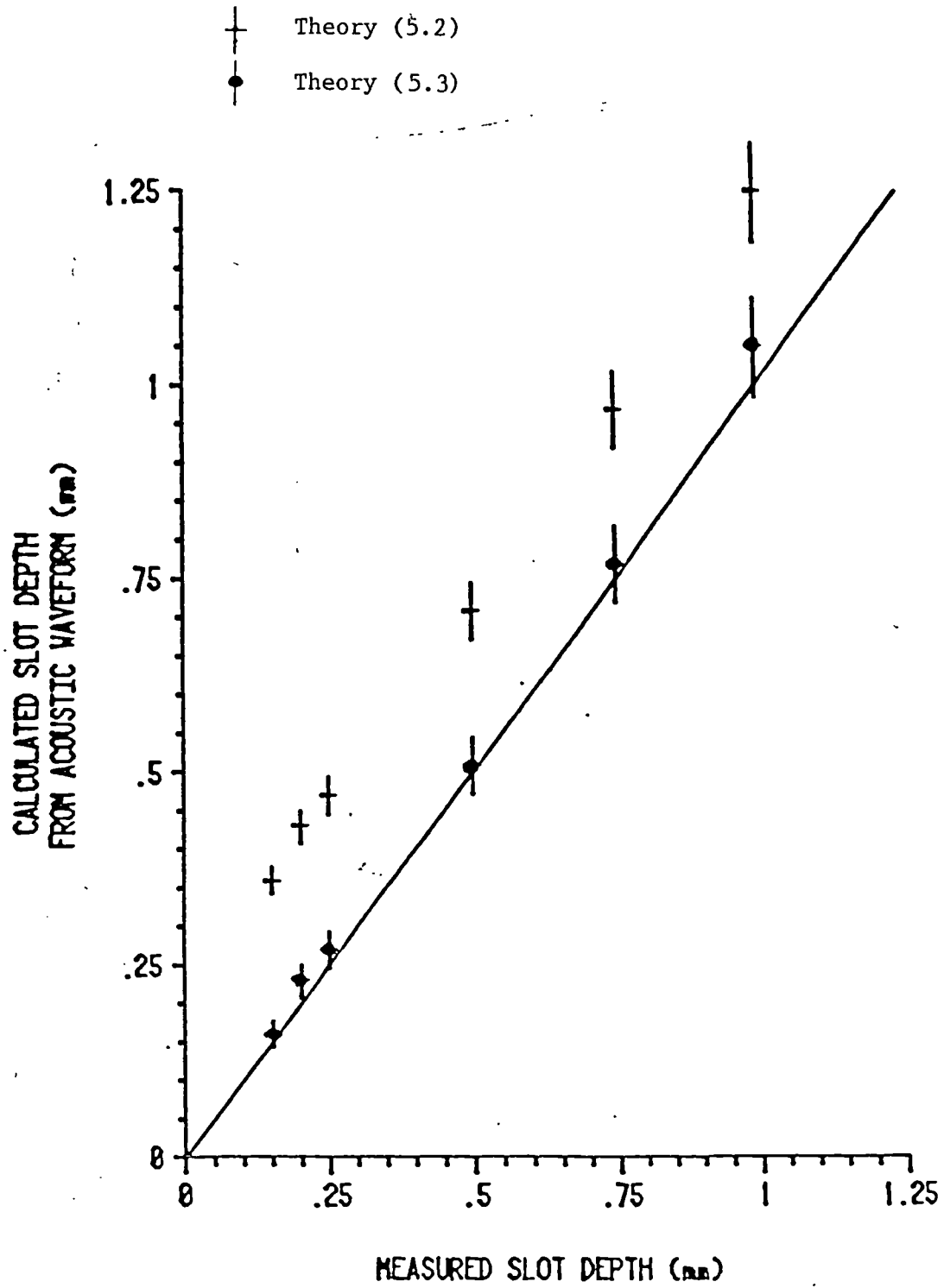


Fig 5.4 Comparison of experimental ultrasonically measured and mechanically measured slot depths.  
 After Cooper et al, (1986).

surface breaking cracks. Interactions of a Rayleigh pulse with real cracks will be examined later on in this chapter.

### 5.3/ Plasma Transferred Arc Clad Samples.

Certain materials, such as those used for the inside of pulverised fuel mills and valve seatings need to be extremely wear resistant. Very hard materials with suitable wear properties may be deposited onto metallic substrates for such applications and it is necessary to ensure that the overlaid material is uncracked and well bonded to the substrate. This is particularly true in the case of a fuel mill where the coating is continually bombarded with fragments of coal since if the coating is flawed large areas of it may become dissociated from its substrate. A surface cladding process is currently being developed at CEGB Marchwood Engineering Laboratories for the cladding of sacrificial protection plates for use in pulverised fuel mills and of valve seats used in PWR valves. This plasma transferred arc cladding process is a high quality weld overlay technique. A schematic diagram of the process is shown in fig 5.5. The tungsten electrode is held typically 1cm above the earthed test piece at a potential of -70V. The metallic gun shield surrounding the electrode is held at an intermediate potential to prevent arcing to it. A pilot arc is struck from the tungsten electrode to the sample, then the weld material is fed into this region, (in this case in powder form). A gas shield of

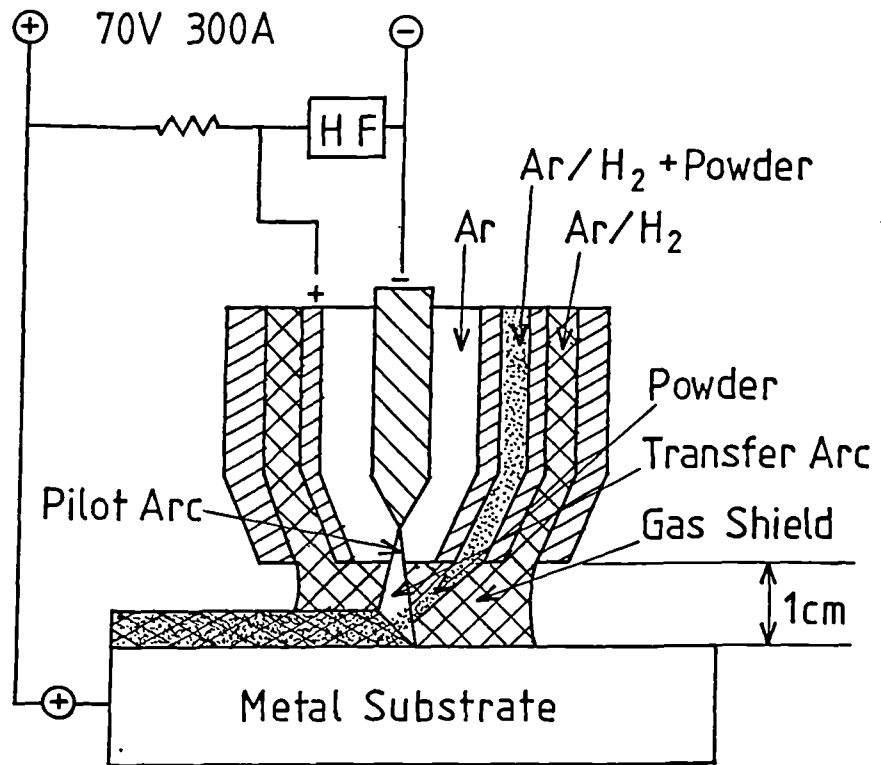


Fig 5.5 Schematic diagram of the plasma transferred arc cladding process.

argon and hydrogen prevents oxidisation of the weld material. The current is set high enough to melt the feed material and to fuse it to the substrate, this setting being critical. If too low a current is used, the weld won't fully fuse to the substrate resulting in adhesion defects, (laminar and porosity). Setting too high a current value results in high dilution of the coating material in the substrate. Here the fused region is large, affecting the hardness and wear properties, though being less likely to contain defects. An intermediate current setting is therefore required between these two regions. Weld dilution of about 5% is found to give optimum properties for any particular alloy. This dilution factor is affected not only by the current setting but also by the weld material, the thermal mass of substrate and the separation between substrate and electrode. Therefore the properties of the cladding may be affected by the geometry of the sample and may also vary from point to point on the sample, the beginning of the deposition being especially affected until the thermal inertia of the substrate has been overcome.

Since the dilution of the weld material is difficult to control, it is desirable to perform some form of NDE on the samples to monitor bond integrity. If this test was remote, then a weld area could be examined immediately after cladding and the information obtained could be used to control the current setting for subsequent areas. A system which uses laser generated ultrasonic

pulses and distinguishes between weld quality of samples manufactured with various current settings will be described later in this chapter.

A further problem with the overlay technique comes from fracture of the weld bead due to the stresses set up during cooling. This has been found to be of particular problem with the nickel based alloy, Colmanoy 5, which is mainly being investigated as a possible alternative to the cobalt based stellites presently used in PWR valves.

It was decided to clad a sample of steel with Colmanoy 5 and to examine it for defects. The sample was prepared using the facilities at CEGB Marchwood. A 52x52x203mm bar of high strength, low alloy steel was coated with a 36mm wide bead of Colmanoy 5 along one surface. The current was set at 160A, high enough to ensure few bond defects but possibly causing more than 5% dilution. The current was then lowered to 150A, (since the weld bead was red hot), and the first bead was overlaid with a second layer for half of its length, about 110mm. The sample was then quenched so as to cause fracture on the surface. A liquid penetrant was used to visually enhance the location of the defects generated, (McGonnagle; 1971). The cleaned sample was sprayed with a fluorescent dye penetrant which was washed off its surface after a few minutes. By this time some of the dye had been drawn into the cracks by capillary action. The fractures were seen by dusting the surface with developer, which drew the penetrant from the defect by a blotting action, and

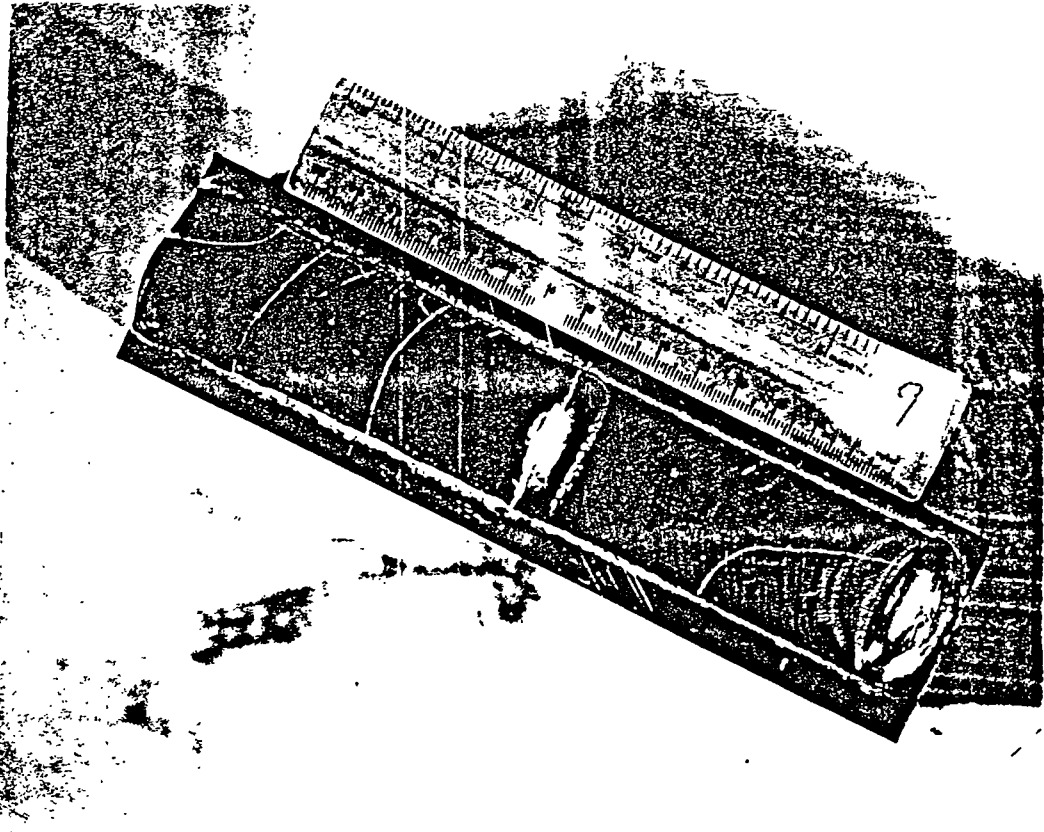


Fig 5.6 Photograph of cracked Colmanoy 5 sample.

examining the sample under ultra-violet light. The fluorescence from the dye in the cracks show as the white lines on the photograph, fig 5.6. The single weld bead is up to 4mm thick at its centre with the double layer being up to 7mm deep. These surface breaking cracks were then examined using the laser-generated Rayleigh pulse technique described in section 5.2.

#### 5.4/ Detection and Sizing of Real Cracks on a Weld Bead.

An experimental arrangement similar to that of Cooper et al, (1986; fig 5.1), was used, fig 5.7. Measurements involved monitoring both transmission and reflection of the incident Rayleigh pulse. The wideband ball capacitance probe, discussed in the previous chapter was used as the detector. The incident laser energy was focused to a ~0.5mm diameter spot on the sample surface to enhance the generation of high frequency components. A layer of silicon resin was spread on the generation point to both enhance the acoustic signal and prevent any u-v created by plasma formation reaching the detector. This layer also helped to minimise any pitting of the surface caused by the high power densities used, ( $10^8$  to  $10^9 \text{ Wcm}^{-2}$ ). Fig 5.8a shows the waveform obtained after transmission across the crack whereas fig 5.8b shows the incident Rayleigh pulse and the subsequent reflections from the defect. The incident Rayleigh, transmitted Rayleigh and reflections from the crack were frequency analysed using the FFT procedure, fig 5.9. As was the case for

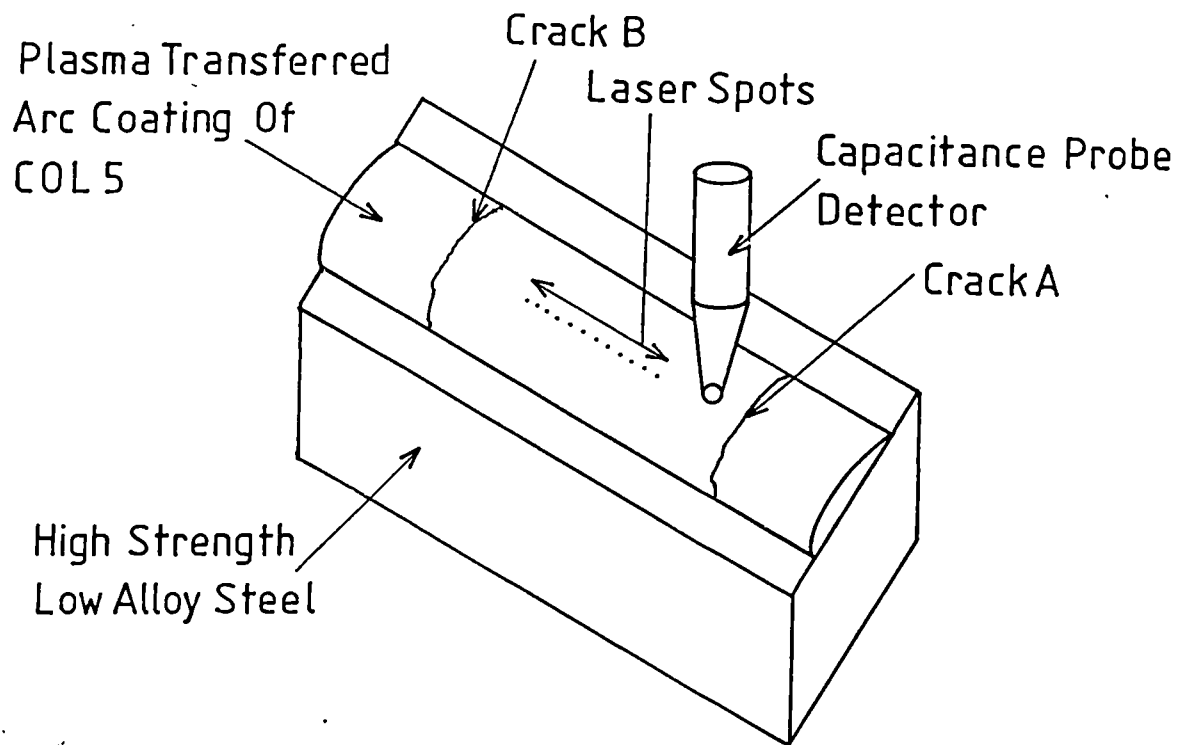
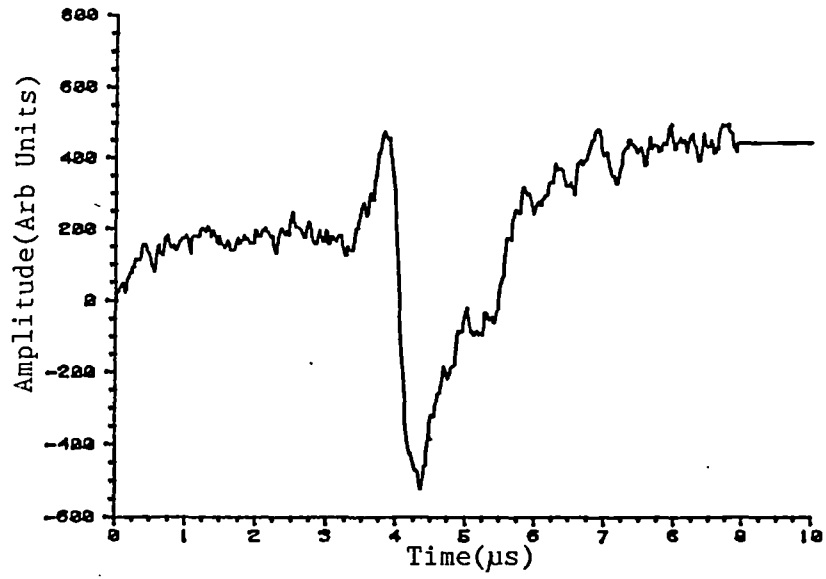
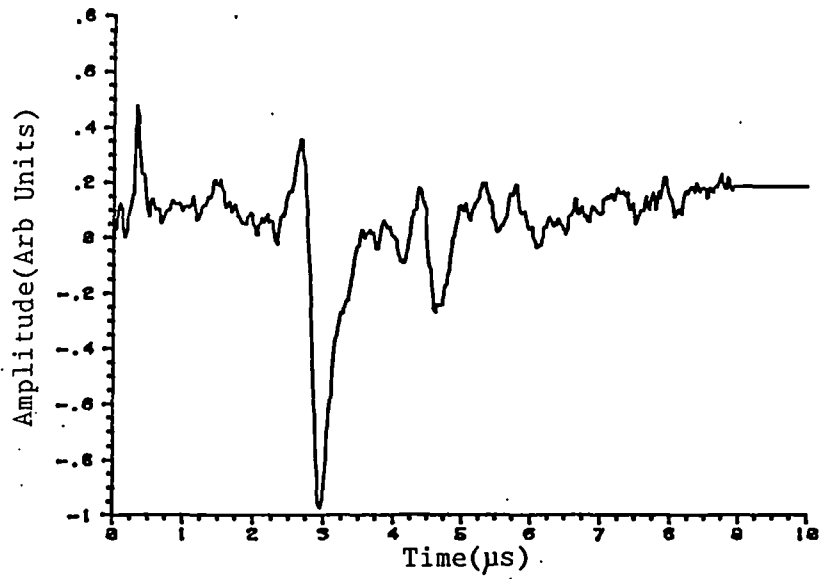


Fig 5.7 Schematic diagram of apparatus used to size cracks on the sample of fig 5.6. The sample and detector were both placed on an x-y table which was moved 1mm between laser shots to produce the waveforms of figures 5.10 and 5.13.



(a)

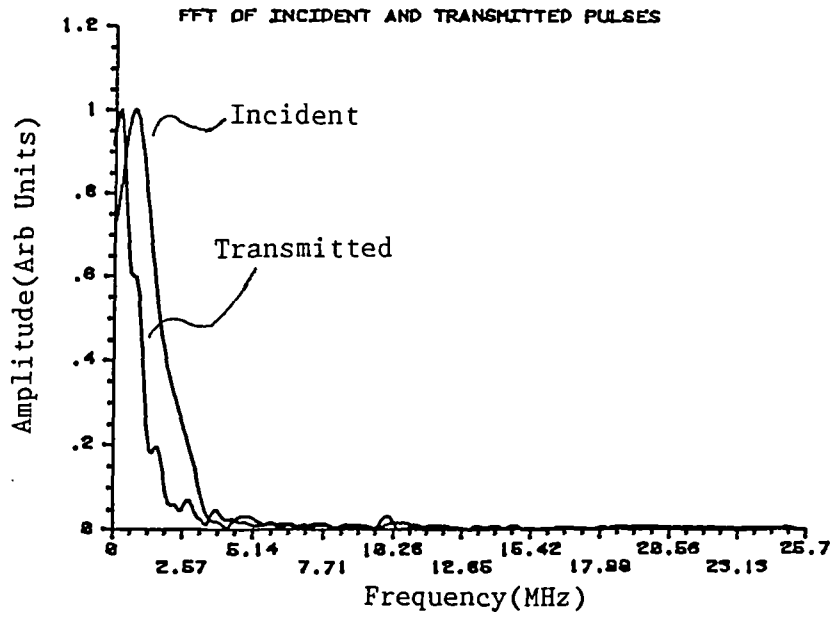


(b)

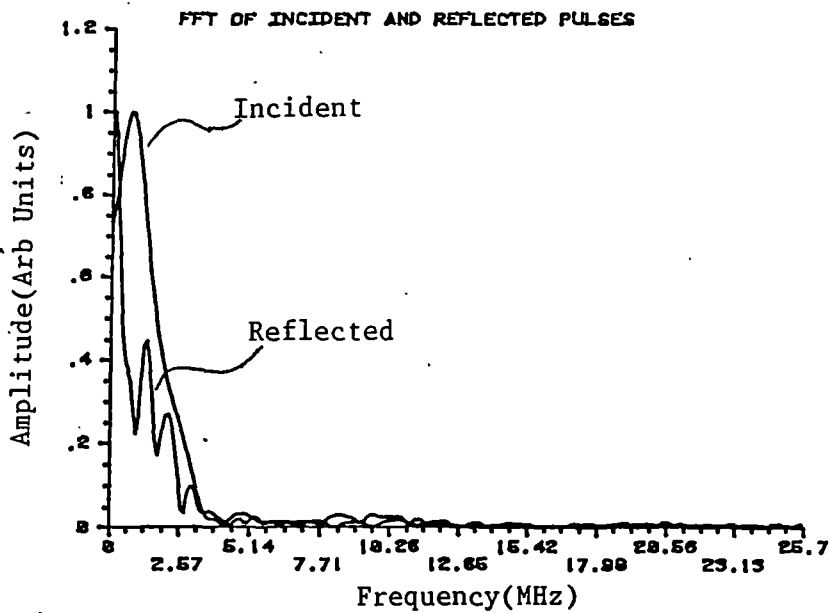
Fig 5.8 Surface waveforms detected from sample of fig 5.6.

(a) after transmission across crack.

(b) Incident and reflected pulses from crack.



(a)



(b)

Fig 5.9 Numerical Fast Fourier Transforms of the data of fig 5.8.  
 (a) High frequency components of the transmitted Rayleigh pulse are attenuated with respect to the incident signal.  
 (b) A loss in low frequency components is evident in the transform of the reflected spectrum although the difference is not as noticeable as for the transforms of similar signals on a milled sample, fig 5.3(b).

milled slots there is a loss of high frequency components in the through transmitted pulse relative to the incident Rayleigh pulse spectrum. Some loss of low frequency components is evident in the FFT of the reflected signal.

Due to the size and geometry of the weld bead, not only were reflections from the crack observed, but reflections from the side walls were also detected. This made it difficult to consistently pick out the reflections from the crack and hence to size the defect in the time domain. As a consequence the signals from the crack in fig 5.8b are not of the simple double pulse nature observed for a milled slot. The crack may also be non-uniform and so cause more scatter than a milled slot, although it will be shown that this is not a dominating effect in this sample. In order to minimise the effect of the side wall echoes a technique similar to synthetic aperture focusing was used. Ten waveforms were collected with the laser spot being moved 1mm closer to the detector and crack between each shot. The resultant waveforms are shown in fig 5.10. The reflections from the crack can be seen arriving after, and with the same velocity as, the incident Rayleigh pulse. These ten waveforms were normalised to the Rayleigh pulse height then added together, each being time shifted relative to its predecessor by  $\delta t$ , the time taken for a Rayleigh pulse to propagate 1mm along the surface of the cladding which was determined from fig 5.10. The Rayleigh pulse and crack reflections were enhanced in the resulting waveform, fig 5.11. Any background noise or acoustic

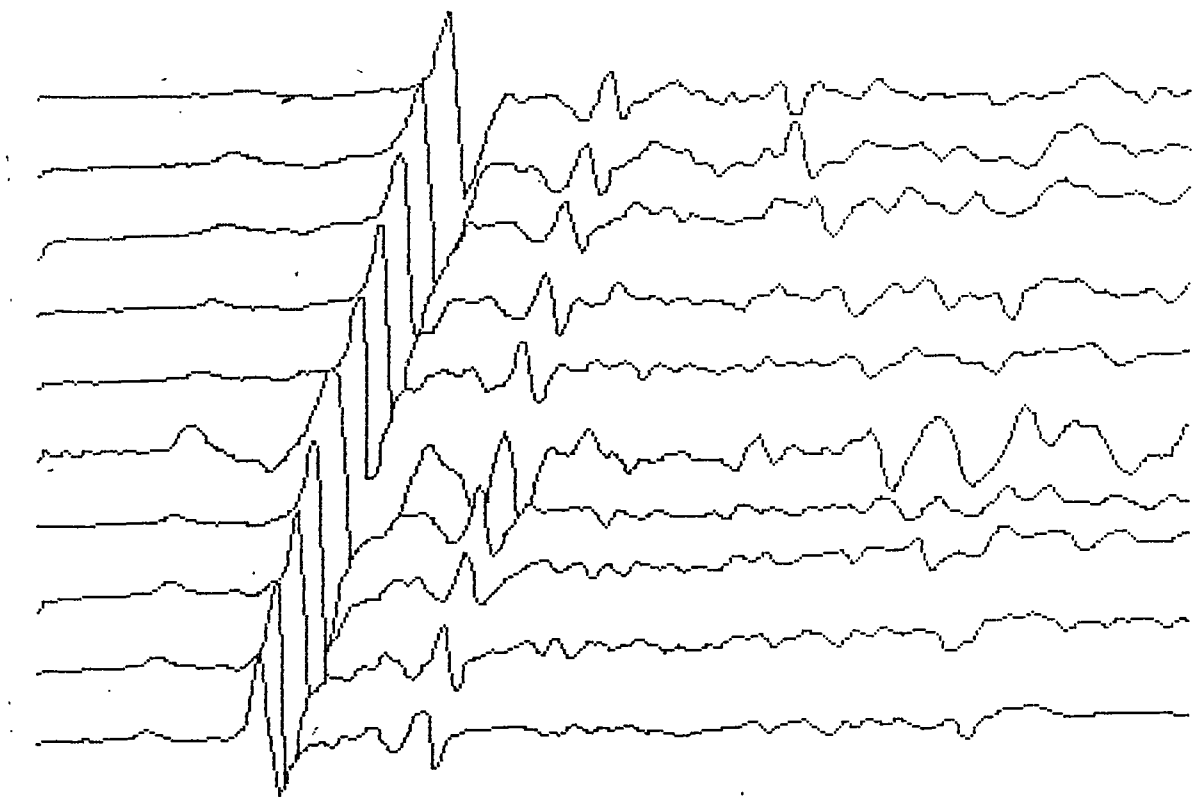


Fig 5.10 Ten surface waveforms from the sample of fig 5.6 with the laser spot moved 1mm closer to the detector and crack A between each waveform. Arbitrary vertical scale, 20 $\mu$ s full horizontal scale.

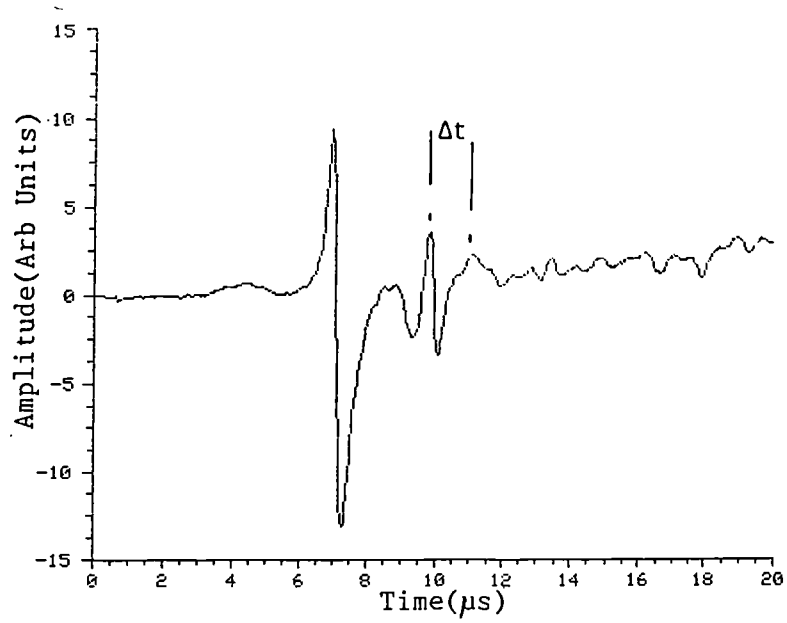


Fig 5.11 Resultant waveform from shifting and adding the traces of fig 5.10 to enhance the incident Rayleigh pulse and signals from crack A.

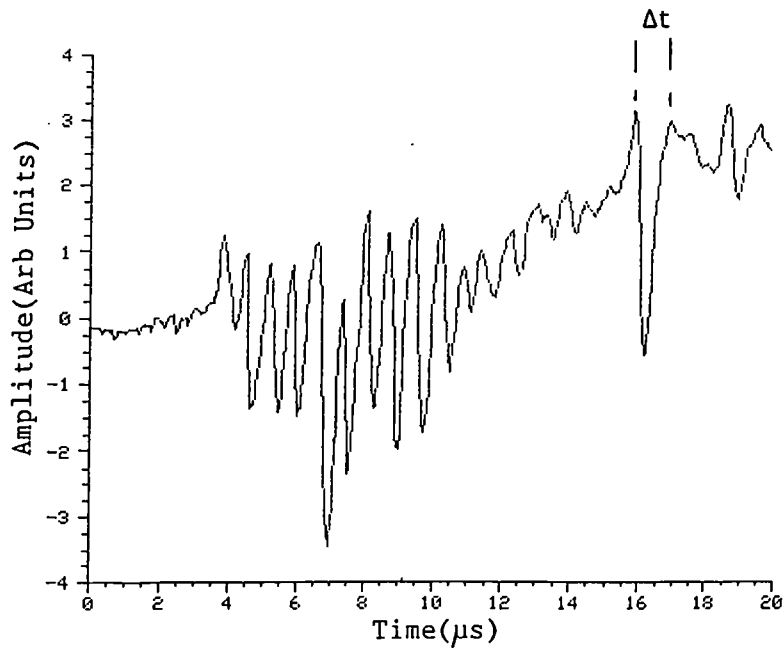


Fig 5.12 Resultant waveform from shifting and adding the traces of fig 5.10 to enhance the signals from crack B.

signals having a velocity other than that of the Rayleigh pulse tended to average out. For example, it can be seen that the longitudinal arrival in fig 5.11 lost its sharpness after the averaging procedure. From fig 5.11, the time difference between the two peaks arising from the interaction of the Rayleigh pulse with the crack was found to be  $(1.3 \pm .1) \mu\text{s}$  and a crack depth of 2.5mm was obtained from equation (5.2). This calculation assumed the width of the crack tip was small and used experimentally determined values of  $C_R = 2940 \text{ms}^{-1}$  and  $C_S = 3090 \text{ms}^{-1}$ . It is likely that the cladding was anisotropic due to the temperature gradient and subsequent stresses present at cooling. Since the model assumed a mode converted shear pulse travelling from the crack tip at an angle of  $30^\circ$  to the surface, some error will be present in this calculation due to both the values used for the shear velocity and "onset" angle.

Another arrival can be seen in the waveforms of fig 5.10 which was due to Rayleigh pulses reflecting from a crack behind the point of generation, (point B in fig 5.7). With the laser spot being moved 1mm further from this crack between successive shots, the time of arrival of this signal changed from shot to shot by the same  $\delta t$ , although being delayed in this case. Hence to enhance this latter arrival, the same shift and add operation was performed on the waveforms of fig 5.10 with the time delay in the opposite sense to before. The resulting waveform, fig 5.12 shows the signal from the second crack arriving after about  $15.5 \mu\text{s}$ , with the time between the two peaks being  $(1.1 \pm .1) \mu\text{s}$ .

inferring a depth of  $\sim 2.1\text{mm}$  for crack B. Unfortunately too few waveforms were collected for the Rayleigh pulses to cancel out when they were added up out of phase, causing the ten peaks from  $3.5\mu\text{s}$  to  $10.3\mu\text{s}$ . However, the signal from the second crack which was barely distinguishable from the noise level in the waveforms of fig 5.10 has been enhanced to be the major feature by this shift and add technique. Due mainly to the increased propagation distance of both the initial Rayleigh pulse and the reflected signals from the crack, the double pulse feature wasn't as sharp as that in fig 5.11.

To check the depth measurement of crack B, the sample was rotated by  $180^\circ$  with respect to the laser and detector, with the ball probe being placed close to crack B. The twelve waveforms of fig 5.13 were collected with the laser spot initially 27mm from the detector being moved 1mm closer for each successive shot. Here the signal following the Rayleigh arrival was due to crack B. Signal enhancement was performed as before to yield fig 5.14. The time difference in the reflected peaks of  $(1.0 \pm 0.1)\mu\text{s}$  agreed with the previous experiment and gave a depth estimation of  $\sim 2.0\text{mm}$ . The reflections from the other crack could not readily be picked out from fig 5.13 but were easily seen when the waveforms were shifted and added in the appropriate direction, fig 5.15. The time delay between the two peaks here was about  $(1.4 \pm 0.1)\mu\text{s}$  which again showed good agreement with the previous measurement,  $(1.3\mu\text{s})$ .

Late on in the investigation it was possible to

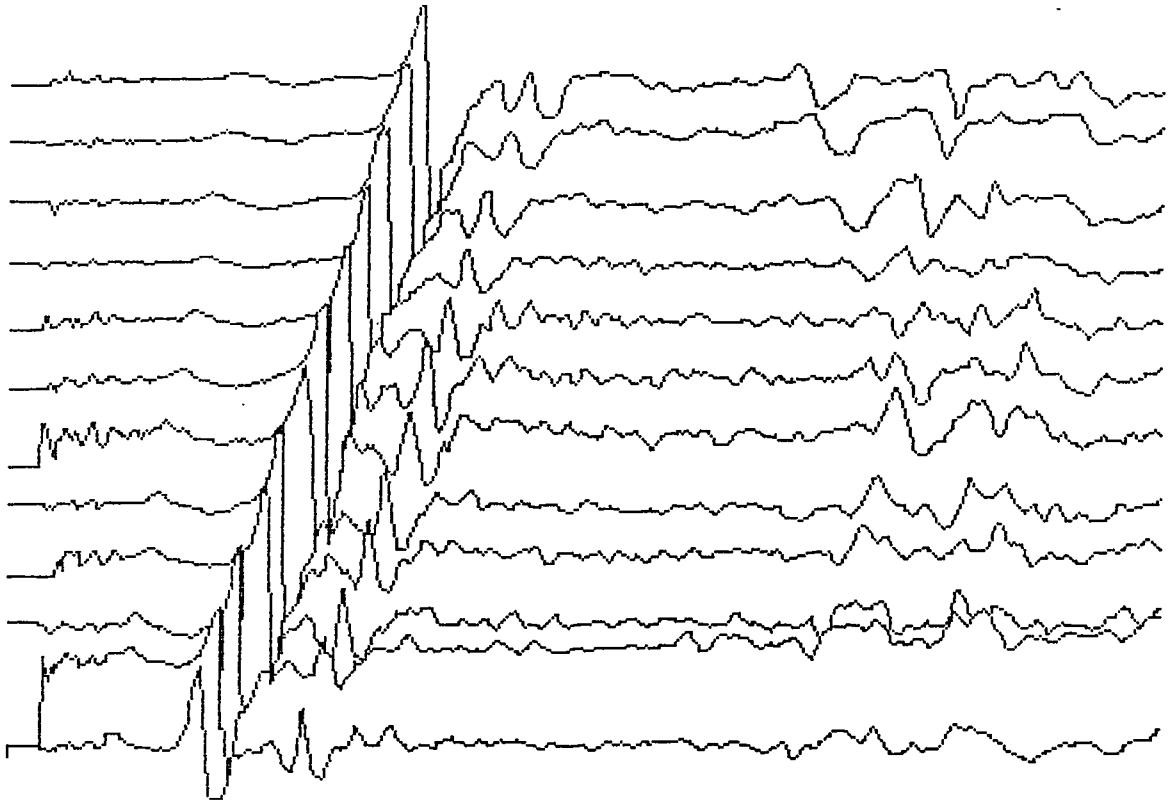


Fig 5.13 Twelve surface waveforms from the sample of fig 5.6 with the laser spot moved 1mm closer to the detector and crack B between each waveform. Arbitrary vertical scale, 20 $\mu$ s full horizontal scale.

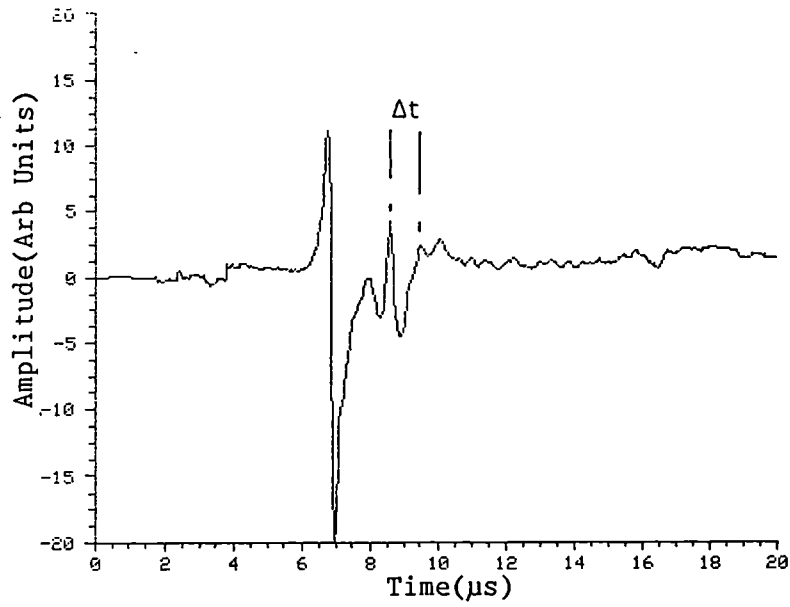


Fig 5.14 Resultant waveform from shifting and adding the traces of fig 5.13 to enhance the incident Rayleigh pulse and signals from crack B.

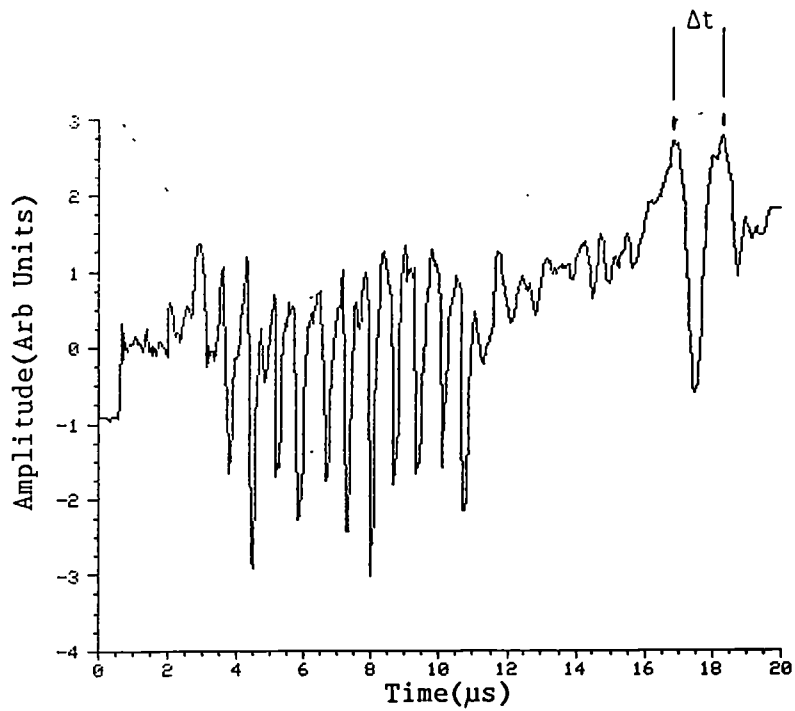


Fig 5.15 Resultant waveform from shifting and adding the traces of fig 5.13 to enhance the signals from crack A.

compare waveforms obtained with the capacitance transducer with those detected by a stabilised Michelson interferometer. Fig 5.16 shows the signal obtained when looking at the reflections from crack B. The sample only required polishing with Brasso to obtain sufficient reflectivity for detection of acoustic pulses using the interferometer. The features are sharper here than with the ball probe due to the increased bandwidth of the optical device. Taking  $\Delta t$  as  $1.0\mu s$ , (inferring a crack depth of 2.0mm), agreed with measurements taken using the capacitance transducer. However, there are other peaks present which may have been due to side wall reflections which, due to the variation in the sample surface affecting the detector, could not be removed by synthetic aperture focusing.

In conclusion, these results show promise for future non-contact non-destructive testing systems. The technique presented relies on the wide bandwidth of both the laser acoustic source and the detector. The use of the Michelson interferometer on a real sample is perhaps the most promising sign for a totally remote testing system. Additionally the use of the shift and add signal processing technique proved useful in locating and sizing flaws, reflections from which were not obvious from individual waveforms. This was necessary due to the geometry of the sample and may not be required for other specimens.

## 5.5/ Variation of Acoustic Scatter with Weld Integrity.

### 5.5a/ Sample Manufacture.

Six high strength steel samples were overlaid with the material Delchrome 90, (Del90), using the process outlined in section 5.3. Various current settings were

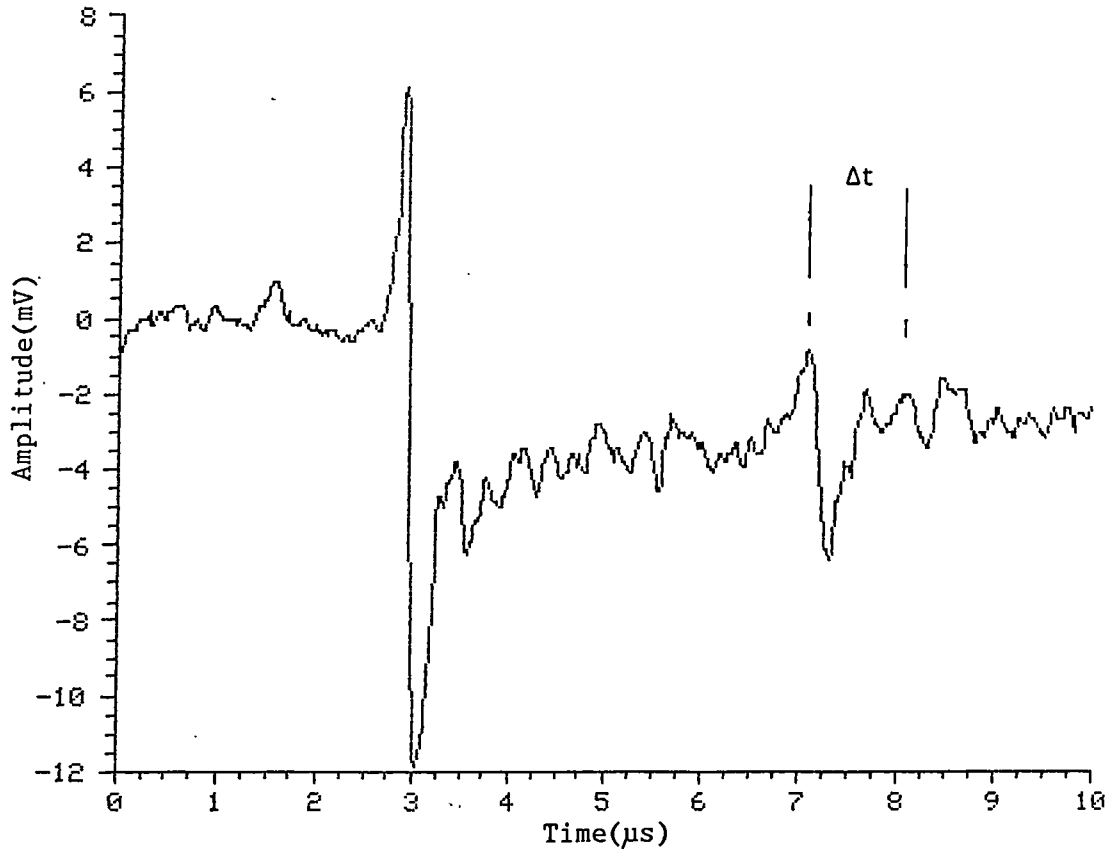


Fig 5.16 Surface waveform detected interferometrically showing the incident Rayleigh pulse and the reflections from crack B.

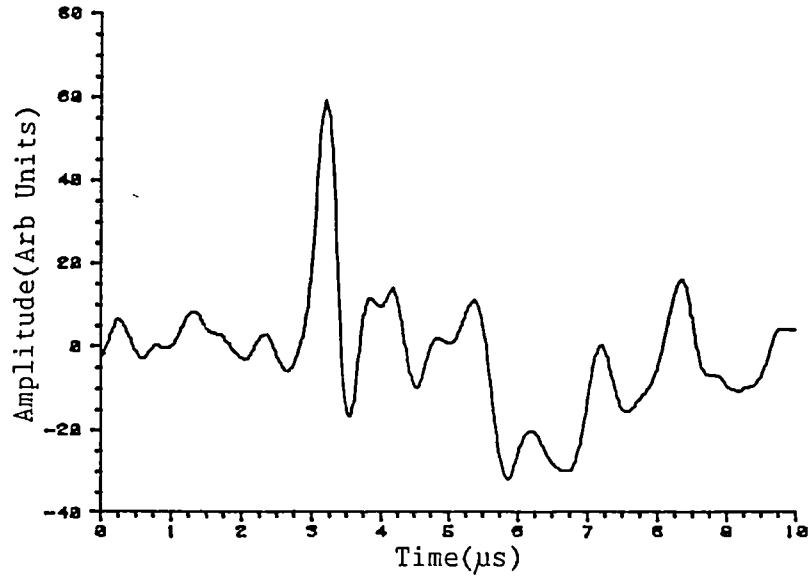
used to achieve a range of bonding conditions. To investigate the relationship between current settings and defect type a range of similar samples was clad with Del90 then sectioned and examined microscopically. Other possible variables were kept constant from weld to weld. The arc length was maintained at ~1cm, the powder feed rate at ~28g/min, the open circuit voltage at ~72V, and the speed of sample movement and gas pressures were also unchanged. It was found that a current setting of 160A gave a well bonded cladding with low dilution, the dilution increasing with current. At 150A and below there was still low dilution, although areas of slightly poor adhesion became more common. Porosity defects were more prevalent for the samples welded at 140A and 130A whereas currents lower than this produced overlays that were not well bonded to the steel. Other samples were clad with two layers, one over the other, of Del90. The top layer required a lower current to ensure good bonding due to the elevated temperature of the sample after the first deposition. Dilution of this second bead is obviously less important. Of the six samples examined ultrasonically, three were single layer and three double layer deposits. Of the latter three samples, two had initial deposits welded with a current setting of 110A, producing porosity and a layer of laminar defects at the interface region. The first of these samples was then clad again with the current reduced to 100A producing a very poor overlay. For the second sample the current was increased to 160A which ensured good

bonding to the bottom deposit, producing a sample with defects buried at about 7mm. The other thick sample had a first deposit at 160A covered with a layer at 150A which was thought to produce a reasonably defect free cladding.

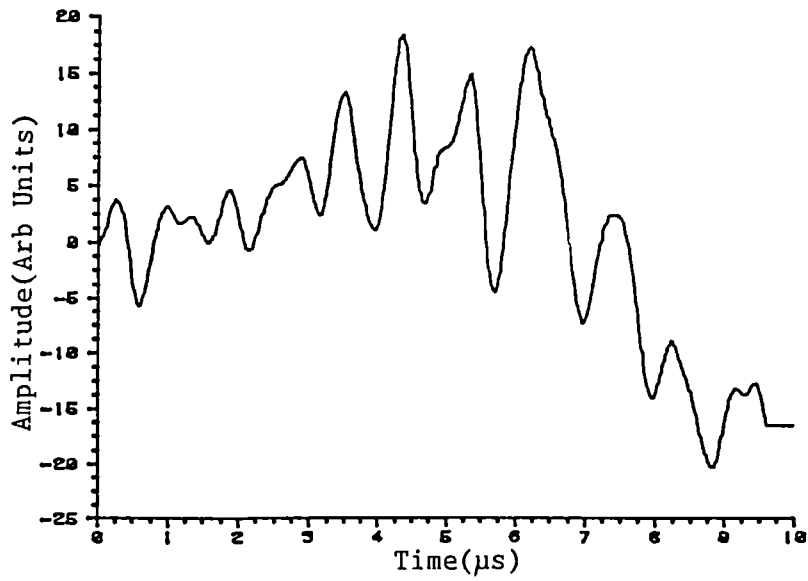
#### 5.5b/ Experimental Technique.

Two distinct sets of experiments were carried out. The first looked at propagation of bulk waves through the cladding and steel substrate, and the second at propagation of a Rayleigh pulse across the weld bead. Both thermoelastic and ablation regimes were used for laser-acoustic generation. The EMAT sensitive to out of plane motion, (Chapter 4), was used and signals detected were fed through a Physical Acoustics Corporation preamplifier. The EMAT was used on epicentre for the first set of experiments and on the same face as the laser for the second. A spherical capacitance transducer was also used for initial investigation of the surface pulse waveforms.

The samples were milled down to leave 14mm of steel substrate below the cladding to make through transmission measurements less prone to side wall reflections. When a plasma source was used for the bulk transmission measurements, the major detected signal was due to the direct compressional pulse. The amplifier used had limited bandwidth, (<1MHz), which distorted the waveforms, and since the EMAT is sensitive to velocity the longitudinal arrival was seen to be bipolar. Fig 5.17a shows a waveform



(a)

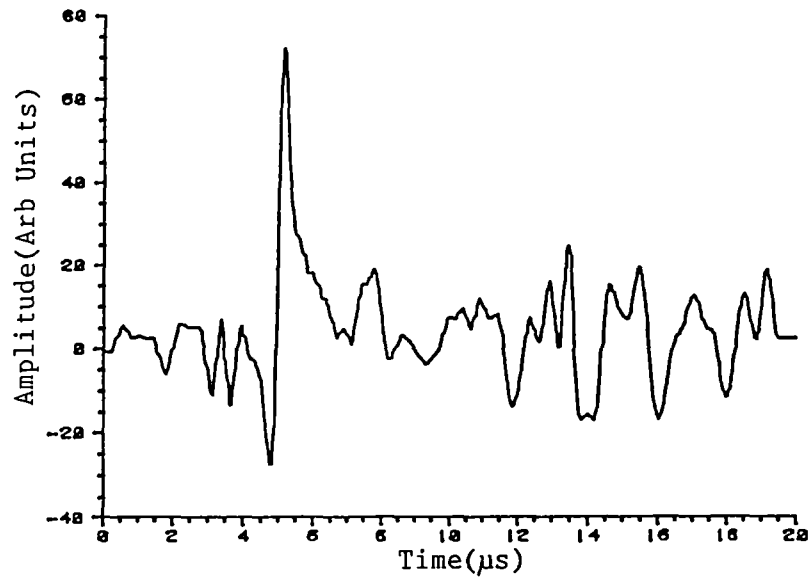


(b)

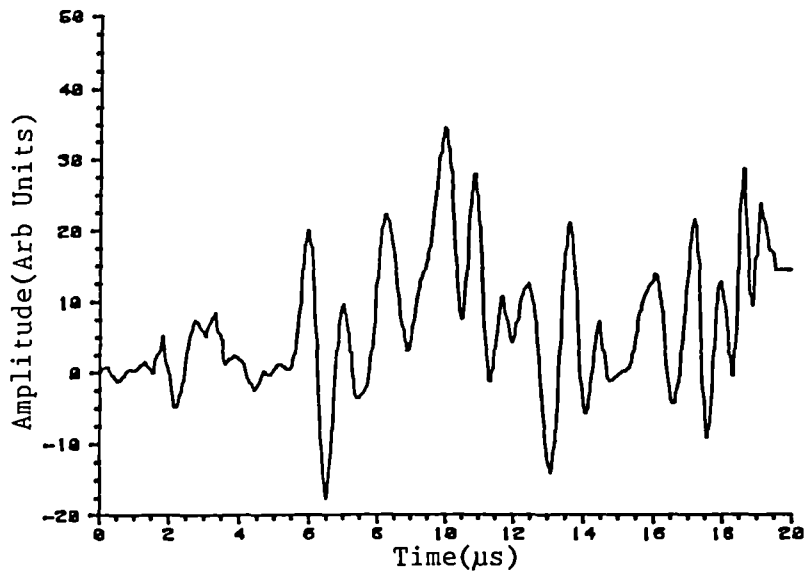
Fig 5.17 Bulk transmission through clad samples. A plasma source was used for generation and an out of plane velocity sensitive EMAT detected on epicentre.

- (a) Single layer sample, current setting of 160A.
- (b) Single layer sample, current setting of 110A.

obtained on the single layer sample deposited with a current setting of 160A. The longitudinal pulse is seen arriving after about  $3\mu\text{s}$  with a falling step at about  $6\mu\text{s}$  possibly being due to the shear arrival. When this signal is compared with a typical waveform from the defective sample welded at 110A, fig 5.17b, it is seen that the initial arrival was indistinct. Instead there is some oscillatory behaviour which is thought to be associated with diffraction and reflections off defects in this latter sample. Similar effects were seen from the waveforms produced with a thermoelastic source, fig 5.18a and 5.18b. However the shear arrival at  $\sim 5.5\mu\text{s}$  was far larger than the compressional pulse detected. To assess the quality of weld deposition at various points it was found unreliable to simply use the amplitude of the first arrival, probably due in part to variations in localised surface conditions and hence difficulty in ensuring consistent sensitivity from the EMAT. Instead, the peak to peak height of the first major acoustic signal detected was compared to the average deviation from the mean of the signal arriving after this pulse and before  $10\mu\text{s}$ . The result of such a treatment on several points on each cladding can be seen from Table 5.1. From this it can be seen that the signal to noise value is low where a low weld current was used, as would be expected. Additionally, the sample deposited at 130A produced a signal to scatter ratio which is indistinguishable from that clad with a current of 160A. It would appear that although the former sample may have a



(a)



(b)

Fig 5.18 As fig 5.17 using a thermoelastic source.  
 (a) Single layer sample, current setting of 160A.  
 (b) Single layer sample, current setting of 110A.

Transmission Through Weld and Substrate. On Epicentre Detection by EMAT.

<u>WELD CURRENT</u> A	EXPECTED INTEGRITY	SIGNAL TO SCATTER RATIO	
		THERM(S)	PLASMA(L)
110	POOR	3.2±1.7	2.4±1.3
130	MODERATE	9.8±2.0	9.6±5.6
160	GOOD	10.8±3.2	7.9±5.0

SINGLE LAYER OF DEL90 DEPOSITED ON STEEL SUBSTRATE

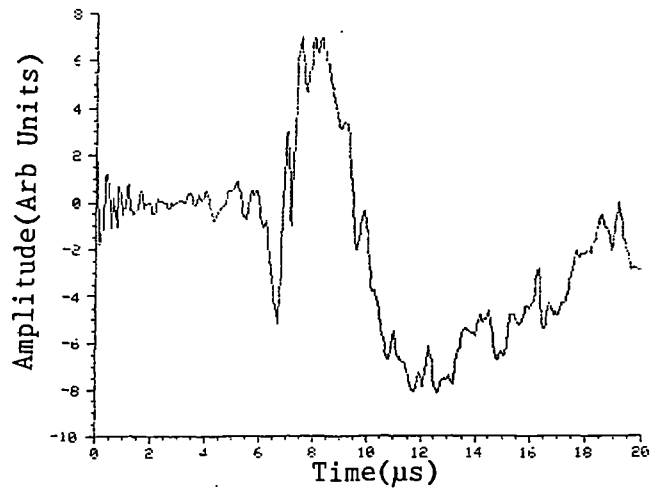
<u>WELD CURRENT</u> A		EXPECTED INTEGRITY		SIGNAL TO SCATTER RATIO	
BOTTOM	TOP	BOTTOM	TOP	THERM(S)	PLASMA(L)
110	100	POOR	POOR	4.9±2.5	3.5±0.8
110	160	POOR	GOOD	3.5±3.5	3.1±0.8
160	150	GOOD	GOOD	12.2±2.8	10.4±5.8

DOUBLE LAYER OF DEL90 DEPOSITED ON STEEL SUBSTRATE

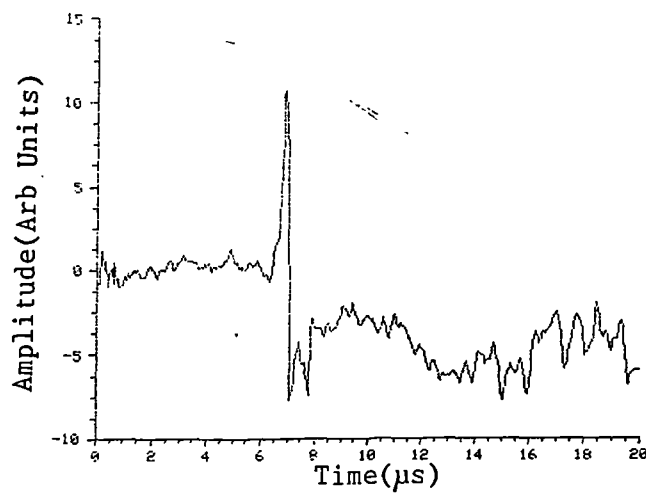
TABLE 5.1

very small fused region, there is still good acoustic coupling between the two substances. Of the double layer samples only the sample coated using high currents on both beads gave a high signal to noise value with there being little difference between the other two samples, the signals detected being close to noise level. These results therefore confirm that the latter two samples do contain a substantial number of defects. There is little difference in the signal to scatter ratio irrespective of the type of source used. The waveforms presented were highly reproducible at a given point on each sample. Large variations were however found between different points on the same sample, the error values in Table 1 being the standard deviation in the set of sample waveforms.

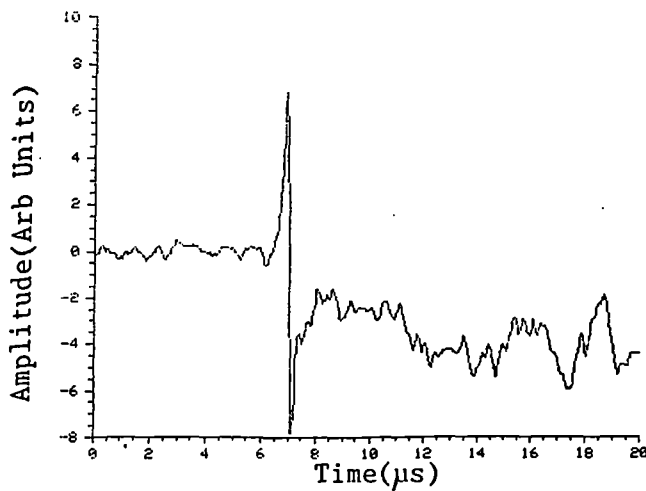
The second set of experiments involved having the detector and the laser spot on the surface of the weld bead. A wideband, (<4MHz), spherical capacitance transducer similar to that described by Aindow et al, (1987), having an electrode diameter of ~6mm was initially used for detection, displaced by approximately 25mm from the ultrasonic source. The incident laser pulse was focused to form a power density of  $\sim 3 \times 10^8 \text{ Wcm}^{-2}$  at the cladding surface. The resultant surface displacement waveforms are shown in fig 5.19 for the single weld and 5.20 for the double weld. The waveforms from the well fused single layered, fig 5.19c, and double layered, fig 5.20c, samples both show a distinct Rayleigh pulse arrival. A clean Rayleigh pulse also propagated along the single



(a)

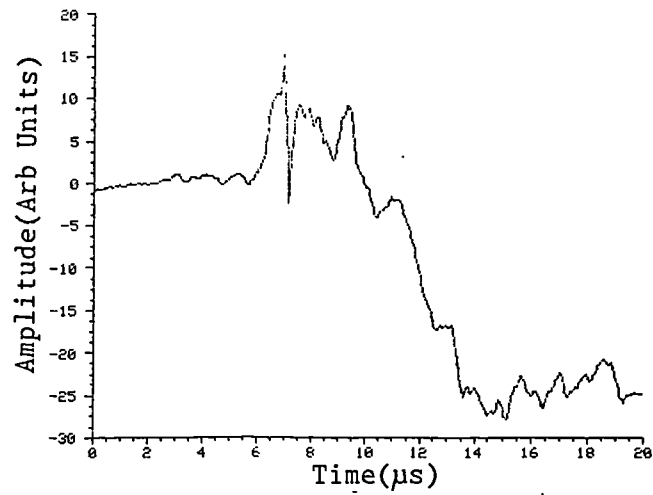


(b)

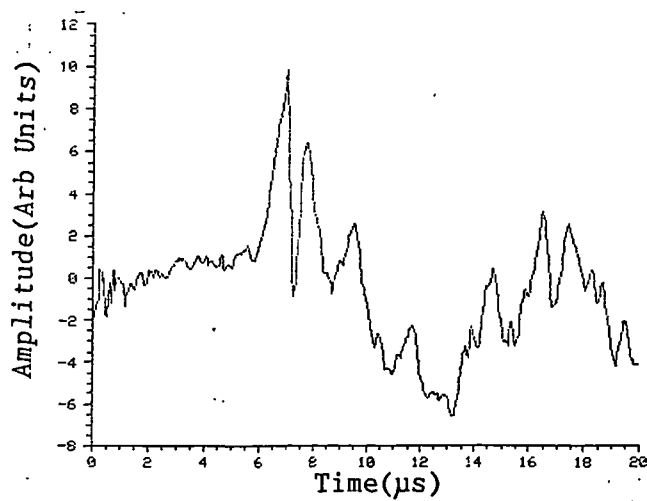


(c)

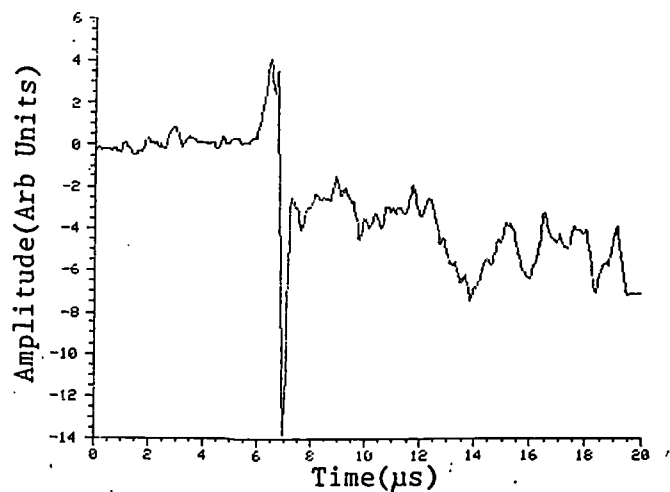
Fig 5.19 Surface waveforms detected by a capacitance displacement detector on various single weld beads. The detector was placed approximately 25mm from an ablation source.  
 (a) Current setting of 110A.  
 (b) Current setting of 130A.  
 (c) Current setting of 160A.



(a)



(b)

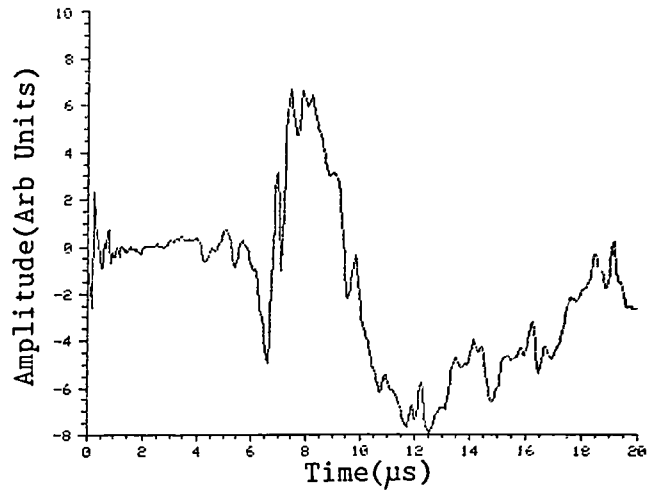


(c)

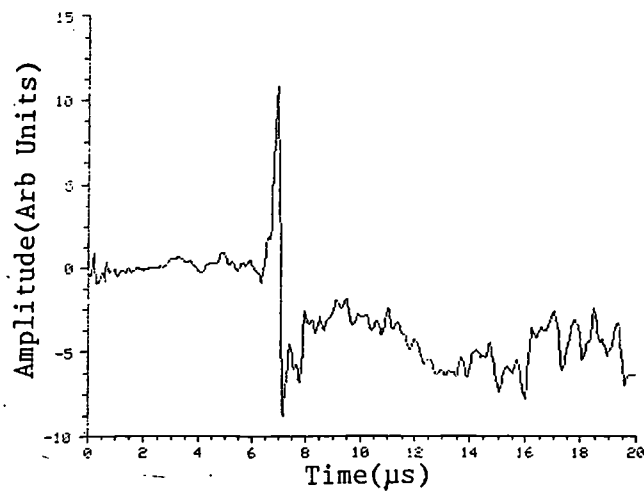
Fig 5.20 Surface waveforms detected by a capacitance displacement detector on various double weld beads. The detector was placed approximately 25mm from an ablation source.  
 (a) Current settings of 110A and 100A.  
 (b) Current settings of 130A and 160A.  
 (c) Current settings of 160A and 150A.

layer fused with a current setting of 130A, fig 5.19b. However the other three waveforms, (figures 5.19a, 5.20a and 5.20b), all show significant distortion of the surface wave after transmission across the cladding. To show that these differences were due mainly to scatter from defects in the claddings and not from noise, the laser was fired eight times on each sample and the resultant eight displacement waveforms were averaged and compared to the single shot waveforms of figures 5.19 and 5.20. Good correlation was evident between the two sets of data. Fig 5.21 shows the averages of eight waveforms collected on the three single weld samples. The major difference between the single shot and averaged traces is the increased resolution of the fast surface pulse.

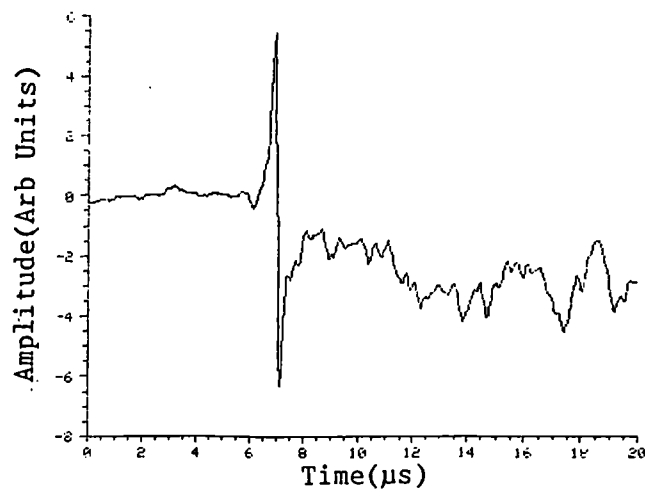
The widths and lengths of the six welds were  $(37 \pm 1)$ mm and  $(60 \pm 5)$ mm respectively with the overall thickness of the single layered samples being  $(18 \pm 0.25)$ mm and that of the double layered samples being  $(21 \pm 0.25)$ mm. Therefore on the timescale the signals were collected over, (up to  $20 \mu\text{s}$ ), reflections from back wall and weld edges will have reached the detector. The laser spot and capacitance probe were incident on corresponding positions on each sample. Hence for a set of well fused samples, with the geometries given above, these secondary arrivals would arrive at approximately the same time. The large variations between the collected waveforms from different samples is therefore thought to be dominated by forward scattering from adhesion defects at the



(a)



(b)



(c)

Fig 5.21 Average of eight surface waveforms detected by a capacitance displacement detector; corresponding to the single shot traces of fig 5.19.  
 (a) Current setting of 110A.  
 (b) Current setting of 130A.  
 (c) Current setting of 160A.

cladding\substrate interface. From fig 5.21c it is seen that the bipolar Rayleigh pulse on a well fused sample arrives between 6 and 7.5 $\mu$ s. The amplitude of the signal was measured as the peak to peak height detected between these times; on each of the six samples. The signal dominated by scatter was calculated as the average deviation from the mean value from 7.5 to 20 $\mu$ s. These values are compared in Table 5.2 for the six samples.

The incident power density was reduced to  $< 5 \times 10^6 \text{ Wcm}^{-2}$  and the experiments were repeated using a thermoelastic source. The waveforms of figures 5.22 and 5.23 were obtained for transmission across the single and double weld samples respectively. Due to the increased transit time across the source diameter, ( $\sim 4\text{mm}$ ), some frequency content is lost w.r.t. figures 5.19 to 5.21. The signals were reproducible and the main effect of averaging was again to enhance the longitudinal arrival. From the signal for the well fused double layer, fig 5.23c, it is seen that the Rayleigh pulse arrives between 4.5 and 8.75 $\mu$ s. The amplitudes of the Rayleigh pulses and scatter dominated signals were measured as before using these new times. The signal to scatter ratios obtained are shown in Table 5.3.

The results presented in Tables 5.2 and 5.3 show good agreement with the expected weld conditions. Focusing the laser spot produces a sharper and larger Rayleigh pulse, which is reflected by the results. The main aim of these experiments however, was to establish a remote NDE

Transmission of Rayleigh Pulse Across Weld Surface. Plasma Source,  
Spherical Capacitance Probe Detector.

These measurements were taken at single points, (without moving source and detector), and were generally repeatable to within 5%. However, over the sample as a whole error values similar to those in Table 5.4 would be expected.

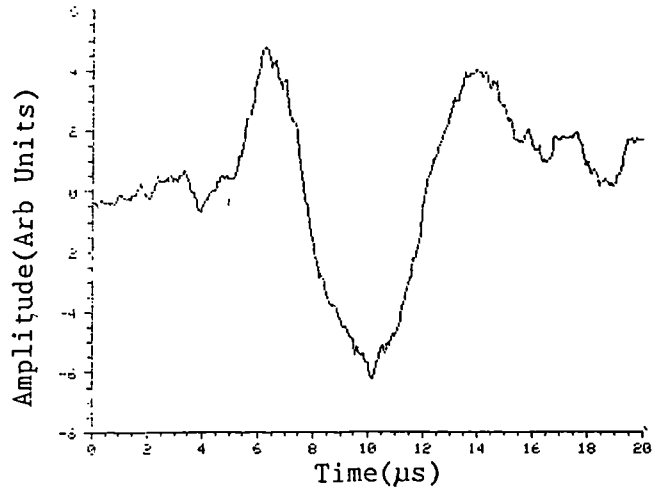
WELD CURRENT A	EXPECTED INTEGRITY	RAYLEIGH TO SCATTER AMPLITUDE RATIO	
		SINGLE SHOT	AVERAGE OF 8
110	POOR	3.9	4.0
130	MODERATE	15	16
160	GOOD	16	17

SINGLE LAYER OF DEL90 DEPOSITED ON STEEL SUBSTRATE

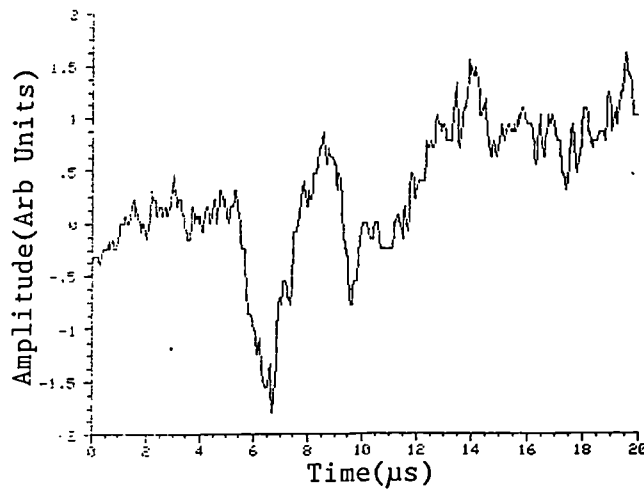
WELD CURRENT A		EXPECTED INTEGRITY		RAYLEIGH TO SCATTER AMPLITUDE RATIO	
BOTTOM	TOP	BOTTOM	TOP	SINGLE SHOT	AVERAGE OF 8
110	100	POOR	POOR	1.6	2.0
110	160	POOR	GOOD	4.6	4.1
160	150	GOOD	GOOD	14	18

DOUBLE LAYER OF DEL90 DEPOSITED ON STEEL SUBSTRATE

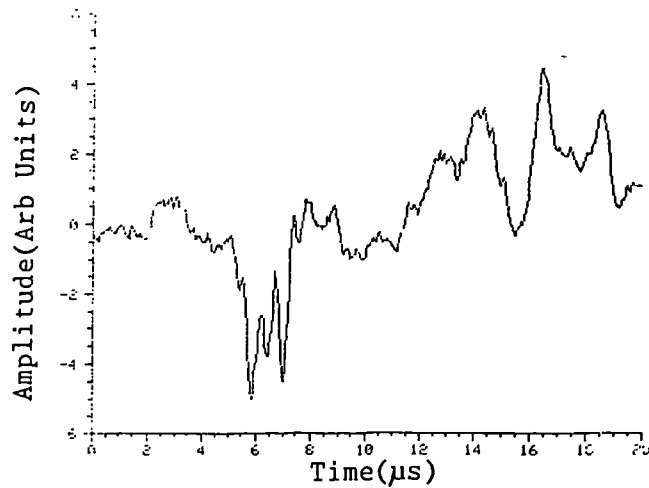
TABLE 5.2



(a)

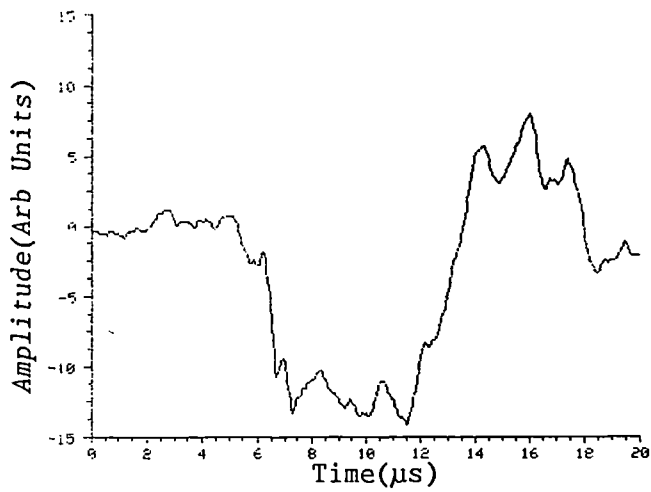


(b)

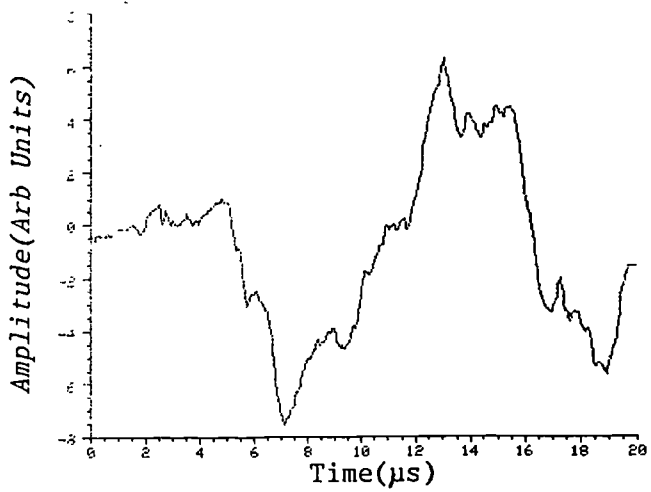


(c)

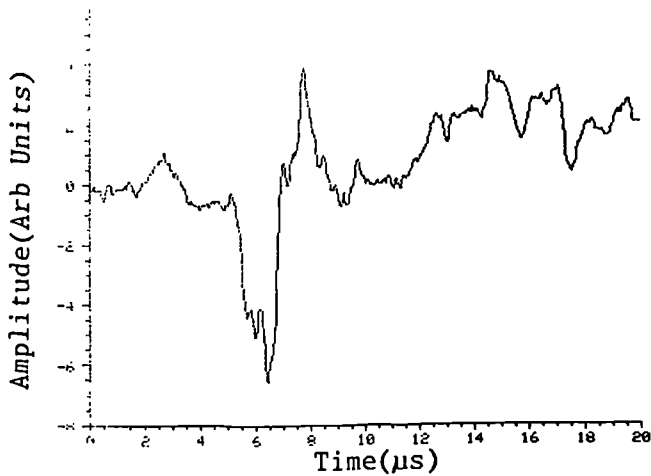
Fig 5.22 Surface waveforms detected by a capacitance displacement detector on various single weld beads. The detector was placed approximately 25mm from a thermoelastic source.  
 (a) Current setting of 110A.  
 (b) Current setting of 130A.  
 (c) Current setting of 160A.



(a)



(b)



(c)

Fig 5.23 Surface waveforms detected by a capacitance displacement detector on various double weld beads. The detector was placed approximately 25mm from a thermoelastic source.  
 (a) Current settings of 110A and 100A.  
 (b) Current settings of 130A and 160A.  
 (c) Current settings of 160A and 150A.

Transmission of Rayleigh Pulse Across Weld Surface. Thermoelastic Source, Spherical Capacitance Probe Detector.

These measurements were taken at single points, (without moving source and detector), and were generally repeatable to within 5%. However, over the sample as a whole error values similar to those in Table 5.4 would be expected.

WELD CURRENT A	EXPECTED INTEGRITY	RAYLEIGH TO SCATTER AMPLITUDE RATIO	
		SINGLE SHOT	AVERAGE OF 8
110	POOR	3.3	3.4
130	MODERATE	6.4	5.3
160	GOOD	5.0	5.1

SINGLE LAYER OF DEL90 DEPOSITED ON STEEL SUBSTRATE

WELD CURRENT A		EXPECTED INTEGRITY		RAYLEIGH TO SCATTER AMPLITUDE RATIO	
BOTTOM	TOP	BOTTOM	TOP	SINGLE SHOT	AVERAGE OF 8
110	100	POOR	POOR	2.2	2.2
110	160	POOR	GOOD	2.8	3.1
160	150	GOOD	GOOD	11	11

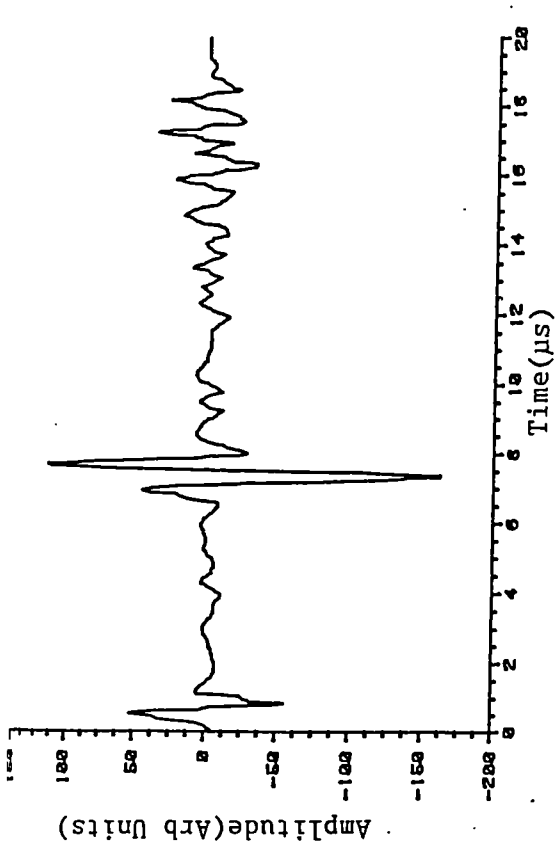
DOUBLE LAYER OF DEL90 DEPOSITED ON STEEL SUBSTRATE

TABLE 5.3

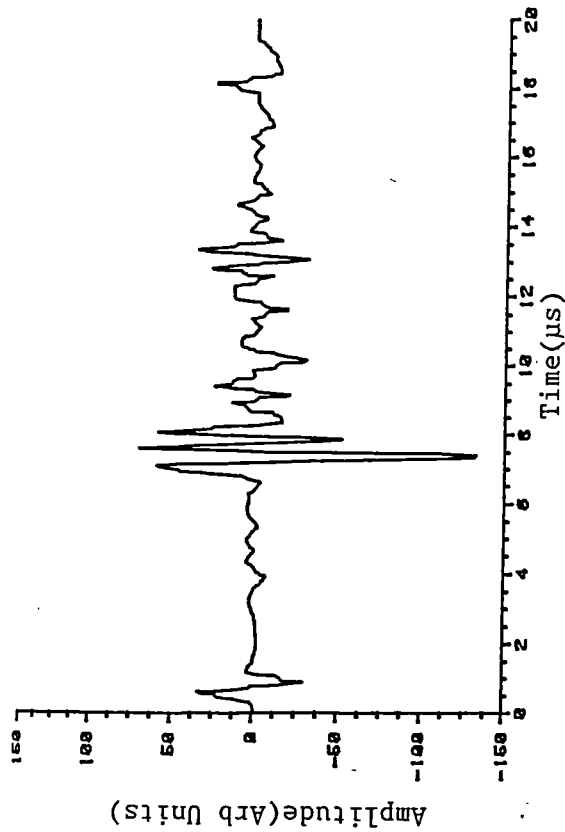
system which could be applied to hot samples. The capacitance transducer used had to be held a few microns above the clad surface. Since the coating thickness varied by  $\sim \pm 0.25\text{mm}$  on any given sample and also because of thermal expansion of hot samples, the use of this transducer would not be practical in a final technique. The experiments were therefore repeated using the EMAT sensitive to out of plane motion held  $\sim 1.0\text{mm}$  above the coating.

The EMAT coil was positioned about 25mm from the laser-ultrasound source. Again better signal to noise was obtained using an ablation source. Fig 5.24a shows the surface longitudinal and Rayleigh pulses followed at some time later by some side wall reflections, the sample used was the well fused double bead. A similar waveform was observed for the single bead deposited at 160A. A distinct Rayleigh pulse also propagated along the single layer sample welded with a current setting of 130A, fig 5.24b. However some scatter is evident compared with a waveform produced in the well fused single layer, fig 5.24c. In contrast, fig 5.24d suggests that the last double layered sample, deposited with low currents, contains many defects. No distinct Rayleigh pulse arrival can be attributed to this waveform since there were so many features due to the various acoustic modes interacting with defects.

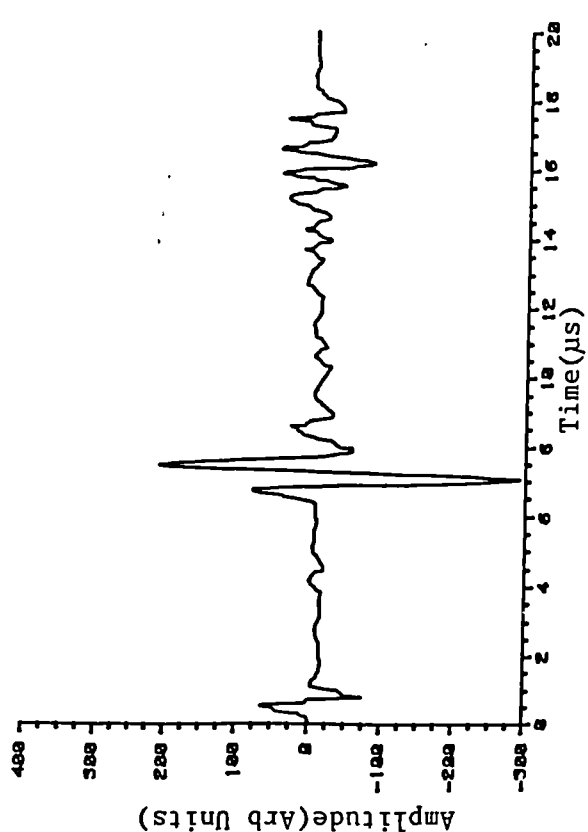
The results obtained using a thermoelastic source showed similar features, although detected signals were not as sharp and as expected the Rayleigh arrival was reversed in polarity.



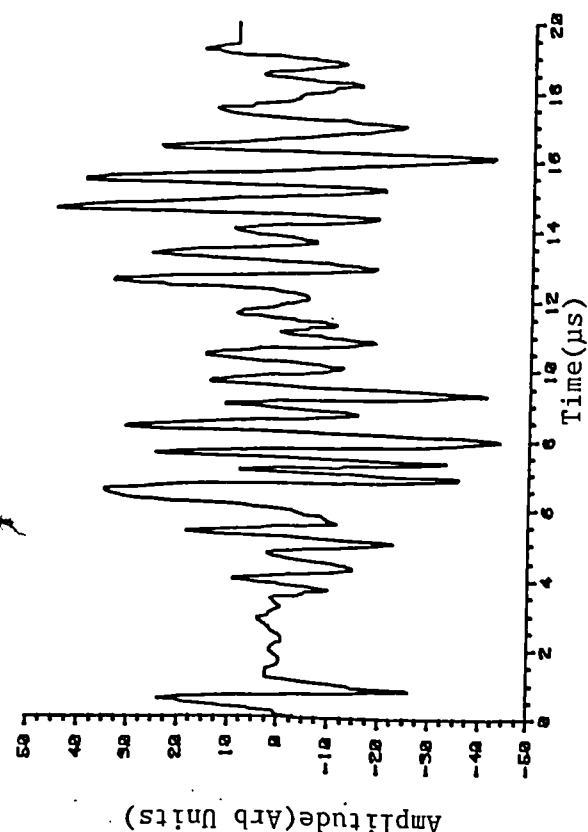
(a) Double bead, current settings 160A and 150A.



(b) Single bead, current setting 130A.



(c) Single bead, current setting 160A.



(d) Double bead, current settings 110A and 100A.

Fig 5.24 Surface waveforms detected by an EMAT on double and single weld beads. Detector placed approximately 25mm from an ablation source.

As before the initial peak to peak height of the Rayleigh arrival was measured and compared to the mean deviation from the average signal arriving after the surface pulse and before  $20\mu\text{s}$ . The source to detector distance was constant between the samples and therefore a time window was set, (from  $\sim 7$  to  $\sim 9\mu\text{s}$ ), to measure the amplitudes at the expected time of arrival of the Rayleigh pulse. The signal to scatter ratios obtained from these surface pulse transmission experiments for both types of laser source are shown in Table 5.4. The general trend of these results was as expected. Again there is little evidence of porosity defects in the moderately bonded single clad sample. The change in signal to scatter ratio is more marked between the samples in Table 5.4 than in the previous two tables where a capacitance detector was used. The EMAT is sensitive to out of plane velocity of the sample surface, unlike the displacement measuring capacitance transducer. When signals from the latter device were convolved over the  $\sim 1\text{MHz}$  bandwidth of the EMAT amplifier and then differentiated, the signal to scatter values of Table 5.5 were produced. These values agree well with those detected by the EMAT although too few signals were recorded for error estimation.

#### 5.5c/ Discussion.

These experiments have shown that it is possible to non-contactively assess the bonding integrity of plasma transferred arc claddings by observing the forward

Transmission of Rayleigh Pulse Across Weld Surface.  
EMAT Detector.

WELD CURRENT A	EXPECTED INTEGRITY	RAYLEIGH TO SCATTER AMPLITUDE RATIO	
		THERM	PLASMA
110	POOR	8.8±1.4	10.6±4.3
130	MODERATE	11.0±2.4	24±5
160	GOOD	11.5±3.1	28±10

SINGLE LAYER OF DEL90 DEPOSITED ON STEEL SUBSTRATE

WELD CURRENT A		EXPECTED INTEGRITY		RAYLEIGH TO SCATTER AMPLITUDE RATIO	
BOTTOM	TOP	BOTTOM	TOP	THERM	PLASMA
110	100	POOR	POOR	6.7±1.2	9.7±3.4
110	160	POOR	GOOD	8.0±2.6	14.2±14
160	150	GOOD	GOOD	12.0±0.6	29±10

DOUBLE LAYER OF DEL90 DEPOSITED ON STEEL SUBSTRATE

TABLE 5.4

Transmission of Rayleigh Pulse Across Weld Surface.  
Spherical Capacitance Probe Detector. Output Convolved  
Over 1MHz Bandwidth then Differentiated.

These measurements were taken at single points, (without moving source and detector), and were generally repeatable to within 5%. However, over the sample as a whole error values similar to those in Table 5.4 would be expected.

<u>WELD CURRENT</u> A	EXPECTED INTEGRITY	SIGNAL TO SCATTER RATIO	
		THERM	PLASMA
110	POOR	6.9	11
130	MODERATE	8.4	28
160	GOOD	12	29

SINGLE LAYER OF DEL90 DEPOSITED ON STEEL SUBSTRATE

<u>WELD CURRENT</u> A		EXPECTED INTEGRITY		SIGNAL TO SCATTER RATIO	
BOTTOM	TOP	BOTTOM	TOP	THERM	PLASMA
110	100	POOR	POOR	6.1	12
110	160	POOR	GOOD	4.7	11
160	150	GOOD	GOOD	19	34

DOUBLE LAYER OF DEL90 DEPOSITED ON STEEL SUBSTRATE

TABLE 5.5

scatter from either bulk or surface laser-generated acoustic pulses. Ideally the coatings would be examined immediately after deposition, yielding information on the weld quality which could be used to adjust the parameters of the plasma transferred arc equipment and hence improve the fusion of subsequent claddings. This is important for components of complex geometry where it is difficult to ensure that all of the weld parameters, (e.g. separation distance), are kept constant. It may also assist optimisation of the quality of the bonding by ensuring there is low dilution of the overlay material. Generally dilution increases with weld time as the substrate heats up and requires less input energy to fuse with the coating.

A spherical capacitance transducer was used for initial measurements of scatter of a Rayleigh pulse caused at the weld interface. This was replaced by a non-contacting EMAT detector, (for surface and bulk measurements), which had to be kept about 1mm above the clad surface. A further improvement would be to replace this with an optical device to eliminate the problem of holding off a detector from a hot surface to which it may be attracted. It has been shown earlier in this chapter that a stabilised Michelson interferometer has sufficient sensitivity to work on certain plasma transferred arc deposits. However in general the surface quality of the claddings may cause too much scatter of incident light to make such a device viable. An optical detector of greater sensitivity, such as the Mach-Zehnder, (Krautkramer;

1979), or Fabry-Perot, (Monchalin; 1985), interferometer may prove more practicable.

Larger signal to scatter ratios were calculated from the surface pulse experiments due to the increased energy contained in these pulses with respect to bulk laser generated disturbances. The surface pulses produced by a plasma source gave the largest ratios and, in general, the best reproducibility. In the bulk waveform studies little difference was evident between measurements from thermoelastic and plasma sources. However, it should be noted that for the bulk plasma signal to scatter calculations; the longitudinal pulse was used, whereas the shear was used in the thermoelastic case. A larger time window for scatter measurements was therefore used in the plasma case, which means that the scatter measurements contain components associated with a direct shear arrival. However the differential of the shear displacement is not large for this source.

This has been a pilot scheme to investigate the feasibility of remotely measuring the weld quality with a view for possible on-line checking of claddings as they are deposited. It would be necessary to examine more samples manufactured under a wider range of weld conditions before such a system was implemented. Further research is required on hot samples and on the type of detector most suitable for this application.

CHAPTER 6.

2-DIMENSIONAL SUB-SURFACE FLAW VISUALISATION.

6.1/ Introduction.

Detection of flaws in the bulk of thin materials has proved difficult for conventional NDT systems. Due to deadtime problems, mentioned in Chapter 4, single sided inspection of a thin material is impractical unless a delay medium is used, as in an immersion tank, which is not practical for large samples. If both sides are accessible then through-transmission measurements may be made. Attenuation measurements, however, rely both on a constant ultrasonic signal being generated and on unvarying sensitivity of the detector which is difficult to ensure for piezoelectric probes.

Lasers have been employed for the detection of flaws in thin materials although it was their production of thermoelastic rather than optoacoustic pulses that was exploited. Rousset et al, (1985), heated the surface of a laminate with focused pulses of 1ms duration from a Nd:YAG laser. The displacement of the surface was monitored by an interferometric probe incident on the same spot as the heating beam. For an unbonded layer the induced thermal

stresses produced a thermoelastic bending, while for a well-bonded layer the surface displacement was reduced to the thermal expansion. A much higher lifting efficiency was found with this technique than with extended bulk heating. The output from a 1W argon ion laser was modulated by a sector wheel light chopper to produce photothermal signals on plasma sprayed coatings by Almond et al, (1983). An infra-red sensitive detector monitored the surface temperature. The resultant photothermal image of a defect in an alumina coating on a steel substrate was compared favourably with the results of an underwater ultrasonic C-scan on the sample. The most attractive feature of such a system could be that it is a surface specific technique and hence much of the overall geometry of the bulk substrate has no effect on the photothermal signals. A photothermal technique was also used by Inglehart et al, (1986), to characterise a composite of woven carbon fibres and epoxy resin consisting of both opaque and transparent parts. A modulated, focused  $Ar^+$  laser was used to produce a periodic heat source with a focused He-Ne laser being used as a probe to monitor the variations in surface temperature by the mirage effect. Subsurface cuts made perpendicular to the fibres were easily detected although there was little evidence for the detection of a simulated delamination in the material.

The work presented here centers around detection of artificial subsurface defects in carbon fibre composite material. Results are also presented from the examination of

plasma sprayed steel coatings. The examination procedure was firstly developed on samples of aluminium containing known defects, before being applied to the above samples. A second NDE technique is described which requires access to only one face of a polished sample. This is a totally remote system, using optical detection of the laser generated ultrasound.

## 6.2/ Samples.

The composite material, supplied by British Aerospace of Warton, was manufactured by overlaying layers of resin preimpregnated sheets of carbon fibre. The fibre orientation was rotated by  $60^\circ$  from layer to layer. The sample had various thickness steps, from 1 to 20mm, each of area 50 by 60mm. Envelopes of folded ptfе were inserted in each step during manufacture to simulate laminar defects. In each case three envelopes of 3 by 3mm and three of 6 by 6mm were inserted before the sample was cured. Fig 6.1a shows a schematic diagram of the sample which was deduced from results presented later in this chapter, the locations of the defects were not known prior to examination.

5.5mm thick mild steel bars which had been plasma sprayed were also examined. In plasma spraying, material in powder form is injected into a high temperature, (16000K), high velocity, ( $300\text{ms}^{-1}$ ), plasma jet where it is melted and propelled onto a component surface. Protective coatings, ( $\sim 0.75\text{mm}$  thick), can be deposited over a wide range of material compositions, (metals, ceramics, carbides

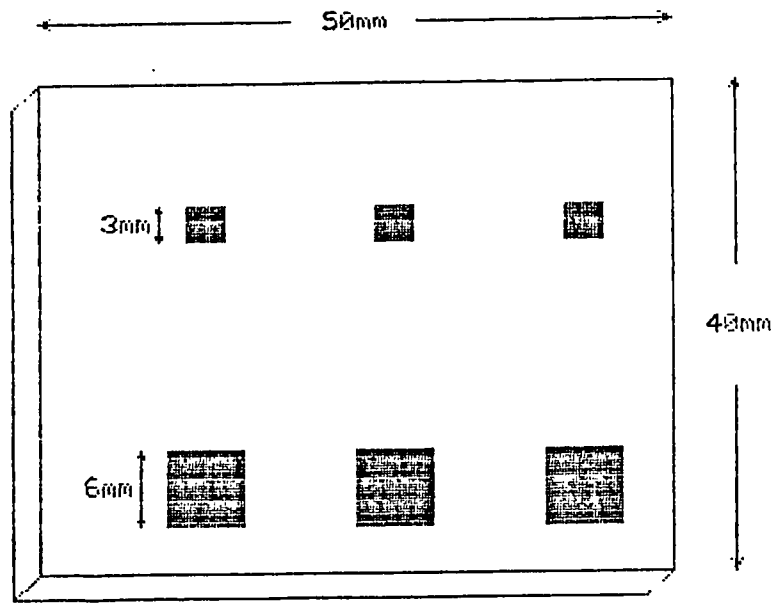


Fig 6.1(a) Schematic diagram of carbon-fibre composite sample showing the approximate locations and sizes of the six inclusions.

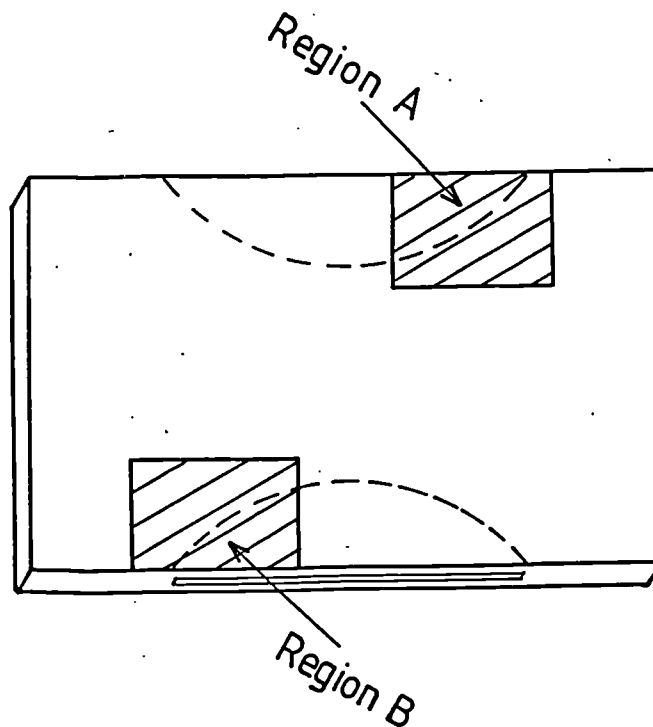


Fig 6.1(b) Schematic diagram of the duraluminium sample showing the approximate locations of the saw-cuts and regions scanned for figures 6.15 and 6.17.

and cements), to provide both wear and corrosion resistance. The coatings examined were of Delcrome 90, and were manufactured during a visit to the C.E.G.B. Marchwood Engineering Laboratories.

In addition a 3mm thick aluminium plate was produced which had two saw-cuts at its midthickness as shown in fig 6.1b. This sample was examined first since the locations and extent of the artificial defects were well known. From the waveforms obtained it was possible to set criteria indicating the presence of defects which could be used for an automated inspection of the other samples.

### 6.3/ Through Transmission Experiments.

#### 6.3a/ Experimental Technique.

The laser source causes radiation of highly reproducible pulses of ultrasound in solid samples. Therefore the consistency problems associated with conventional ultrasonic through transmission testing do not exist, given that a suitable non-contact detector is used. Also alignment is simpler with this system since the detector can be centred easily using a He-Ne guide laser. For the experiments on the aluminium sample it was possible to use the EMAT sensitive to out of plane motion, described in Chapter 4. The experimental arrangement was as shown in figure 6.2. The Nd:YAG laser was focused to a spot size of 0.2mm to produce a plasma at the surface of the metal, (power density  $\sim 10^9 \text{Wcm}^{-2}$ ), and hence launch a strong longitudinal signal into the bulk, normal to the surface.

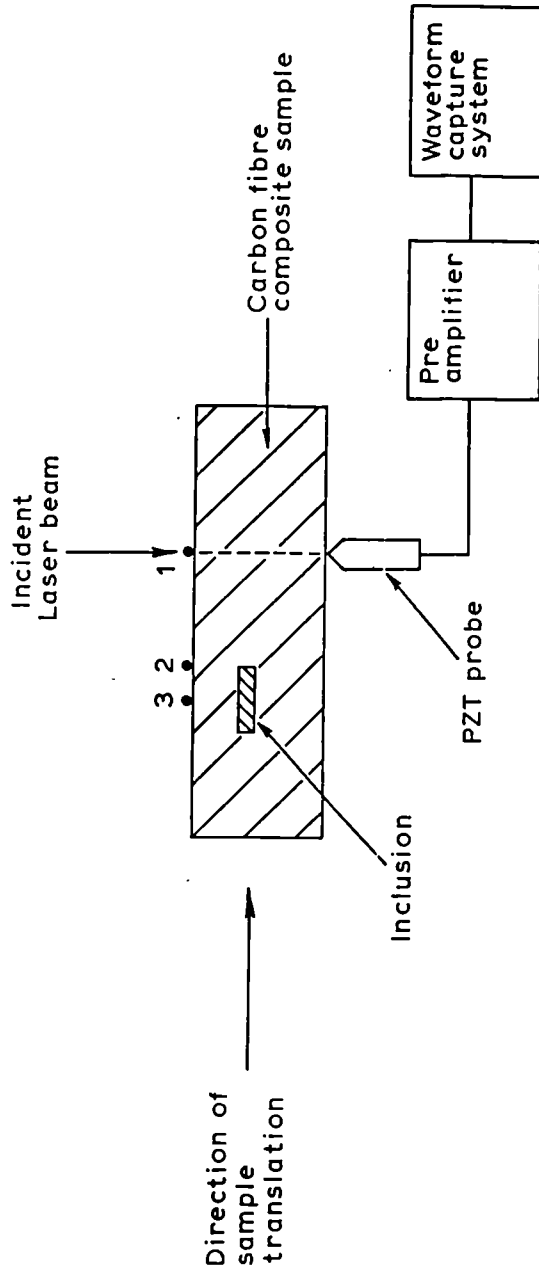


Fig 6.2 Scheme for the scanning system. Laser and probe are held whilst the sample is incrementally moved on the x-y table.

The EMAT was placed on epicentre and detected signals which were amplified before digitisation and storage. The sample was mounted on an x-y table, powered by two Superior Electric stepping motors type MO61-FD-6002. Two McLennan IDB controllers activated the motors using commands from the Tektronix mini-computer via an IEEE-488 interface.

Waveforms from such a system are shown in fig 6.3. Some oscillatory behavior is evident from these traces; probably due to poor matching between the EMAT and Physical Acoustics Corporation amplifier used. The techniques described below rely only on the initial acoustic events detected and so this "ringing" is acceptable. The signal from the direct longitudinal pulse propagating without encountering the saw-cut reached a maximum after about  $1.2\mu\text{s}$ , fig 6.3a. Moving the sample so that the acoustic generation was near the edge of the artificial defect had the effect of increasing the transit time, fig 6.3b. This increase in time and accompanying loss in amplitude continued as the sample was moved further, fig 6.3c, until the saw-cut had almost totally masked the acoustic energy reaching the detector.

For consistent sensitivity the EMAT would have to be positioned the same distance above the metal surface at each point examined. This is difficult to ensure in a mechanised scanning system. It was also found that if the spring loaded conical PZT probe described in Chapter 4 was used for detection then the same effects were observed as the sample was scanned across a flawed region. However, the

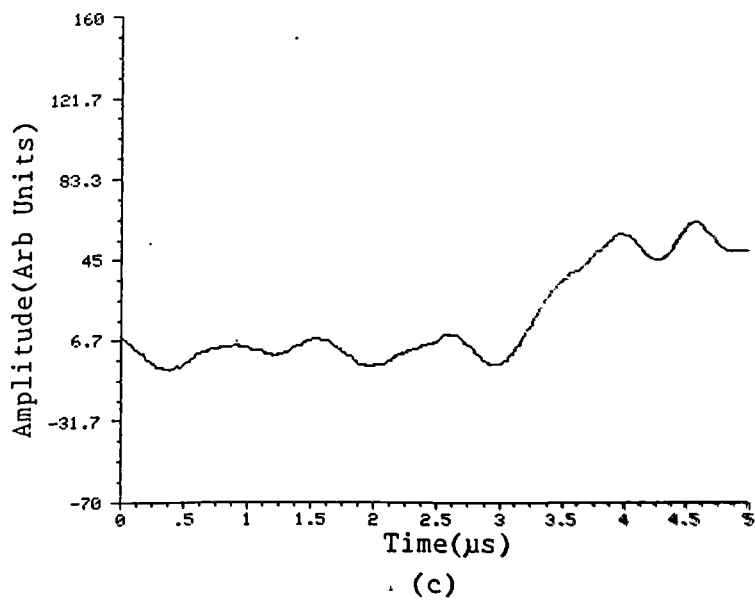
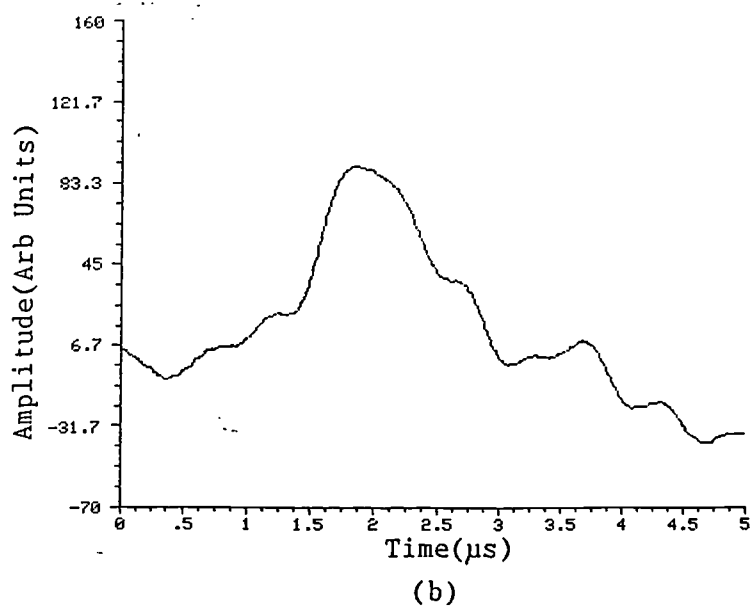
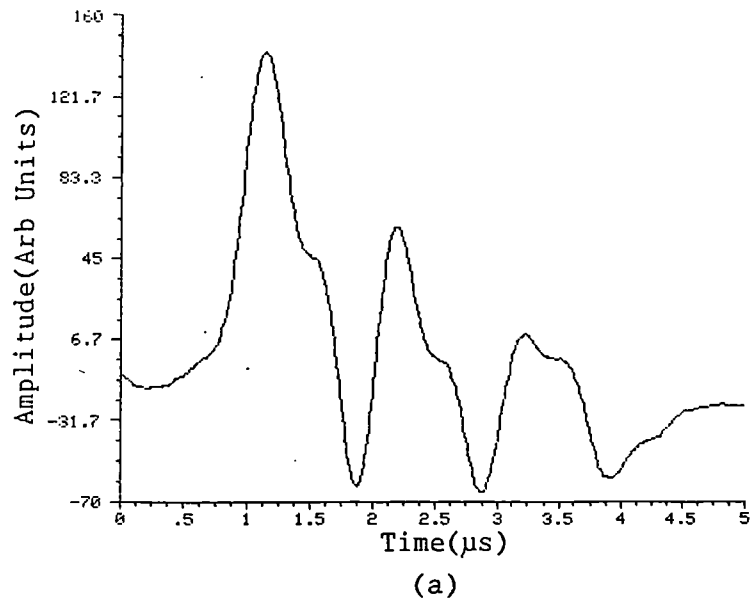


Fig 6.3 Variation of ultrasonic signal detected as sample is moved.  
 Ablation source.  
 (a) No defect, corresponding to generation at point 1 in Fig 6.2.  
 (b) Edge of defect encountered, (point 2).  
 (c) Generation over inclusion, (point 3).

amplitude of the signal from the latter detector was not as reproducible, perhaps due to variable loading. For these reasons it was thought that a measurement of the maximum amplitude of the detected signal would not be a suitable criterion; so two other data points from each waveform were collected for evaluation. The first of these points gave a measure of the time of flight of the compressional pulse through the sample. The amplitude of the first arrival,  $A_0$ , say, was about 150mV from fig 6.3a. By measuring the time when the detected signal first reaches a threshold value of  $A_0/2$  an approximation for the arrival time of this pulse is made. This arrival time was measured from figures 6.3a and 6.3b to be 1.1 $\mu$ s and 1.8 $\mu$ s respectively with the waveform of fig 6.3c failing to reach a high enough value. Other threshold values may be used, e.g.  $A_0/3$  or  $A_0/4$ , which would enable smaller acoustic signals to be detected so long as the noise level is suitably low. The second criteria was a measure of the amplitude at the time,  $T_0$ , when the initial compressional peak reached its maximum value on unflawed material. From fig 6.3a this is about 1.3 $\mu$ s for the case of our 3mm thick aluminium sample. The amplitude at time  $T_0$  dropped from this value as the defect was encountered and so could also be used for an NDE of the sample.

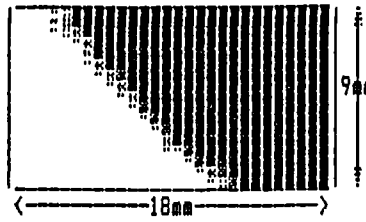
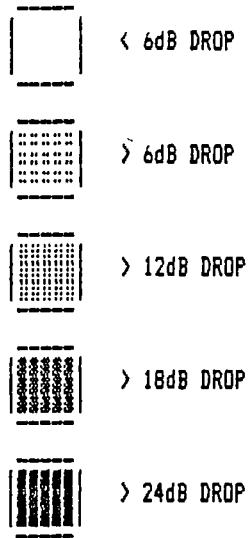
### 6.3b/ Results.

#### (i) Dural Test Sample.

The x-y table was positioned so that the laser spot was incident over a region known to be defect free and values for  $A_0$  and  $T_0$  were measured from the waveform collected. The sample was then scanned over the shaded area of fig 6.1b, two data points being collected for each sample position as described above to produce the two data-files of fig 6.4. Both methods easily detected the presence of the saw cut. The resolution of the edge of the defect was good since a small generating spot size was used although some surface pitting of the sample was caused. The diameter of the source was increased to  $\sim 2.5\text{mm}$ , hence decreasing the power density to  $\sim 5.5\text{MWcm}^{-2}$  and the experiment was repeated. Sample waveforms were collected over a defect free region, fig 6.5a, and over the saw cut, fig 6.5b. Since a thermoelastic source was used the normal displacement caused by the longitudinal arrival, (L), was smaller than that from the ablation source, (c.f. fig 6.3a). The L pulse was relatively reduced and slightly delayed in fig 6.5b. The L pulse of fig 6.5a was therefore used to set  $A_0$  and  $T_0$  for a scan of one of the complete saw cut areas to produce the files of fig 6.6. Again the saw cut was easily detected although the resolution was reduced from that in fig 6.4 due to both the larger source width and the weaker longitudinal signal produced, however no surface pitting occurred.

Hence two techniques have been developed which can

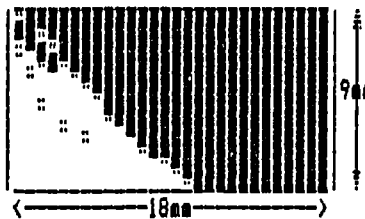
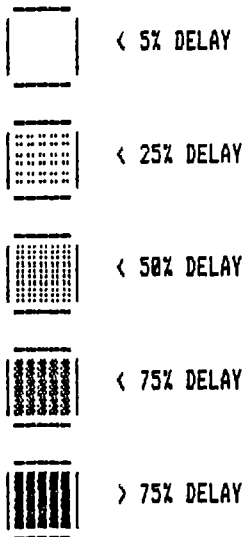
AMPLITUDES



28 BY 16 POINT SCAN OF A 3mm THICK ALUMINIUM SAMPLE  
PLASMA SOURCE EMAT DETECTOR ON EPICENTRE

(a)

ARRIVAL TIMES



28 BY 16 POINT SCAN OF A 3mm THICK ALUMINIUM SAMPLE  
PLASMA SOURCE EMAT DETECTOR ON EPICENTRE

(b)

Fig 6.4 Grey scale representation of saw-cut in a 3mm thick Dural sample.  
(a) Discriminator is the amplitude of the first longitudinal arrival.  
(b) Discriminator is the arrival of the direct longitudinal pulse, set as half of the amplitude over defect free area.

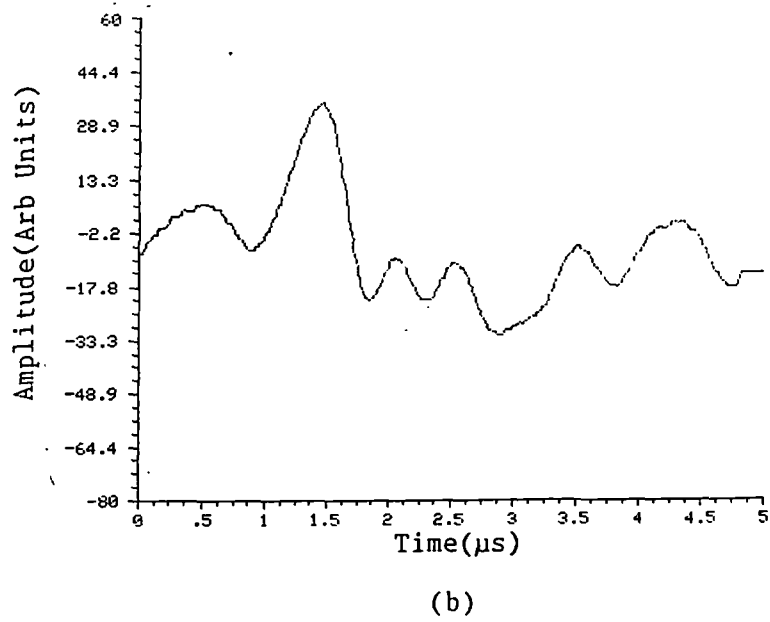
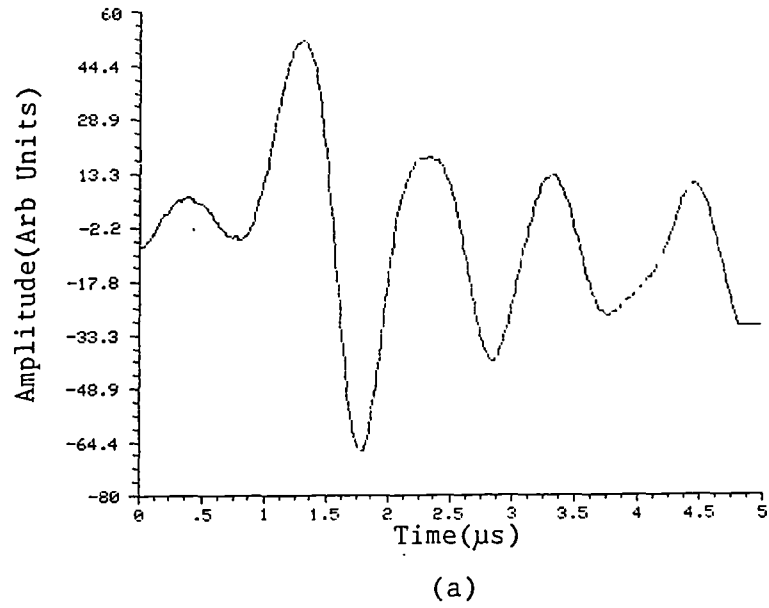
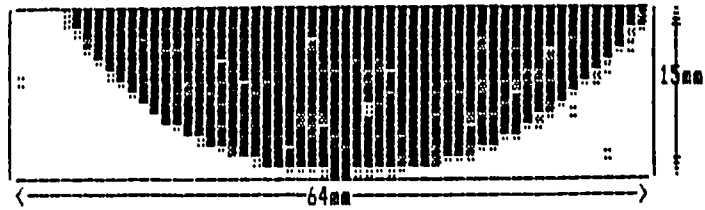
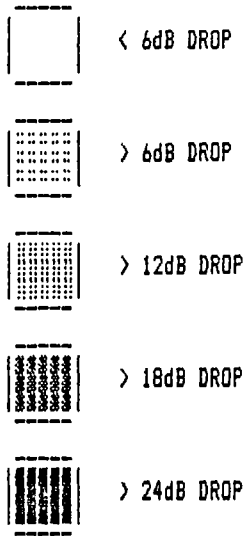


Fig 6.5 Variation of ultrasonic signal detected as sample is moved.  
 Thermoelastic source.  
 (a) Large signal from a defect free region.  
 (b) Signal decreased over a saw cut region.

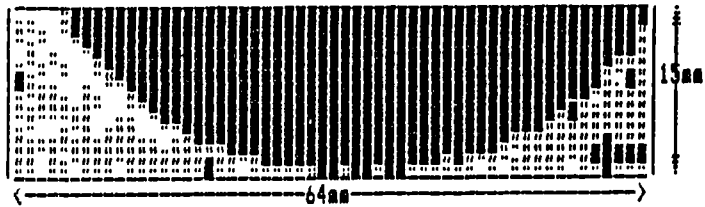
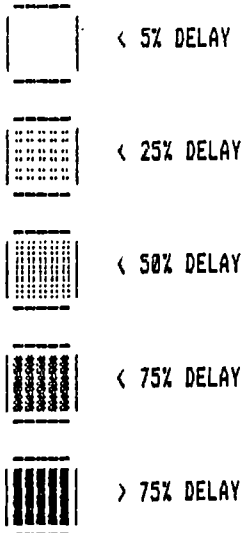
AMPLITUDES



56 BY 15 POINT SCAN OF A 3mm THICK ALUMINIUM SAMPLE  
THERMOELASTIC SOURCE EMAT DETECTOR ON EPICENTRE

(a)

ARRIVAL TIMES



56 BY 15 POINT SCAN OF A 3mm THICK ALUMINIUM SAMPLE  
THERMOELASTIC SOURCE EMAT DETECTOR ON EPICENTRE

(b)

Fig 6.6 Grey scale representation of saw-cut in a 3mm thick Dural sample.  
(a) Discriminator is the amplitude of the first longitudinal arrival.  
(b) Discriminator is the arrival of the direct longitudinal pulse, set as half of the amplitude over defect free area.

detect sub-surface flaws in aluminium. These techniques were then used on plasma sprayed samples and on the carbon-fibre composite samples shown schematically in fig 6.1a. The defects in the latter sample were envelopes of folded ptfе and thus the acoustic impedance mismatch over these regions was not as great as it was between aluminium and saw cut.

(ii) Plasma Sprayed Steel Samples.

Conventional ultrasonic techniques have been used to detect defects in plasma sprayed samples. Cox et al, (1980), detected defects in steel samples coated with alumina and molybdenum. These experiments were carried out in an immersion tank. Backwall reflection was found to be more effective than through transmission, although it was not possible to distinguish between attenuation caused by porosity and attenuation caused by adhesion defects. Initial results from a laser based method of flaw detection on plasma sprayed coatings have already been presented, (Cooper et al; 1985). The scan of a sample coated with a ~0.6mm thick layer of alumina resolved defects which confirmed results from conventional immersion testing. It was found that measuring the arrival time of the longitudinal pulse was more reliable than measuring the initial amplitude. This was mainly due to the variation in acoustic amplitude generated by the laser due to the uneven nature of the sample surface.

It was hoped to extend these experiments to encompass different coatings. The coating process requires

the substrate to be cleaned and roughened by grit blasting prior to deposition. In an effort to manufacture defects of known shapes and positions, areas of the substrates were masked during the grit blasting stage or marked in various ways before deposition. Several samples, manufactured in this way, were tested ultrasonically and then sectioned and visually examined for defects. For the NDE the focused spot from the Nd:YAG laser was incident on the coating with the out of plane sensing EMAT at epicentre on the substrate. Detected signals were amplified by a high input impedance Harwell amplifier before capture. The detected waveforms were reproducible from point to point on a given sample but varied between samples. Fig 6.7a shows typical waveforms from points on four samples. The corresponding micrographs are shown in figures 6.7b and c with magnifications of x75 and 1200 respectively. From fig 6.7b it was noted that there is a distinct line between the coating and substrate. This line was present on all of the micrographs taken and so was possibly related to the cutting and polishing process rather than being an indication of bond quality. The coatings are shown in more detail in fig 6.7c. The structures were not constant over the cross-sections examined, (figures 6.7a and c), and the difficulties of interpreting the ultrasonic signals in terms of scattering or attenuation by the coating are evident. The lack of information on bond quality rendered analysis of these waveforms impossible.

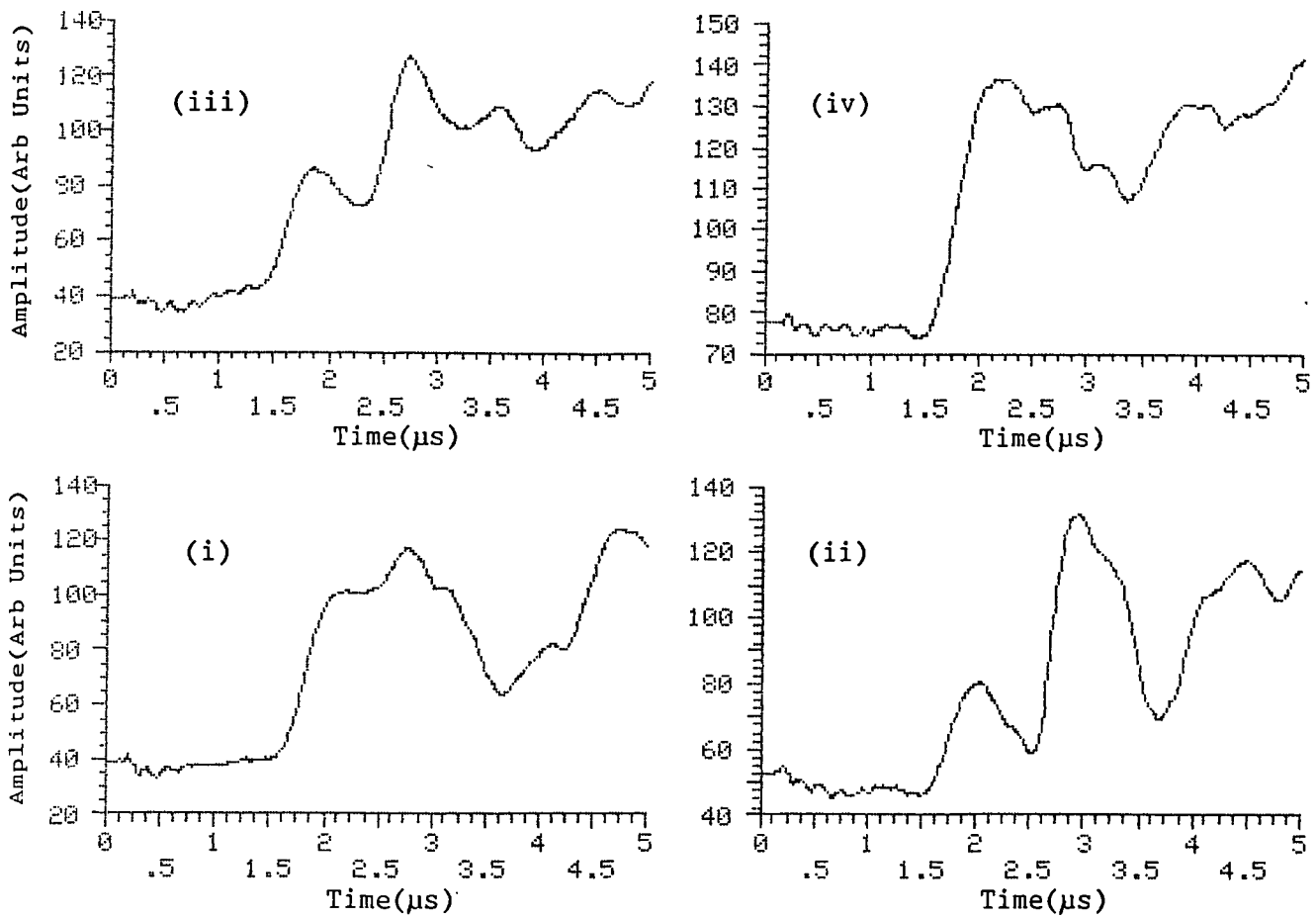
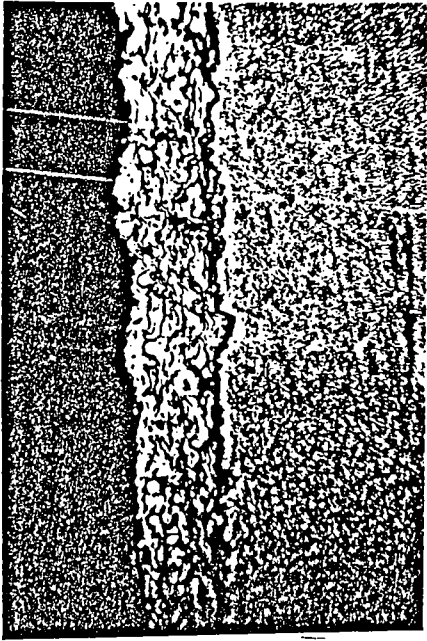
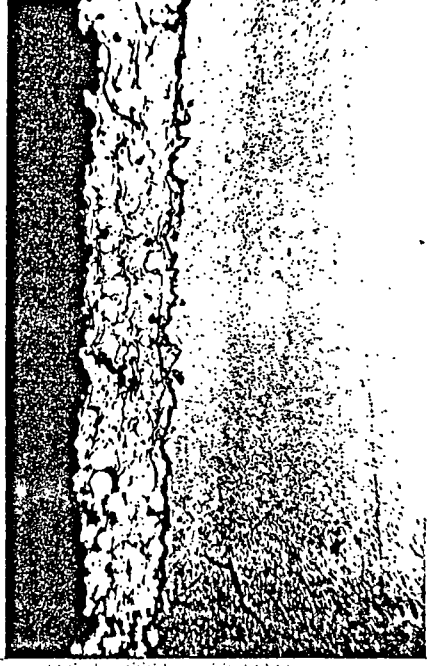


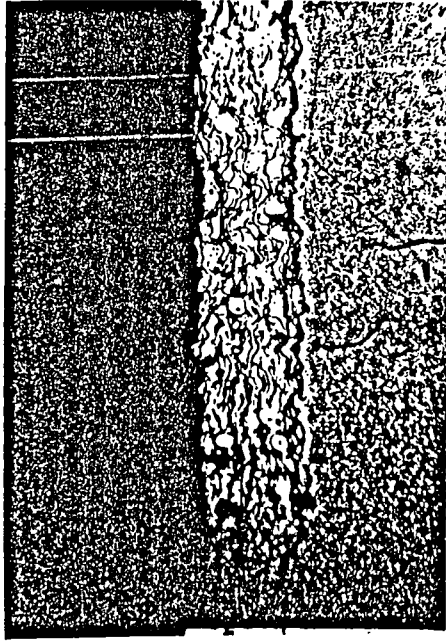
Fig 6.7(a) Typical waveforms after transmission through steel bars which had been plasma sprayed with a cast iron based material. An ablation laser source was used with an EMAT detector.



(iii)



(iv)



(i) (ii)

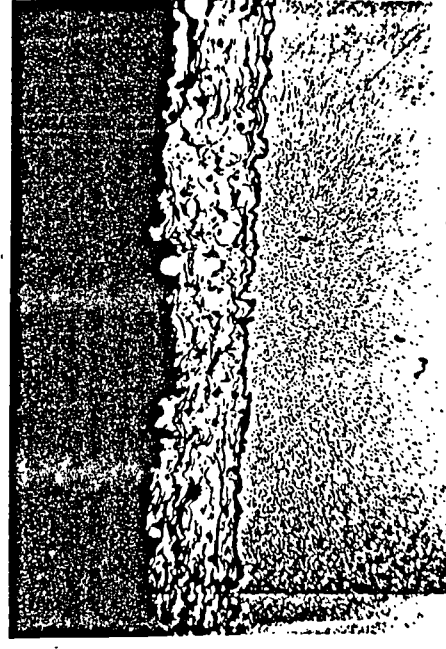


Fig 6.7(b) Micrographs of the samples used in (a), magnification of x75.



(iii) (iv)



(i) (ii)



Fig 6.7(c) Micrographs of the samples used in (a), magnification of x1200.

(iii) Carbon-fibre Composite Samples.

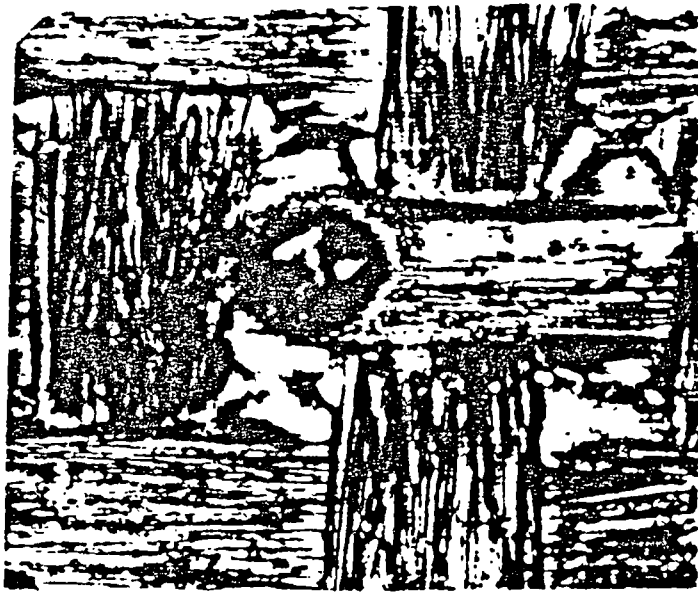
A lower power density was required to form a plasma at the surface of the carbon-fibre composite than for aluminium. To assess the damage caused by laser irradiation a piece of carbon fibre composite was subjected to pulses from the laser operating over a range of conditions followed by visual examination. For this inspection the required surface was ground and polished and the irradiated areas were examined using an optical microscope at a magnification of x75. The damage caused by a non-Q-switched pulse is shown in fig 6.8a and can be compared with that caused when the laser is Q-switched, fig 6.8b. The widths and depths of the damage for the various laser conditions are listed in Table 6.1. It can be seen that the non-Q-switched pulses produced damage through the surface resin and into the fibres to a depth of approximately half a ply. Q-switching the laser output, and hence reducing its duration, confined the damage to the surface resin with no further penetration into the laminate. This is the region of interest for ultrasonic generation. To further reduce the power density the surface was confined by a transparent overlay, (Fairand and Clauer; 1979). Silicon resin was used as the constraining medium hence giving a buried source which enabled power densities of less than  $5\text{MWcm}^{-2}$  to be used to produce a strong longitudinal lobe normal to the surface.

The conductivity of graphite is about 500 times less than that of aluminium. It has a low resistivity for a



Sectioned View

Not Q-S, 25mJ, f=5cms ~x75

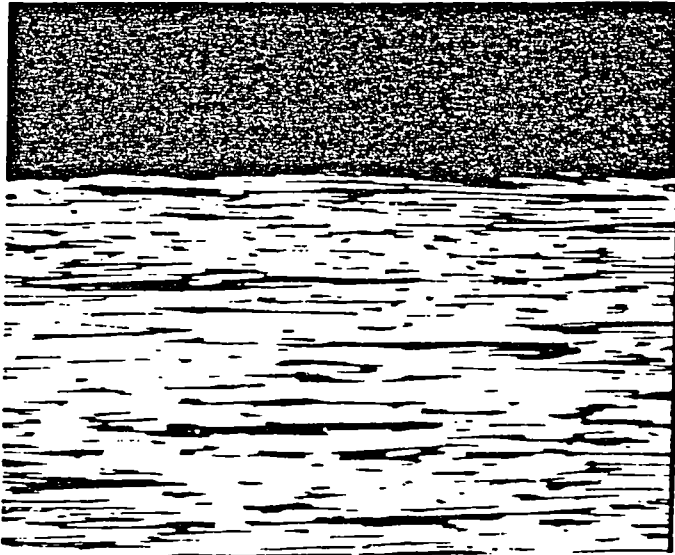


Plan View

Not Q-S, 25mJ, f=5cms. ~x 75

Fig 6.8 Micrographs of laser damage caused to carbon fibre composite samples.

(a) Non-Q-switched pulse.



Sectioned View

Q-S, 20mJ, f=5cms ~x75



Plan View

Q-S, 20mJ, f=5cms. ~x75

Fig 6.8 Micrographs of laser damage caused to carbon fibre composite samples.  
(b) Q-switched pulse.

Q SWITCH	LASER	FOCUSING	SURFACE	SECTION VIEW DAMAGE	
	ENERGY mJ	LENS cm	DIAMETER mmxmm	WIDTH mm	DEPTH mm
NO	25	5	.21x.24	0.36	0.066
NO	25	10	.37x.27	0.6	0.05
NO	25	25	1.0x1.0	0.87	0.02
YES	20	25	1.3x1.5	NSD	NSD
YES	20	10	.8x.6	NSD	NSD
YES	20	5	.56x.51	NSD	NSD

NSD = No. Significant Damage.

Damage dimensions measured to  $\pm 20\%$

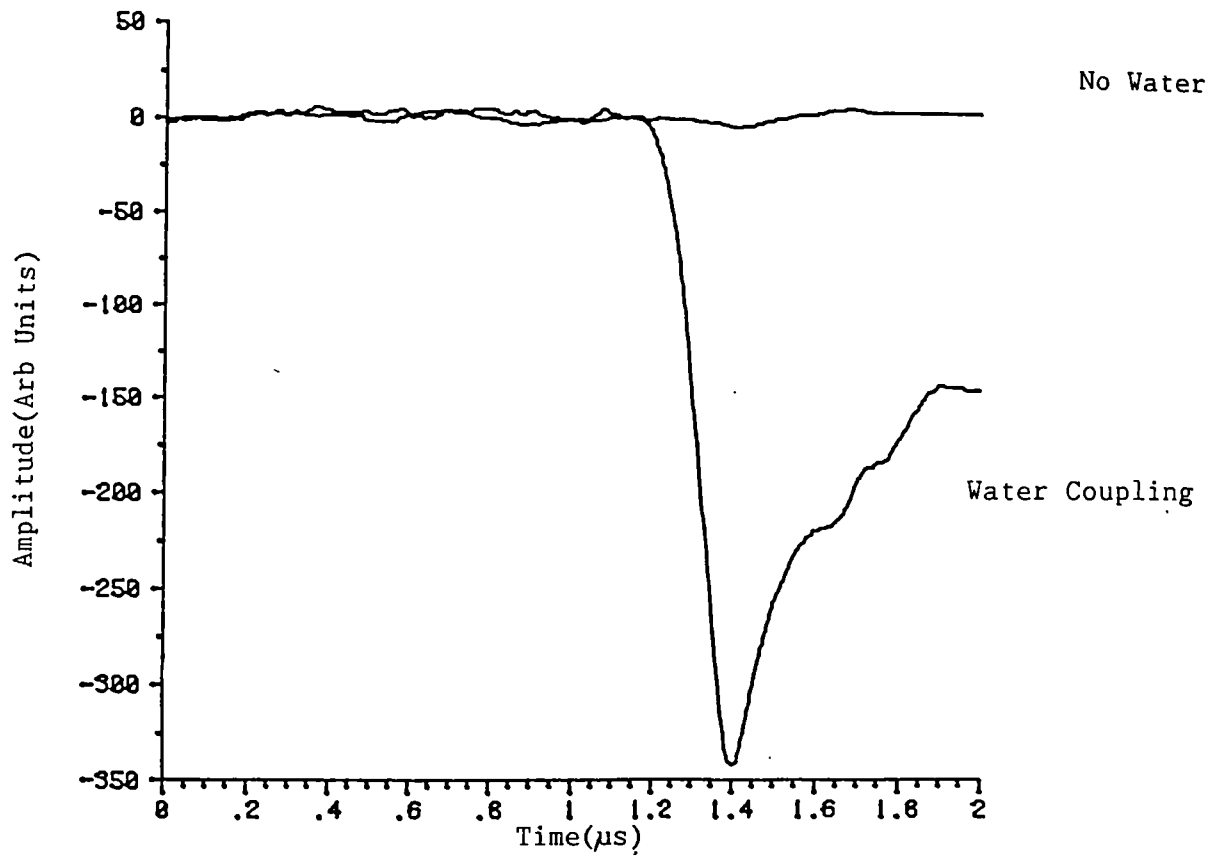
Damage Caused by Irradiating a Carbon-fibre Composite

Sample with Pulses from a Nd:YAG Laser.

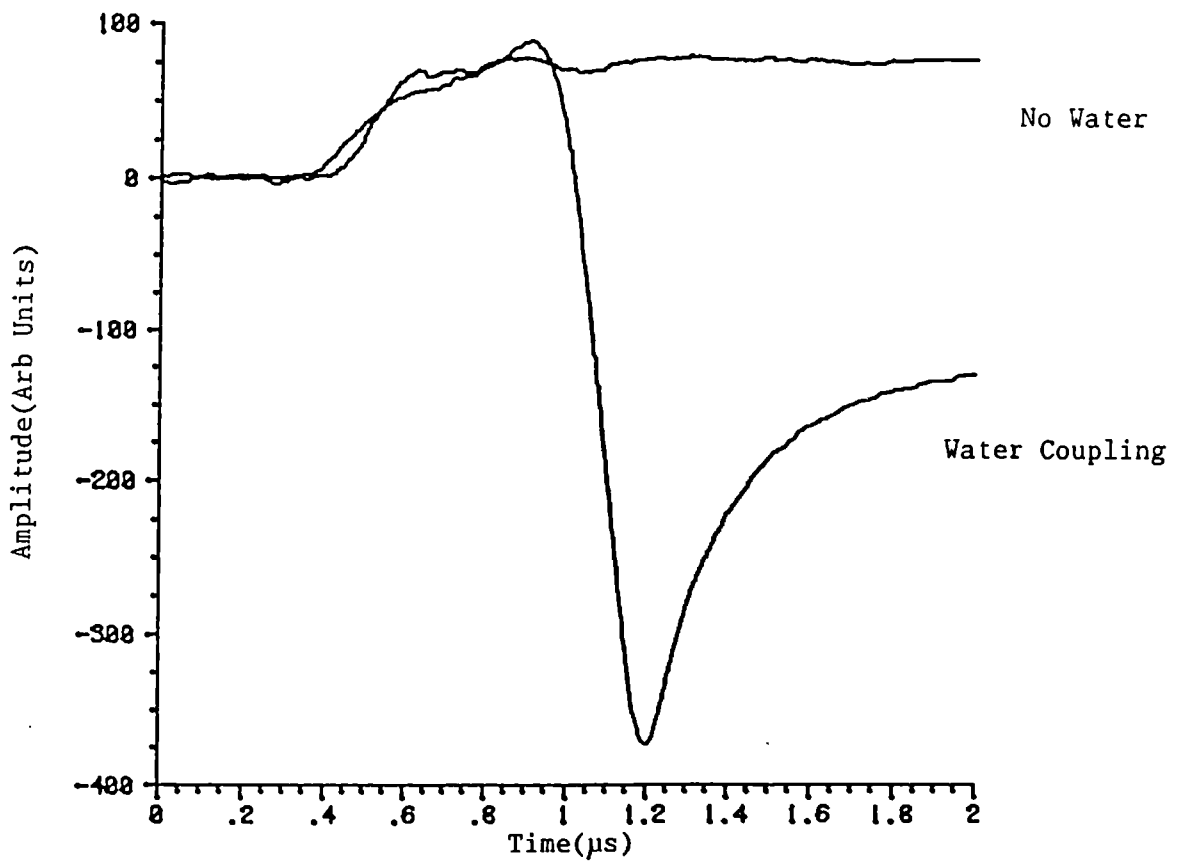
TABLE 6.1

non-metal,  $1375\mu\text{ohm cm}$ , although the sample would not support sufficiently large eddy currents to be used with an EMAT. This may have been due to the nature of the samples construction, i.e. parallel strands of graphite fibre separated by an insulating resin. However by placing the EMAT coil in direct contact with the sample the arrival of acoustic pulses caused movement of the coil in a magnetic field and hence produced a detectable signal. Due to wear problems it was not practical to place the coil and sample in direct contact during scanning. It was found however that a layer of liquid placed between the coil and sample would couple acoustic energy across the gap. This effect has previously been noted by Filipczynski, (1966), who measured ultrasonic intensities in non-conducting liquids using a moving coil receiver located in the gap of a permanent magnet. The whole assembly being immersed in the liquid under test.

Fig 6.9a shows waveforms detected on epicentre of a 2mm thick section of carbon fibre composite by the EMAT held  $\sim 1\text{mm}$  below the sample surface, in both the presence and absence of a film of water between the sample and detection coil. The signals were fed through a high input impedance Harwell amplifier before capture. Again the sample surface was modified so that a strong, normal incidence, longitudinal signal was produced by the laser. It is seen that when no couplant was used then no significant signal was detected. In the presence of coupling fluid a pulse arrived after approximately  $1.2\mu\text{s}$  which is thought to



(a)

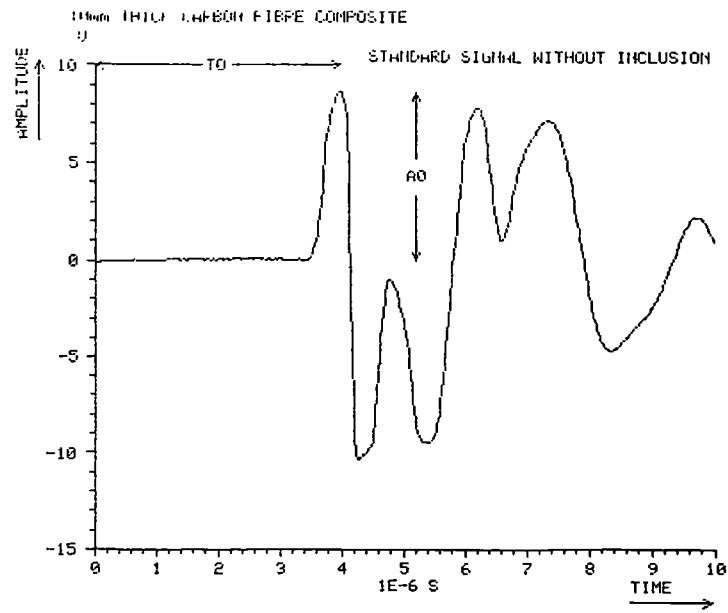


(b)

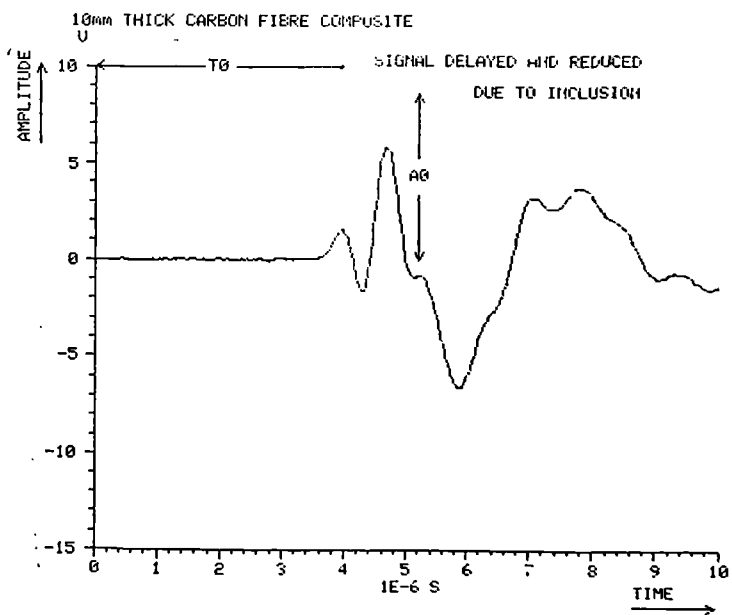
Fig 6.9 Waveforms detected at epicentre of a buried source by an EMAT in both the presence and absence of a coupling water film.  
 (a) 2mm thick carbon fibre composite sample.  
 (b) 2mm thick duraluminium sample.

be due to a longitudinal pulse coupling energy to the liquid which subsequently moved the coil held in a magnetic field. Further evidence of this effect is given in figures 6.9b where similar waveforms are shown for the case of a 2mm thick dural plate. Here a signal was detected after  $0.4\mu\text{s}$  due to Lorentz force interaction irrespective of whether coupling was present or not. When a coupling film was introduced a second, larger, signal arrived after approximately  $1\mu\text{s}$ . The increase in time of  $\sim 0.6\mu\text{s}$  gives a propagation distance in water of  $\sim 0.8\text{mm}$ , in agreement with the estimated sample to transducer distance of  $(1\pm 0.3)\text{mm}$ .

Fig 6.10a shows a waveform from an elastic pulse which propagated through 10mm of carbon fibre composite. Detection was by the water coupled EMAT device. Moving the x-y table so as to position the detector below an inclusion again delayed and reduced the longitudinal arrival, fig 6.10b. The relative time change was less than for the dural test sample due to both the increased acoustic path length caused by the liquid and to the direct transmission of some energy through the ptfе as well as diffraction around it and possibly forward scattering from the fibres. The sample was scanned in a 51 by 36 array, the results of which are shown in fig 6.11. Two time files are compared in figures 6.11a and 6.11b. The former was produced when detecting the arrival time of signals of amplitude  $0.9A_0$ . Although all six inclusions were detected this threshold was too high, resulting in no signal being detected from some defect free regions. The threshold was lowered to

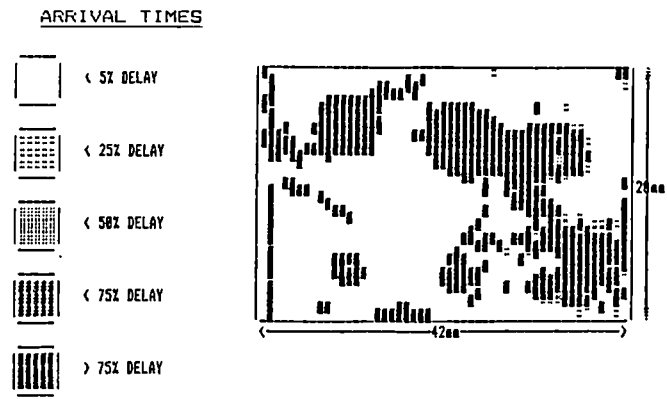


(a)

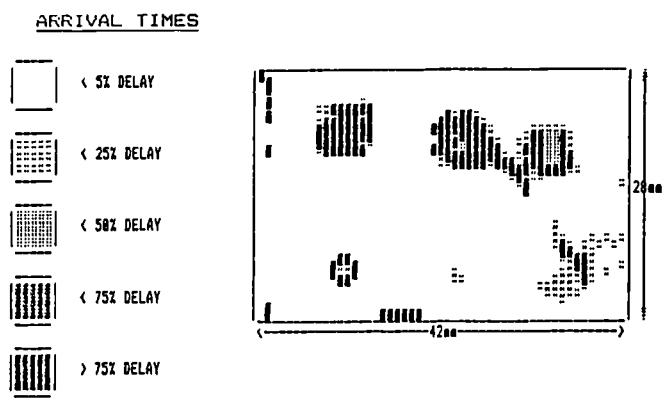


(b)

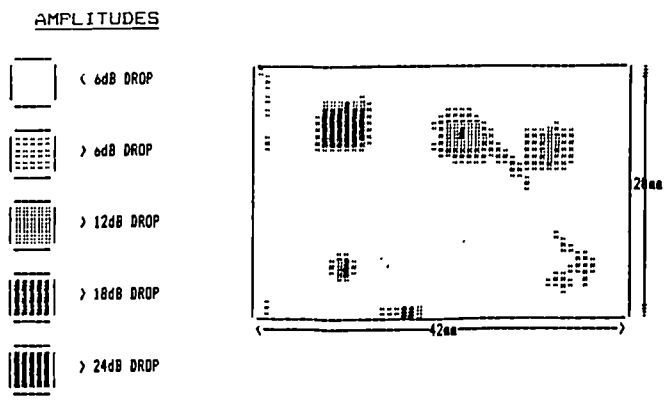
Fig 6.10 Water coupled EMAT used to detect signals from a buried source, (i.e. the incident laser energy focused to a point on the sample covered with a layer of resin).  
 (a) No inclusion.  
 (b) Inclusion.



(a)



(b)



(c)

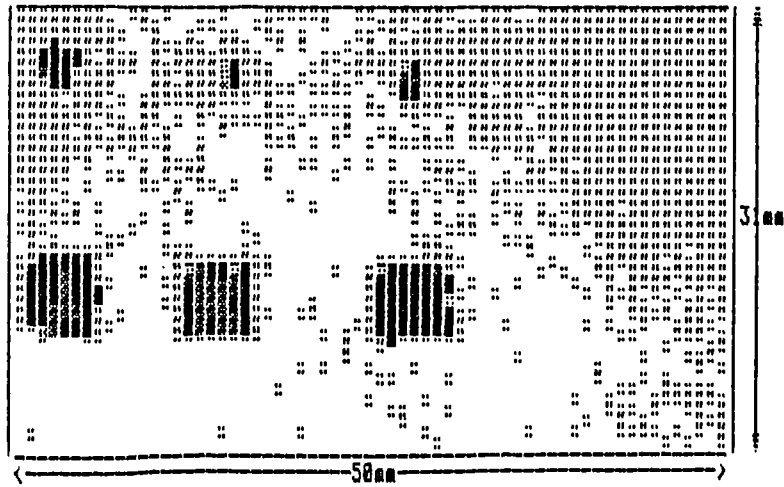
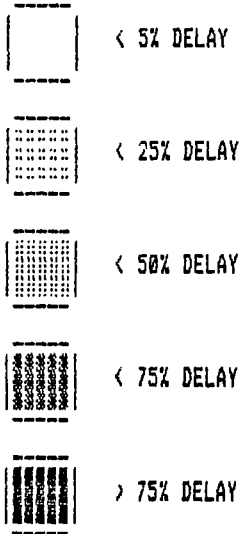
Fig 6.11 51 by 36 point scan of a 10mm thick carbon fibre composite sample. Buried source, water coupled EMAT detector on epicentre.  
 (a) Detection of arrival time of signal amplitude  $0.9A_0$ .  
 (b) Detection of arrival time of signal  $0.5A_0$ .  
 (c) Measurements of the amplitudes at time  $T_0$ .

$0.5A_0$  for the file of fig 6.11b which has adequate resolution of all defects. This file compares very well with that which uses the amplitudes of signals at time  $T_0$ , (about  $4\mu s$  here), as the discriminator, fig 6.11c. All three large defects and two of the smaller ones are highlighted in fig 6.11c. Further experiments confirmed that a threshold value of  $0.5A_0$  was suitable for time of flight measurements.

The resolution of the inclusions increased as the sample thickness decreased given that the source size and scanning density were kept constant. This was mainly due to the relative increase in size of the shadow zone for thin samples, (see fig 4.12a). The results from a scan of the 4mm thick section are shown in fig 6.12. The source and detector were the same as before but the density of points was increased slightly from 1.56 to 1.67 points/mm<sup>2</sup>. There was some slight noise detected on the time of flight file, fig 6.12a, with the signal through a number of regions being delayed by between 5 and 25%. There were however six areas where the delay was over 75% giving greater contrast to the defect regions. All of these regions show a drop of at least 18dB on standard signal from the amplitudes file, fig 6.12b, with background noise not showing so strongly on this scale.

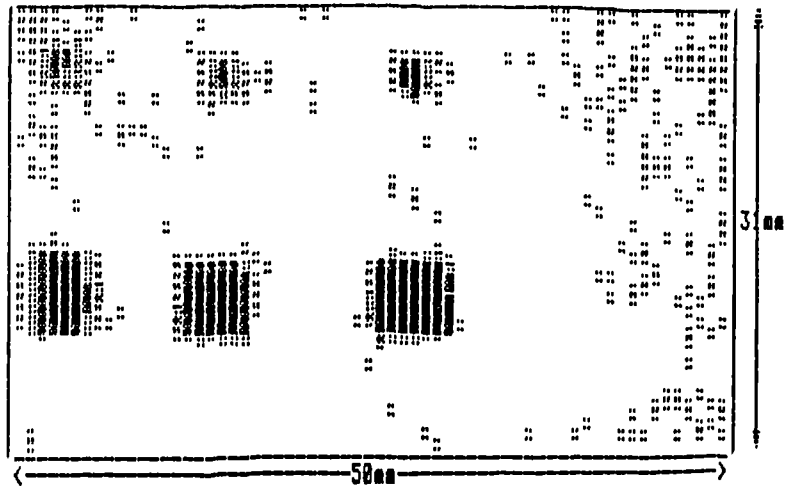
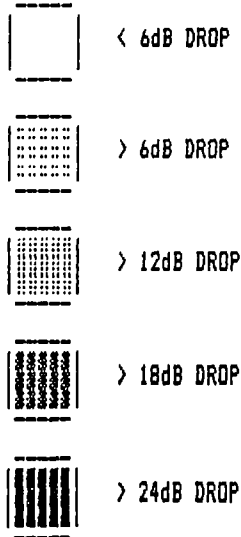
Two scans were performed on the thinnest section of carbon fibre composite material. Firstly to locate all of the inclusions the 1mm thick section was scanned using a density of about 1.75 points/mm<sup>2</sup>. All six inclusions were located from the amplitude file, fig 6.13a, however the

ARRIVAL TIMES



(a)

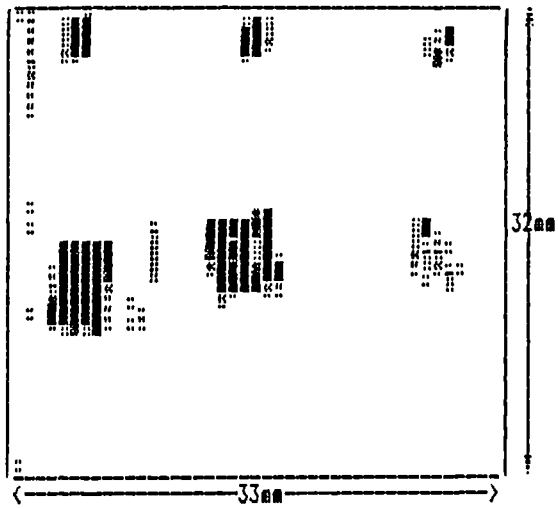
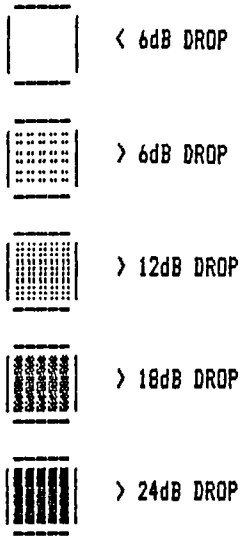
AMPLITUDES



(b)

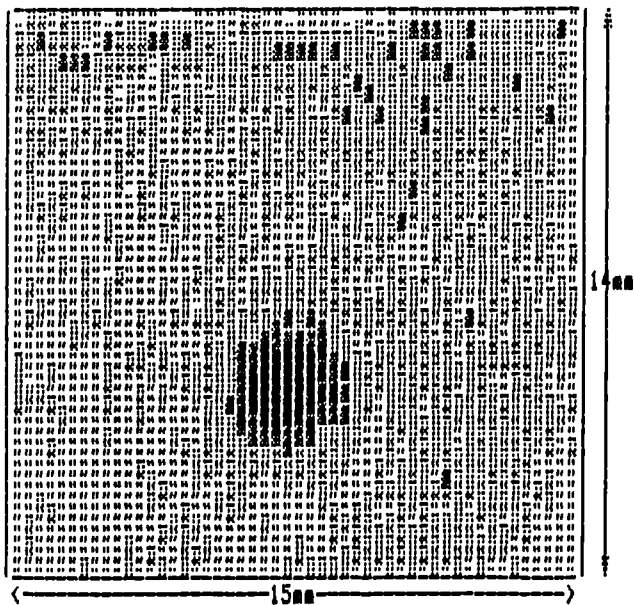
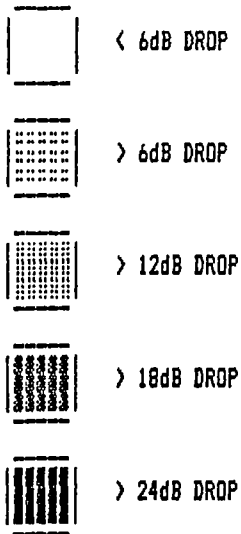
Fig 6.12 63 by 41 point scan of a 4mm thick carbon fibre composite sample. Buried source, water coupled EMAT detector on epicentre.  
 (a) Detection of arrival time of signal amplitude  $0.5A_0$ .  
 (b) Measurements of the amplitudes at time  $T_0$

AMPLITUDES



(a)

AMPLITUDES



(b)

Fig 6.13 Scan of a 1mm thick carbon fibre composite sample using a buried source. Measurements of amplitudes at time  $T_0$ .

(a) 43 by 43 point scan using a water coupled EMAT on epicentre.

(b) Detailed 50 by 52 point scan of a single inclusion using a PZT detector on epicentre.

defect shown towards the bottom right of this scan did not show as great an amplitude drop as was expected. It was unfortunately not possible to section the material after inspection to check if this was due to difficulty in inserting an inclusion in such a thin sample. For the second experiment on this sample the area around the middle defect shown near the top of fig 6.13a was examined in greater detail. A buried source was again used for generation but detection was done by the damped PZT probe, of diameter 2.5mm, described in Chapter 4. The scanning density was increased to 12.4 points/mm<sup>2</sup> enabling an estimation of the defect size to be made. From the C-scan representation of the amplitudes detected at T<sub>0</sub>, fig 6.13b, the shadow zone, (24dB drop), caused by the inclusion was measured to be (2.8±0.3)mm by (3.0±0.5)mm which was as expected.

#### 6.4/ Single Sided Non-contact Inspection.

The second laminar flaw detection method developed required access to only one face of the sample. The stabilised Michelson interferometer developed by McKie, (1985), was used as detector on the polished face of the aluminium sample shown in fig 6.1b. This was held on a kinematic mount, adjustable through two micrometers, which in turn was placed on the x-y table. The sample, although polished, was not optically flat which caused the alignment of the interferometer to be affected with movement of the table. To achieve sufficient sensitivity it was necessary to correct for this using the micrometers, each time the sample

was moved. This was very time consuming and prevented the collection of large amounts of data.

The unfocused spot from the Nd:YAG was incident  $\sim 3.5\text{mm}$  to the left of the interferometer probe beam. A 10 by 15 point scan of the upper left corner of the sample was made, a selection of the waveforms obtained as the edge of the defect was encountered is shown in fig 6.14. The first arrival would be expected to be a surface skimming longitudinal pulse, after about  $0.6\mu\text{s}$ , followed by a pulse travelling with or close to the Rayleigh velocity. Due to the geometry used, the reflection of the compressional pulse from the bottom of the 3mm thick section should arrive around about the same time as this surface pulse, at about  $1.2\mu\text{s}$ . Peaks can be seen in fig 6.14 from waveforms collected away from the defect, near point B, at both of these times. When the sample was moved so that the laser spots were over the saw cut, point A, then the initial arrival was still after  $0.6\mu\text{s}$ , however the signal at  $1.2\mu\text{s}$  was reduced. This suggests that the peak at  $1.2\mu\text{s}$  at point B was predominantly due to a bulk acoustic pulse and not a surface constrained one. The sample is too thin to support a true Rayleigh pulse. In addition a thermoelastic source of diameter  $\sim 2.5\text{mm}$  was used which even in a semi-infinite solid would not produce a sharp Rayleigh pulse. It is difficult to distinguish separate arrivals from these signals, however they may be compared to the theoretical waveforms of Pao et al, (1979), (see Chapter 3). Over a long time scale the sample moved towards the detector with the motion being

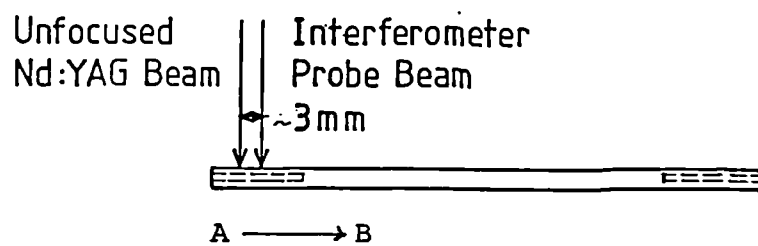
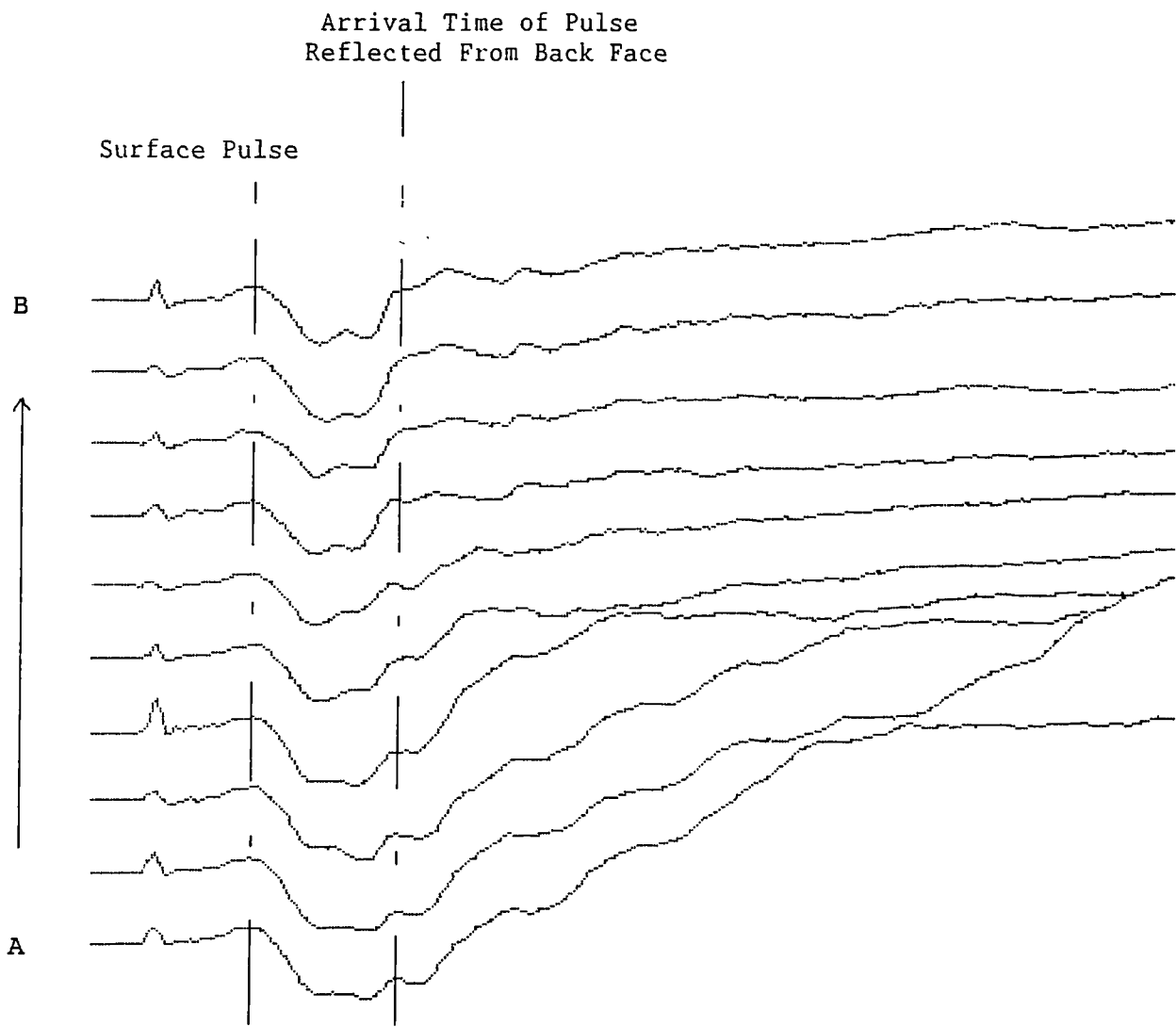
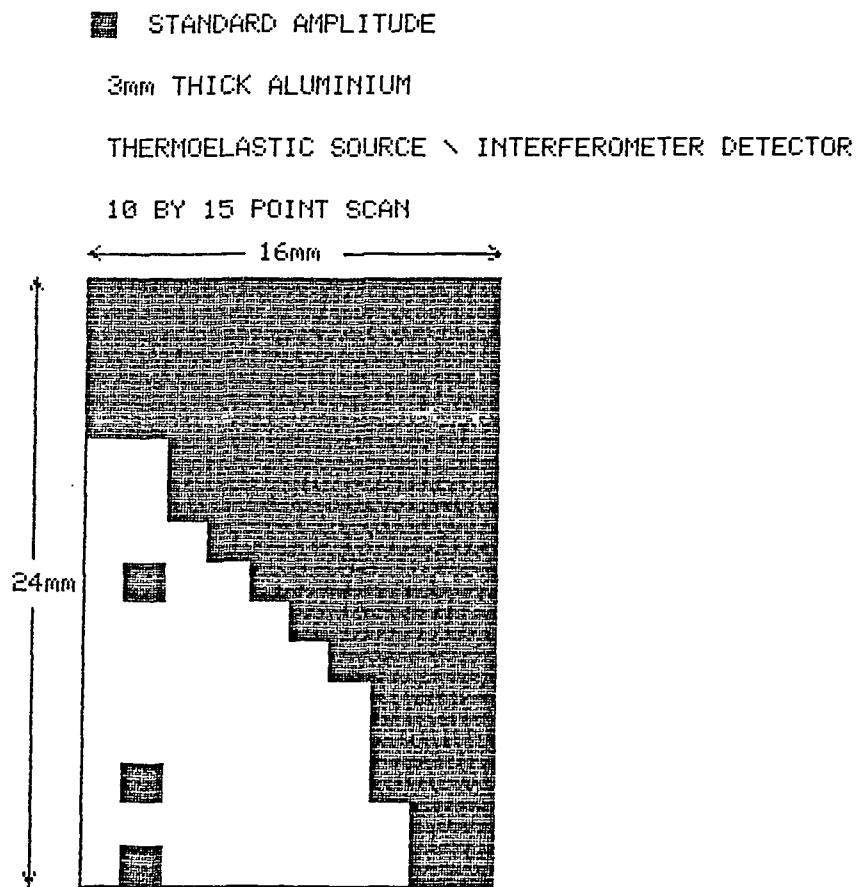


Fig 6.14 Waveforms from a single sided linear scan of the sample of fig 6.1(b). Unfocused Nd:YAG spot incident  $\sim 3.5$ mm to the left of the interferometer probe beam. Arbitrary vertical scale, 5 $\mu$ s full horizontal scale.

greater over the saw cut although the difference between the two regions was most prominent at about  $1.2\mu\text{s}$ .

Since the sample surface caused the interferometer sensitivity to fluctuate it would not have been satisfactory to simply measure the amplitude at this, (or any other), time. However, comparing the signal at  $1.2\mu\text{s}$  to that at  $0.6\mu\text{s}$  would to some extent compensate for this. Using such a technique on the collected waveforms produced the diagram of fig 6.15, the light area here representing the region where the signal at  $1.2\mu\text{s}$  was outwith  $4\text{mV}$  of that at  $0.6\mu\text{s}$ . The edge of the saw cut was reasonably well resolved given the number of points scanned.

A second region, part of the other saw cut, was also examined using the same set up. It was instantly obvious from the waveforms collected as to where the edge of the flaw lay, fig 6.16. When the laser spots were both fully over either the 3mm section or the saw cut then the signals were similar to those of the previous experiment. However when only the Nd:YAG spot was over the 3mm thick section then much of the energy transmitted to the bulk was prevented from reaching the detector via reflections from the back face by the saw cut. This caused a large dip in the signal observed by the interferometer with the largest positive signal being from the surface longitudinal pulse. The direct and bulk reflected longitudinal pulses were compared as before to give figure 6.17. Again the edge of the defect was picked out well and the number of spurious points was low considering the fluctuating sensitivity of



Region A of fig 6.1(b)

Fig 6.15 Single sided, two-dimensional, remote scan of a duraluminium sample with artificial defects.

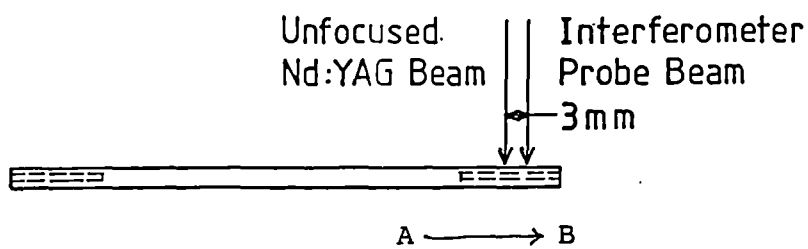
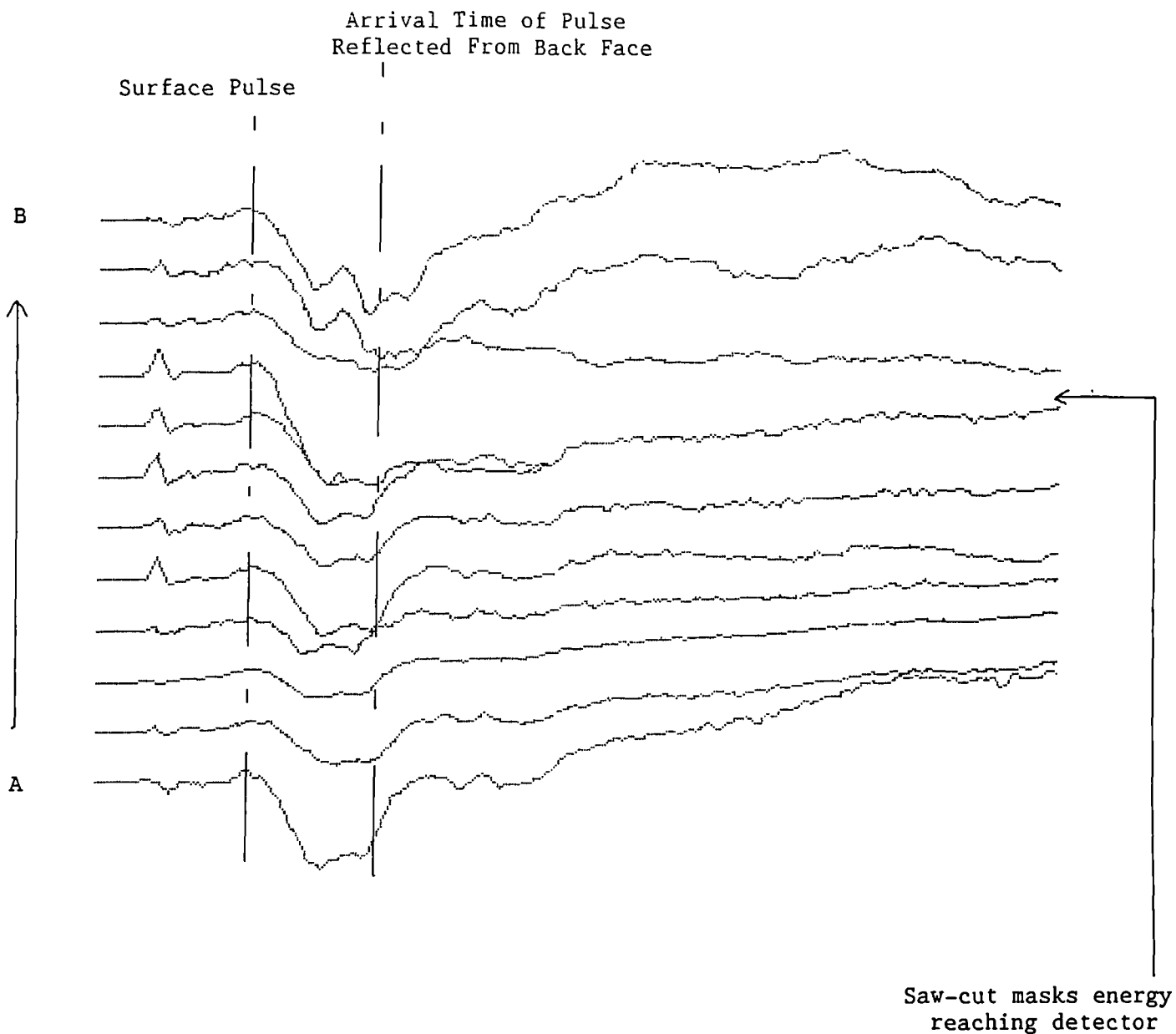


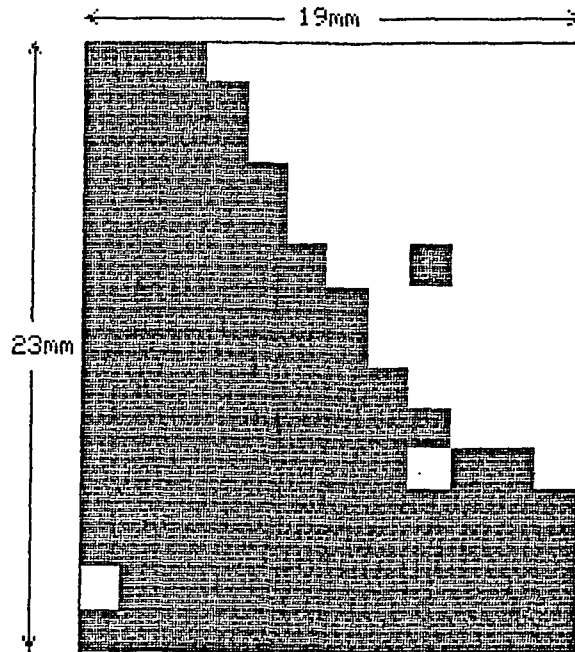
Fig 6.16 Waveforms from a single sided linear scan of the sample of fig 6.1(b). Unfocused Nd:YAG spot incident 3.5mm to the left of the interferometer probe beam. Arbitrary vertical scale, 5 $\mu$ s full horizontal scale.

■ STANDARD AMPLITUDE

3mm THICK ALUMINIUM

THERMOELASTIC SOURCE \ INTERFEROMETER DETECTOR

12 BY 15 POINT SCAN



Region B of fig 6.1(b)

Fig 6.17 Single sided, two-dimensional, remote scan of a duraluminium sample with artificial defects.

the detection system due to the samples variable reflectivity.

#### 6.5/ Discussion.

These latter results show promise for a future fully remote laser based NDE system. There are major disadvantages however in the optical quality of the sample surface required and also in the adjustment of alignment and hence the time necessary to do such scans. It would be possible to adjust the alignment automatically by using stepping motors to move the kinematic mount after each shift of the x-y table. In such a system the background, low frequency, noise from the interferometer could be observed at each position and used to adjust the sample to achieve a set sensitivity before switching on the low frequency stabilisation circuit then collecting a waveform. This compensation could be controlled by the computer already used in the system. Despite these problems it has been demonstrated that single sided laser ultrasonic inspection can locate subsurface defects. This is the first fully remote laser\ultrasound system used for a two dimensional inspection of a defect.

The first, through transmission, system described is perhaps more practical although requiring access to two sample faces. Initial measurements on the aluminium sample enabled two flaw detection techniques to be developed which were then used to locate saw cuts at the mid-thickness of the 3mm thick sample. It was demonstrated that a range of

incident power densities could be used, (down to less than  $6\text{MWcm}^{-2}$ ), with resolution increasing with decreasing source size. These two techniques were then applied to a carbon fibre composite sample which contained inclusions of ptfе.

It was firstly shown that pulses from the laser caused no significant surface damage when operating in the regime of interest for ultrasonic generation. Three inclusions of dimension 3 by 3mm and three of 6 by 6mm were detected in sections of composite varying from 10 to 1 mm thickness. The resolution of these defects improved with decreasing thickness which suggests that the method may be suitable for this material since it is normally used as a thin over-skin. A detailed scan was done on the thinnest section and resolved one of the smaller inclusions to within 0.5mm. The diameter of the PZT probe, (2.5mm), used for detection was a limiting factor here. Unfortunately the material did not easily lend itself to non contact detection, however an EMAT type device was developed where the acoustic energy was transmitted through a water layer to the detection coil.

Plasma sprayed samples were also examined, although lack of information of actual defects made interpretation of the waveforms impossible.

CHAPTER 7.

FLEXURAL RESONANCE MEASUREMENTS OF DISKS.

7.1/ Introduction.

Poisson calculated axially symmetric resonant frequencies of a disk with a traction free boundary by using a two-dimensional theory in 1829. Since then much theoretical work has been done by many authors on the resonances of elastic bodies under various boundary conditions, (see for example Leissa 1969). There have however been few reported cases of experimental measurements of resonant frequencies in plates. This is perhaps due to problems of exciting the specimen and recording its natural vibration frequency non-contactingly so as not to disturb the vibrating system.

Aprahamian and Evansen, (1970), excited a 1/16" thick aluminium sheet to resonance using a piezoelectric transducer bonded to the rear surface of the sample. The 8" by 10" sheet was clamped in a rectangular frame and as many as 110 vibration modes, up to 20kHz, were observed remotely using holographic interferometry. A laser holographic method was also used by Eastep and Hemmig, (1982), to obtain the natural frequencies and mode shapes of a 7"

diameter circular plate under various boundary conditions. A low-carbon steel sheet of thickness 0.031" was clamped between two 1/2" thick steel plates with a 7" diameter circular cutout. The disk region was acoustically excited, although it was not made clear what the driving mechanism and coupling medium were. By varying the clamping at the boundary the natural frequencies of the first six resonance modes were obtained. For the fully clamped case the highest mode reported was the fifth having a frequency of 831kHz.

Reismann et al, (1980), monitored noncontactively the motion of a clamped disk. Stresses were set up by irradiating the sample with pulses from a Nd:glass laser which caused the sample to resonate at about 100Hz. The displacements were monitored using a capacitance device which did not perturb the oscillating system. The sample in this case was a stainless steel sheet of mass 260g with thickness  $5 \times 10^{-2}$  cm and radius 11.45cm. Due to the sample size laser energies of approximately 2J were necessary.

For all of the above cases the sample geometry was such that the results can be explained satisfactorily using classical two-dimensional plate theory. Aindow et al, (1984), however investigated the resonances of thicker disk like samples, (radii 3.2mm with thicknesses ranging from 1 to 5mm), and found that agreement with the above mentioned theory was limited. These samples were flat bottomed holes milled into blocks of aluminium alloy, fig 7.1a, which were excited to resonance by  $(33 \pm 2)$  mJ pulses from a Q-switched Nd:YAG laser. An interferometric device monitored the

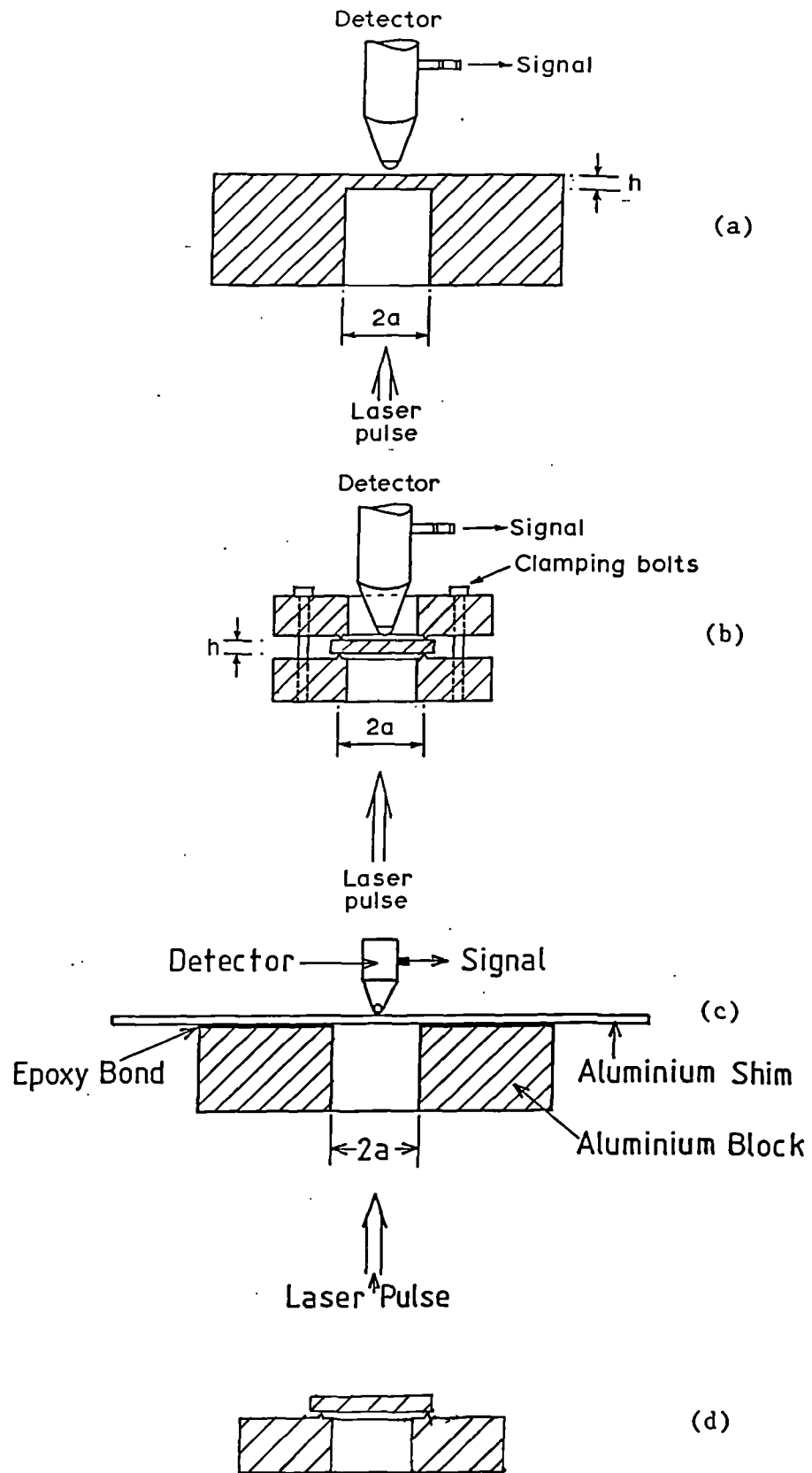


Fig 7.1 Schematic diagrams of samples.

- (a) Flat-bottomed holes milled into duraluminium blocks.
- (b) Fully clamped aluminium shims.
- (c) Duraluminium shims bonded over drilled duraluminium blocks.
- (d) Sketch representing a sample having simply supported boundary conditions.

resultant displacements. The sample geometries were chosen in order to simulate practical sized flaws in metals. Although naturally occurring defects in components are generally of an irregular and complex shape, an initial evaluation of a non-destructive testing technique is often carried out on artificial standard flaws. Flat-bottomed holes may be used to approximate for laminar defects in rolled sheet metal or for cavitation in castings, (Krautkramer and Krautkramer 1983). Aindow et al proposed using resonance measurements together with thickness estimations obtained using ring-around ultrasonic pulses to determine the depth,  $h$ , and diameter,  $2a$ , of the flat bottomed holes. The sample geometry led to far higher resonant frequencies, ( $>150\text{kHz}$ ), and the agreement with classical plate theory was found to decrease with decreasing values of the aspect ratio,  $a/h$ . It was suggested that this discrepancy between experiment and theory may have been due to the clamping of the flat bottomed holes not fully satisfying the assumed boundary conditions for a clamped disk.

Cielo et al, (1985), also used a spot-heating thermoelastic technique to examine the dependence of flexural resonant frequency on the diameter of plates. Again agreement with theory improved at large  $a/h$  ratios. Shear deformation and rotatory inertia effects, believed to be important, were not taken into account by the authors in the analysis of the data. In a later paper however the same research group, (Rousset et al, 1986), used numerical

simulations for thick plates with both clamped, fig 7.1b, and simply supported edges, fig 7.1d, which agreed with the behaviour previously noted by Celep, (1980). Due to inadequate clamping at the boundary of their samples experimental measurements were found to lie mid-way between the simulations for the two sets of boundary conditions.

In the following section the classical theory of thin plate motion is used to calculate the resonant frequencies of disks. The effects that shear deformation and rotatory inertia have on the vibrations of thicker disks is then calculated in sections 7.3 and 7.4 for three sets of boundary conditions. These theoretical expressions are then evaluated and compared with experiments described in later sections.

## 7.2/ Classical Two-dimensional Theory of Flexural Motions of Elastic Plates, (Thin Plate Theory).

The resonant frequency of a membrane will depend upon its geometry, elastic properties and on the applied tension. In a thin plate however the restoring force is due solely to the stiffness of the diaphragm, hence its resonant frequency depends only on the elastic properties of the material and its geometry along with the appropriate boundary conditions.

The equation of motion, based on Poissons treatment, given by Morse, (1936), can be written as, (Kinsler and Frey 1961, Nowacki 1963).

$$\frac{\delta^2 W}{\delta t^2} = - \frac{\kappa^2 E}{\rho(1-\nu^2)} \nabla_r^4 W \quad (7.1)$$

where  $\rho$  =density,  $\nu$  =Poissons ratio,  $E$ =Youngs modulus,  
 $\kappa$  =surface radius of gyration =  $\frac{h}{\sqrt{12}}$ ,  $h$ =plate thickness.

Assuming periodic vibrations of the form

$$w = W(r, \theta) e^{ipt} \quad (7.2)$$

we obtain

$$\nabla_r^4 W = \frac{\rho(1-\nu^2) p^2 W}{\kappa^2 E} = K^4 W \quad (7.3)$$

where

$$K^4 = \frac{p^2 \rho(1-\nu^2)}{\kappa^2 E} \quad (7.4)$$

Hence we can write (7.3) as

$$(\nabla_r^4 - K^4) W = 0 \quad (7.5)$$

The above equation has two solutions which yield the following admissible solution for a full circular plate,

$$W(r, \theta) = \frac{\sin(m\theta)}{\cos} [AJ_m(Kr) + BI_m(Kr)] \quad (7.6)$$

where A and B are arbitrary constants.  $J_m(x)$  is the Bessel function of the first kind of order  $m$  and  $I_m(x)$  is the modified Bessel function of the first kind of order  $m$ .

For a fully clamped disk, of radius  $a$ , there will be no displacement and no gradient at the edge. Hence

$$W_{r=a} = 0 \quad \text{and} \quad \left( \frac{\delta W}{\delta r} \right)_{r=a} = 0 \quad (7.7)$$

Putting the boundary conditions into (7.6) yields

$$\frac{J_{m-1}(Ka) - J_{m+1}(Ka)}{J_m(Ka)} = \frac{I_{m-1}(Ka) + I_{m+1}(Ka)}{I_m(Ka)}$$

which for  $m=0$  gives

$$\frac{J_0(Ka)}{J_1(Ka)} = - \frac{I_0(Ka)}{I_1(Ka)} \quad (7.8)$$

This equation was solved on our MS4101 computer and was found to be in agreement with the solutions of Nowacki, (1963), who used tables of Bessel functions. The equation is satisfied when

$$Ka = 3.20, 6.30, 9.44, 12.57 \dots \quad (7.9)$$

or approximately by  $Ka = n\pi$  ;  $n=1,2,3,4,\dots$  with approximation better for large  $n$ .

From (7.4) and substituting  $\kappa = \frac{h}{\sqrt{12}}$  and  $K = 3.2/a$  for the fundamental mode we obtain

$$y_{10} = \frac{p_{10}}{2\pi} \approx 0.47 \frac{h}{a^2} \sqrt{\frac{E}{\rho(1-\nu^2)}} \quad (7.10)$$

and since from (7.4)  $p \propto K^2$ , it can be seen from (7.9) that

$$y_{20} = \left(\frac{6.30}{3.20}\right)^2 y_{10} \approx 3.88 y_{10} \quad (7.11)$$

Hence Poissons treatment leads to the relationship

$$y_{nm} \propto \frac{h}{a^2}$$

### 7.3/ Effects of Shear Deformation and Rotatory Inertia, (Thick Plate Theory).

According to equation (7.1) the wave velocity of one-dimensional waves is inversely proportional to the wavelength. This is true only for waves which are long in comparison with the plate thickness (Rayleigh 1889, Lamb 1917). As the wavelength diminishes, the velocity in the three-dimensional theory has as its upper limit the velocity of Rayleigh surface waves. Classical plate theory

therefore cannot be expected to give good results for sharp transients, for the frequencies of modes of vibration of higher order, or for the frequencies of vibration of acoustically thick plates.

Correction factors have to be introduced to take into account the effects of shear deformation and rotatory inertia. These terms are analagous to the factors introduced in the classical one-dimensional theory of flexural motions of elastic bars leading to the Bernoulli-Euler equations. Correction terms were supplied firstly by Rayleigh, (1926), (for rotatory inertia), and then by Timoshenko (1937), who included the effect of transverse shear deformation. The analogous equations of motion to Timoshenkos bar equation for the case of plates have been given by Uflyand (1948) with a corresponding theory of plate equilibrium given by Hencky (1947). It has been shown however that a more comprehensive two-dimensional theory of flexural motions of plates may be deduced directly from the three-dimensional equations of elasticity, Mindlin (1951).

Since in the present case we are interested in the fundamental vibration mode of a thick plate, we can simplify the problem by considering only the axially symmetric case. The treatment of Deresiewicz and Mindlin, (1955), for a disk with a free edge has been followed and extended for two more sets of boundary conditions.

The plate stress equations of motion (7.12) and the plate stress-displacement relations in polar co-ordinates, (7.13), were given by Deresiewicz and Mindlin (1955) for the

axially-symmetric case. These are simplified forms of the general equations previously given by Mindlin and Deresiewicz (1954).

$$\frac{\delta M_r}{\delta r} + \frac{M_r - M_\theta}{r} - Q_r = \frac{\rho h^3}{12} \frac{\delta^2 \psi}{\delta t^2}$$

(7.12)

$$\frac{\delta Q_r}{\delta r} + \frac{Q_r}{r} = \rho h \frac{\delta^2 w}{\delta t^2}$$

$$M_r = D \left( \frac{\delta \psi}{\delta r} + \frac{\nu}{r} \psi \right)$$

$$M_\theta = D \left( \nu \frac{\delta \psi}{\delta r} + \frac{\psi}{r} \right)$$

$$Q_r = \kappa^2 \mu h \left( \psi + \frac{\delta w}{\delta r} \right) \quad (7.13)$$

$$M_{r\theta} = 0$$

$$Q_\theta = 0$$

where the plate modulus  $D = \frac{Eh^3}{12(1-\nu^2)}$  and  $\kappa^2$  is given from the solution to the Rayleigh equation,

$$4\sqrt{(1-\alpha\kappa^2)(1-\kappa^2)} = (2-\kappa^2)^2, \quad 0 < \kappa < 1$$

where  $\alpha = \frac{(1-2\nu)}{2(1-\nu)}$ . For  $\nu = 0.34$ ;  $\kappa^2 = 0.87$ .

Since this is the axially symmetric case the

circumferential component of the displacement,  $u_\theta$ , is zero. The functions  $\psi$  and  $w$  are related to the radial and axial components of the displacement according to the approximations

$$\begin{aligned} u_r &= z\psi(r,t) \\ u_z &= w(r,t) \end{aligned} \quad (7.14)$$

The plate displacement equations of motion are generated by inserting equations (7.13) in (7.12). The time factor  $e^{ipt}$  may be omitted to obtain

$$\left( \frac{d^2}{dr^2} + \frac{1}{r} \frac{d}{dr} - \frac{1}{r^2} + \frac{\rho p^2 h^3}{12D} \right) \psi - \frac{\kappa^2 \mu h}{D} \left( \psi + \frac{dw}{dr} \right) = 0 \quad (7.15)$$

$$\left( \frac{d}{dr} + \frac{1}{r} \right) \psi + \left( \frac{d^2}{dr^2} + \frac{1}{r} \frac{d}{dr} + \frac{\rho p^2}{\kappa^2 \mu} \right) w = 0$$

The second of the above equations is differentiated once and the result is subtracted from the first to obtain an expression for  $\psi$  in terms of  $w$ , (7.16). This may then be inserted into the second of the above equations, hence uncoupling the equations and yielding an equation in  $w$  only, (7.17).

$$\psi = (R\delta_0^4 - S^{-1}) \frac{d}{dr} \left[ \frac{d^2}{dr^2} + \frac{1}{r} \frac{d}{dr} + S\delta_0^4 + S^{-1} \right] w \quad (7.16)$$

$$\left( \frac{d^2}{dr^2} + \frac{1}{r} \frac{d}{dr} + \delta_1^2 \right) \left( \frac{d^2}{dr^2} + \frac{1}{r} \frac{d}{dr} + \delta_2^2 \right) w = 0 \quad (7.17)$$

where

$$\delta_1^2, \delta_2^2 = \frac{\delta_0^4}{2} \left[ R + S \pm \sqrt{(R-S)^2 + 4\delta_0^{-4}} \right] \quad (7.18)$$

and  $\delta_0^4 = \frac{\rho h p^2}{D}$ . The rotatory inertia factor being  $R = \frac{h^2}{12}$  and the shear deformation term  $S = \frac{D}{(\kappa^2 \mu h)}$ .

Equation (7.17) may be solved for  $w$  by noting that

$$w = w_1 + w_2 \quad (7.19)$$

Mindlin, (1951), where  $w_1$  and  $w_2$  satisfy

$$\left( \frac{d^2}{dr^2} + \frac{1}{r} \frac{d}{dr} + \delta_i^2 \right) w_i = 0, \quad i = 1, 2. \quad (7.20)$$

Both of the above equations are Bessel equations of order zero. Their approximate solutions are

$$w_1 = A_1 J_0(\delta_1 r) ; \quad w_2 = A_2 J_0(\delta_2 r) \quad (7.21)$$

where  $A_1$  and  $A_2$  are arbitrary constants.

The expression for  $\psi$  in terms of  $w$ , (7.16), may be written

$$\psi = (\sigma_1 - 1) \frac{dw_1}{dr} + (\sigma_2 - 1) \frac{dw_2}{dr} \quad (7.22)$$

where  $\sigma_1, \sigma_2 = (\delta_2^2, \delta_1^2)(R(\delta_0^4 - S^{-1}))^{-1}$  (7.23)

#### 7.4/ Boundary Conditions.

It was proposed that in this thesis samples of various geometries would be examined, (described in section 7.5). It was therefore necessary to investigate three different sets of boundary conditions, these were free, simply supported and fully clamped edge. The method of obtaining the frequency equation was the same for each case and is derived here for a fully clamped disk. For the other two cases the boundary conditions and their resulting frequency equations are given at the end of this section.

The boundary conditions for clamped edges of a thick

plate are, (Epstein 1942),

$$\psi = w = 0 \quad \text{at} \quad r=a \quad (7.24a)$$

We can therefore substitute equations (7.24a) in (7.19), (7.21) and (7.22) to yield,

$$\frac{(\sigma_1 - 1) \delta_1 J_0(\delta_2 a)}{(\sigma_2 - 1) \delta_2 J_1(\delta_2 a)} = \frac{J_0(\delta_1 a)}{J_1(\delta_1 a)} \quad (7.25)$$

where

$$\frac{(\sigma_1 - 1)}{(\sigma_2 - 1)} = \frac{(1-g) + 2g \left(\frac{\bar{p}}{p}\right)^2 - \sqrt{(g-1)^2 + 4g \left(\frac{\bar{p}}{p}\right)^2}}{(1-g) + 2g \left(\frac{\bar{p}}{p}\right)^2 + \sqrt{(g-1)^2 + 4g \left(\frac{\bar{p}}{p}\right)^2}}$$

and  $g = R/S$ ,  $\bar{p}$  is the frequency of the first thickness shear mode of an infinite plate.

For the case when  $R = S = 0$ , then

$$\delta_1^2 = \delta_0^2$$

$$\delta_2^2 = -\delta_0^2$$

Equation (7.25) condenses to the solution given by classical plate theory when the effects of rotatory inertia and shear deformation are removed, (7.8).

Equation (7.25) may be rewritten in the form

$$\beta \Gamma_1 - \frac{(\sigma_1 - 1)}{(\sigma_2 - 1)} \Gamma_2 = 0 \quad (7.26a)$$

where  $\beta = \frac{\delta_2}{\delta_1}$ ;  $\gamma = \delta_1 a$ ;  $\Gamma_1 = \frac{J_0(\gamma)}{J_1(\gamma)}$ ;  $\Gamma_2 = \frac{J_0(\beta\gamma)}{J_1(\beta\gamma)}$

Since  $\delta_1$  is real for all positive values of the frequency,  $p$ , while  $\delta_2$  is real or imaginary depending on whether  $p$  is greater or less than  $\bar{p} = \frac{\pi}{h} \left(\frac{\mu}{\rho}\right)^{1/2}$ ,  $\beta$  will be real or imaginary according as  $p > \bar{p}$ . For the range  $p < \bar{p}$  we let  $\beta = i\beta_1$ , the frequency equation may be transformed to the more convenient form

$$\Gamma_1 \beta_1 + \frac{(\sigma_1 - 1)}{(\sigma_2 - 1)} G_2 = 0 \quad (7.26b)$$

where  $G_2 = \frac{I_0(\beta_1 \gamma)}{I_1(\beta_1 \gamma)}$

An explicit formula for the frequency was given by Deresiewicz and Mindlin, (1955), by means of the relation

$\beta = \frac{\delta_2}{\delta_1}$  and the expressions for  $\delta_1$  and  $\delta_2$ , (7.18). Thus

$$\frac{p}{\bar{p}} = \left[ 1 - \frac{\beta^2(1+g)^2}{g(1+\beta^2)^2} \right]^{-1/2}, \quad p > \bar{p} \quad (7.27)$$

$$\frac{p}{\bar{p}} = \left[ 1 + \frac{\beta_1^2(1+g)^2}{g(1+\beta_1^2)^2} \right]^{-1/2}, \quad p < \bar{p}$$

He also derived the following from the relationship

$$\gamma = \delta_1 a$$

$$\frac{d}{h} = \frac{2a}{h} = \gamma \left( \frac{\bar{p}}{p} \right) \left[ \frac{(1+\beta^2)}{3(1+g)} \right]^{1/2}, \quad p > \bar{p} \quad (7.28)$$

$$\frac{d}{h} = \frac{2a}{h} = \gamma \left( \frac{\bar{p}}{p} \right) \left[ \frac{(1-\beta_1^2)}{3(1+g)} \right]^{1/2}, \quad p < \bar{p}$$

where  $d$  is the diameter of the disk.

The above three equations, (7.26), (7.27), and (7.28) give the complete solution to the problem. The value of Poisson's ratio is determined by the material of the plate, a choice of  $\beta$  or  $\beta_1$  determines  $p/\bar{p}$  by equation (7.27) and yields an infinite set of roots of equation (7.26). Each of these roots gives a ratio  $d/h$  from equation (7.28) so that there results an infinite set of values of  $d/h$ , related to the various axially symmetric modes of vibration, corresponding to each value of  $p/\bar{p}$ .

The boundary conditions for both free and simply

supported edges are given by Timoshenko and Woinowsky-Krieger, (1959). For the former case the conditions at  $r=a$  are

$$Q_r = 0 ; \quad M_r = 0 \quad (7.24b)$$

Again by substituting the above in (7.19), (7.21) and (7.22) the following frequency equation was obtained.

$$\frac{(\sigma_1-1)}{(\sigma_2-1)} \left\{ 1 - \frac{\gamma}{(1-\nu)} \Gamma_1 \right\} = \beta^2 \left\{ 1 - \frac{\gamma\beta}{(1-\nu)} \Gamma_2 \right\} \quad (7.26c)$$

$$\frac{(\sigma_1-1)}{(\sigma_2-1)} \left\{ 1 - \frac{\gamma}{(1-\nu)} \Gamma_1 \right\} = -\beta_1^2 \left\{ 1 - \frac{\gamma\beta}{(1-\nu)} G_2 \right\} \quad (7.26d)$$

The above is a different form but equivalent to the frequency equation calculated by Deresiewicz and Mindlin, (1955), for a circular plate with a traction free edge, (equation 13 in the reference).

The simply supported edge boundary conditions are given as

$$w = 0, \quad M_r = 0 \quad \text{at } r = a \quad (7.24c)$$

This yielded the following frequency equation after application of the recurrence formulas for Bessel functions given by Spiegel, (1971), or Watson, (1922).

$$\frac{(\sigma_1-1)}{(\sigma_2-1)} \left\{ 1 - \frac{(1-\nu)}{\gamma} \Gamma_1^{-1} \right\} = \beta^2 \left\{ 1 - \frac{(1-\nu)}{\beta\gamma} \Gamma_2^{-1} \right\} \quad (7.26e)$$

$$\frac{(\sigma_1-1)}{(\sigma_2-1)} \left\{ 1 - \frac{(1-\nu)}{\gamma} \Gamma_1^{-1} \right\} = -\beta_1^2 \left\{ 1 - \frac{(1-\nu)}{\beta_1\gamma} G_2^{-1} \right\} \quad (7.26f)$$

### 7.5/ Experimental Procedure.

A mild steel clamping ring of mass 1kg was used to clamp aluminium shims of thickness 0.2 to 1.57mm and produced disks with diameters  $(36 \pm 1)$ mm and  $(15 \pm 0.25)$ mm, fig 7.1b. Studies were also made of flat-bottomed holes in order to investigate the viability of measuring resonance modes as an NDE method of inspection. For these experiments the samples consisted of 15mm thick aluminium blocks into which flat-bottomed holes of diameters between 6.35mm and 44.5mm had been milled normal to the plate surface, fig 7.1a. The amount of material left above the hole ranged from 0.5 to 2.5mm. A third set of samples was examined which were similar to the flat-bottomed holes, fig 7.1c. These were bonded samples having a well-defined natural vibrational frequency.

Pulses from the laser having energies of  $(20 \pm 2)$ mJ, which produced power densities of less than  $5\text{MWcm}^{-2}$ , were incident on the centre of the samples. Detection of the resultant acoustic response was carried out on epicentre by the wide-band capacitance device described in chapter 4.

The shims used for the fully clamped experiments were made of aluminium with the rest of the samples being fabricated from dural. The following materials constants for aluminium were used in calculations,

$$E = 70.3\text{GMm}^{-2}, \quad \rho = 2.7 \times 10^3 \text{kgm}^{-3}, \quad \nu = 0.345.$$

Kaye and Laby (1978).

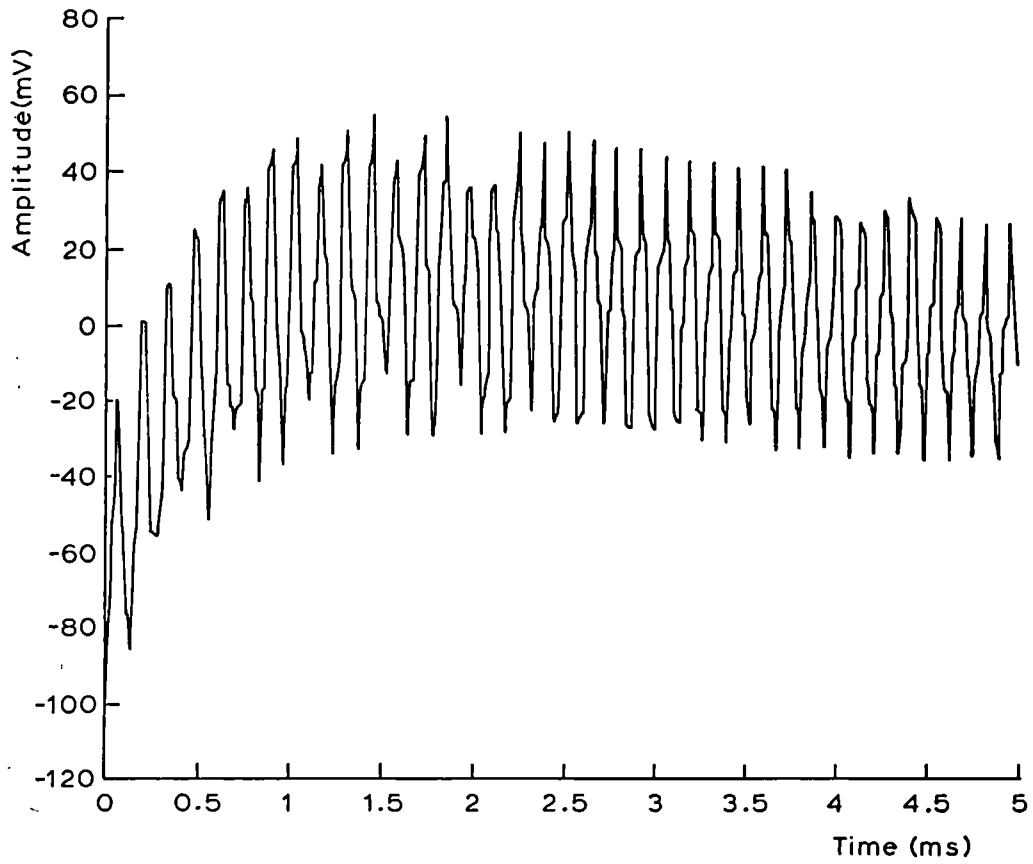
## 7.6/ Results and Discussion.

### 7.6a/ Fully Clamped Disks.

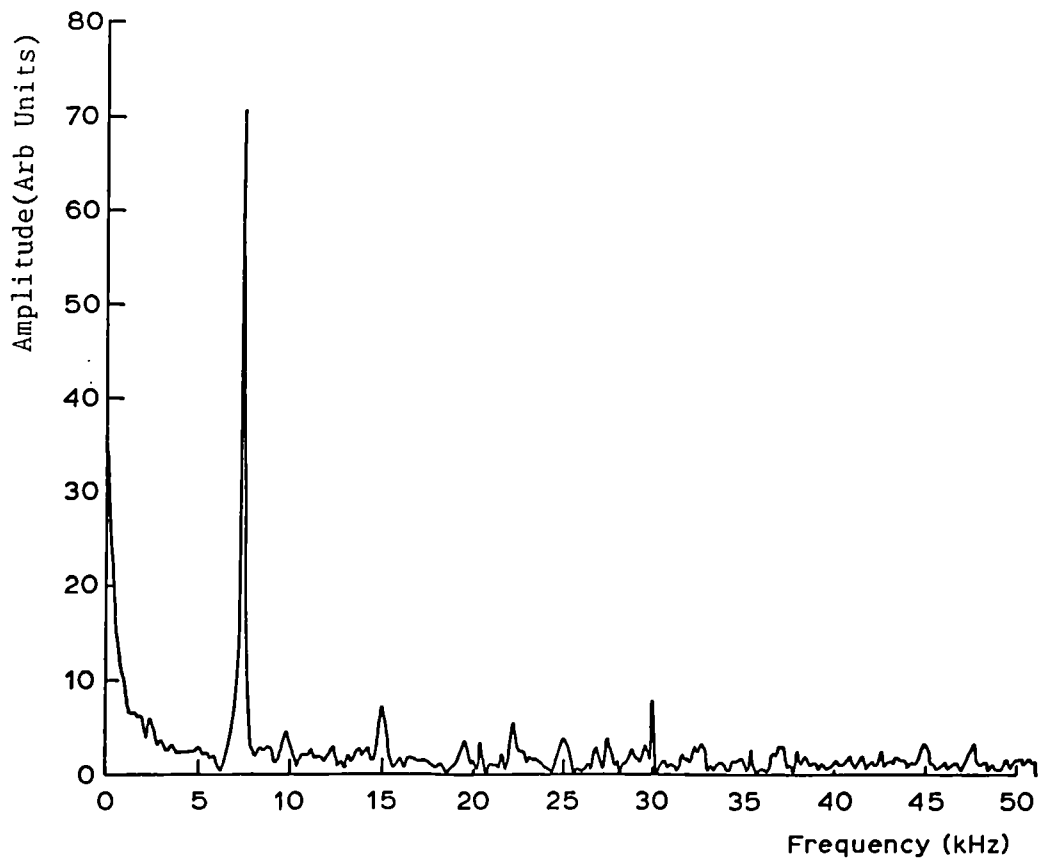
Initial experiments were carried out on the fully clamped disks, fig 7.1b, mainly to examine the region of applicability of equations (7.10) and (7.11).

Fig 7.2a shows the motion of a 1.02mm thick clamped disk of diameter  $(36 \pm 1)$ mm. A Fast Fourier Transform, (FFT), procedure was used to convert this waveform to frequency space, fig 7.2b. From the FFT the presence of not only the fundamental mode but also some higher order resonances are seen. Classical two-dimensional plate theory predicts a fundamental resonance of  $(7.9 \pm 0.45)$ kHz which compares with the major peak in the FFT centered at 7.43kHz. The second axially symmetric mode,  $\nu_{20}$ , was calculated to be  $(31.3 \pm 1.7)$ kHz which shows as the peak at 30.1kHz. A peak is also evident at 15.1kHz which may have been due to the first asymmetric mode,  $\nu_{11}$ , (Morse 1936), calculated as  $(16.7 \pm 0.9)$ kHz.

A number of samples were examined and the resultant resonant frequencies plotted against  $h/a^2$ , fig 7.3. Solid lines on the graph represent the behaviour predicted from equations (7.10) and (7.11). It can be seen that overall there is good agreement with two-dimensional plate theory for the range of sample sizes used here. The theory does however tend to overestimate the frequencies for higher values of  $h/a^2$ , this was more noticeable for the  $\nu_{20}$  resonance where shear deformation and rotatory inertia have a larger effect. The results were replotted so that



(a)



(b)

Fig 7.2(a) The displacement waveform from a fully clamped 1.02mm thick, 36mm diameter aluminium shim excited by a laser pulse.  
 (b) FFT of above showing peaks at 7.43, 15.1 and 30.1kHz.

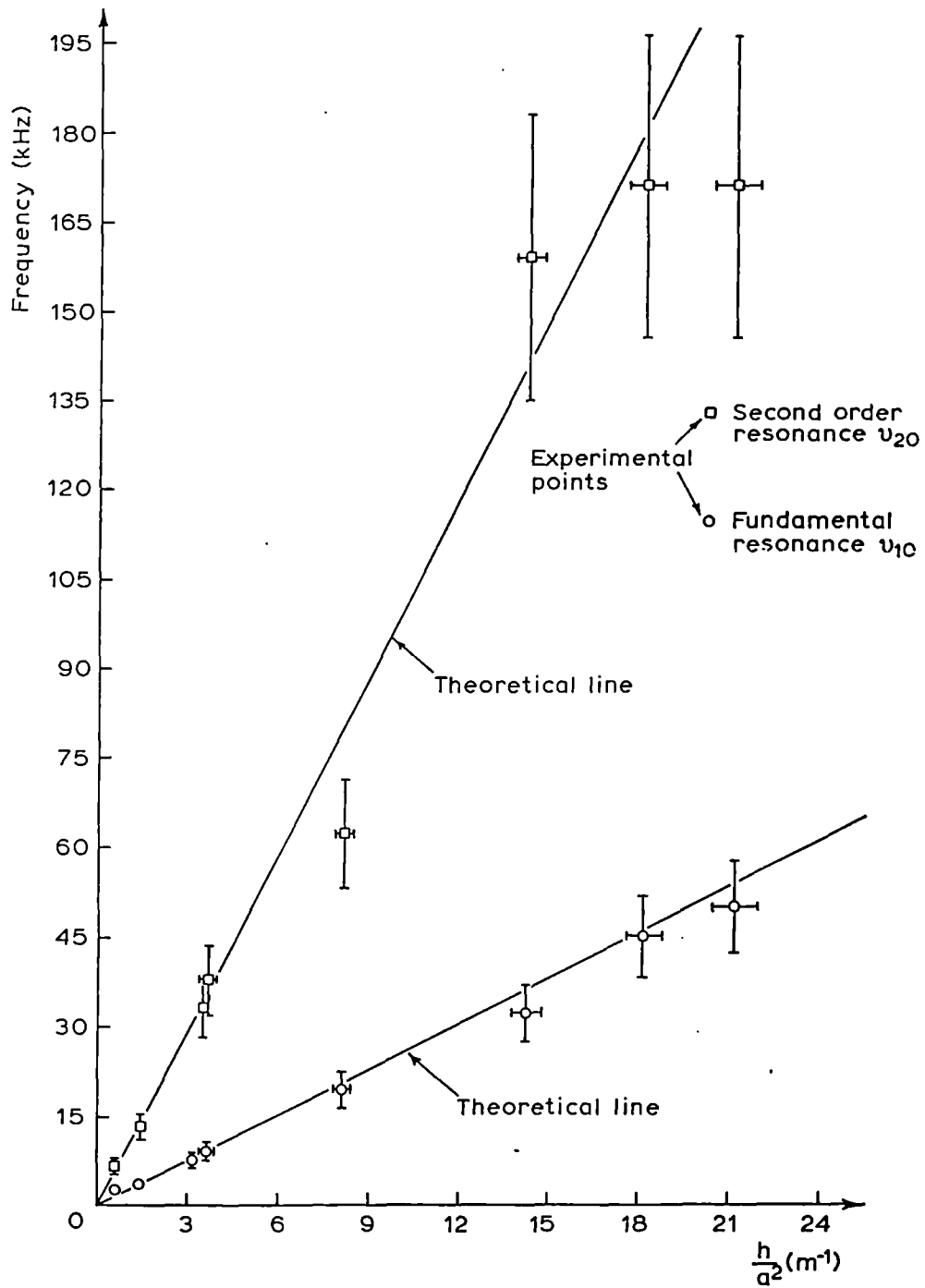


Fig 7.3 Experimentally measured values of the first two axially symmetric modes compared with values calculated from thin plate theory for a fully clamped disk.

they could be compared with the theory accounting for the effects of shear deformation and rotatory inertia, fig 7.4. It is seen that the modified theory for a clamped disk, given by equations (7.26), (7.27) and (7.28), provides a better fit for the  $J_{20}$  resonance mode for small  $d/h$ . It is for small ratios of  $d/h$  that the difference between the theories becomes more apparent and therefore this region was investigated more fully using the flat bottomed-hole samples. These were easier to examine because of their geometry. The capacitance transducer had an outside diameter of 15mm and thus the inside diameter of the clamping ring needed to be wider than this. However, for the flat-bottomed hole samples the transducer was placed close to the flat surface with the excitation laser beam incident on the milled face, enabling disks having smaller radii to be examined. The diameter of the laser beam was the limiting factor here.

#### 7.6b/ Flat-bottomed Holes.

The thickness of a plate was estimated by measuring the time taken,  $\Delta T$ , for a longitudinal pulse to propagate across the thickness of the flat-bottomed hole, given that,  $c_L$ , the longitudinal acoustic velocity in the medium was known. The initial response of the sample, fig 7.5, revealed a small high frequency periodicity in the plate motion associated with propagation of the longitudinal pulse which could be used to make this measurement.  $\Delta T$  was measured as  $(0.33 \pm 0.01) \mu s$  from fig 7.5 which gave a hole depth of  $(1.04 \pm 0.04) mm$  for  $c_L = 6320 ms^{-1}$ . This was in keeping with

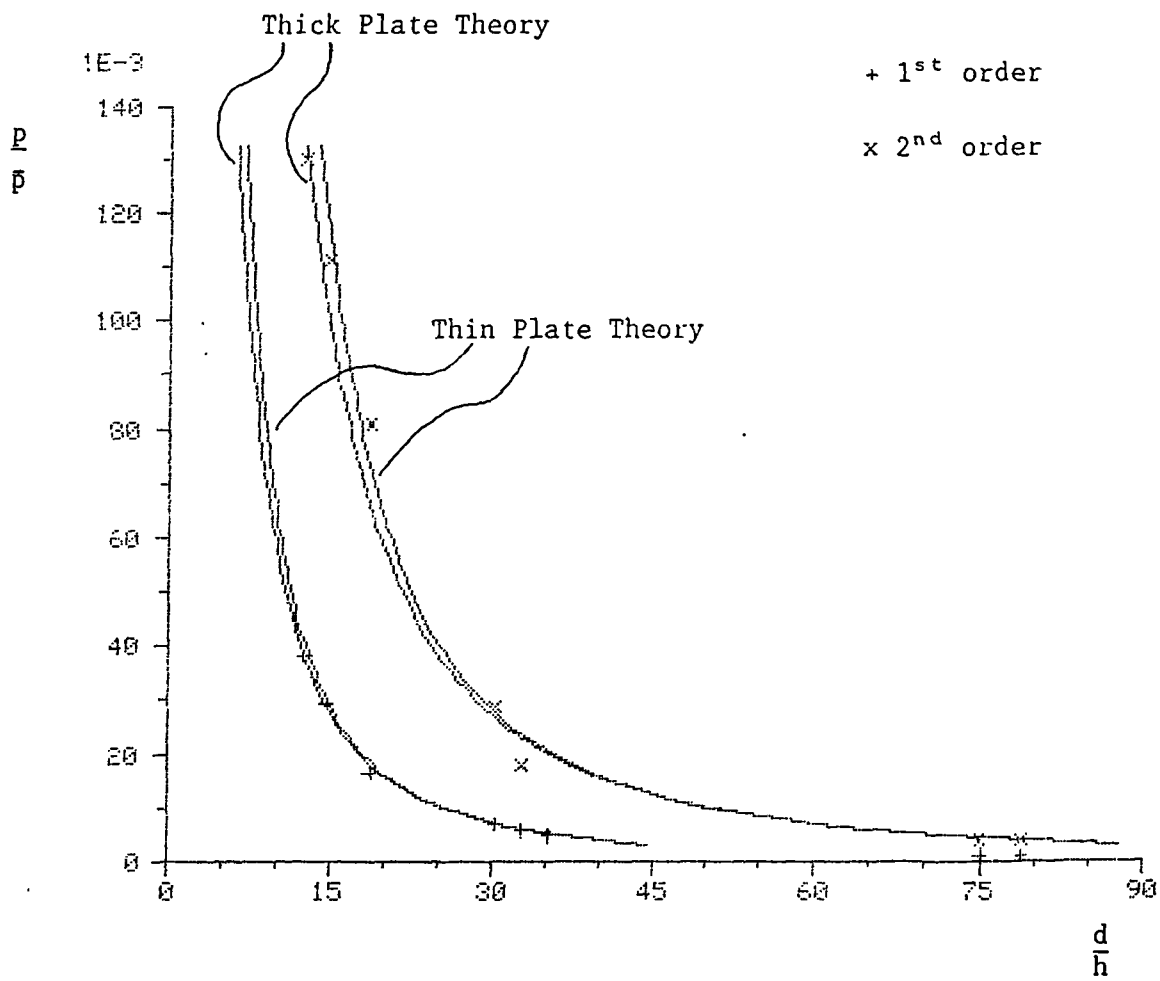


Fig 7.4 Experimentally measured values of the first two axially symmetric modes compared with values calculated from both thin and thick plate theories for a fully clamped disk.

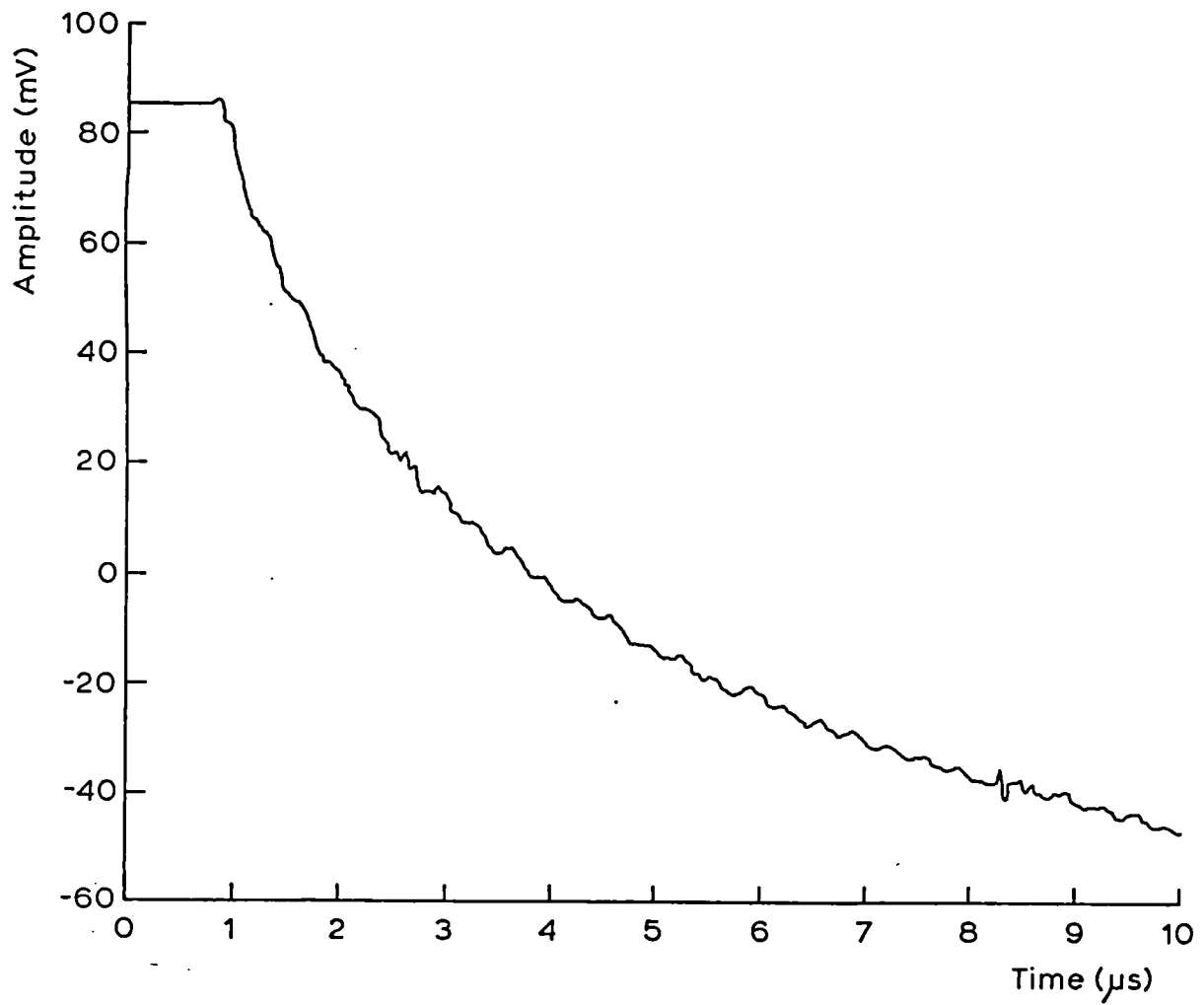


Fig 7.5 The initial elastic response of a flat-bottomed hole sample, ( $h=1.04\text{mm}$ ), to an ablation source. This shows the high frequency periodicity associated with the propagation of the longitudinal pulse.

a micrometer measurement of  $(1.04 \pm 0.03)$ mm. Additional thickness measurements were made on samples between 0.5 and 2.5mm thick, and all ultrasonic measurements were found to be within 0.05mm of the corresponding mechanical measurement using this ring-around technique. This experimentally determined thickness could then be used to calculate the frequencies of the first thickness shear modes,  $\bar{p}$ , enabling the results to be compared with both classical and modified plate theories.

Measurements of the resonant frequencies of the disks were made by examining the motion of the samples over a longer time,  $>1$ ms. The fundamental resonance modes were again plotted against  $h/a^2$  and compared with classical plate theory for a fully clamped disk, as shown in fig 7.6. From this graph it was clear that the agreement with classical plate theory was poorer when working with higher values of  $h/a^2$ . This was not thought to be solely due to the change in geometry of the sample affecting the boundary conditions, but also on the increased effects of shear deformation and rotatory inertia. The fundamental resonance mode measurements were replotted again as  $p/\bar{p}$  against  $d/h$  for comparison with both thin and thick plate theories, fig 7.7. Fig 7.7a compares the experimental frequency measurements with calculated values for plates having a free edge, fig 7.7b with a simply supported edge and lastly fig 7.7c with a fully clamped edge. It is seen from these graphs that the effects of shear deformation and rotatory inertia on the resonant frequency increases with decreasing  $d/h$  as

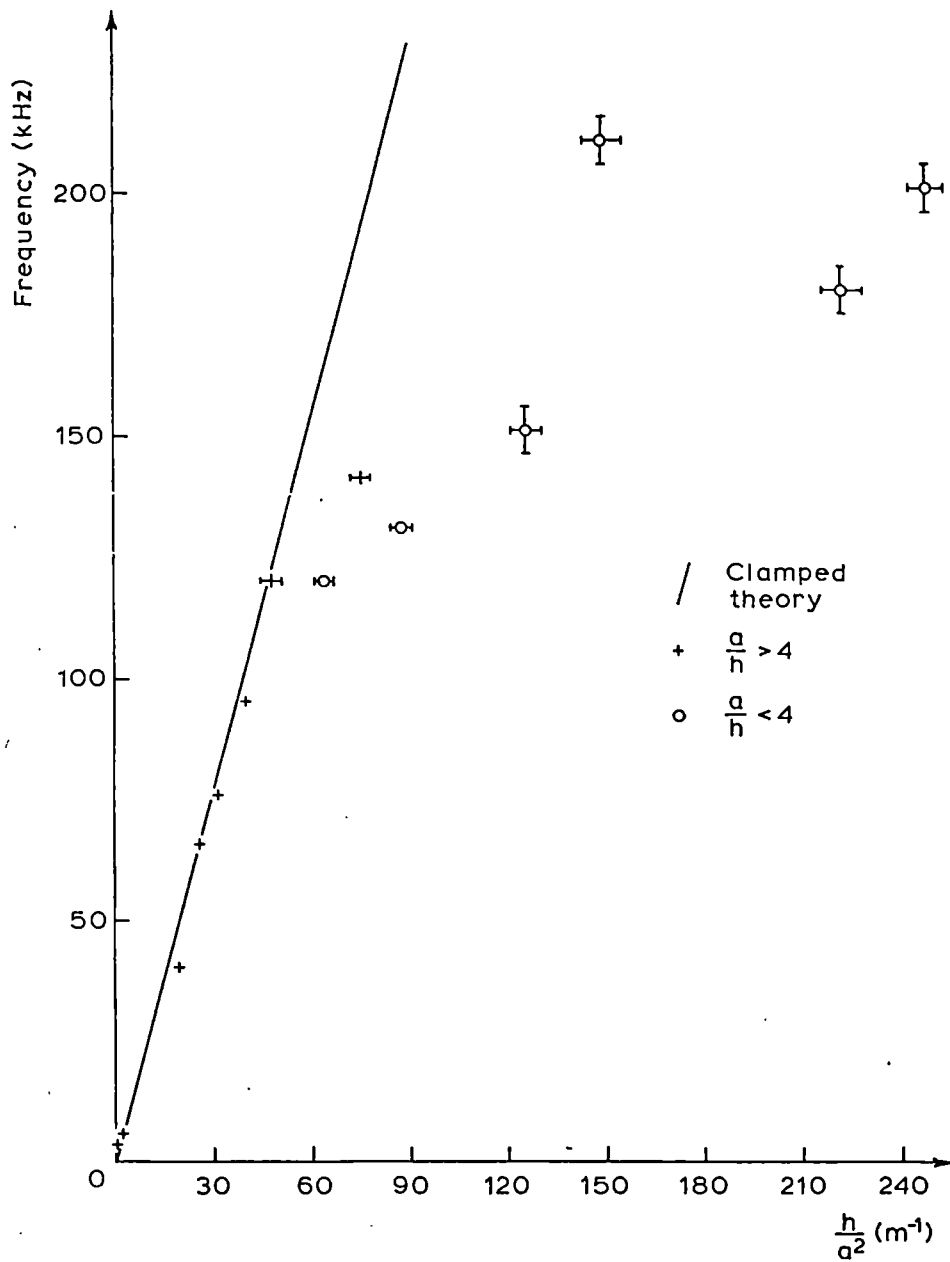


Fig 7.6 Experimentally measured values of the first axially symmetric mode of flat-bottomed holes compared with values calculated from thin plate theory for a fully clamped disk.

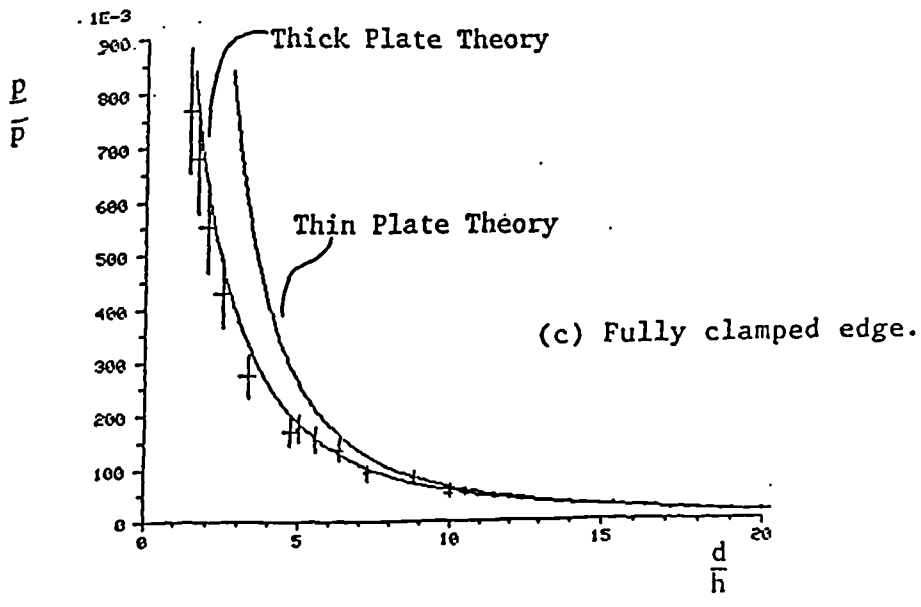
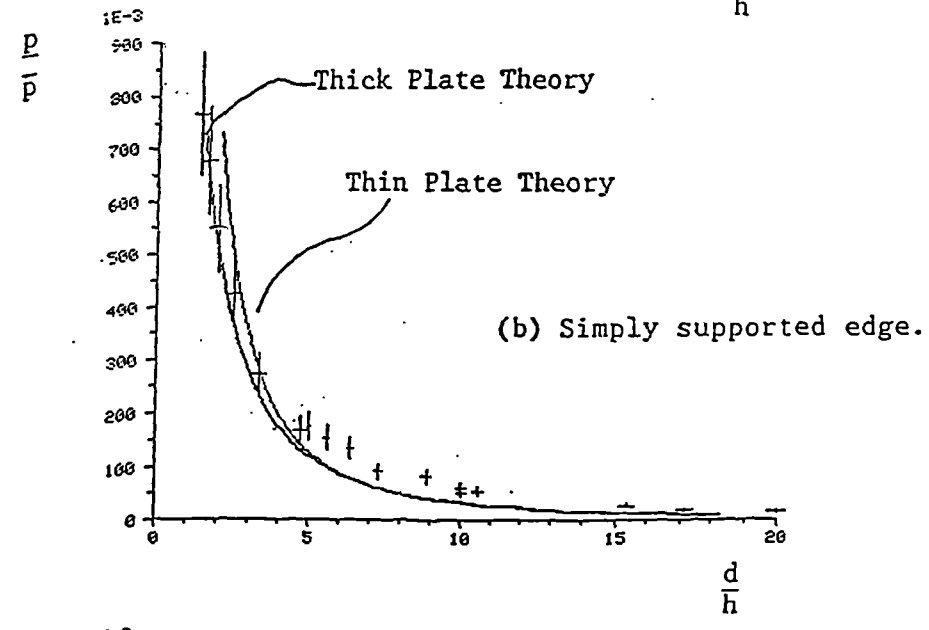
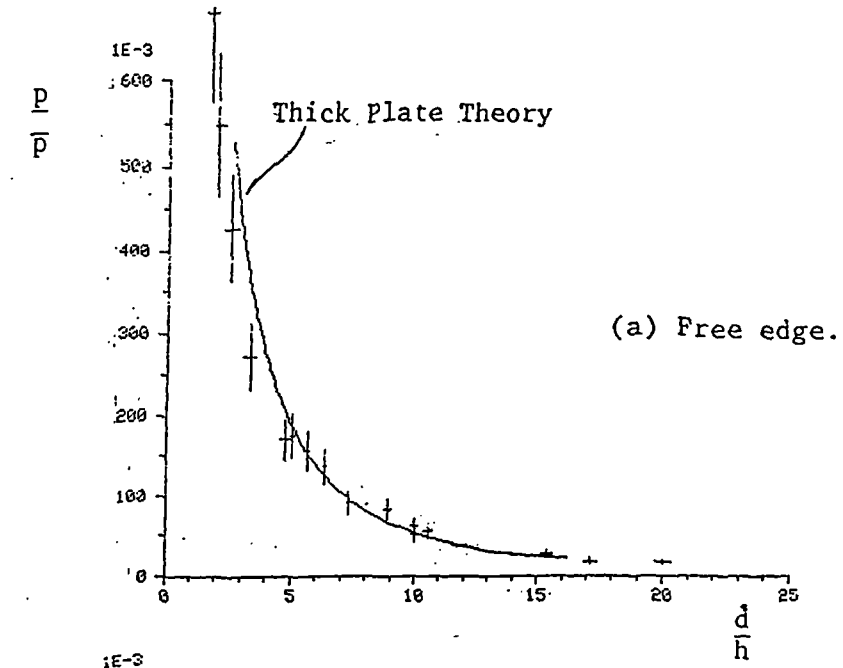


Fig 7.7 Experimentally measured values of the first axially symmetric mode of flat-bottomed holes compared with values calculated from both thick and thin plate theory with various boundary conditions assumed.

expected. Celep, (1978), using the method of initial functions, predicted that when  $d/h$  is less than 20 then classical plate theory overestimates the flexural resonant frequencies of a clamped disk, which is in agreement with the results presented here.

The simply supported edge theory, fig 7.7b, provided a poor fit to the data. The theory quickly tends to low values of frequency for large  $d/h$ , showing that the classical theory using these boundary conditions would be unapplicable for this sample geometry. When a free boundary was assumed in the theory, fig 7.7a, then the fit improved for larger  $d/h$  although the fall off at higher frequencies was more marked. The best fit to the data was given by the fully clamped case, fig 7.7c.

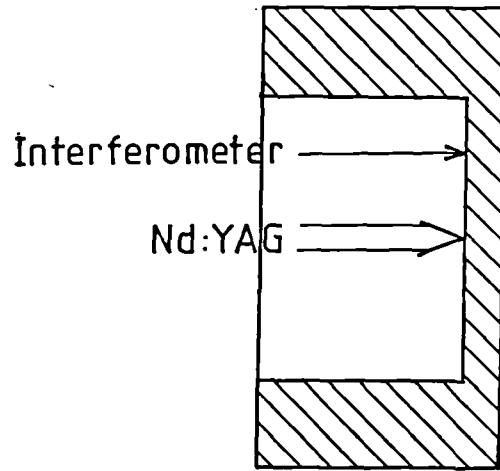
Due to this agreement we may speculate that a non-contacting NDE technique can be developed to estimate the dimensions of delaminations lying close to the sample surface. The depth of a particular defect could be measured using a ring-around longitudinal pulse as described above. With a known value of  $h$ ,  $\bar{p}$  and  $p$  may be calculated using equations (7.26), (7.27) and (7.28) and it would then be possible to infer a flaw radius by measuring the flexural resonance of the debond area. It was also observed that the amplitude of the resonant response, as well as that of the initial longitudinal elastic response, increased as the amount of material left under the hole decreased. In this region the classical thin-plate theory may be used. These techniques therefore are best suited to the detection of

laminar flaws lying close to the surface where conventional contacting ultrasonic techniques have 'dead time' problems.

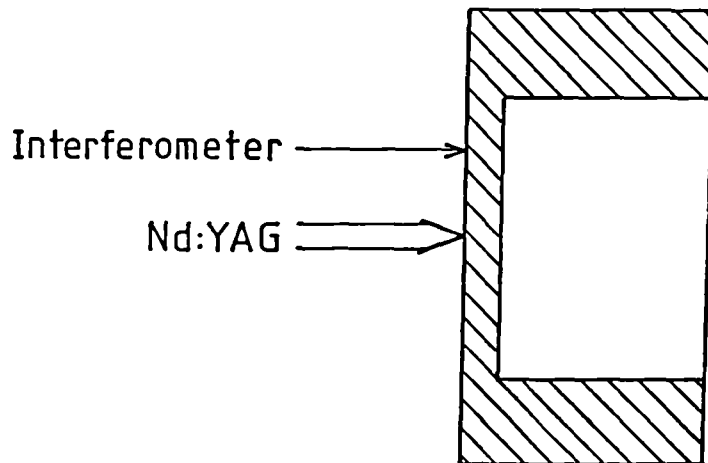
Given the boundary conditions assumed in the theory, good agreement with the flat-bottomed hole experiments may not have been expected. To examine the importance of boundary conditions a set of experiments was carried out to investigate the build up of the resonance on either face of the disk.

#### 7.6c/ Resonance Build up.

The Michelson interferometer described in Chapter 4, (McKie 1985), was used as the remote detector for these experiments. This enabled the generating and detection spots to be incident close together on the same sample face as shown in fig 7.8a. The spot from the Nd:YAG laser was incident on the centre of the disk with the detection spot about 7.5mm away. The flat-bottomed hole sample had a diameter and thickness of 55.8mm and 1mm respectively. Waveforms were collected over various time scales in order to observe the resonance building, fig 7.9. From the first of these waveforms, fig 7.9a, the first acoustic event detected by the interferometer peaked after  $\sim 3.9\mu\text{s}$  which corresponded to a velocity in the region of  $\sim 1.9\text{mm}/\mu\text{s}$ . This is slower than for a Rayleigh wave propagating along a half space due to the guiding effect of the other surface. Using this velocity the peak at  $\sim 12\mu\text{s}$  and the change in gradient at around  $25\mu\text{s}$  may be explained by assuming they came from reflections of the initial pulse off the edge of the disk. Similar features were seen over longer time scales, fig



(a)



(b)

Fig 7.8 Schematic diagrams showing the relative positions of the Nd:YAG and interferometer laser spots on flat-bottomed hole samples.

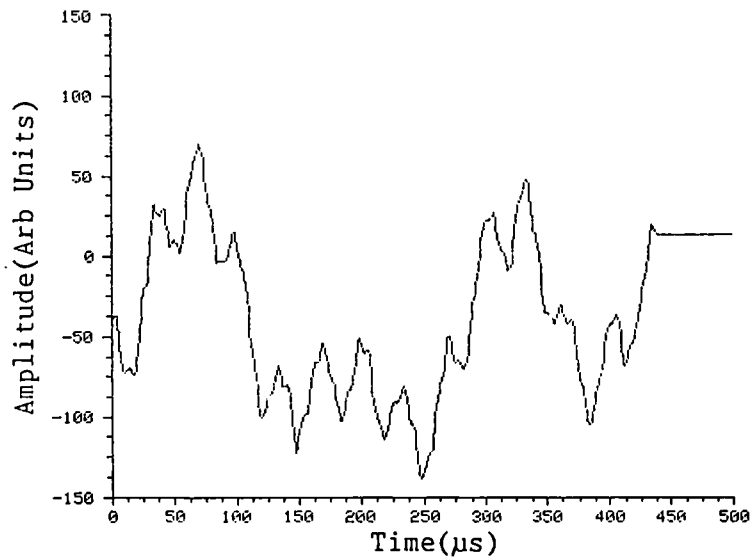
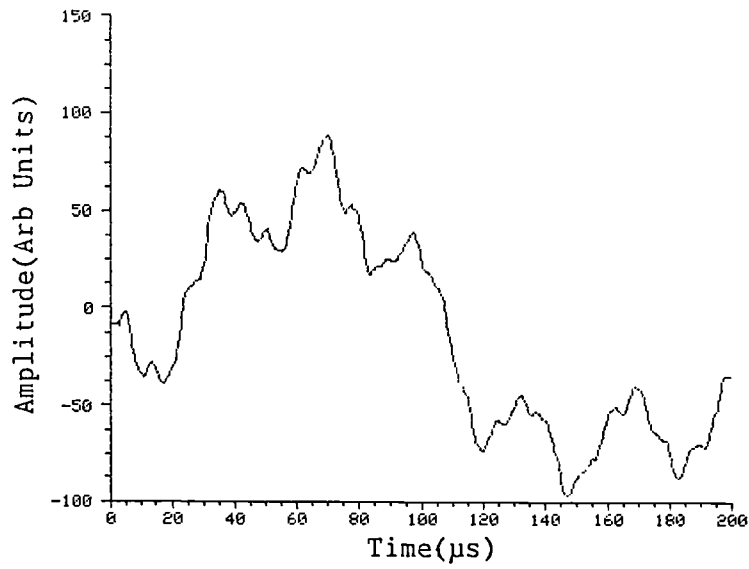
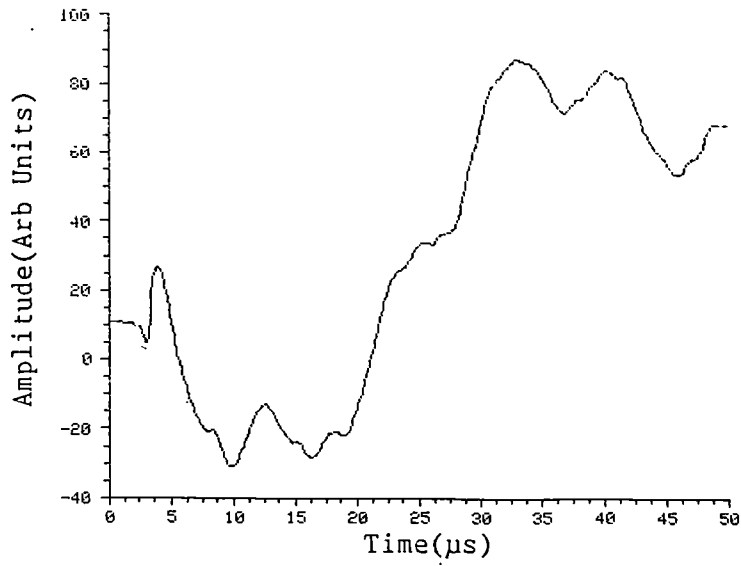
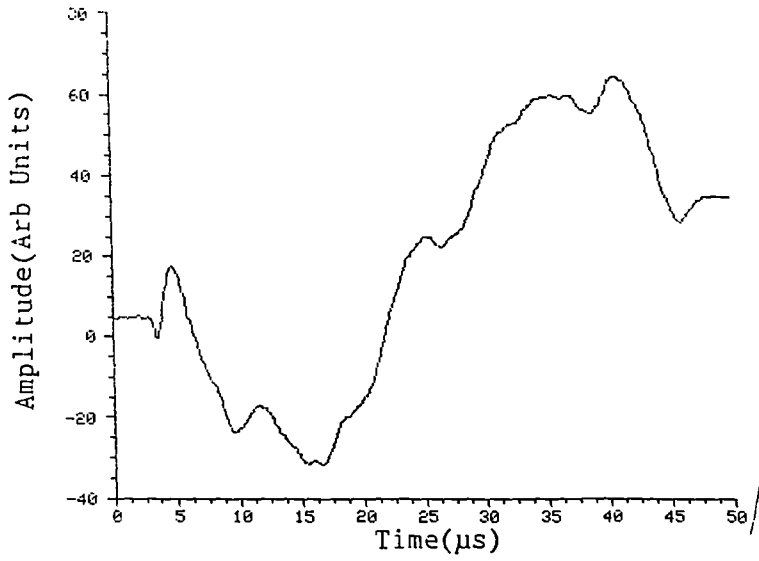


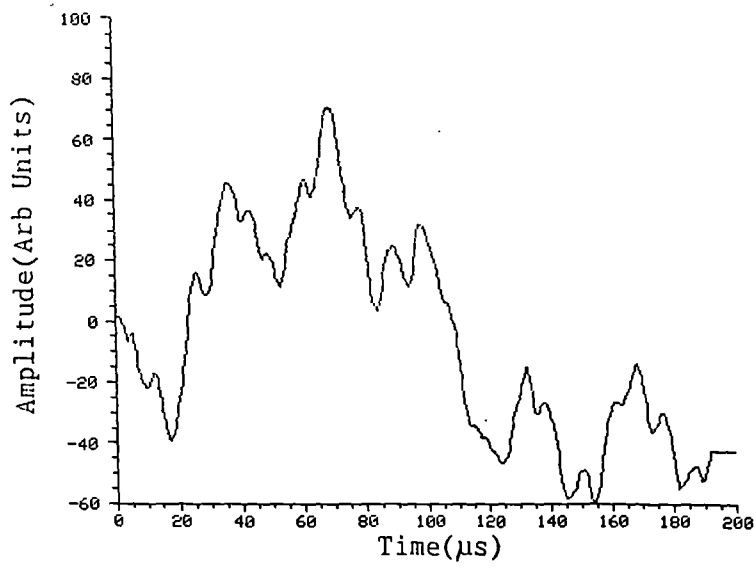
Fig 7.9 Waveforms depicting the resonance build-up in a flat-bottomed hole, for  $h=1\text{mm}$ ,  $a=27.9\text{mm}$ , set-up as shown in fig 7.8(a).

7.9b, where the initial resonance build up was starting before becoming apparent, fig 7.9c, vibrating with a fundamental frequency of  $\sim 3.3\text{kHz}$ , (period of  $\sim 300\mu\text{s}$ ).

The sample was then inverted, fig 7.8b, with the generating spot still as close to the centre as possible but now separated from the probe beam by about 9mm. The initial pulse was detected after about  $4.5\mu\text{s}$  with its reflections arriving at around  $11\mu\text{s}$  and  $25\mu\text{s}$ , fig 7.10a. This suggested that the pulse interacted with the boundary at about the same place on both faces of the sample. Despite the sample being examined on its "unclamped" face, peaks were again observed over a longer time scale, fig 7.10b, which were thought to be due to interactions of acoustic energy with the disk boundary. The similarity of the waveforms of figs 7.9 and 7.10 suggests that there was little difference experienced by the acoustic pulse between sample faces. A 1MHz Rayleigh wave propagating along a semi-infinite aluminium half space would have a wavelength of about 6mm and the acoustic events leading to the build up of the disk resonance have an upper velocity limit in the Rayleigh velocity. It is therefore understandable that the pulses observed in fig 7.10 appear to have interacted with a boundary buried at 1mm. We therefore conclude that for thin samples the ultrasonic pulses were affected by the boundary irrespective of the face they were generated and detected on.



(a)



(b)

Fig 7.10 Waveforms depicting the resonance build-up in a flat-bottomed hole, for  $h=1\text{mm}$ ,  $a=27.9\text{mm}$ , set-up as shown in fig 7.8(b).

7.6d/ Bonded Samples.

A final set of samples were examined which had a geometry similar to that of the flat-bottomed holes. Holes of various diameter were drilled through a 10mm thick block of aluminium and a sheet of aluminium was bonded to its surface using an epoxy resin, fig 7.1c. The thickness of the sheet could be accurately measured mechanically and the diameter of the disk was taken to be the same as that of the drilled hole. Sheets of 1.6 and 0.89mm thick were used with hole diameters ranging from 4.6 to 12.6mm. Certain structures, such as those used in the aviation industry have a similar geometry as the above. For example an aluminium or carbon-fibre sheet bonded to a honeycomb structure. Each section has a characteristic resonant frequency which would be affected by any bonding defect. Therefore the bonding integrity could be examined using a similar method to that used to examine the flat-bottomed holes.

The results from resonance measurements were plotted as before and are shown in fig 7.11. The agreement between experiment and theory is poorer here due to the boundary conditions not being satisfied. If it is assumed that the effective diameter of the disk is larger than the drilled hole due to the weak clamping of the resin then agreement with theory improves. In fig 7.12 a disk diameter of that of the hole plus the thickness of the sheet was assumed to achieve better agreement with fully clamped theory.

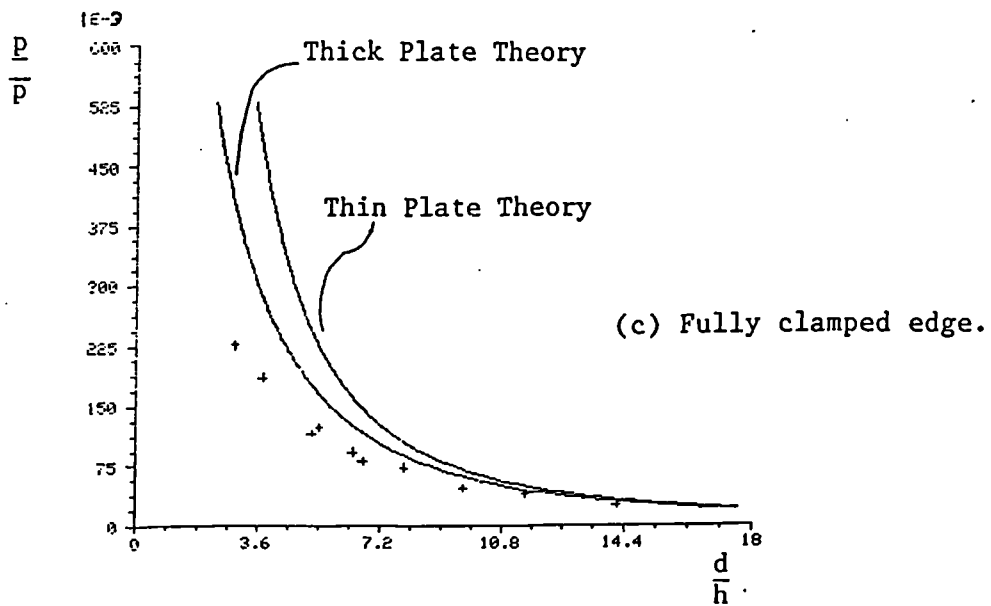
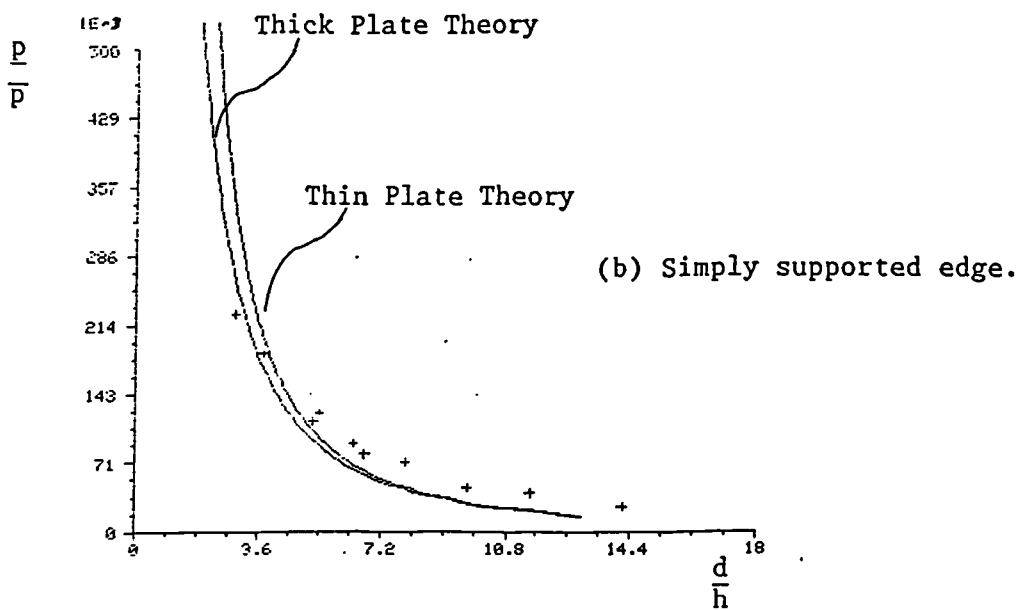
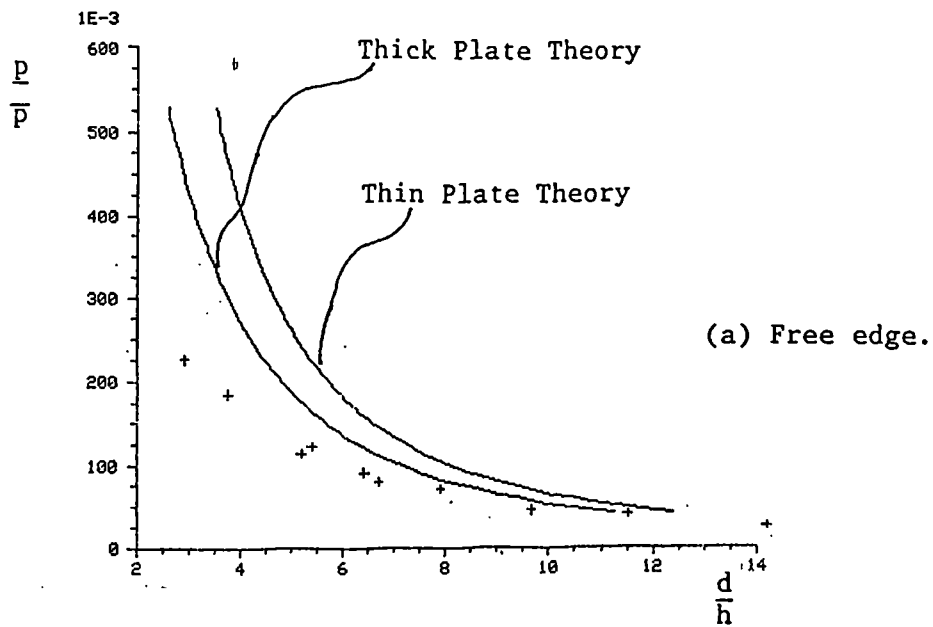


Fig 7.11 Experimentally measured values of the first axially symmetric mode of dural shims bonded over drilled dural blocks, (fig 7.1(c)), compared with values calculated from both thick and thin plate theory with various boundary conditions assumed.

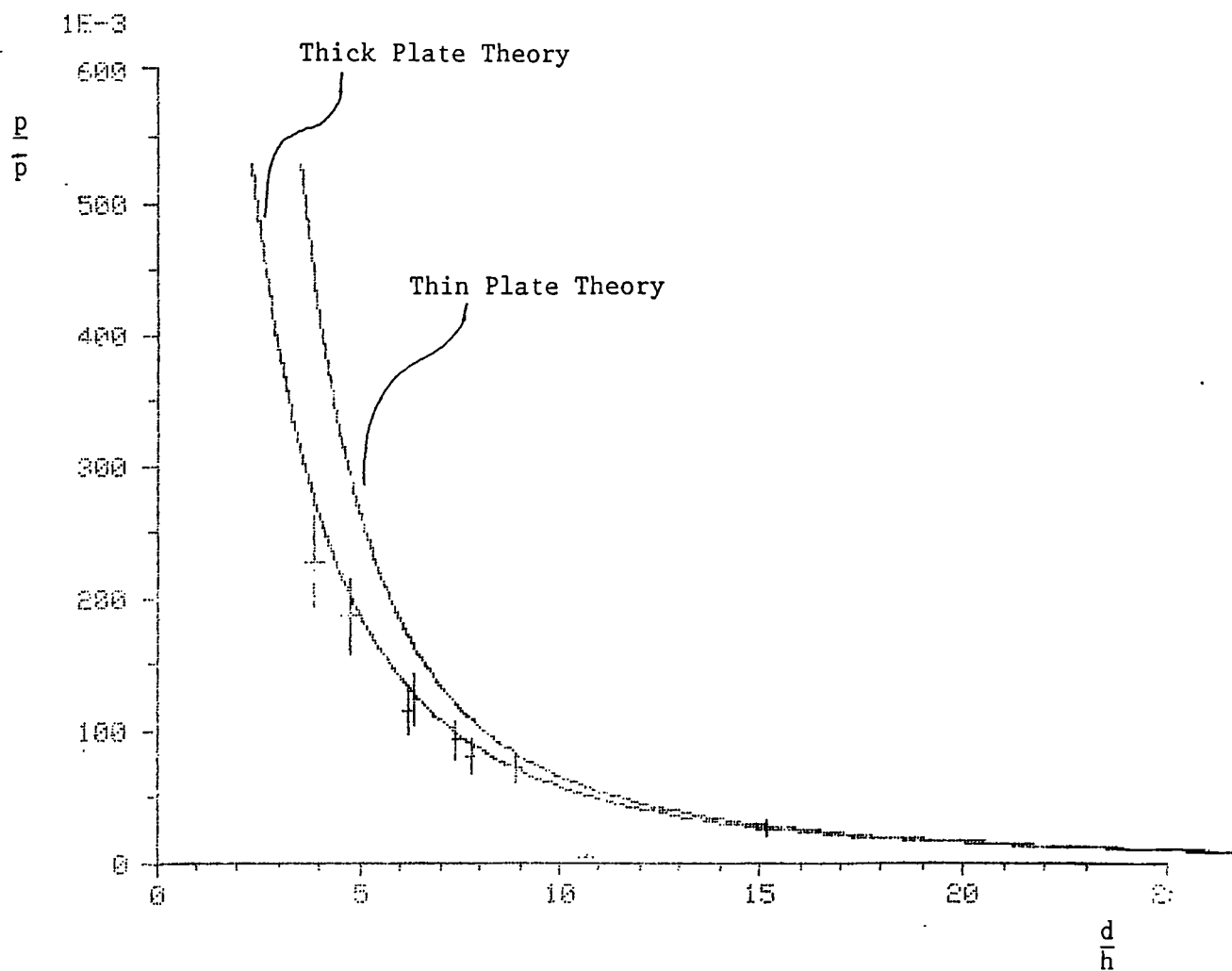


Fig 7.12 Experimentally measured values of the first axially symmetric mode of dural shims bonded over drilled dural blocks, (fig 7.1(c)), compared with values calculated from both thick and thin plate theory. A fully clamped edge and an effective disk diameter of  $d+h$  were assumed in the calculations.

### 7.7/ Conclusions.

Mindlin's treatment of circular plates has been examined and adapted to calculate axially symmetric resonant frequency modes under three sets of boundary conditions. Its deviation from classical theory, which neglected the effects of shear deformation and rotatory inertia, was also investigated.

A series of experiments was carried out to measure the resonant frequencies of fully clamped thin aluminium shims which gave good agreement with the clamped two-dimensional disk theory. The fundamental resonances of flat-bottomed holes were examined over a larger range of  $d/h$  and it was found that the best fit to these data was given by the clamped theory accounting for shear deformation and rotatory inertia effects. These two sets of results overlapped at large, ( $>20$ ),  $d/h$ . A ring-around longitudinal pulse technique was also used on these samples to measure their thicknesses. Samples of thickness 0.5 to 2.5mm were examined with the non-contacting method giving agreement to within 0.05mm of micrometer measurement. This method was suggested as a non-destructive evaluation method for the detection and sizing of delaminations lying close to the surface.

An experiment was also reported which showed that for thin flat-bottomed holes, the edge affects the ultrasonic pulse on both faces of the disk in the same manner, hence confirming that constant boundary conditions exist on either sample face.

A further NDE technique was suggested which relied on the natural vibrational frequencies of certain structures. Deviations from the expected frequency would suggest bond defects. It was found for the samples examined in this initial study that the epoxy resin used for bonding provided insufficient clamping at the boundary. This resulted in the disk having a larger effective diameter than expected, by an amount approximately equal to the plate thickness.

CHAPTER 8.

DISCUSSION.

It has been shown in this work that laser generated ultrasonic pulses can be used to locate and size defects in solids. Since we were able to generate ultrasound non-contactingly complimentary non-contacting detectors were used whenever practical. This gave systems of wide bandwidth which in many instances were suitable for scanning. Both thermoelastic, (which does not damage the sample surface), and ablation sources, (which has directivity and rise time advantages for some applications), were used in most of the methods described.

The propagation of the various acoustic modes produced by a laser source in plates was investigated in Chapter 3. Experimental waveforms were compared to those of the generalised ray theory developed by Pao et al, (1979). Generally there was good agreement, however the difference in elastic constants of the plates used in the experiments reported here and those presented by Pao et al produced discrepancies which were most noticeable on long timescales. A simpler theory based on the work of Pilant, (1979), was shown to accurately reproduce off-epicentral experimental

waveforms for small source-detector distances. The plasma source used in the experiments was unable to produce a true Heaviside force over the long timescales assumed in both theories. Discrepancies were caused both by this and the low frequency limitations of the amplifier used. The latter theory also assumed a normal Heaviside vertical force acting on a line on the surface. It was not possible to experimentally realise such a source due to the limited output energy of the laser available, however we were able to input the appropriate elastic constants to the theory through the acoustic velocities in the medium. It was found that Knopoff's, (1958), approach of evaluating only the most significant arrivals, i.e. longitudinal shear and head-waves produced adequate agreement. If required a complete evaluation of expressions (3.20), (3.27) and (3.38) convolved with the source time dependence should yield better agreement for direct pulses detected off-epicentre from the source. This would also yield an alternative method of calculating the directivity patterns given by Hutchins et al, (1981), (see Chapter 2).

Detail was given in Chapter 4 of two EMATs which were developed for use in this work. One of these devices was used for directivity measurements of polarised pulses from a thermoelastic line source. Experiments indicated that the waveforms obtained from the detection system using an out of plane sensitive EMAT was a representation of surface velocity and not displacement. These are practical non-contacting detectors which were used in experiments

reported in Chapters 5 and 6. Other detectors of ultrasound and current methods of ultrasonic NDE were also reviewed in Chapter 4.

Chapters 5, 6 and 7 concentrated on the evaluation of real and artificial surface breaking and sub-surface flaws. In the first of these chapters plasma transferred-arc depositions on steel bars were examined for surface breaking cracks and internal defects. The cracks were examined using a method similar to that of synthetic aperture focusing, the technique relying on the wide bandwidth of both the Rayleigh pulses produced by a focused laser pulse and the detection system. Crack depths of between 2.0 and 2.5mm were measured on a coating of Colmanoy 5. It was also demonstrated that an interferometer could be used on such samples hence giving not only a non-contact system but an NDE method which is remote from the test piece. Steel samples coated with Delcrome 90 were also assessed non-contactingly for bond integrity and porosity. The forward scatter of both bulk and surface ultrasonic pulses were examined from a range of samples manufactured under various conditions. The direct signal to scatter signal ratios were found to be directly related to the weld currents used during sample manufacture. Both thermoelastic and ablation sources were used with the latter producing the largest direct signal amplitudes and best reproducibility of signal to scatter ratios. This is thought to be partly due to the constant background noise included in the scatter signal although the directivity of the source is also important in certain cases.

Two techniques were described in Chapter 6 which examined plates for sub-surface flaws. The first of these was an automated system which relied on measurements of attenuation of ultrasonic pulses after transmission through thin samples. This required access to two faces of the sample and, in general, couplant between the sample and detector. It was shown that in some instances the variation in pulse transit time could also be used to detect the presence of defects. Inclusions of PTFE of dimensions 3 by 3mm and 6 by 6mm were detected successfully in sections of carbon fibre composite of thicknesses 1 to 10mm. The resolution of a small defect in the thinnest sample was better than 0.5mm. Plasma sprayed coatings on steel bars were also examined although the manufacture of these samples was such that it was difficult to ensure what the quality of bond at any given area would be. This made interpretation of the ultrasonic waveforms impossible, although the technique may still prove viable if it could be tested on better quantified samples. The technique produced data files which contained details on the signal amplitude or transit time at a given position and this information was output in C-scan format to illustrate the positions of any defects but not their depths. This method was firstly developed on a 3mm thick duraluminium sample which contained artificial defects. A second scanning technique was developed using the same sample which relied on optical detection of the ultrasound and required access to one sample face only. It is the first fully remote laser\

ultrasound system used for a two dimensional inspection of sub-surface defects.

The sensitivity of the above detection system varied due to the uneven sample surface therefore a simple single amplitude measurement was not possible. Instead the heights of a surface pulse and a bulk reflected pulse were compared and the data was displayed in C-scan format. Although this system is remote from the test piece it is currently only semi-automatic. Further work is necessary on automating sample alignment with the detection system.

In Chapter 7 sub-surface flaws are again considered although in a more specific manner. The natural frequencies of vibration of disks were calculated using both thin and thick plate theories for a range of boundary conditions. The resonant frequencies of fully clamped aluminium shims and flat-bottomed holes, representing laminar defects, were measured experimentally by exciting the disk to resonance with a laser pulse and monitoring the resultant displacements with a capacitance displacement transducer. The limitation of applicability of thin plate theory was shown. Sample thicknesses of between 0.5 and 2.5mm were measured using a ring-around longitudinal pulse technique which gave agreement to within 0.05mm of micrometer measurements. It was shown that, provided the sample had well clamped edges, the thickness and diameter of the disk shape could be assessed non-contactingly. An alternative system was suggested which investigated the quality of bonding of thin plates over structures of known geometry.

Here the thickness and other dimensions of the structure are known and resonance measurements can be used to assess boundary conditions, i.e. how well the layer is bonded to the substrate. Such a system could have practical importance in the aviation industry where materials are commonly used which consist of honeycombe structures overlaid with thin skins.

Laser based ultrasonic NDE methods have yet to find practical use in industry. A factor affecting this in the past has been the price of a complete system. However with the cost and availability of transient waveform recorders and computers improving in recent years this should no longer be a major drawback. Automation is increasingly becoming more common. Laser based techniques have advantages in scanning speed where the beam is steered instead of mechanically moving transducers. The major disadvantage to the adoption of such systems is the lack of a suitable non-contact, wideband detector which could be moved as quickly as the generating laser beam. Optical detectors which work on poor surfaces need to be further developed, however alignment will still be a problem. EMATs may prove to be suitable for many applications, although they are a compromise to some extent. They require to be just above the test piece, (~1mm), and have bandwidth limitations compared to optical devices. However as detectors of transient signals they compare favourably to conventional piezoelectric transducers, are relatively inexpensive and non-contacting. They can thus work on hot samples and do not

have couplant or wear problems.

To summarise, artificial and real defects in solids have been quantitatively detected using a variety of non-contacting, ultrasound based systems. The suitability of Rayleigh pulses for the detection of surface breaking and near surface flaws has been demonstrated. Automated systems have been developed to detect and size subsurface flaws, with further methods relying on the resonancies of well defined structures for quantitative assessment. These techniques demonstrate the suitability of laser generated ultrasound based systems for the detection of near surface defects or flaws in thin samples. The limitations of detectors currently available have been discussed with suggestions being made for future developments. It has also been shown that low incident laser power densities may be used in many applications, hence avoiding any surface damage.

REFERENCES

CHAPTER 1.

J.A. Cooper, R.J. Dewhurst and S.B. Palmer. Phil. Trans. R. Soc. Lond. A320, pp 319-328, 1986.

Y-H. Pao, R.R. Gajewski and A.N. Ceranoglu. J. Acoust. Soc. Am. 65, pp 96-105, 1979.

W.L. Pilant. "Elastic Waves in the Earth", Elsevier Scientific, Amsterdam. pp 103-118, 1979.

REFERENCES

CHAPTER 2.

- J.D. Achenbach. "Wave Propagation in Elastic Solids", North-Holland, Amsterdam, 1973.
- A.M. Aindow. PhD Thesis, University of Hull, 1986.
- A.M. Aindow, R.J. Dewhurst, D.A. Hutchins and S.B. Palmer. J. Acoust. Soc. Am. 69, pp 449-455, 1981.
- A.M. Aindow, R.J. Dewhurst and S.B. Palmer. Opt. Comm. 42, pp 116-120, 1982.
- A.M. Aindow, J.A. Cooper, R.J. Dewhurst and S.B. Palmer. In "Quantum Electronics and Electro-Optics", Ed by P.L. Knight, Wiley, pp 427-430, 1983.
- A.M. Aindow, J.A. Cooper, R.J. Dewhurst and S.B. Palmer. Proc. Ult. Int. '83, Halifax, Canada. 1983b.
- N.C. Anderholm. Appl. Phys. Lett. 16, pp 113-115, 1970.
- A. Atalar, V. Jipson, R. Koch and C.F. Quante. Ann. Rev. Mater. Sci. pp 255-261, 1979.
- Y. Bar-Cohen. Br. J. NDT. 21, pp 76-78, 1979.
- G. Birnbaum and G.S. White. "Laser Techniques in NDE", In "Research Techniques in Nondestructive Testing", vol 7. Ed by R.S. Sharp, Academic Press, New York. pp 259-365, 1984.
- A.N. Bondarenko. Yu.b. Drobot and S.V. Kruglov. Sov. J. NDT. 12, pp 655-658, 1976.
- J.I. Burov. K.P. Branzalov and D.V. Ivanov. Appl. Phys. Lett. 46, pp 141-142, 1985.
- C.A. Calder and W.W. Wilcox. Mat. Eval. pp 86-96, Jan 1978.
- P. Cielo, F. Nadeau and M. Lamontagne. Ultrasonics. pp 55-62, March 1985.

- J.A. Cooper. PhD Thesis, University of Hull, 1985.
- R.J. Dewhurst, D.A. Hutchins, S.B. Palmer and C.B. Scruby. J. Appl. Phys. 53, pp 4064-4071, 1982.
- P.A. Doyle. J. Appl. Phys. D. 19, pp 1613-1623, 1986.
- B.P. Fairand, A.H. Clauer, R.G. Jung and B.A. Wilcox. Appl. Phys. Lett. 25, pp 431-433, 1974.
- J.A. Fox. Appl. Phys. Lett. 24, pp 461-464, 1974.
- D.A. Hutchins, R.J. Dewhurst and S.B. Palmer. Acoust. Lett. 4, pp 95-99, 1980.
- D.A. Hutchins, R.J. Dewhurst and S.B. Palmer. J. Acoust. Soc. Am. 70, pp 1362-1369, 1981.
- D.A. Hutchins, R.J. Dewhurst and S.B. Palmer. Ultrasonics, pp 103-108, May 1981b.
- D.A. Hutchins, R.J. Dewhurst and S.B. Palmer. Appl. Phys. Lett. 38, pp 677-679, 1981c.
- D.A. Hutchins. Can. J. Appl. Phys. 64, pp 1247-1264, 1986.
- D.A. Hutchins and A.C. Tam. IEEE Trans. on UFFC, 33, pp 429-449, 1986.
- C.K. Jen, P. Cielo, J. Bussiere, F. Nadeau and G.W. Farnell. Appl. Phys. Lett. 46, pp 241-243, 1985.
- H.M. Ledbetter and J.C. Moulder. J. Acoust. Soc. Am. 65, pp 840-842, 1979.
- R.E. Lee and R.M. White. Appl. Phys. Lett. 12, pp 12-14, 1968.
- J.D. O'Keefe and C.H. Skeen. Appl. Phys. Lett. 21, pp 464-466, 1972.
- Y.H. Pao. "Optoacoustic Spectroscopy and Detection", Academic Press, New York. 1977.

- C.L. Pekeris. Proc. Nat. Acad. Sci. 41, pp 469-480, 1955.
- J.F. Ready. "Effects of High Power Laser Radiation", Academic Press, New York. 1971.
- L.R.F. Rose. J. Acoust. Soc. Am. 75, pp723-732, 1984.
- A. Rosencwaig. "Photoacoustics and Photoacoustic Spectroscopy", John Wiley, New York. 1980.
- W. Sachse and N.N. Hsu. "Ultrasonic Transducers for Materials Testing and their Characterization", in "Physical Acoustics" vol XIV, Ed by W.P. Mason, Academic Press, New York. PP 277-406, 1980.
- C.B. Scruby, R.J. Dewhurst, D.A. Hutchins and S.B. Palmer. J. Appl. Phys. 51, pp 6210-6216, 1980.
- C.B. Scruby, H.N.G. Wadley, R.J. Dewhurst, D.A. Hutchins and S.B. Palmer. Mat. Eval. 39, pp 1250-1254, 1981.
- C.B. Scruby, R.J. Dewhurst, D.A. Hutchins and S.B. Palmer. "Laser Generation of Ultrasound in Metals", in "Research Techniques in Nondestructive Testing", vol 5. Ed by R.S. Sharp, Academic Press, New York. pp 281-327, 1982.
- C.B. Scruby and B.C. Moss. "The Launching of Rayleigh Waves from Surface Point Sources", Harwell Report No AERE R11833, 1985.
- C.B. Scruby, R.L. Smith and B.C. Moss. NDT Int. 19, pp 307-313, 1986.
- A.C. Tam. "Photoacoustics: Spectroscopy and other Applications", in "Ultrasensitive Laser Spectroscopy", Ed by D. Klinger, Academic Press, New York. 1983.
- A.C. Tam and W.P. Leung. Appl. Phys. Lett. 45, pp 1040-1042, 1984.

A.C. Tam. Rev. Mod. Phys. 58, pp 381-431, 1986.

R.J. von Gutfeld and R.L. Melcher. Appl. Phys. Lett. 30, pp 257-259, 1977.

R.J. von Gutfeld. Ultrasonics. pp 175-181, July 1980.

R.J. Wellman. "Laser Systems for the Detection of Flaws in Solids", Harry Diamond Lab. Report No. HDL-TR-1902. 1980.

R.M. White. J. Appl. Phys. 34, pp 3559-3567, 1963.

H.K. Wickramasinghe, R.C. Bray, V. Jipson, C.F. Quate and J.R. Salcedo. Appl. Phys. Lett. 33, pp 923-928, 1978.

W.W. Wilcox and C.A. Calder. Instr. Tech. 25, pp 63-68, 1978.

REFERENCES

CHAPTER 3.

- J.D. Achenbach. "Wave Propagation in Elastic Solids", North-Holland, Amsterdam, 1980.
- L. Knopoff. J. Appl. Phys. 29, pp 661-670, 1958.
- Y-H. Pao and R.R. Gajewski. In Physical Acoustics vol 13, Ed by W.P. Mason and R.N. Thurston, Academic Press, London. pp 183-265, 1977.
- Y-H. Pao, R.R. Gajewski and A.N. Ceranoglu. J. Acoust. Soc. Am. 65, pp 96-105, 1979. (See also T.M. Proctor, F.R. Brekenridge and Y-H. Pao. J. Acoust. Soc. Am. 74, pp 1905-1907, 1983.)
- W.L. Pilant. "Elastic Waves in the Earth", Elsevier Scientific, Amsterdam. pp 103-118, 1979.
- C.B. Scruby. "Studies of Laser-generated Ultrasonic Waveforms at Different Orientations". Harwell Report, AERE-R11686, 1985.

REFERENCES

CHAPTER 4.

- R. Adler, A. Korpel and P. Desmares. IEEE Trans. on Sonics and Ultrasonics vol SU-15, pp 157-161, 1968.
- A.M. Aindow. PhD Thesis, University of Hull, 1986.
- A.M. Aindow, J.A. Cooper, R.J. Dewhurst and S.B. Palmer. J. Phys. E: Sci. Instrumen. 20, pp 204-209, 1987.
- J. Blitz. "Fundamentals of Ultrasonics", Butterworths, London, 1963.
- F.M. Boler, H.A. Spetzler and I.C. Getting. Rev. Sci. Instrum. 55, pp 1293-1297, 1984.
- A.N. Bondarenko, Yu.B. Drobot and S.V. Kruglov. Soviet J. of NDT, 12(6), pp 655-658, 1976.
- J.E. Bowers. J. Appl. Phys. Lett. 41, pp 231-233, 1982.
- L. Bui, H.J. Shaw and L.T. Zitelli. Electronics Letters, 12, pp 393-394, 1976.
- C.A. Calder and W.W. Wilcox. Proc. of the 6th International Conf. on Expt. Stress Anal. pp 181-186, 1978.
- J.A. Cooper. PhD Thesis, University of Hull, 1985.
- C.H. Desch, D.O. Sproule and W.J. Dawson. J. Iron Steel Inst. 153, pp 319-352, 1946.
- R.J. Dewhurst, D.A. Hutchins, S.B. Palmer and C.B. Scruby. Ultrasonics, pp 79-84, March 1983.
- E.R. Dobbs. "Electromagnetic Generation of Ultrasonic Waves", In Physical Acoustics, vol X, Ed by W.P. Mason, Academic Press. pp 127-191, 1973.
- D.C. Emmony, M.W. Godfrey and R.G. White. In "Review of Progress in Quantitative NDE", Ed by D.O. Thompson and D.E.

- Chimenti, Plenum Press, New York, vol 2A, pp 533-538, 1983.
- H.M. Frost. "Electromagnetic-Ultrasound Transducers: Principles, Practice and Applications", In Physical Acoustics, vol XIV, Ed by W.P. Mason, Academic Press. pp 179-275, 1979.
- F.A. Firestone. "Flaw Detecting Device and Measuring Instruments", U.S. Patent 2,280,130, 1940.
- V.F. Gantmaker and V.T. Doloplov. JETP Lett. 5, pp 12-14, 1967.
- A.O. Garg and R.O. Claus. Mat. Eval. 41, pp 106-109, 1983.
- D.A. Hutchins and J.D. MacPhail. J. Phys. E: Sci. Instrumen. 18, pp 69-73, 1985.
- D.A. Hutchins and F. Nadeau. IEEE Ult. Symp. pp 1175-1177, 1983.
- D.A. Hutchins and D.E. Wilkins. Appl. Phys. Lett. 47, pp 789-791, 1985.
- D.A. Hutchins, D.E. Wilkins and G. Luke. Appl. Phys. Lett. 46, pp 634-635, 1985.
- J. Krautkramer. Proc. of the 9th WCNDT, Cologne, 1979.
- J. Krautkramer and H. Krautkramer. "Ultrasonic Testing of Materials", 3rd Ed, Springer-Verlag, New York, 1983.
- A.D.W. McKie. 1st Year Report, University of Hull, 1985.
- V.M. Milenin, M. Fujiwara and Y. Kawai. Japan J. of Appl. Phys. 8, pp 974-975, 1969.
- J-P. Monchalain. Appl. Phys. Lett. 47, pp 14-16, 1985.
- N. Murayama, K. Nakamura, H. Obara and M. Segawa. Ultrasonics, pp 15-22, Jan 1976.
- C.H. Palmer, R.O. Claus and S.E. Fick. Appl. Opt. 16, pp

1849-1856, 1977.

J.M. Piggins and J.M. Farley. Proc. of Ultrasonics International 79. pp 339-344, 1979.

M.J. Rudd. In "Review of Progress in Quantitative NDE", Ed by D.O. Thompson and D.E. Chimenti, Plenum Press, New York, vol 2B, pp 1763-1782, 1983.

C.B. Scruby and H.N.G. Wadley. J. Phys. D. Appl. Phys. 11, pp 1487-1494, 1978.

M.G. Silk. "Ultrasonic Transducers for Nondestructive Testing", Adam Hilger, Bristol, 1984.

S.J. Sokolov. ENT Heft 11 Band 6, pp 454-461, 1929. (In German). See also "Means for Identifying Flaws in Materials", U.S. Patent 2,164,125, June 1939

J. Szilard. "Ultrasonic Testing, Non-conventional testing techniques", (Ed by J. Szilard, John Wiley & Sons, New York), 1982.

I.A. Victorov. "Rayleigh and Lamb Waves", Plenum Press, New York, 1967.

D. Vilkomerson. Appl. Phys. Lett. 29, pp 183-185, 1976.

H. Wustenberg, J. Kutzner and G. Engl. Proc. of the 8th WCNDT Cannes. Paper 3H4, 1976.

REFERENCES

CHAPTER 5.

- J.D. Achenbach, A.K. Gautesen and D.A. Mendelsohn. IEEE Trans. on Sonics and U-S. 27(3), 1980.
- A.M. Aindow, J.A. Cooper, R.J. Dewhurst and S.B. Palmer. Proc. of Ult. Int.'83. Halifax, Canada. pp 20-24, July, 1983.
- A.M. Aindow, J.A. Cooper, R.J. Dewhurst and S.B. Palmer. J. Phys. E: Sci. Instrumen. 20, pp 204-209, 1987.
- L.J. Bond. Ultrasonics, pp 71-77, March 1979.
- C.P. Burger and A.J. Testa. Proc. of Ult. Int.'81. pp 271-276. 1981.
- D. Cook. Brit. Acc. Soc. Spring Meeting, Loughborough, 1972.
- J.A. Cooper. PhD Thesis, University of Hull, 1985.
- J.A. Cooper, R.J. Dewhurst and S.B. Palmer. Phil. Trans. R. Soc. Lond. A320, pp 319-328, 1986.
- D.A. Hutchins. F. Nadeau and P. Cielo. Can. J. Phys. 64, pp 1334-1340, 1986.
- M. Hirao and H. Fukuoka. J. Acoust. Soc. Am. 75, pp 602-606, 1982.
- R.J. Hudgell L.L. Morgan and R.F. Lumb. B.J. NDT. 9, pp 144-149, 1974.
- J. Krautkramer. Proc. of the 9th WCNDT, Cologne, 1979.
- B.H. Lidington and M.G. Silk. B.J. NDT. 17, pp 165-170, 1975.
- E.A. Lloyd. B.J. NDT. 17, pp 172-176, 1975.
- W.J. McGonnagle. "Nondestructive Testing", 2nd Ed, Gordon and Breach, New York, 1971.

J-P. Monchalin. Appl. Phys. Lett. 47, pp 14-16, 1985.

C.L. Morgan. Acustica, 30, pp 222-225, 1974.

C.L. Pekeris and H. Lifson. J. Acoust Soc. Am. 29, pp 1233-1238, 1957.

I.A. Viktorov. "Rayleigh and Lamb Waves, Physical Theory and Applications", (Plenum Press; New York), 1967.

C.H. Yew, K.G. Chen and D.L. Wang. J. Acoust. Soc. Am. 75, pp 185-194, 1984.

REFERENCES

CHAPTER 6.

- D.P. Almond, P.M. Patel and H. Reiter. Journal De Physique, C6(10), pp 491-495, 1983.
- J.A. Cooper, R.A. Crosbie, R.J. Dewhurst and S.B. Palmer. Proc. Ult. Int. '85, pp 207-212, 1985.
- R.L. Cox, D.P. Almond and H. Reiter. NDT Int. pp 291-296, Dec 1980.
- B.P. Fairand and A.H. Clauer. J. Appl. Phys. 50, pp 1497-1502, 1979.
- L. Filipczinski. Proc. 3rd Nat. Conf. on NDT. Warsaw, p 499, 1966, (See also J. Blitz. "Fundamentals of Ultrasonics", 2nd Ed. Butterworths. London. p 79, 1967).
- L.J. Inglehart, F. Lepoutre and F. Charbonnier. J. Appl. Phys. 59, pp 234-240, 1986.
- A.D.W. McKie. 1st Year Report. University of Hull. 1985.
- Y-H. Pao, R.R. Gajewski and A.N. Ceranoglu. J. Acoust. Soc. Am. 65, pp 96-105, 1979.
- G. Rousset, P. Cielo and L. Bertrand. J. Appl. Phys. 57, pp 4396-4402, 1985.

REFERENCES

CHAPTER 7.

- A.M. Aindow, R.J. Dewhurst, S.B. Palmer and C.B. Scruby. N.D.T. International, 17, pp 329-336, 1984.
- R. Aprahamian and D.A. Evansen. J. Appl. Mech. 37, pp 1083-1090, 1970.
- Z. Celep. Ingenieur-Archiv. 47, pp 411-420, 1978.
- Z. Celep. J. Sound Vib. 70, pp 379-383, 1980.
- P. Cielo, X. Maldague, G. Rousset and C.K. Jen. Mat. Eval. pp 1111-1117 Aug. 1985.
- H. Deresiewicz and R.D. Mindlin. J. Appl. Mech. pp 86-88, March 1955.
- F.E. Eastep and F.G. Hemmig. J. Sound and Vib. 84, pp 359-370, 1982.
- P.S. Epstein. J. Maths. and Phys. 21, pp 198-209, 1942. H. Hencky. Ingenieur-Archiv. 16, p.p.72-76, 1947.
- G.W.C. Kaye and T.H. Laby. "Tables of Physical and Chemical Constants and some Mathematical Functions". Longman, New York, 14th Ed, 1978.
- L.E. Kinsler and A.R. Frey. "Fundamentals of Acoustics", (John Wiley and Sons, New York, 1961), pp 109-111.
- J. Krautkramer and H. Krautkramer. "Ultrasonic Testing of Materials", (3rd Ed. Springer-Verlag, New York, 1983), p 90.
- H. Lamb. Proc. Royal Soc. London, Series A, 93(648), 1917.
- A.W. Leissa "Vibrations of Plates", NASA Report NASASP-160, 1969.
- A.D.W. McKie. 1st Year Report, Hull University. 1985.
- R.D. Mindlin. J. Appl. Mech. Trans. ASME. 73, pp 31-38, 1951.

- R.D. Mindlin and H. Deresiewicz. J. Appl. Phys. 25, pp 1329-1332, 1954.
- P.M. Morse. "Vibration and Sound", (McGraw-Hill, New York, 1936), pp 173-173. See also P.M. Morse and K.U. Ingard. "Theoretical Acoustics", (McGraw-Hill, New York, 1968), pp 213-222.
- W.Nowacki. "Dynamics of Elastic Systems", (Chapman & Hall, London, 1963), pp 218-221.
- S.D. Poisson. Memoires de l'Academie, Paris, 8, 1829. See also I. Todhunter and K. Pearson. "A History of the Theory of Elasticity", (Cambridge University Press. England, 1886), Vol 1, p 262.
- Lord Rayleigh. Proc. of the London Math. Soc. London, 10. pp 225-234, 1889.
- Lord Rayleigh. "Theory of Sound", (2nd Ed. Macmillan Co. New York.), Vol 1, p 258.
- H. Reismann, D.P. Malone and S.P. Pawlik. S M Archives, 5 Issue 3, pp 253-321, 1980.
- G. Rousset, D. Levesque, L. Bertrand, X. Maldague and P. Cielo. Can. J. Phys. 64, pp 1293-1296, 1986.
- M.R. Spiegel. "Theory and Problems of Advanced Mathematics for Engineers and Scientists", (McGraw-Hill, New York, 1971), pp 224-241.
- S. Timoshenko. "Vibration Problems in Engineering", (2nd Ed. D. Van Norstrand Co. Inc. New York, 1937), p 337.
- S. Timoshenko and S. Woinowsky-Krieger. "Theory of Plates and Shells", (2nd Ed. McGraw-Hill, New York, 1959), p 171.
- Ya. S. Uflyand. Akad. Nauk SSSR. Prikl. Mat. Meh. Vol. 12,

pp 289-300, 1948, (Russian).

G.N. Watson. "A Treatise on the Theory of Bessel Functions",  
(Cambridge University Press, London, 1922), p 45 and 79.

REFERENCES

CHAPTER 8.

D.A. Hutchins, R.J. Dewhurst and S.B. Palmer. J. Acoust. Soc. Am. 70, pp 1362-1369, 1981.

L. Knopoff. J. Appl. Phys. 29, pp 661-670, 1958.

Y-H. Pao, R.R. Gajewski and A.N. Ceranoglu. J. Acoust. Soc. Am. 65, pp 96-105, 1979.

W.L. Pilant. "Elastic Waves in the Earth", Elsevier Scientific, Amsterdam. pp 103-118, 1979.